

# **Atomistic insights into flexibility of nanoporous crystals**

© 2018 Salvador Rodríguez Gómez  
*Todos los derechos reservados*  
All rights reserved

ISBN: 978-84-09-00004-3  
No commercial

*Cover image:* fractal map from a photography of a circuit board of a smartphone, done with GIMP code on 02 February 2018.

# **Atomistic insights into flexibility of nanoporous crystals**

**Perspectiva atomística de la flexibilidad en cristales  
nanoporosos**

Thesis

to obtain the Degree of Doctor of Philosophy at Pablo de Olavide University under the authority of the Rector Magnificus, Prof. Vicente Guzmán Fluja, to be defended in public on 23th March 2018 in the morning, in accordance with the decision of the Doctoral Committee

by

**Salvador Rodríguez Gómez**

a.k.a

**S. R. G. Balestra**

in Seville, Andalusia, Spain

## PhD Supervisors:

Prof. Dr. Sofía Calero Díaz

Pablo de Olavide University

Department of Physical, Chemical and Natural Systems

Dr. David Dubbeldam

University of Amsterdam

Van 't Hoff Institute for Molecular Sciences (HIMS)

## PhD Evaluation Committee:

Res. Sci. Dr. Germán Ignacio Sastre Navarro

Spanish National Research Council (CSIC)

Institute of Chemical Technology (ITQ)

S. L. Dr. Dewi Wyn Lewis

University College London (UCL)

Physical Chemistry Section

Dr. María del Rocío Sánchez de Armas

Pablo de Olavide University

Department of Physical, Chemical and Natural Systems

## PhD External Committee:

Dr. Ariana Torres Knoop

University of Amsterdam

Dr. Ana Martin Calvo

Vrije Universiteit Brussel

The research leading to these results was performed at the Department of Physical, Chemical and Natural System of the Pablo de Olavide University (Seville, Spain), at Van't Hoff Institute for Molecular Sciences of the University of Amsterdam (Amsterdam, The Netherlands) and at the Institut Charles Gerhardt of the University of Montpellier (Montpellier, France). This thesis has received funding from the European Research Council (ERC Consolidator Grant), from the Spanish *Ministerio de Economía, Industria y Competitividad* (MINECO) from the Andalusian Plan R&D&i (*Proyecto de Excelencia*), and the Netherlands Council for Chemical Sciences through a VIDI Grant. This dissertation has been supported with a predoctoral fellowship from the Spanish *Ministerio de Economía y Competitividad*.



# Contents

<b>Preface</b>	<b>1</b>
<b>Summary</b>	<b>3</b>
<b>Resumen</b>	<b>6</b>
<b>1. Introduction</b>	<b>9</b>
1.1. Nanoporous materials . . . . .	9
1.2. Flexible nanoporous materials . . . . .	13
1.3. Statistical mechanics and molecular simulation . . . . .	16
1.4. Interatomic potentials . . . . .	21
<b>2. Methodology</b>	<b>27</b>
2.1. Molecular Dynamics . . . . .	27
2.2. Lattice energy minimisation . . . . .	29
2.3. Electronic structure techniques	
Density Functional Theory . . . . .	31
2.4. Monte Carlo . . . . .	32
<b>I Zeolites</b>	<b>35</b>
<b>3. Temperature-induced zeolite framework flexibility:</b>	
<b>RHO-type zeolite I</b>	<b>37</b>
3.1. Introduction . . . . .	38
3.2. Simulation methods . . . . .	39
3.3. Results and discussion . . . . .	39
3.4. Conclusions . . . . .	48
<b>4. Structural distortions by cation migration and hydration:</b>	
<b>RHO-type zeolite II</b>	<b>51</b>
4.1. Introduction . . . . .	52
4.2. Computational Section . . . . .	55
4.3. Results . . . . .	57
4.4. Conclusions . . . . .	70

---

<b>5. Structure and stability of Ge<sup>4+</sup>/Si<sup>4+</sup> bearing STW-type zeolites</b>	<b>73</b>
5.1. Introduction . . . . .	74
5.2. Methodology . . . . .	75
5.3. Results and discussion . . . . .	78
5.4. Conclusions . . . . .	84
<b>II Metal–organic frameworks</b>	<b>85</b>
<b>6. Atomic charges for modelling metal-organic frameworks: Why and How</b>	<b>87</b>
6.1. Introduction . . . . .	87
6.2. Methods for calculating atomic charges in MOFs . . . . .	91
6.3. Learning from two examples . . . . .	96
6.4. Influence of the chosen charges on structural properties . . . . .	99
6.5. Conclusions . . . . .	100
<b>7. Changes in thermal expansion in a rigid MOF: MOF-5</b>	<b>103</b>
7.1. Introduction . . . . .	103
7.2. Conceptual Design, Methods and Computational Details . . . . .	105
7.3. Results and Discussion . . . . .	107
7.4. Conclusions . . . . .	115
<b>Conclusions</b>	<b>117</b>
<b>Conclusiones</b>	<b>118</b>
<b>Bibliography</b>	<b>123</b>
<b>Appendices</b>	<b>145</b>
<b>A. Chapter 3</b>	<b>147</b>
<b>B. Chapter 4</b>	<b>149</b>
<b>C. Chapter 5</b>	<b>153</b>
C.1. Introduction . . . . .	153
C.2. Methodology . . . . .	154
C.3. Results and discussion . . . . .	155
C.4. Supporting Information . . . . .	165
<b>D. Chapter 7</b>	<b>173</b>
<b>List of publications</b>	<b>185</b>

# Preface

How you expect to run with the  
wolves come night when you spend  
all day sparring with the puppies?

---

Omar, *The Wire*

Antes de empezar con el asunto me gustaría declarar que esta tesis no podría haberse realizado sin la ayuda y apoyo de muchas personas. Así pues comienzo este relato agradeciéndoselo a ellos. First I would like to thank my supervisors, Sofía and David. **Sofía** gracias por la confianza que pusiste en mi, por la paciencia y los consejos durante estos años. Sin tu apoyo no habría tenido oportunidad para dedicarme a la investigación, una de las cosas que más me gustan en mi vida. Gracias por poner sensatez a mis locuras. **David**, you are a great teacher who always respond kindly and promptly all my questions. Thank you for all support during this time and for being so nice with me in Amsterdam.

También quiero recordar y agradecer ahora a la gente del grupo RASPA y a otros parroquianos del Edificio 47, con la que he compartido todos estos años *laboratorio*, viajes, congresos y demás movidas científicas y académicas. Particularmente *ar cubano* y *ar pisha*, por ser tan buenos profesores y mejores personas. **Rabdel**, gracias por compartir las miles de ideas que se te ocurren y confiar ciegamente en cada una de ellas. **Said**, eres un mago de la simulación, gracias además por poner sensatez cuando se nos va la cabeza. Gracias por enseñarme tanto, socios. A **Rocío**, por los cafeses, los forfiles, las caminatas al metro, las conversaciones y discusiones. Sin ti este último año hubiera sido más complicado. A **Jose el Chico**, por enseñarme que en Córdoba también puede haber buen vino. A **Hulio**, amo y señor de Kraken y Triton, por todos estos años *trabajando* juntos. A **Jose el Padre**, anteriormente conocido como Jose el Viejo, Jose o Vicent, gracias por tu *seny* y por poner sentido común en el laboratorio. Gracias, además, por usar Fortran y no C, como quería Hulio. A **Ismael** por las conversaciones absurdas en la mesa sobre movidas raras. A **Azahara** por tu bondad innata y porque siempre eres amable. A **Paco** porque eres un tío grande y un artista. A **Patrick** por tus camisetas, tu gorro y tus primáticos. Gracias por enseñarme algunos entresijos de la simulación, sobre todo el primer año. A **Pauliña**, porque eres muy cabezona y porque te echamos de menos en el grupo. Al **OTRI**, Jose Luís, por estar con nosotros estos años, salvándonos el culo. Gracias a la *RASPA: Next Generation*, **Madero**, **Pilar**, **Carmen** y **Diego**. Because you are the future. Al **Chema**, por enseñarme las artes ocultas de las certificaciones. A **Ali**, por hacer que Nautilus sea mejor que Seaquest.

I would like to thank specially all the persons I collaborated with during these years: **Ariana**, **Krishna** (UvA), **Ricardo** (UoR), **F. Rey**, **S. Valencia**, **M. Palomino** (ITQ-CSIC), **A. Sławek**, **B. Marszałek**, **W. Makowski** (UJ), **J. Sánchez-Laínez**, **A. Veiga**, **B. Zornoza-Encabo**, **C. Téllez-Arís**, **J. Coronas** (INA), **M. Cambor**, **R. Tiago** (ICMM-CSIC), **J. Gi Min** and **S. Bong Hong** (POSTECH). I would like to thank all the members of my **Dissertation Committee**. Not only for their time to read and evaluate my thesis but also for comming to my defense.

To all the persons that become part of my life during my short stay in Amsterdam. **David** (again), **Ariana** (again), **Peter**, **Evert Jan**, **Aurora** por ser tan buena gente, **Nick**, **Jurn**, **Faidon**, **Arthur**, and others, thank you all for make Amsterdam home. I am especially grateful to Ariana, ipor darne un manta y hacerme la vida más fácil! I had a great time with all you, watching the World Cup and the pool we did.

I am also in debt with the research team at Montpellier. Thanks to **Guillaume**, **Naseem**, **Sabine** and **Pascal** for welcoming me and gave me the opportunity of work with you. It was a great and pleasant experience working with such a large group of international students: thanks to **Rocío** por las conversaciones en español, **Ioannis**, **Mohammad**, **Renjith** and others, for nice discussions in the cantine!

No puedo pasar por alto en estos agradecimientos a la gente cuyas vidas se entremezclan con la mía en estos años de tesis doctoral. Gente con la que he vivido tanto y a las que quiero muchísimo. Muchas ideas relacionadas con la tesis han surgido fuera del laboratorio, estando tranquilo, relajado y en buena compañía. Empiezo por mis compañeros de piso, los wasas. A **Pierluigi** porque eres un hermano. Gracias por traerme tantas horas de buena música a casa. A **Rocío** (again) por traernos Black Label cuando hacía falta y tener siempre la nevera llena de botellines. A **Cayetana** porque le gustan las salchichitas. A los mapashes, porque sois mi familia: **Pilar** eres un amor, **Jaime** eres un bribón, **Gome** que te gusta la natita y haces *iAs! iAs!*, **Mapashe** con *lah gafah* y *er jevi* metal, **Pierluigi** (again) con los pedazos de temazos y **Mariane** con el taconeo. Nunca olvidaré la experiencia de La Casa Mapashe, porque fue todo un mundo de recuerdos: el agüita caliente en el salón, las barbacoitas y las pedasos de fiestas en la azotea, el *solarium*, las plantitas, el chillout, las partidas de *Age of Mythology* en la red de la oficina y la bañera de botellines. A las parroquianas y parroquianos de la Jerónima, **Maraver**, el **Nota**, **Ragera** con el guitarreo, **Eva**, **Yosune** con su "hoy tienes mejor cara", el **Lolo** con los ojillos cerraos, **David**, **Concha**, . . . porque dais color a la noche, cuando vuelvo de la UPO. También quiero dar las gracias a **Celia** porque me ha enseñado mucho de Asturias y Extremadura, por su entusiasmo y *madurez* y a **Ángel** por tu constancia, entusiasmo y bondad. Os echo de menos en Sevilla. A mis amigas de la Facultad, **Domingo** todo en orden, **Carmen** mordisquitos, **Elisa** con la risa, **Ana Ansar** con la güasa, **Havi** con el youtube, **Marina Normal** con las rabo-galaxias, **Marina Fashion** por poner orden, **Amparo** por tu dinamismo vital, **JP** por tu *gracia*, la **Moreno** con su locura y amor por los animalitos y **Octavio** *porque mola mogollón*. Sois todas increíbles y un ejemplo para mí. En este momento hay que señalar, también, a aquellas personas que hicieron mi trabajo más difícil. Especialmente al Clú y sus compinches. **Vov**, **Pato**, **Mapashe** (otro) y **Gordo**: sois unos niñatos, pero os quiero. Gracias por las gambas. A ti, Gordo, gracias por las salchichas al vino, estaban espectaculares.

A **Vir**, porque admiro tu coraje, lo bondadosa y sensible que eres, tu entereza, tu capacidad crítica, tu sentido de la justicia y tu amor por los animales. Simplemente gracias por todo, por estar juntos y apoyarnos, por ser compañeros en la vida. A **Pepi**, **Marilú** y **Juanjo**, porque me tenéis muy mimado.

Por supuesto, a mis padres, **Paula** y **Federico**, porque me han apoyado siempre, por muy extrañas que les resultaran mis decisiones. Gracias por su amor y cariño. Es imposible decir en pocas palabras todo lo que hay que agradecer. Gracias a mi hermano **Fede**, porque siempre has sido un apoyo y un guía para mi. Estando cerca o lejos, te tengo presente. Pero mejor cerca, pisha. A **Nadja**, que tiene una sólo neurona pero mucho amor y a la **Gorda**, porque hemos crecido juntos y te echo de menos. A mis tíos: **Lurde**, er **Juaqui** y ar tito, **Antonio José**. A mi prima **Lurde**, que te quiero mucho y, por supuesto, a mis abuelos, a los que tengo presente siempre.

Gracias.



# Summary

This thesis is focused on the study of nanoporous soft crystals. Atoms in crystalline material in general fluctuate around their equilibrium positions. External stimuli and thermal effects distort the atoms, possibly resulting in a loss of crystallinity. The main **hypothesis** of the dissertation that I present is: *a)* the lack of crystalline regularity has an impact on the microscopic porosity, the void-channels and pockets available to guest molecules, and an effect in the sorption- and transport-properties, but likewise *b)* adsorbates could affect the pore structure, in a bidirectional causal relation, and *c)* these phenomena can be modelled with appropriate simulation techniques.

The aim and scope of the thesis is twofold:

1. To study thermal-induced and guest-induced distortions in soft nanoporous materials by means of computer simulation.
2. To develop new computational algorithms which improve the efficiency of simulations and ensure convergence to true equilibrium.

This thesis is structured as follows:

Chapter 1 covers the theoretical basis behind this study. The detailed methodology, as well as hardware and software specifications required for all the analyses, is presented in Chapter 2. The main results are divided in two well-differentiated parts. The first part covers structural distortions in zeolitic materials: pure silica and aluminosilicates. In Chapter 3, we cover in detail, within a molecular mechanic approach, how temperature can induce phase transitions between two space groups in the zeolite RHO. As we will see, this is achieved by studying the structural distortions of these zeolites as a function of varying many input parameters. Following this result, in Chapter 4 I study the *migration* of extra-framework cations and the effect they have on the phase transitions covered in Chapter 3. Interestingly, the pressure-temperature effect and the effect of the collective migration of *influential* guest (extra-framework cations and water) on the structure are related, and a good agreement with experimental data is found. The results are obtained using the "hybrid-MC/EM/MD" method, a new methodology for calculations for simulations of flexible structures with guest-molecule present. In Chapter 5, we covers in detail the  $\text{Ge}^{4+}/\text{Si}^{4+}$  cation distribution in the whole compositional range ( $\text{Ge}_f = \text{Ge}/(\text{Ge}+\text{Si}) = 0$  to 1) of zeolite STW and their effect on the structural stability. This is achieved by using an Effective Hamiltonian which deals with the problem related to the colossal configuration space.

In the second part of this thesis, the influence of relative big linkers on the structural changes of metal-organic frameworks is investigated. In Chapter 6 the calculation of atomic charges of nanoporous crystals, including an in-depth discussion of the state-of-the-art methods, is presented and applied to two cases of metal-organic frameworks: MOF-5 and DMOF-1. Chapter 7 deals with the dramatic effect of the molecular pressure on controlling the thermal expansion of MOFs, showing negative, zero and positive regimes in MOF-5.

The final part is dedicated to the conclusions as well as a brief discussion on the perspective this work can have for future work-directions.

# Resumen

Esta tesis está orientada al estudio de cristales nanoporosos flexibles. Como se verá a lo largo del desarrollo del trabajo, algunas consecuencias y consideraciones emergen al tener en cuenta que los átomos del cristal pueden moverse más allá de los límites que marcan las fluctuaciones térmicas. A esto hay que añadir una posible pérdida de la regularidad cristalina. La principal **hipótesis** de este trabajo de tesis es: *a)* la disminución de regularidad cristalina tiene un impacto en la porosidad microscópica accesible, en general, a adsorbatos, y un efecto en las propiedades de adsorción y transporte, pero a su vez *b)* los adsorbatos pueden afectar la estructura del poro en un proceso de retroalimentación causal, *c)* siendo estos fenómenos modelables usando las técnicas apropiadas de simulación.

Los objetivos de esta tesis son:

1. Estudiar las distorsiones inducidas por la temperatura y por moléculas adsorbidas en materiales nanoporosos flexibles mediante simulación por ordenador.
2. Desarrollar algoritmos computacionales que mejoren la eficiencia de estas simulaciones y que aseguren una convergencia real a estados de equilibrio.

La tesis se estructura de la siguiente manera:

El Capítulo 1 está dedicado a cubrir los aspectos teóricos en los que se basa el estudio. Una detallada metodología, tanto como las especificaciones de hardware y software requeridos en los análisis se presentan en el Capítulo 2. Los resultados principales se dividen en dos partes. La primera estudia distorsiones estructurales en zeolitas de varias composiciones: pura sílice y aluminosilicato. En el Capítulo 3 se estudia con detalle, desde una perspectiva de la mecánica molecular, la forma en que la temperatura induce transiciones de fase entre dos grupos espaciales de simetría en la zeolita RHO. Como se explicará, esto se consigue estudiando las distorsiones de la zeolita variando parámetros en su mecánica. Siguiendo estos resultados, en el Capítulo 4 se estudian las *migraciones* de los cationes y su efecto en las transiciones de fase vistas en el Capítulo 3. Sorprendentemente, los efectos de presión y temperatura están conectados a los efectos de migraciones de moléculas que interaccionan fuertemente con la estructura (cationes libres y agua), además de los acuerdos con los resultados experimentales son muy buenos. Los resultados se obtienen siguiendo el método híbrido de MC/EM/MD, una nueva metodología implementada para el estudio de estructuras flexibles (adsorbentes) y (adsorbatos). En el Capítulo 5 se estudia con detalle la distribución de cationes  $\text{Ge}^{4+}/\text{Si}^{4+}$  en el germanosilicato STW y su

efecto sobre la estabilidad estructural. El estudio se hace usando un hamiltoniano efectivo que estudia el gigantesco espacio de configuración en todo el intervalo  $Ge_f = Ge/(Ge+Si) =$  de 0 a 1.

En la segunda parte de la tesis se investiga la influencia de ligandos relativamente grandes sobre los cambios estructurales en redes metalorgánicas. En el Capítulo 6 el cálculo de cargas atómicas en cristales nanoporosos, con una amplia discusión de los métodos más avanzados y recientes. Esto se aplica a dos tipos de redes metalorgánicas: MOF-5 y DMOF-1. En el Capítulo 7 se aborda el tremendo efecto que ejerce la presión molecular en el control de la expansión térmica en redes metalorgánicas, mostrando regímenes negativos, cero y positivos para el MOF-5.

La parte final de la tesis está dedicada a las conclusiones y discusión breve de la proyección que puede llegar a tener este trabajo en el futuro.

---

# Chapter 1

## Introduction

There were many paths that led up into those mountains, and many passes over them. But most of the passes were infested by evil things and dreadful dangers.

---

*The Hobbit, J. R. R. Tolkien*

### 1.1. Nanoporous materials

Nanoporous crystals –such as zeolites, metal-organic frameworks (MOFs) or covalent-organic frameworks (COFs), form an interesting family of materials. Its relevance in the scientific community has been growing in the last decades.<sup>1</sup> These nanoporous crystals exhibit a huge variety of structural properties which are characterised by high surface area and pore volume. They possess a wide range of structural topologies with tunable regularity structures and interesting host-guest complexation behaviour [1].

Zeolites were the first porous crystals to be widely studied. Towards the end of the 1930s zeolitic structures such as analcite, cancrinite, natrolite and sodalite, were reported by Taylor [2], Pauling [3] and Bragg [4] and Taylor [5]. Nowadays, more than 230 different zeolite topologies are identified [6] by diffraction techniques. Zeolites have a three-dimensional framework of  $\text{TO}_4$  tetrahedra, assembled through oxygen atoms in Secondary Building Units (SBUs) such as cubes (double four-rings or D4R) or octahedra (single eight-ring, S8R), among other configurations. These units are linked in

---

<sup>1</sup>Although this growing interest is not restricted to the scientific community. They have a wide variety of uses, including separation and storage of different compounds. Most compounds frequently used in the chemical or pharmaceutical industry are naturally found in an impure state and nanoporous materials act as molecular sieves for this indispensable separation. Synthetic drugs, petroleum industry or purification of metals are examples of the polyvalency of these crystals.

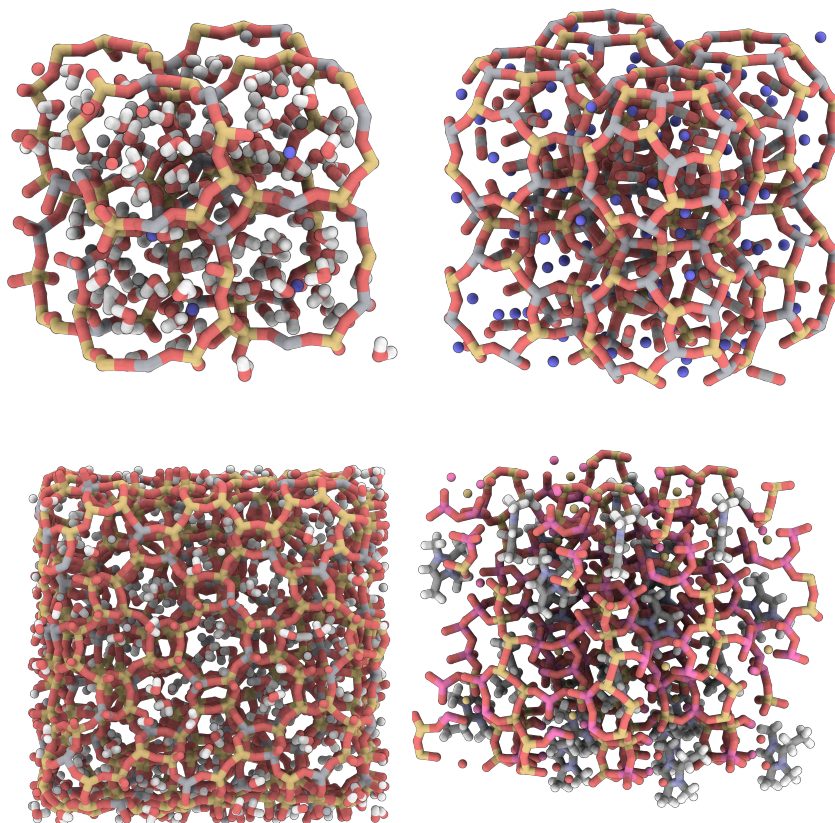


**Figure 1.1:** Top-Left: Hydrated CHA-type zeolite or Chabacite with  $\text{Si}/\text{Al} = 2.5$  with  $\text{Na}^+$  and  $\text{Ca}^{2+}$  cations. Top-Right: Adsorption of  $\text{CO}_2$  in dehydrated Linde Type A (LTA) with  $\text{Si}/\text{Al} = 1$  and 96  $\text{Na}^+$  per unit cell. Bottom-Left: Hydrated PAU-type with  $\text{Si}/\text{Al} = 4.3$  with  $\text{Sr}^{2+}$  cations. Bottom-Right: STW-type germanosilicate zeolite, a flexible structure with a helicoidal medium pore channel. In the snapshot are showed the organic structure directing agents (SDA) –i.e. 2-ethyl-1,3,4-trimethylimidazolium organic cation, and fluoride anions. All snapshots are taken from molecular dynamic simulations at 300 K.

a way that form a regular 3-dimensional structure (framework), which contains *pores*, *windows* and *channels* of molecular size (circa 3–10 Å in diameter). This porosity is reflected the fact that between 20 and 50% of the volume of a zeolite structure is empty and, in general, accessible to guest molecules. The central T atom is usually either silicon or aluminium. However, in the last decades new materials have been synthesised where the  $\text{Si}^{4+}$  or  $\text{Al}^{3+}$  ion are substituted by  $\text{Ga}^{3+}$ ,  $\text{Br}^{3+}$  or  $\text{Ge}^{4+}$ . Aliovalent substitutions change the overall charge within the framework, but the zeolite must

remain neutral. This negative charge is, then, balanced by an extra-framework cation. The chemical formula of aluminosilicate zeolite is:  $\text{Me}_{x/n}^{n+}[(\text{AlO}_2)_x(\text{SiO}_2)_{1-x}]@w\text{H}_2\text{O}$ , where Me is the cation (organic or inorganic),  $n$  their valence,  $x$  the molar fraction of Al atoms and  $w$  the number of water molecules in the unit cell of the structure. The  $\text{Al}^{3+}/\text{Si}^{4+}$  cation-ordering stability is governed by well-known rules, established by Lowenstein and Dempsey [7, 8]. They state that no Al-O-Al chains are allowed and the number of Al-O-Si-O-Al chains must be minimised (or, what is equivalent the Al-Al pair distance is maximised). In some particular cases, however, these rules are broken. The presence of divalent cations  $\text{Me}^{2+}$  allows the Al-O-Si-O-Al chains are stabilised. As a matter of fact, the heteroatom distribution in zeolite frameworks has been subject of major interest for a long time, with some controversial issues arising, such as the much debated  $\text{Si}^{4+}/\text{Ge}^{4+}$  cation distribution.

Extra-framework cations are linked to the oxygen atoms of the framework through relatively weak ionic interactions compared to the stronger covalent bonds of the atoms that form the framework. For this reason, extra-framework cations have a high degree of mobility and can *migrate* from its preferential cation sites to another. We will see that these extra-frameworks cations play a very important role in adsorption properties at zeolites because of their electrostatic nature.

Zeolites normally exhibit high surface area, thermal stability (at high Si/Al ratio at least), ion exchange capacity and, of course, catalytic capacity. A notable feature of the high Si/Al ratio zeolites (those that appear in nature, also called natural zeolites) is its hydrophilic character, which is the reason behind the fact that these zeolites are often saturated with water. This hydrophilic character is due to various reasons : 1) relative large ratio of surface area per crystal volume, 2) presence of extra-framework cations, 3) existence of dipoles between crystallographic defects of aliovalent substitutions in tetrahedra. The two last conditions become weaker as Si/Al ratio increases, which eventually leads to a phase transition from hydrophilic to hydrophobic behaviour for ratios close to 8–10. As an example of this behaviour we have the silicalite structure (MFI-type pure silica structure or ZSM-5), which has a higher adsorption for paraffin compared to water [9].

Metal-organic frameworks (MOFs) are a relatively new class of porous materials formed by the assembly of inorganic metal clusters and organic ligand linkers. The first appearance of these crystals was in 1995 [10], a structure with the formula  $\text{Cu}_2(4,4'\text{-bipy})_3(\text{NO}_3)_2$ . However, there were the two subsequent structures synthesised in 1999, named MOF-5 [11] and HKUST-1 (or Cu-BTC) [12], which have largely fuelled the explosion of interest for these materials. More than 20,000 different MOFs have been reported [13] in the past two decades, and possibly many more will come. Due to the large diversity in metal nodes and organic linkers available as chemical building blocks, as well as their variable topological connectivity, the potential for new MOFs creation is almost limitless. However an increase of the topological connectivity decreases the probability of the synthesis because the rearrangement among linkers and nodes is harder. Metallic centres can be hidden or exposed to the pore (so-called open-metal sites) improving some interesting properties, like adsorption or catalysis, but can decrease the MOF stability by humidity influence too.

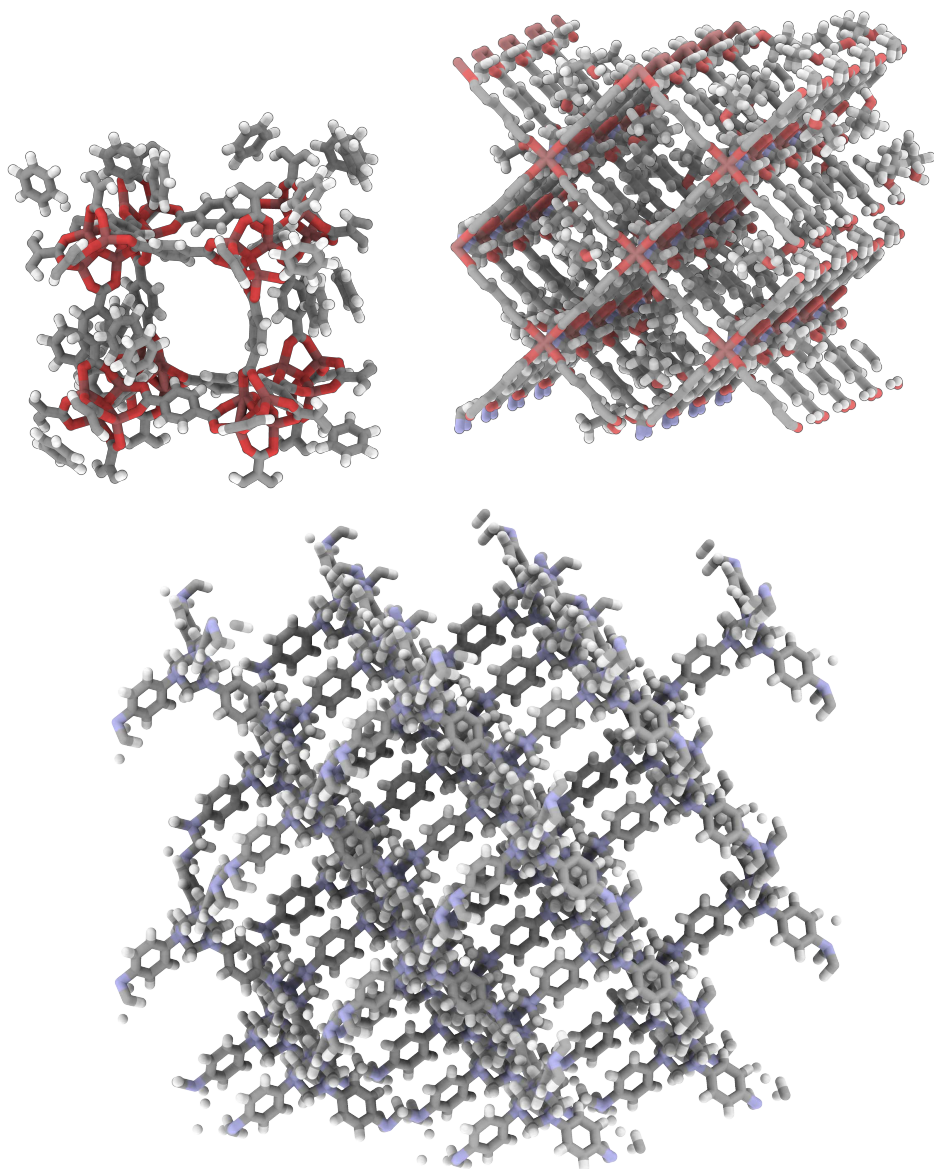


**Figure 1.2:** Top Left: Adsorption of benzene in IRMOF-1 or MOF-5. Distortions in ligands can be distinguished. Snapshots are taken from molecular dynamic simulations in the  $N\sigma T$  at 450 K. Top Left: Snapshot from MC simulations of isopropanol in DMOF-1 in the  $\mu VT$  ensemble. Bottom: Hypothetical COF with tetrahedral structure of diamond. The structure was obtained from energy minimisation calculations.

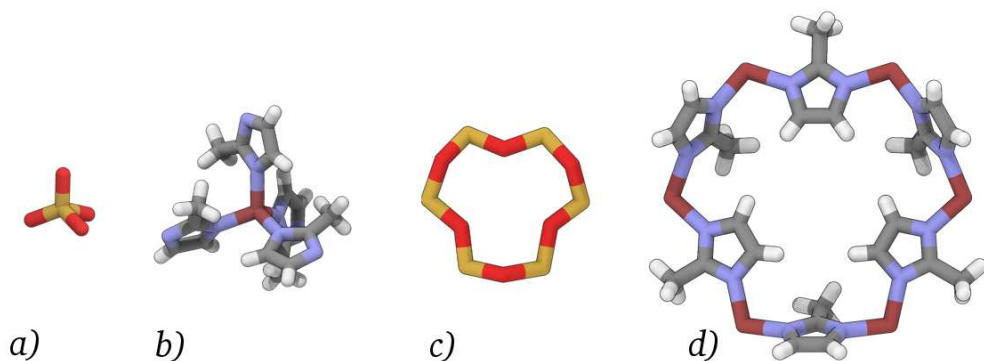


**Figure 1.3:** Tetrahedral structure of a)  $\text{SiO}_4$  and b)  $\text{Zn}(\text{methylimidazole})_4$ . SBUs of 6-membered rings in c) zeolites and d) ZIFs. In the ZIF structure the size of the *window* is enlarged by a factor 2 compared to the zeolite structure.

The relative big size of the *nodes* and *linkers* of MOFs, compared to those of the zeolite,  $\text{Si}^{4+}$  and  $\text{O}^{2-}$  ions respectively, confers upon MOFs gas adsorption properties that exceed those of the highest performing zeolites. One example of this difference in performance is the upper limit of BET surface area, which in zeolites is circa  $900 \text{ m}^2 \text{ g}^{-1}$  and for MOFs is circa  $7,000 \text{ m}^2 \text{ g}^{-1}$ . The upper limit of the pore aperture is another difference, it is  $20 \text{ \AA}$  for zeolites but  $100 \text{ \AA}$  for MOFs[14].

Within these Metal-Organic Frameworks materials, a subgroup called Zeolitic Imidazol Frameworks or ZIFs, can be regarded as hybrids between zeolites and MOFs. They are made up of organic ligands linked via metal atoms, like MOFs, but they have a zeolitic topology nonetheless. Thus, they are composed by tetrahedral structural building units (SBU). Zn or Co occupy the position of Si or other tetrahedral atom and imidazole based ligands replace the oxygen atoms. In this way, the relevant distances, including pore size, are enlarged by a factor at about 2 in ZIFs as compared to their relative topology zeolites. This kind of MOF usually has bigger thermal and humidity stability because the metallic centre is hidden.

## 1.2. Flexible nanoporous materials

All materials are *flexible* in some way: atoms move and vibrate at certain temperature. However, at certain conditions, we can study or predict some sorption or transport observables and other macroscopic properties of these materials with structural rigid models where the framework atomic positions are fixed. Why and how structural rigid models can correctly predict these observables is related to the time scales of the typical process in nanoporous crystals: changes in the electron density, the moves of the atomic cores and adsorption and transport processes of guest molecules evolve

at different times scales. Due to the success of the rigid models in the field of the adsorption processes, sometimes the *structural flexibility* is understood like a patch to fix a failure of the rigid models in the prediction of some observables –i.e. we use flexible structures when we can not correctly predict some observable with rigid models. However, the structural flexibility is, sometimes, the key to understand some processes.

Zeolites are known to show relative small structural deformations, with high degree of crystalline regularity. Their rigid regular pores have significant roles in sieving the size and shape of guest species. In contrast, solvated protein molecules provide a porous environment for specific interactions with guest molecules. The structural reformation of their channels and cavities enhances selective recognition and capture of guest molecules. Both are extreme behaviours: *rigidity* and *regularity* versus *softness*. However, some structures, a few zeolites and a wide variety of MOFs can be characterised by a compromise between both extremes, i.e. softness and regularity [1]. So, according with Horike et al. [1], soft porous crystals are "bistable or multistable crystalline materials with long range structural ordering, a reversible transformability between states, and permanent porosity". Its regularity is affected by external stimuli – i.e. external temperature, external pressure or adsorption processes of guest molecules. These are essentially phase transitions.

There is a plethora of phenomena and properties that take place in nanoporous crystals during adsorption processes. The adsorption of molecules that interact strongly with the pore can induces large structural variations, i.e. porous *soft* structures do not act as simple boxes where guest molecules are allocated. Exploiting the wide range of compositions and topologies that flexible nanoporous crystals show could help us understand the relative small number of identified different behaviours, such as phase transitions between symmetry space groups, breathing-like moves, dramatic changes in thermomechanical properties –such as thermal expansion–, linker reorientations, etc. However, we observe in the literature the appearance of colligative properties, universal phenomena or common behaviours in materials of very different kinds [15–17]. Those structural changes occur without a relevant loss of crystalline *regularity* and it is commonly known as *structural flexibility*.

The majority of zeolites show small deformations under hydration. Notwithstanding the beginning of this section, there are a small number of soft zeolites which show phase transitions under changes of external stimuli beyond normal fluctuations. Perhaps, the most famous is RHO-type aluminosilicate, which exhibits changes in its space group of symmetry and cell volume changes under CO<sub>2</sub> and H<sub>2</sub>O adsorption. Paulangite, PAU-type aluminosilicate, exhibits the same phase transition. The presence of heteroatoms, like Germanium or Gallium atoms, can increases the structural flexibility [15, 18].

On the contrary, even so-called rigid MOFs are usually more flexible than the majority of zeolites due to the organic ligand size and deformability, as well as weak host–host supramolecular interactions and the kind of the interaction among metallic cluster and organic linker. These structural features give rise to multiple, easily accessible metastable states and they can exhibit a diverse structural behaviour. For example,

so-called breathing MOFs [16] are prominent examples of soft porous crystals generally, and of flexible MOFs in particular. They show an abrupt change in unit cell volume (pore volume) upon external stimuli like MIL-53 [19–21] or DMOF-1 [22].

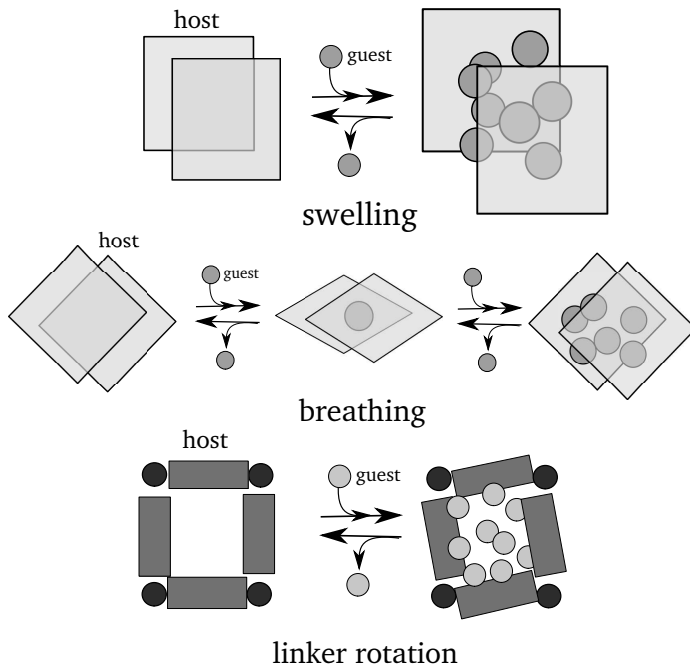


**Figure 1.4:** Classification of some flexibility modes of soft nanoporous crystals. Swelling and breathing imply changes in volume and linker rotation implies changes in shape.

Following the review article of Schneemann et al. [16] and Zhang et al. [23] we have summarised here the different modes of framework flexibility (see Figure 1.4). **Breathing phenomena** consist on reversible transitions, generating step-like, large displacements of the atoms, as well as large changes in the volume of the cell, typically larger than 10%. Hence, there are variations in the cell axes and angles and, in most cases, the *open* and *closed* forms of the materials having different space groups. In contrast, **swelling** phenomena consist on gradual enlargements of the unit cell of the MOF. In this case, there are also changes in the volume of the unit cell, but the cell shape and space group of the structure usually remain unaffected. Some MOFs also experience other flexible effects that do not necessary involve phase transitions. For example, the **rotation of the metallic clusters** alters properties of the structure such as thermal expansion and the **rotation of the organic ligands** creates in most cases the gate opening effect or the most recently identified shape-memory effect. The latter is directly related to the size of the crystal in such a way that the enlargement or shrinkage of the crystal acts as selective control of guest adsorption.

This property opens up exciting perspectives for applications in chemical and phar-

maceutical industry, as well as in medicine and sensors technologies. However, large deformations of the adsorbent may be unwanted in other industrial applications, such as separation processes, in which excessive deformation leads to erosion and eventual collapse of the adsorbent.

Most of the work of this thesis is aimed at investigating and understanding the structural flexibility with the hope of finding ways of improving current materials or creating new ones.

### 1.3. Statistical mechanics and molecular simulation

All the analyses performed in this thesis rely on the theoretical framework of **statistical mechanics**. The use of this tool enables to work with systems composed of a large number of atoms in a clear and consistent way. In classical thermodynamics the system is described with a relatively small set of **macroscopic** variables and the only available option is a phenomenological study, based on measuring and tabulating system variables for various materials. Statistical mechanics provides exact methods to connect those thermodynamic quantities (such as temperature, volume or pressure) to the microscopic behaviour of the  $N$  particles composing the system. By keeping track of their positions and momenta (microstates) over long times we can accurately predict the thermodynamic properties (macrostate).

Molecular simulations play a very important role in the description and characterisation of structures within the framework. One of the most important aspect to consider, in order to characterise structural distortions on nanoporous materials, is the importance of having *realistic* models for the interactions in the material we want to study. There are different ways to study this, but the concept of the *system model* is central in all of them. A system model is a theoretical construction aimed at reproducing some aspect of the behaviour of the original system. In our case, we are interested in reproducing the energy and other observables that are susceptible to be experimentally measured in mechanical systems. More precisely, in this work system models are used to emulate the physical basis behind the interactions among atoms and molecules in periodic systems. The use of these models, together with the principles and tools of the classical mechanic, is the core of the **molecular simulation**. This approach was initiated in the 30's and 40's of the last century and provides a microscopic description and hence a deep understanding of molecular systems. Molecular simulation also provides the possibility to create hypothetical scenarios and future predictions. It is worth mentioning that in the fields of physical–chemistry and chemical–physics, by *simulations* we refer to all those methods that rely on the use of interatomic potentials (an energetic model of interactions among atoms in a physical system) for the calculation of the physical properties of a material. These potentials are analytical (or numerical) functions that describe the variation in the energy of an ion system depending on the coordinates of the nuclei, and without taking into account the electronic shell. The electronic structure methods, on the other hand, are those that with some level of approximation solve the Schrödinger equation of a given

problem. In this case, the nature of interactions between atoms is quantum. However, classical simulation has also proven very useful, in particular for large systems and long time scales.

Returning to the theoretical core of molecular simulation, analytical mechanics, the Hamiltonian formulation provides the positions and momenta of the  $N$  particles of the system. The general method is to make use of differential principles to obtain, either analytically or by numerical calculation, the equations of motion. The general variational principle used in the Hamiltonian formulation is the **Principle of Least Action**. Application of this principle leads to the conclusion that the equations of motion must satisfy a series of requirements, represented by the canonical equations of Hamilton:

$$\dot{q}_i = \frac{\partial \mathcal{H}}{\partial p_i}, \quad \dot{p}_i = -\frac{\partial \mathcal{H}}{\partial q_i} \quad (1.1)$$

for all  $i = 1, \dots, N$ , where  $q_i$  are generalised coordinates (e.g. positions  $r$ , angles between atoms  $\theta$  or dihedral angles  $\phi$ ),  $p_i$  are their corresponding momenta, and  $\mathcal{H}$  is the Hamiltonian, defined as:

$$\mathcal{H} = \mathcal{K} + \mathcal{U} \quad (1.2)$$

where  $\mathcal{K}$  is the kinetic energy and  $\mathcal{U}$  is the total potential energy. The key assumption is that for every ensemble of positions of the atoms  $\{\vec{q}_i\}_{i=1}^N$  in a physical system, the total potential energy surface  $\mathcal{U} = \mathcal{U}(\vec{q}_1, \dots, \vec{q}_N)$  can be defined. The total potential energy can be expressed, in classical systems, as an expansion in bonded and non-bonded interactions:

$$\mathcal{U}(\vec{r}, \vec{\theta}, \vec{\phi}) = \sum_{\text{non-bonded}} U_{\text{nb}}(r) + \sum_{\text{bonds}} U_r(r^{\text{bonds}}) + \sum_{\text{bends}} U_\theta(\theta) + \sum_{\text{dihedral}} U_\phi(\phi) \quad (1.3)$$

which is historically referred to as a *force field* (Equation 1.3).

The integration of these  $2N$  first-order differential equations (Equation 1.1) provides the generalised coordinates  $q_i(t)$  and momenta  $p_i(t)$  as a function of time, that is they define the evolution of the dynamical system. I will not further discuss more details regarding the basis of analytical mechanics. For that, I refer to the books and the Lectures of Gantmakher [24], Goldstein [25] and Chandler [26] and Tuckerman et al. [27].

In order to introduce the statistical approach, we assume that there are many replicates of the same system, each of which represents a possible microstate that the real system might be in  $x = \{q, p\}$ . All these possible systems form an **statistical ensemble**. In other words, it is a probability distribution for the state of the system. An statistical ensemble contains several conservation laws and physical constrains that must be satisfied in the macrostate <sup>2</sup>. The ensemble formalises the notion that an experimenter repeating an experiment again and again under the same macroscopic

<sup>2</sup>The energy conservation, for example, is a conservation law  $\delta(\mathcal{H}(x) - E)$

conditions, but unable to control the microscopic details, may expect to measure an observable fluctuating around its average value. Different macroscopic constraints lead to different types of ensembles, with particular statistical characteristics. Some important thermodynamic ensembles that we will use are:

- **Microcanonical ensemble or  $NVE$  ensemble:** It is used to describe an isolated system in equilibrium. The isolated system will have a well-defined fixed value of energy  $E$ , a fixed number of particles  $N$  and a fixed volume  $V$ . If we apply the total energy conservation law,  $\rho(x) = \delta(\mathcal{H}(x) - E)$ , the probability is zero to all microstates whose energy  $\mathcal{H}(x)$  is not exactly the value of the macroscopic state  $E$ .
- **Canonical ensemble or  $NVT$  ensemble:** It is appropriate for describing a closed system which is in weak thermal contact with a heat bath. In order to be in statistical equilibrium the system must remain totally closed (fixed number of particles  $N$  and volume  $V$ ). The probability density function in this ensemble is proportional to the Boltzmann factor  $\exp(-\beta\mathcal{H}(x))$ , where  $\beta = 1/k_B T$ , with  $k_B$  the Boltzmann constant.
- **Macrocanonical or Grand Canonical ensemble or  $\mu VT$  ensemble:** is appropriate for describing an open system where we keep the volume  $V$  fixed, and the system is in equilibrium with a reservoir of particles (fixed chemical potential  $\mu$  and temperature  $T$ )
- **Isothermal-isobaric ensemble or  $NPT$ :** is used for describe system with a variable volume. It allows for fluctuations in the volume  $V$  keeping fix the number of particles  $N$  (closed system) and the temperature  $T$ .

The functional form of the *probability density of the ensemble*  $\rho$  depends on how we select the imposed conservation laws or physical constrains. Table 1.1 shows the expression for probability densities in all the different ensembles. However, in a general sense this density will be given by the product of density of probabilities allowed by the chosen  $n_c$  conservation law  $\delta(\Lambda_k(x) - \lambda_k)$ :

$$\rho(x) = \prod_{k=1}^{n_c} \delta(\Lambda_k(x) - \lambda_k) \quad (1.4)$$

As we have said before, each of those physical system is described by a set of  $2N$  canonical variables  $x \equiv \{q, p\}$ , and the equations of motion (Equation 1.1) can be written as

$$\dot{x} = G(x) \quad (1.5)$$

where  $G(x) = \{\partial\mathcal{H}/\partial p, -\partial\mathcal{H}/\partial q\}$ .

By integrating the phase-space volume it is possible to obtain one of the fundamental tools in analytical mechanics, the Liouville's theorem:

$$\Gamma = \int dx = \int \dots \int dp_1 dp_2 \dots dp_n dq_n \quad (1.6)$$

**Table 1.1:** Most common ensembles partition function and probability density functions. The momenta have already been integrated out.

Ensemble	Partition function $Z$ and probability density $\rho(x, V)$ where $x \equiv \{\bar{q}^N\}$ and $s \equiv \{\bar{q}^N, \bar{p}^N\}$
Microcanonical	$\Omega(N, V, E) = \frac{1}{h^{3N} N!} \int ds \delta(E - \mathcal{H}(s))$ $\rho(s, V) \propto \delta(E - \mathcal{H}(s))$
Canonical	$Z = Q(N, V, T) = \frac{V^N}{\Lambda^{3N} N!} \int dx e^{-\beta U(x)}$ $\rho(x, V) \propto e^{-\beta U(x)}$
Grand canonical	$Z = \Xi(\mu, V, T) = \sum_{N=0}^{\infty} \frac{V^N e^{\beta \mu N}}{\Lambda^{3N} N!} \int dx e^{-\beta U(x)}$ $\rho(x, V) \propto \frac{V^N e^{\beta \mu N}}{\Lambda^{3N} N!} e^{-\beta U(x)}$
Isothermal–isobaric	$Z = \Delta(N, P, T) = \frac{\beta P}{\Lambda^{3N} N!} \int dV V^{N+1} e^{-\beta P V} \left( \int dx e^{-\beta U(x)} \right)$ $\rho(x, V) \propto V^{N+1} e^{-\beta P V} e^{-\beta U(x)}$

This theorem shows that if an ensemble of initial conditions  $x^0$  occupies a initial phase-space volume ( $\Gamma_0 = \int dx_0$ ) after a time  $t$  the transformation  $x_t = x(t, x_0)$ , that is the time evolution of the system, will change the phase volume  $\Gamma_0 \rightarrow \Gamma$  such that  $\Gamma = \int J(x_t; x_0) dx_0$  where

$$J(x_t; x_0) = \left| \frac{\partial(q_1^t, p_1^t, \dots, q_n^t, p_n^t)}{\partial(q_1^0, p_1^0, \dots, q_n^0, p_n^0)} \right| \quad (1.7)$$

is the determinant of the Jacobian matrix of the transformation ( $\mathcal{M}_{ij} = \partial x_t^i / \partial x_0^j$ ).

It can be shown that the Jacobian satisfies the general equation:

$$\frac{d}{dt} J(x; x^0) = J(x; x^0) \kappa(x, t). \quad (1.8)$$

where the magnitude  $\kappa(x_t, t) = \vec{\nabla} \cdot G(x)$  is called *compressibility of the dynamic system*. For **Hamiltonian systems** the compressibility is zero ( $\kappa(x_t, t) = 0$ ) and the Jacobian  $J(x_t; x^0) = 1$ , so the phase volume is conserved, which can be translated as:

$$dx_0 = dx_t \quad (1.9)$$

Because we are working with a statistical ensemble where all the systems are identical and since the phase-space volume is conserved in Hamiltonian systems:

$$\frac{d\rho}{dt} \equiv \frac{\partial \rho}{\partial t} + \{\rho, \mathcal{H}\} = 0 \quad (1.10)$$

where  $\{\rho\mathcal{H}\}$  represents the Poisson bracket.<sup>3</sup> The density of a statistical ensemble is always, as we have seen, an integral of motion [24, 28]. This can be expressed as in Equation 1.10, known as Liouville's equation. By solving the stationary solutions of the Liouville's equation we obtain the stationary probability density  $\rho(x_t)$  which does not depend on the time.<sup>4</sup> Once we know this, the number of microstates (all  $N$  individual position and momenta) that are compatible with a macrostate, (with  $n_c$  system constrains) that is the *Partition Function*, is given by

$$\Omega = \int dx_0 \rho(x_0) = \int dx_t \rho(x_t) \quad (1.11)$$

and the **expected value of a generic observable**  $A$  is defined as

$$\langle A \rangle = \frac{1}{\Omega} \int dx A(x) \rho(x). \quad (1.12)$$

and both are time independent since the density function does not depend on the time.

However, in the isobaric-isothermal ensemble, as well as the  $N\sigma T$  ensemble and some others, require the integration of the equations of motion of **non-Hamiltonian systems**, since the volume of the system  $V$  is not fixed and phase volume neither, so  $\kappa(x_t, t) \neq 0$ . The study of those systems is covered in detail in Tuckerman et al. [27]. Below I describe some details and considerations of non-Hamiltonian systems and the calculation of expected values or density probabilities in these cases.

For non-Hamiltonian systems the general solution to Equation 1.8 is

$$J(x_t, x_0) = \exp \left[ \int_0^t \kappa(x, \mu) d\mu \right] = e^{w(x,t) - w(x_0,0)} \quad (1.13)$$

By replacing Equation 1.13 in Equation 1.9 we obtain a more general expression of the phase-space volume, that is now compressible

$$e^{-w(x_t,t)} dx_t = e^{-w(x_0,0)} dx_0. \quad (1.14)$$

The exponential  $e^{-w(x_t,t)}$  can be written as  $\sqrt{g(x,t)}$ , where  $g(x,t) = \det(\mathbf{g}_{\mu\nu}(x,t))$ , with  $\mathbf{g}_{\mu\nu}(x,t)$  the metric tensor of the transformation  $x_t = x(t, x_0)$  [29], that now allows changes in the volume.

A Generalised non-Hamiltonian Liouville's equation can be expressed as:

$$\frac{\partial(\rho\sqrt{g})}{\partial t} + \text{div}(\rho\sqrt{g}\dot{x}) = 0. \quad (1.15)$$

---

<sup>3</sup>If  $\varphi(t, q_i, p_i)$  and  $\psi(t, q_i, p_i)$  are two random functions, the Poisson bracket is

$$\{\varphi, \psi\} = \sum_{i=1}^n \frac{\partial\varphi}{\partial q_i} \frac{\partial\psi}{\partial p_i} - \frac{\partial\varphi}{\partial p_i} \frac{\partial\psi}{\partial q_i}.$$

<sup>4</sup>Stationary solutions verify  $\frac{\partial\rho}{\partial t} = 0$ .

and the partition function (number of all microstates) is now obtained as:

$$\Omega(C_1, \dots, C_{n_c}) = \int dx' \sqrt{g(x')} \prod_{k=1}^{n_c} \delta(\Delta_k(x') - C_k) \quad (1.16)$$

where  $n_C$  and  $C_k$  are invariants,  $\frac{\partial \sqrt{g}}{\partial t} = 0$  and  $\delta(\Delta_k(x') - C_k)$  are the corresponding conservation laws. Finally, the expected value of a generic observable  $A$  in non-Hamiltonian systems can be computed as:

$$\langle A \rangle = \frac{1}{\Omega} \int dx \sqrt{g(x)} A(x) \rho(x). \quad (1.17)$$

## 1.4. Interatomic potentials

In the Equation 1.3 I have introduced the concept of force field: a set of functions and parameters needed to model the interactions in a physical system. There are many generic force fields available in the literature, such as Dreiding [30], UFF [31], OPLS [32], TraPPE [33–36] or AMBER [37], as well as specific force fields developed for particular materials like aluminosilicate zeolites (like Sanders et al. [38][39–41]), metal–organic frameworks such as IRMOF-1 (Dubeldam et al. [42]), MIL-53 (Vanduyfhuys et al. [20]), or well-defined interactions between special molecules like water (Higgins et al. [43]).

As it appears in Equation 1.3, the total potential energy of the system can be arranged in two parts, corresponding with intramolecular (bonded) and intermolecular (non-bonded) interactions:

$$\mathcal{U}(\vec{q}^N) = U_{\text{bonded}} + U_{\text{non-bonded}}. \quad (1.18)$$

### Intermolecular interactions

Intermolecular interactions of the Equation 1.18 are due to atomic electrostatics and the electrodynamics. Suppose there are  $N$  charged atoms at positions  $\vec{r}^N = \{\vec{r}_i\}_{i=1}^N$  within the unit cell satisfying  $q_1 + \dots + q_N = 0$ . The unit cell is defined by the vectors  $\vec{a}_\alpha$ , which need not be orthogonal. The atoms interact according Born–Mayer potentials [44, 45],

$$U_{\text{non-bonded}}(\vec{r}^N) = \frac{1}{4\pi\epsilon_0} \sum_{\vec{n}} \sum_{i < j}^N \frac{q_i q_j}{r_{ij}} + \sum_{ij}^N \varphi_{ij}(r_{ij}) \quad (1.19)$$

where  $\vec{n} = n_1 \vec{a}_1 + n_2 \vec{a}_2 + n_3 \vec{a}_3$  (terms with  $i = j$  for  $\vec{n} = 0$  are omitted) and  $r_{ij} = \|\vec{r}_i - \vec{r}_j + \vec{n}\|$  is the distance among atoms and the energy depend on the atomic distribution  $\{\vec{r}_i\}_{i=1}^N$ . The first term is the **coulombic interaction** and the second one,  $\varphi$  referred to collectively as short-range interactions (because is  $\propto r^{-d}$  with  $d > 6$ ),

represents the **van der Waals interactions** (Keesom, Debye and London interactions) plus the **exchange interaction** (or Pauli repulsion for electrons).

Taking into account the columbic interaction, a long-range interaction proportional to  $r^{-1}$ , atoms interact with all other charges in the unit cell as well as with all their periodic images. The first corresponding term in the Equation 1.19 can be evaluated directly for finite system but for a periodic system the complete series is then *conditionally convergent*, i.e. the sum depends on the order in which the terms are summed. **Ewald summation** method solved this problem [46–48].

Regarding short-range interactions, it is sufficient to take just the neighbouring simulation volumes into account, leading to the *minimum image* configuration.

Keesom and Debye interactions only occur with molecules which have permanent dipole moments. Considering non-polar atoms London [49] found, from their quantum-induced instantaneous polarisation multipoles, that this dispersion interaction follow the functional form:

$$U_{\text{dispersion}} \cong -\frac{3}{2} \frac{I_i I_j}{I_i + I_j} \frac{\alpha_i \alpha_j}{r_{ij}^6} = -c_{ij}^{(6)} r_{ij}^{-6} \quad (1.20)$$

where  $\alpha_i$  is the dipole polarisability and  $I_i$  is the first ionisation potentials of the respective atom  $i$ . The repulsion of orbital atoms can be expressed as an exponential or potential decline factor with the distance,  $\propto \exp(-r_{ij}/\rho_{ij})$  or  $\propto r_{ij}^{-12}$ . In the first one,  $\rho_{ij}$  or atomic *softness* parameter is related to the ionisation potentials too:  $\rho_{ij} = 2^{1/2}(I_i^{1/2} + I_j^{1/2})^{-1}$  [45]. This parameter is related with the single bond lengths between two atoms,  $R_{ij}$ , the atomic size  $r_i = R_{ii}/2$ , and the electronegativity of the atoms,  $c_i$ .

The most common short-range functional forms are:

- the Lennard–Jones potential

$$\varphi_{ij}(r_{ij}) = 4\epsilon_{ij} \left[ \left( \frac{\sigma_{ij}}{r_{ij}} \right)^{12} - \left( \frac{\sigma_{ij}}{r_{ij}} \right)^6 \right] = A_{ij} r_{ij}^{-12} - B_{ij} r_{ij}^{-6} \quad (1.21)$$

The parameters for generic force fields are usually self-parameters and a **mixing-rules** is needed to compute the interaction between different type of atoms. Common mixing-rules are:

- Lorentz–Berthelot (arithmetic):

$$\epsilon_{ij} = \sqrt{\epsilon_{ii}\epsilon_{jj}} \quad \sigma_{ij} = \frac{1}{2}(\sigma_{ii} + \sigma_{jj}) \quad (1.22)$$

- Jorgensen (geometric):

$$\epsilon_{ij} = \sqrt{\epsilon_{ii}\epsilon_{jj}} \quad \sigma_{ij} = \sqrt{\sigma_{ii}\sigma_{jj}} \quad (1.23)$$

- the Buckingham potential function (also known as Hill),

$$\varphi_{ij}(r_{ij}) = A_{ij} \exp(-r_{ij}/\rho_{ij}) - c_{ij} r_{ij}^{-6} \quad (1.24)$$

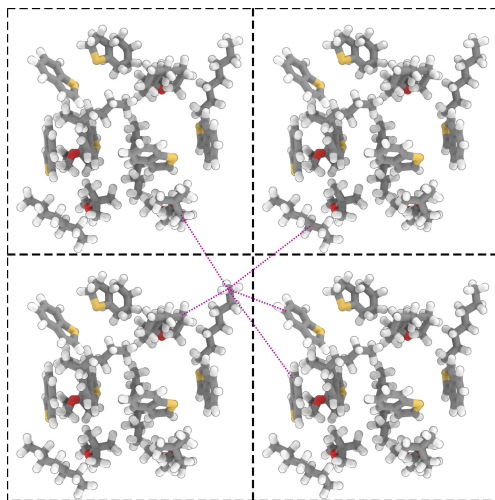


**Figure 1.5:** Schematic representation of the periodical boundary condition. Each atom interacts with all other atoms in the unit cell as well as with all their periodic images. In the particular case of the image there are sulphur compounds of petroleum residues and gasoline additives.

Having three adjustable parameters is more accurate than Lennard–Jones potential and, taking into account the Equation 1.20, it is possible to use the known values of dipole polarisability and ionisation of atoms to adjust the  $c_{ij} \equiv c_{ij}^{(6)}$  parameters. The Buckingham potential is appropriate to describe ionic or semi-ionic materials. A downside of the Buckingham potential is its divergence to large negative energies at  $r \rightarrow 0$  (Buckingham catastrophe). In MD, assuming that all atoms do not overlap, the repulsive part of the potential avoids this issue (at realist temperatures at least). However, in MC a translation move may put a particle too near another particle’s position. Therefore, in MC simulation Buckingham potential needs to be adapted with a shell around particles which blocks undesirable moves using, for example, the following Equation 1.25:

$$\varphi_{ij}(r_{ij}) = \begin{cases} 10^{10} & \text{if } r_{ij} < 1 \text{ \AA} \\ A_{ij}e^{-\rho_{ij}/r_{ij}} - c_{ij}r_{ij}^{-6} & \text{otherwise} \end{cases} \quad (1.25)$$

- the Morse potential

$$\varphi_{ij}(r_{ij}) = D_{ij} \left\{ 1 - \exp \left[ -a_{ij}(r_{ij} - r_{ij}^e) \right] \right\}^2 \quad (1.26)$$

The Morse potential is appropriate to describe covalent interactions –preferably intermolecular.  $r_{ij}^e$  is the equilibrium bond distance,  $D_{ij}$  is the well depth (defined relative to the dissociated atoms), and  $a_{ij}$  controls the width of the potential (the smaller  $a_{ij}$  is, the larger the well).

Short-range interactions tend to zero rapidly when the interatomic distance increases. Therefore, we can assume that every atom interacts not with all the atoms, but only with those atoms inside a certain spherical region of radius  $r_c$ . This cut-off radius must be large enough to ensure that the interaction with the atoms outside this region is indeed negligible. In our case, a cut-off radius between 12 and 16 Å (depending on the material) was found to be sufficient.

### Intramolecular interactions

In the bonded interactions part of the Equation 1.18 we consider the different interactions between two, three and four *consecutive* particles.<sup>5</sup> The main contribution to the bonded energy is the **bonding** or two-body energy. It is necessary when dealing with strong covalent bonds. It is usually expressed as a harmonic potential:

$$U_{ij}^{(\text{bonding})} = \frac{k_r}{2} (r_{ij} - r_{ij}^0)^2 \quad (1.27)$$

where  $r_{ij}^0$  is the equilibrium distance between the two atoms and  $k_r$  is a fitted constant.

The second main contribution to the bonded energy is the **bending** or three-body energy. It is necessary when dealing with covalent bonds, because of the directionality of the bonding. It is usually expressed as a harmonic potential too:

$$U_{ijk}^{(\text{bending})} = \frac{k_\theta}{2} (\theta_{ijk} - \theta_{ijk}^0)^2 \quad \text{where} \quad \theta_{ijk} = \cos^{-1} \left[ \frac{\vec{r}_{ij} \cdot \vec{r}_{jk}}{r_{ij} r_{jk}} \right] \quad (1.28)$$

and  $\theta_{ijk}^0$  is the equilibrium angle between the three consecutive atoms and  $k_\theta$  is a fitted constant.

The contribution of the **torsion** or four-body energy to the total energy of ionic or semi-ionic systems is small, so usually it is not taken into account. For covalent systems, it may be necessary to have a good description of a certain torsional angle of the system, as in the benzene molecule or in the organic ligands of MOFs for example. In a chain of atoms  $ijkl$  the dihedral angle is defined as the angle between the plane containing the first three atoms  $ijk$  and the plane containing the last three atoms  $jkl$  of the chain. The most common form of the dihedral torsion is as follows:

$$U_{ijkl}^{(\text{torsion})} = k_{ijkl} [1 + \cos (n_{ijkl} \phi_{ijkl} - \delta_{ijkl})] \quad (1.29)$$

where

$$\phi_{ijkl} = \cos^{-1} \left[ \frac{(\vec{r}_{ij} \times \vec{r}_{jk}) \cdot (\vec{r}_{jk} \times \vec{r}_{kl})}{|\vec{r}_{ij} \times \vec{r}_{jk}| |\vec{r}_{jk} \times \vec{r}_{kl}|} \right] \quad (1.30)$$

is the dihedral angle,  $k_{ijkl}$  is the torsional energy barrier,  $n_{ijkl}$  is the number of minima occurring in the function in the range of the torsional angle, and  $\delta_{ijkl}$  is a phase factor.

<sup>5</sup>We consider consecutive particles those that are connected by chemical bonds.

## Polarisability

In the model we have described so far every atom is modelled by a point charge, without any dipole or quadrupole moment. Although an acceptable approximation in some cases, there are many atoms for which polarisability plays a crucial role. Simple point dipole models are generally inadequate for ionic crystals, as they often result in excessive polarisation energies. To overcome this problem Dick and Overhauser [50] developed the **shell model**. Within this model the polarisable ion is treated as a pair of charges. The whole mass of the ion is in the core, which is a positive point charge of value  $q_{\text{core}}$ . Around this core there is a mass-less negative point charge,  $q_{\text{shell}}$ , referred to the shell. These two charges do not interact by Coulombic interactions. They are bound a harmonic spring force,

$$U_{cs}^{(\text{spring})} = \frac{k_{cs}}{2} r_{cs}^2 \quad (1.31)$$

where  $r_{cs}$  is the core-shell separation,  $k_{cs}$  is the spring constant, and  $q = q_{\text{core}} + q_{\text{shell}}$ .

The higher the distance between core and shell  $r_{cs}$ , the higher the dipole moment of the ion,  $\vec{p} = q\vec{d}$ .

The polarisability on the ion,  $\alpha$ , is given by

$$\alpha = \frac{q_{e^2\text{shell}}^2}{k_{cs}} \quad (1.32)$$

The short-range interaction forces are mainly due to the interaction between electron clouds. Therefore, in the shell model, short-range forces act between shells. Despite its simplicity, this model works well in static and dynamical simulations of ionic crystals. An alternative to simulation a more accurate charge distribution of a molecule is to add artificial charge-sites. For water, there exist in addition to the 3-sites model, a 4-site and even 5-site model with one and two additional charge sites, respectively. Quadrupoles of small dimers can be handled by placing artificial sites at the centre of the bond.



---

# Chapter 2

## Methodology

Never trust a computer you can't  
throw out a window.

---

Stephen Wozniak

In this chapter, we will discuss the different techniques employed in our study. The main methodology used in this study is Molecular Dynamics (MD) simulation, in which particles trajectories are calculated by integrating the equations of motion. Energy minimisation calculations (EM) are used too. Here, we minimise the total energy of the lattice in order to determine the structure, employing interatomic potentials. In order to perform simulations of adsorption of guest molecules in the pore of the structures, Monte Carlo (MC) simulations were used. Moreover, we have verified some of the structural changes and point-charges calculations with electronic structure techniques using Density Functional Theory (DFT) i.e. quantum calculations. DFT is a powerful but time consuming technique, so we only use it in few key cases, in order to check the results obtained with classical calculations.

### 2.1. Molecular Dynamics

Intuitively, Molecular Dynamics simulations are the *simplest* type of simulation: particles move around in the system, following trajectories determined by Newton's laws (or by the Hamilton Equations 1.1). In an iterative scheme, the forces they exert on one another are calculated from their positions; based on the forces, the velocities are updated; and these velocities, kept fixed for one time-step  $\tau$ , yield the new positions one time-step away.

The velocity-Verlet algorithm is the most widely used method for integrating the equations of motion [51]. This is implemented in most of simulations codes according

to the following equations:

$$\vec{r}_i(t + \tau) = \vec{r}_i(t) + \vec{v}_i(t)\tau + \frac{\vec{f}_i(t)}{2m}\tau^2 + \mathcal{O}(\tau^3) \quad (2.1)$$

$$\vec{v}_i(t + \tau) = \vec{v}_i(t) + \frac{\vec{f}_i(t) + \vec{f}_i(t + \tau)}{2m}\tau + \mathcal{O}(\tau^3) \quad (2.2)$$

where  $\vec{r}_i(t)$ ,  $\vec{v}_i(t)$  and  $\vec{f}_i(t)$  are the position, velocity and force vector at time  $t$ , respectively.  $\tau$  is the time-step and  $m$  the mass of the atom  $i$ . Note that this algorithm is time-reversible. An unphysical drift in the energy appears after long integration time or as a result of the use of large time-steps,  $\tau$ . To test this energy drift for a given time-step after  $\lambda$  integration steps, we can check the integration validity by requiring the drift is lower than a typical energetic value  $\delta$ :

$$\sum_{i=1}^{\lambda} \|1 - E(i\tau)/E(0)\| < \delta\lambda \quad (2.3)$$

There are several ensembles in which we can run calculations, depending on the conserved quantities:  $NVE$ ,  $NVT$ ,  $NPT$ , etc. In this thesis, we mainly use the  $NVT$  and  $NPT$  ensembles. The numerical integration was performed using the Nose-Hoover style non-Hamiltonian equations of motion, which are designed to generate positions and velocities sampled from  $NVT$  and  $NPT$  ensembles following the scheme of Martyna et al. [52] and Tuckerman et al. [53].

The ergodic hypothesis states that ensemble averages can be obtained from time averages. So, the time average value,  $\langle \dots \rangle_t$ , of a generic property  $A$  can be obtained by the following expression

$$\langle A \rangle_t = \lim_{t \rightarrow \infty} \frac{1}{t} \int dt A(x, t). \quad (2.4)$$

where  $x \equiv \{\vec{r}^N\}$ . If Equation 1.12 is equal to the Equation 2.4 the system is **ergodic**.

An important dynamic quantity is the self-diffusivity coefficient  $D_s^\alpha$  (in the directions  $\alpha = x, y, z$ ) of  $N$  particles, which can be computed by evaluating the mean-square displacement, which reads in three dimensions

$$D_s^\alpha = \frac{1}{2N} \left\langle \sum_{i=1}^N (r_{i\alpha}(t) - r_{i\alpha}(0))^2 \right\rangle_t \quad (2.5)$$

where  $r_{i\alpha}$  is the  $\alpha$ -component of the center-of-mass of particle  $i$ . The directionally averaged diffusion coefficient is given by

$$D = \frac{D_x + D_y + D_z}{3} \quad (2.6)$$

We have used the order- $n$ -algorithm incorporated in the RASPA code [54, 55] to measure accurate mean-square displacements at long times in a fast way.

## 2.2. Lattice energy minimisation

In the previous Chapter 1, in Section 1.4, different models for calculating the energy of the systems have been presented. We are interested in finding the minimum state of the system.<sup>1</sup> However, the calculations presented in this section are performed at  $T = 0K$ . That is, they do not include thermal effects. This state corresponds to a minimum in the potential energy hypersurface, in which:

$$\frac{\partial \mathcal{U}(\vec{r}^N)}{\partial r_i} = 0 \quad \forall i = 1, \dots, N \quad (2.7)$$

where  $\mathcal{U}(\vec{r}^N)$  is the total potential energy of the system, as defined in Equation 1.3, and  $N$  is the number of atoms.

Transition states and local minima also satisfy Equation 2.7, therefore it is necessary to calculate the second derivative to distinguish between a minimum and a transition state (see Figure 2.1).

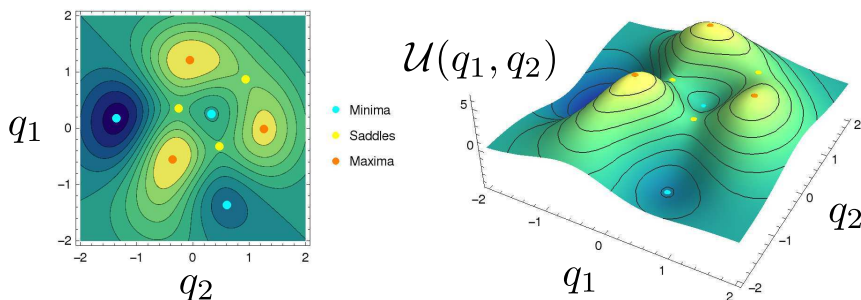


**Figure 2.1:** Cartoon of the potential energy surface of two generalised coordinates  $\mathcal{U}(q_1, q_2)$  in a fictional system. Local and global minima (cyan dots) and maxima (red dots) and saddle points (yellow) are indicated on the surface.

There are several minimisation algorithms. The simplest algorithm is the **Steepest Descents** (SD) method [56], which follows the force vector from an initial configuration to a zero in the force:

$$\vec{x}_{n+1} = \vec{x}_n - k_n \vec{\nabla} f(\vec{x}_n) \quad (2.8)$$

where  $k_n$  is a self-adjustable parameter for each minimisation step. However it is known to converge slowly in *stiff* systems [57]. The **Conjugate Gradient** (GC) method

<sup>1</sup>After some considerations can be proved that, under certain conditions, the state of energy minimum state is the most probable.

requires both the energy and first derivative evaluations, and is the most efficient method at intermediate distances from the minimum. The CG method improves upon the SD method by following conjugate search directions instead of always following the force. In the LAMMPS code it is implemented the Polak and Ribière [58] version of the CG algorithm:

$$\vec{x}_{n+1} = \vec{x}_n - k_n \vec{h}_n \quad \text{with} \quad \vec{h}_n = \vec{\nabla} f(\vec{x}_n) + \gamma_n \vec{h}_{n-1} \quad (2.9)$$

where

$$\gamma_n = \frac{\vec{\nabla} f(\vec{x}_n) \left( \vec{\nabla} f(\vec{x}_n) - \vec{\nabla} f(\vec{x}_{n-1}) \right)^T}{\left\| \vec{\nabla} f(\vec{x}_{n-1}) \right\|^2} \quad (2.10)$$

The norm of the gradient is checked to ascertain whether to switch from one method to another. When the system is very close to the energy minimum this method is very slowly convergent. When that happens we switch to the **Newton-Raphson** method [59], which makes use of the second derivatives of the energy, in order to reach rapidly the energy minimum. Newton-Raphson method approximates the objective function by a quadratic surface at each step and moves to the minimum of that surface:

$$\begin{aligned} f(\vec{x} + \Delta\vec{x}) &\simeq f(\vec{x}) + \vec{\nabla} f(\vec{x})^T \cdot \Delta\vec{x} + \frac{1}{2} \Delta\vec{x}^T \cdot \mathcal{H} \cdot \Delta\vec{x} \\ \vec{\nabla} f(\vec{x} + \Delta\vec{x}) &\simeq \vec{\nabla} f(\vec{x}) + \mathcal{H} \cdot \Delta\vec{x} \\ \Delta\vec{x} &= -\mathcal{H}^{-1} \cdot \vec{\nabla} f(\vec{x}) \end{aligned}$$

where  $\mathcal{H} := (\partial^2 \mathcal{U} / \partial x_i \partial x_j)$  is the Hessian. This method has a computationally high CPU cost. The most expensive and memory demanding part of Newton-Raphson method is the calculation of the Hessian. The basic Newton-Raphson method requires the Hessian to be non-singular and tends to develop problems if any of its eigenvalues become negative. A simple fix for this is to add a regularisation matrix (often a unit matrix)

$$\Delta\vec{x} = -(\mathcal{H} + \lambda \mathcal{S})^{-1} \cdot \vec{\nabla} f(\vec{x}) \quad (2.11)$$

**Rational Function Optimization** (RFO) introduces a step size dependent denominator [60], which prevents the algorithm from taking large steps:

$$f(\vec{x} + \Delta\vec{x}) \simeq f(\vec{x}) + \frac{\vec{\nabla} f(\vec{x})^T \cdot \Delta\vec{x} + \frac{1}{2} \Delta\vec{x}^T \cdot \mathcal{H} \cdot \Delta\vec{x}}{1 + \Delta\vec{x}^T \cdot \mathcal{S} \cdot \Delta\vec{x}} \quad (2.12)$$

Both Newton-Raphson and RFO minimisation methods were used to ensure convergence to true energy. However, RFO behaves better than Newton-Raphson in the vicinity of inflection points. Both methods are included in the GULP code [61]. Baker [62] and Banerjee et al. [63] developed a Eigenvector-Following method. This method

solves this limitation of the Newton-Raphson technique by shifting some of the eigenvalues to change their sign and achieve the desired curvature. This algorithm is included in the RASPA code [64].

We have used RASPA, GULP and LAMMPS codes [55, 61, 65] for energy minimisation calculations and to locate saddle points between structural phase-transitions.

## 2.3. Electronic structure techniques

### Density Functional Theory

In order to obtain accurate structures or to provide energetic values, point charges or energy barrier of new or hypothetical structures, when a classical interatomic potential is not available, we need to perform quantum calculations. The basis of the electronic structure techniques is the Schrödinger equation  $\hat{H}|\Psi\rangle = \epsilon|\Psi\rangle$ . It has all the information needed for a complete quantum description of a time-independent physical system. The Hartree-Fock method [66–70] (HF) gives an approximate solution, but does not account for electronic correlation. Post-HF [70] techniques (Moller-Plesset, Configuration Interaction, etc.) include correlation effects but these methods are very time consuming and are only applicable to relatively small systems.

In the 60's, Hohenberg and Kohn [71] presented a new method for solving the Schroedinger equation: The Density Functional Theory, which has grown in applicability in recent years. Hohenberg and Kohn proved that the external potential  $V(r)$  and the total number of electrons  $N$  are uniquely determined by the electronic density  $\rho(r)$  of the ground state of the system, i.e. these magnitudes can be calculated as a functional of the electron density. They also proved that  $V(r)$  and  $N$  uniquely determine  $\rho(r)$ , as well as the Hamiltonian. Therefore, all properties of a physical system can be calculated if  $\rho(r)$  is known. Another result of their work is that there is a universal functional that allows calculation of the energy of a quantum mechanical system from this electronic density. For a given potential  $V(r)$  the energy of the fundamental state is written as:

$$E[\rho(\vec{r})] = \int V(\vec{r})\rho(\vec{r})d\mathbf{r} + F[\rho(\vec{r})] \quad (2.13)$$

where  $E[\rho(\vec{r})]$  is a functional,<sup>2</sup> of  $\rho(\vec{r})$ .  $F[\rho(\vec{r})]$  refers to the sum of the kinetic, Coulombic electron-electron and exchange-correlation energies. Hohenberg and Kohn [71] also extended the Variational Principle to this function: the energy  $E[\rho(\vec{r})]$  calculated with a given electronic density  $\rho(\vec{r})$  is higher than the energy of the real system,  $E_0$ . So,  $E[\rho(\vec{r})]$  equals  $E_0$  only when  $\rho(\vec{r})$  is the exact electronic density of the system. Therefore, the minimisation of the energy (the SCF iterative process) allows the calculation of the electronic density of the ground state of the system, and consequently all its properties.

---

<sup>2</sup>A functional refers to a linear mapping from a function, for example  $\rho(\vec{r})$ , into a field of numbers (the energy  $E$  in this case).

There are several functionals proposed for  $F[\rho(\vec{r})]$ , and there has been a steady increase in their quality over the years. In the works related to this thesis we have used the PBE exchange-correlation functional [72], normally with the inclusion of van der Waals interactions by using D3 Grimme's dispersion corrections [73].

## 2.4. Monte Carlo

Monte Carlo is a numerical statistical method that uses random numbers and probability theory to solve problems. In particular, we are interested in finding compatible microstates according to imposed macroscopic conservation laws. So, the probability of finding a system in a given microstate is proportional to the phase-space volume associated with it, i. e., the most probable state would be that occupying the maximum volume in phase-space.

MC is nothing more than a computer-assisted exploitation of the Law of Large Numbers to estimate a certain expectation. In this case, the average properties of systems with many accessible states can be estimated by using the Markov Chain Monte Carlo method (MCMC).

The MCMC algorithm generates random trial *moves* from the current old state  $o$  to a new state  $n$  and computes the average value of a property as the average over the elements of the Markov chain. Thus, instead of calculating time averages (like Equation 2.4), MC simulations calculates phase space averages (as in Equation 1.12). To show that an arbitrary initial distribution eventually relaxes to the equilibrium distribution, it is often convenient to apply the detailed balance condition. If  $P_{\text{eq}}(o)$  and  $P_{\text{eq}}(n)$  denote the probability of finding the system in state  $o$  and  $n$ , respectively, and  $\alpha(o \rightarrow n)$  and  $\alpha(n \rightarrow o)$  denote the conditional probability to perform a trial move from  $o \rightarrow n$  and  $n \rightarrow o$ , respectively, then the **detailed balance** condition is given by

$$P_{\text{eq}}(o)\alpha(o \rightarrow n)P_{\text{acc}}(o \rightarrow n) = P_{\text{eq}}(n)\alpha(n \rightarrow o)P_{\text{acc}}(n \rightarrow o) \quad (2.14)$$

In equilibrium, the flow from the old state  $o$  to any other state  $n$  is exactly equal to the reverse flow. Metropolis et al. [74] assumed that  $\alpha$  is a symmetric matrix,

$$\alpha(o \rightarrow n) = \alpha(n \rightarrow o) \quad (2.15)$$

and the following acceptance rule is given by

$$P_{\text{acc}}(o \rightarrow n) = \min \left( 1, \frac{P_{\text{eq}}(n)}{P_{\text{eq}}(o)} \right) \quad (2.16)$$

where each ensemble has a characteristic probability distribution according to the Table 1.1. Thus, the acceptance criteria will vary depending on the ensemble we are working with.

In general, to generate trial configurations of positions of particles that depends on the energy of the configuration i.e.  $\alpha(o \rightarrow n) = f[\mathcal{U}(n)]$ . So, if we want to sample

changes in  $NVT$  ensemble, imposing detailed balance, the appropriate acceptance rule is:

$$P_{\text{acc}}(o \rightarrow n) = \min \left( 1, \frac{f[\mathcal{U}(o)]}{f[\mathcal{U}(n)]} \exp(-\beta(\mathcal{U}(n) - \mathcal{U}(o))) \right) \quad (2.17)$$

so we can use non-Metropolis sampling methods (biased sampling techniques) to enhance the efficiency of a simulation.

The following types of molecular moves can be performed in a MC (MC-moves) simulation.

### Translation and Rotation

The selected molecule is given a random translation or a random rotation around the centre of mass. The acceptance rule is:

$$P_{\text{acc}}(\vec{r}_o^N \rightarrow \vec{r}_n^N) = \min (1, \exp(-\beta(\mathcal{U}(\vec{r}_n^N) - \mathcal{U}(\vec{r}_o^N)))) \quad (2.18)$$

### Regrow

To improve the conformational sampling of long and/or bulky molecules and increase the efficiency of insertions, **configurational bias Monte Carlo** technique is used [51]. This method inserts a molecule bead by bead, by generating  $k$  trial orientations for each bead according to the *internal* energy  $\mathcal{U}_{\text{int}}$  (based on the local bonded potential energy of the molecule), and selecting the most favourable orientation based on the external energy  $\mathcal{U}_{\text{ext}}$  (based on the non-bonded interactions with other particles) for each trial position  $j$  of each bead  $i$ .

In order to generate a trial conformation  $n$  of the molecule we generate an ensemble of  $k$  trial segments  $\{\vec{b}_i\}_{i=1}^k$  which are distributed according Boltzmann weight according with the internal energy  $\mathcal{U}_{\text{int}}$ . The probability for each segment is given by

$$P_i^{\text{int}}(\vec{b}) d\vec{b} \propto \exp(-\beta \mathcal{U}_{\text{int}}(\vec{b})) d\vec{b} \quad (2.19)$$

Thus, the most favourable trial segment  $n$  is selected according to the external energy:

$$P_i^{\text{ext}}(\vec{b}_n) = \omega_i^{\text{ext}}(n)^{-1} \exp(-\beta \mathcal{U}_i^{\text{ext}}(\vec{b}_n)) \quad (2.20)$$

where  $\beta = 1/(k_B T)$ ,  $k_B$  is the Boltzmann constant,  $T$  is the temperature, and  $\omega_i$  is the Rosenbluth weight defined as

$$\omega_i^{\text{ext}}(n) = \sum_{j=1}^k \exp(-\beta \mathcal{U}_i^{\text{ext}}(\vec{b}_j)). \quad (2.21)$$

When the entire chain (molecule) is grown we calculate the entire Rosenbluth factor of the molecule (the partition function of virtual segment)

$$W^{\text{ext}}(n) = \prod_{i=1}^l \omega_i^{\text{ext}}(n), \quad (2.22)$$

where  $\omega_1^{\text{ext}}$  correspond with the Boltzmann weight according with the external energy of the starting bead.

For the old configuration  $o$ , the procedure is similar but starting from the old position and calculating the  $U_{\text{ext}}(o)$ .

The same procedure is repeated and the selected trial orientation is added to the growing chain. Then, the acceptance of the whole molecule is calculated based on the Rosenbluth factor:

$$P_{\text{acc}}(o \rightarrow n) = \min \left( 1, \frac{W^{\text{ext}(n)}}{W^{\text{ext}(o)}} \right). \quad (2.23)$$

### Insertion/Deletion

A molecule is inserted at a random position and accepted using the following acceptance-rule::

$$P_{\text{acc}}(N \rightarrow N + 1) = \min \left( 1, \frac{W^{N+1}\beta V}{N + 1} \frac{\phi p}{\langle W^{\text{ideal}} \rangle} \right) \quad (2.24)$$

and is deleted using:

$$P_{\text{acc}}(N \rightarrow N - 1) = \min \left( 1, \frac{N}{W^{N-1}\beta V} \frac{\langle W^{\text{ideal}} \rangle}{\phi p} \right) \quad (2.25)$$

where  $W^{N+1}$  and  $W^{\text{ideal}}$  are the Rosenbluth factors of the new state and the reference of the ideal gas,  $p$  is the pressure in the reservoir and  $\phi$  is the fugacity coefficient. The pressure  $p$  of the reservoir is related to the chemical potential by

$$\mu - \mu^0 = k_B T \log(f/k_B T) \quad (2.26)$$

where  $f := \phi p$ , and  $\mu^0$  is the value of the chemical potential in the reference state. If this state is the ideal gas then  $\mu^0 := k_B T \log(\Lambda^3)$ . The fugacity coefficient is given by

$$\phi = \exp \left( \frac{g(T, p) - g^0(T, p)}{RT} \right) \quad (2.27)$$

However, the relation between pressure and fugacity can be calculated using the equation of state of the gas in the reservoir [75]. These MC-moves are usually used in adsorption simulations.

**Part I**

**Zeolites**



# Chapter 3

## Temperature-induced zeolite framework flexibility: RHO-type zeolite I

Flexibility in zeolite RHO manifests itself in its ability to adopt one of two structures, depending on the composition and the applied external conditions. In this work, structural changes of dehydrated zeolite RHO of composition  $(\text{Na}_6\text{Cs}_3)\text{Al}_9\text{Si}_{39}\text{O}_{96}$  and  $\text{Si}_{48}\text{O}_{96}$  were investigated by molecular dynamics (MD) and Monte Carlo methods using the force field by Nicholas et al. (*J. Am. Chem. Soc.* **1991**, 113, 4792). The structure was found, depending on temperature, to be stable in the acentric form (space group  $I\bar{4}3m$ ) below  $\sim 300$  K and in the centric form ( $\text{Im}\bar{3}m$ ) above, in qualitative agreement with experimental findings from the literature. Additionally, the structure may remain in the centric form in metastable conditions at all temperatures and exhibits a negative thermal expansion (NTE) of  $-(13 \pm 3) \times 10^{-6} \text{ K}^{-1}$ . Calculated X-ray diffraction patterns match the experimental ones closely confirming the assignments to space groups made on the basis of lattice sizes. Modifications on the force field were investigated and other established force fields probed. A detailed knowledge and control over the behaviour of this structure should lead to more reliable predictions on applications like separation of gases.

The publication related with this section can be found in:

- S. R. G. Balestra, J. J. Gutierrez-Sevillano, P. J. Merklings, D. Dubbeldam and S. Calero. "Simulation Study of Structural Changes in Zeolite RHO". *J. Phys. Chem. C* 117, 11592–11599, **2013**. DOI: 10.1021/jp4026283.

### 3.1. Introduction

Zeolites are crystalline aluminosilicate materials that possess intra-crystalline voids of molecular dimensions. All of the frameworks they form are known to show small deformations, although some structures are particularly flexible [77]. Amongst these, zeolite RHO exhibits unique structural changes. Depending on the conditions, it has been shown to appear in one of two cubic space groups, a centric  $\text{Im}\bar{3}\text{m}$  form or an acentric  $\text{I}\bar{4}3\text{m}$  form, as shown in Figure 3.1. Factors that affect the preferred form include the nature of the cations [78], amount of hydration [79], temperature [80] and pressure [81]. This high sensitivity to the conditions and composition of this zeolite makes it an excellent candidate for a theoretical study modelling it as a flexible framework.

The RHO topology is composed of  $\alpha$ -cages linked *via* double 8-rings. The double 8-rings are deformable and have a degree of ellipticity or distortion as shown in Figure 4.1. It is quantified by a parameter  $\Delta$  as defined by Parise and Prince [82]:

$$\Delta_{ijkl} = \frac{1}{2} \|r_{ij} - r_{kl}\| \quad (3.1)$$

where  $r_{ij} = |\vec{r}_i - \vec{r}_j|$  and  $i, j, k, l$  are defined in Figure 4.1. The distortions in double 8-rings are accompanied by a large change in unit cell length  $a$  [80].

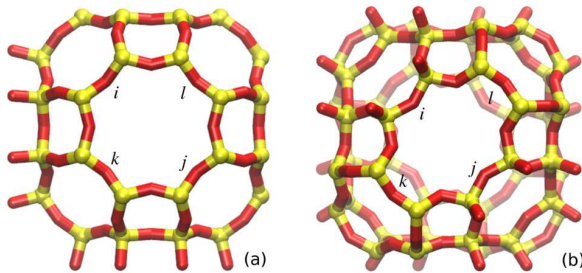


**Figure 3.1:** Zeolite RHO (a)  $\text{Im}\bar{3}\text{m}$  space group with  $a \sim 15.0 \text{ \AA}$ , (b)  $\text{I}\bar{4}3\text{m}$  space group with  $a \sim 14.6 \text{ \AA}$ .

The flexibility of this zeolite has been extensively studied in the past. However, to the best of our knowledge, this aspect has not been studied by simulation previously. The aim of this work is to study zeolite RHO of an ideal composition at low pressure using flexible force fields. The success of predictions critically depends on the force fields chosen. Several of them have been previously reported and found wide use in the area of flexible zeolites, such as the model of Nicholas et al. [83], Hill and Sauer [84, 85] and Demontis et al. [86], and a core-shell model of Schröder and Sauer [87]. A recent simulation study supports Nicholas' model as the one that performs better in

infrared studies than other force fields investigated [88]. Unless indicated otherwise, this is the default force field used in this work.

Another recent experimental study reports high selectivity of zeolite RHO for CO<sub>2</sub> in CO<sub>2</sub>/CH<sub>4</sub> separations. The authors find that the partial pressure of CO<sub>2</sub> causes a change in structure and hypothesise that the phenomenon is induced by interactions between the flexible framework and the CO<sub>2</sub> in the proximities of the window [89]. Understanding this phenomenon may lead to interesting contributions to environmental technology and the capture of greenhouse gases, but before that it is necessary to gain a better, more fundamental understanding of the flexibility of zeolite RHO.

## 3.2. Simulation methods

Zeolitic frameworks are treated as periodic networks based on periodic boundary conditions (PBC). This crystalline tessellation –the framework– is performed from the simulation box by endless Euclidean translations in all three spatial directions. The interactions between particles are calculated according to the force field chosen. Unless specified otherwise, this is the force field by Nicholas et al. [83]. Electrostatic energy of a crystalline system is conditionally convergent. To avoid infinities, Ewald summation was used. The cut off radius for short-range interactions was set to 12 Å.

The crystal is considered vacuous and in vacuum. To make the structures (Im $\bar{3}$ m and I $\bar{4}$ 3m forms) we have used the atomic coordinates provided by the crystallographic study of Palomino et al. [89].

To calculate micro-states compatible with environmental conditions (constant particle number, volume, and temperature) canonical Monte Carlo (abbreviated MC NVT) was used. Isothermal-isobaric ensemble (constant particle number, pressure, and temperature, abbreviated NPT) molecular dynamics (MD) was used to study the evolution of the system. The method used to equilibrate is the Parrinello–Rahman barostat[90]. The Martyna et al. [52] algorithm is used for velocity Verlet integrators –validated by Tuckerman et al. [27, 53]–. When we keep fixed the pressure, it is equal to 1 mTorr –an experimental vacuum–. Simulations were run for 100-1000 ps using an integration time step of  $\tau = 5 \times 10^{-4}$  ps. Energy minimisations have been calculated at fixed volume using the Baker method [62].

Since the space groups involved in this study are cubic but cell lengths in the simulations are allowed to evolve independently from each other, the length of the unit cell at temperature  $T$  was considered as the time average  $a_T = \frac{1}{3} \langle a_{xT}^t + a_{yT}^t + a_{zT}^t \rangle_t$ .

## 3.3. Results and discussion

A first concern that arises when dealing with this structure is the observation that the phase transition Im $\bar{3}$ m  $\leftrightarrow$  I $\bar{4}$ 3m was observed in zeolite RHO of composition Na<sub>6</sub>Cs<sub>3</sub>)O<sub>96</sub>Al<sub>9</sub>Si<sub>39</sub>, [89] while a pure silica version has yet to be synthesised. It is there-

fore important to assess the role of tetrahedral aluminium in enabling this structural change.

Atomic coordinates were taken from Palomino et al. [89] for the  $I\bar{4}3m$  form. The aluminium atoms have a non-periodic occupation of lattice sites in the crystalline structure. To model this system, a crystalline configuration is set up in which a random replacement of 9  $\text{SiO}_4$  by 9  $\text{AlO}_4$  tetrahedra is undertaken and bound to obey Lowenstein's rule. Monovalent cations (6  $\text{Na}^+$  and 3  $\text{Cs}^+$ ) were randomly added to compensate for the charge of the framework. Around  $\sim 1000$  different configurations were generated and MC simulations run on them that yielded as many values for internal energies  $U$ . Volume, temperature, and number of atoms were fixed (NVT ensemble) so that the experimental density was reproduced and temperature was set to a low 3 K. Each configuration  $k = 1, \dots, 1000$  is characterised by its average distance between aluminium atoms  $\langle \text{Al Al} \rangle_k$  and its internal energy  $U_k$  and represented in Figure 3.2 (top). Internal energies were computed because of their independence from pressure so the simulations were expected to be a bit more robust. However, they compare favourably with simulations in the isothermal-isobaric ensemble. Under these conditions of low temperature, the internal energy  $U$  is almost equal to the free energy  $F$  and therefore the internal energy serves as a measure of the stability of the framework. If each configuration  $k$  is in equilibrium at temperature  $T$ , it can be assigned a weighting factor  $P_k \propto \exp(-U_k/k_B T)$ . In Figure 3.2, the obtained probability density is depicted in a histogram. The distance *vs* internal energy data on the other side scatter strongly. A line corresponding to a linear fit was laid through the simulation data and showed a correlation that is essentially within the error bars. The correlation coefficient is  $r^2 \simeq 0.035$ .

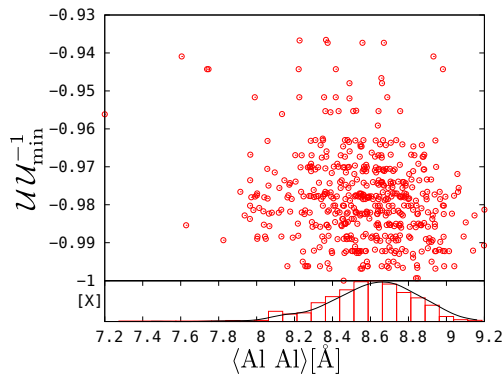


**Figure 3.2:** Top: Dimensionless internal energy  $U U_{\min}^{-1}$  (with  $U_{\min}^{-1} \simeq 6.4 k_B \times 10^6$  K, absolute value of the configuration with lowest energy) *versus* average distance between Al atoms in randomly generated RHO frameworks. The dashed line represents a linear fit through the data. Bottom: Probability density as a function of average distance between aluminium atoms. The dashed line represents a normal distribution fit.

Any configurations of  $\text{SiO}_4 \rightarrow \text{AlO}_4$  replacements in presence of monovalent cations is valid as long Lowenstein's rule is fulfilled. Since, the aluminium distribution does not seem to be the primary cause of the structural changes of ideal flexible zeolite RHO, and to gain simplicity it will assumed that the role of aluminium should not be critical for the observation of structural changes. From now on, only the hypothetical pure silica zeolite RHO will be considered.

### 3.3.1. Temperature effect

Changes in temperature affect the volume in two ways: on the one hand, the structural change between space groups  $Im\bar{3}m$  and  $I\bar{4}3m$ , and on the other hand, the dependence of unit cell volume on temperature within the same space group. By use of neutron diffraction and X-ray diffraction, Parise et al. [80] observed a gradual increase in unit cell volume upon heating from 11 to 573 K, together with a decrease in the geometrical parameter  $\Delta$  that is defined in Equation 4.1. Their results led them to conclude that upon heating, the structure changes progressively from  $I\bar{4}3m$  to  $Im\bar{3}m$  and estimated by extrapolation that this process would complete at 800 K. In the current work, the temperature effect was studied by molecular dynamics in the NPT ensemble under conditions described in the Methods Section. The length of unit cell  $a$  was computed and attention paid to its evolution during simulation. The temporal evolution of the length of the unit cell for temperatures 11, 295 and 423 K is shown in Figure 3.3 (left). The system in these early stages of the simulation is obviously outside of thermodynamic equilibrium conditions, and was started with the experimental 11 K cell parameters and  $I\bar{4}3m$  space group. It is striking how fast the equilibrium value of the cell parameter is reached, even at a nominal 11 K. The space group on the other side was stable in the simulations at 11 and 295 K, but switched to the high-symmetry  $Im\bar{3}m$  form at 423 K within a picosecond of simulated time. The average values  $a_T = \langle a_T^t \rangle_t$  achieved above 10 ps can be represented in a systematic way versus temperature  $T$ , as shown in Figure 3.3 (right) when simulations are investigated using both the  $Im\bar{3}m$  and  $I\bar{4}3m$  initial conditions. As can be seen from this figure, at 423 K and 800 K frameworks adopt the high-symmetry form. At 300 K and below on the other side, the frameworks retained their symmetry over the duration of the simulations. One of the interesting consequences is that it is possible to follow the evolution of the volume of the high-symmetry structure over the whole range of temperatures in these simulations. A linear regression of the  $a_T$  values of structures that retain the centric form yields

$$a_T \simeq a_0 + T \left( \frac{\partial a}{\partial T} \right)_P \quad (3.2)$$

where  $a_0 = 14.012\text{\AA}$  and  $(\partial a / \partial T)_P = -(6 \pm 1)10^{-5}\text{\AA}$  with  $r^2 \simeq 0.75$ . Thus, an intrinsic negative thermal expansion (NTE) was observed with a coefficient of thermal expansion  $\alpha_V$  of  $\frac{3}{a} \left( \frac{\partial a}{\partial T} \right)_P = -(13 \pm 3) \times 10^{-6} \text{ K}^{-1}$ . This value is consistent with the results given by Miller et al.[91] It can be noted also that while transitions from the acentric

to the centric form have been observed, no transition took place from the centric to the acentric form.

While in the case of zeolite RHO the overwhelming effect of the structural change  $Im\bar{3}m \leftrightarrow I\bar{4}3m$  on the unit cell length  $a$  prevents an experimental confirmation of the phenomenon of NTE, the results from the simulations are consistent with the behaviour of zeolites with LTA topology where similar, although slightly bigger NTE values were reported by Carey et al. [92]. Although it has been taken so far for granted

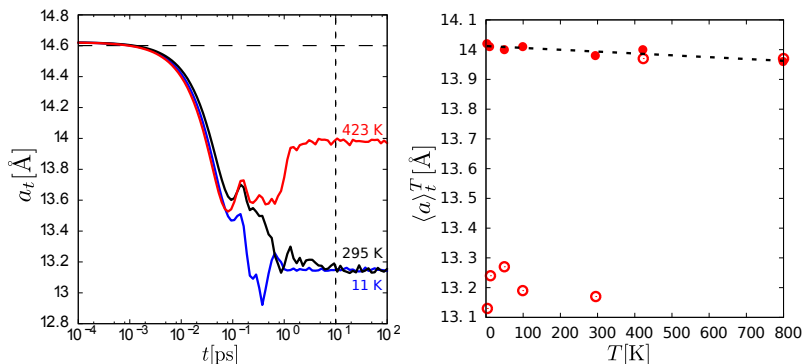


**Figure 3.3:** Left: length of unit cell  $a^t$  versus time  $t$  at 11 K (blue), 295 K (black) and 423 K (red). The dashed lines marks (horizontal) the experimental length of the unit cell at 11 K, and (vertical) the time in which we start to calculate the mean value. Right:  $\langle a \rangle_t^T$  versus temperature  $T$ ; the simulations started with  $Im\bar{3}m$  (●) and  $I\bar{4}3m$  (○). The dashed line represents a linear fit to the  $Im\bar{3}m$  form.

that big changes in unit cell lengths are associated with a change in structure, these can be probed in a more authoritative way by calculating powder X-ray diffraction patterns and comparing them to available experimental data. Given that there is a significant difference in average cell lengths between simulations and experiments and according to Bragg's law this would lead to a shift in  $2\theta$  values, the simulation cells were rescaled. Using this approach, the identification of the symmetry is made easier and less ambiguous. The results for a  $CuK_\alpha$  radiation ( $\lambda = 1.5418$  Å) are shown in Figure 3.4 and compared with experimental data from Palomino et al. [89]. Changes in the diffraction patterns are most prominent in the  $23^\circ < 2\theta \leq 29^\circ$  region. The identification of the framework symmetry of the simulations that were shown in Figure 3.3 (left) is confirmed by the representations in Figure 3.4. Clearly, the data for the simulation at 11 K agree well with experimental  $I\bar{4}3m$  data. It can be concluded that the simulation maintains the lower-symmetry form it started with, while simulations at 295 and 423 K both are found to belong to the high-symmetry form. The simulation at 423 K is especially interesting because it is the only one of the three simulations shown that was started with  $I\bar{4}3m$  symmetry but was converted to  $Im\bar{3}m$ . In Figure 3.4, the unit cells had been rescaled to the corresponding experimental values, as has been stated previously. One might check that the XRD calculated does indeed

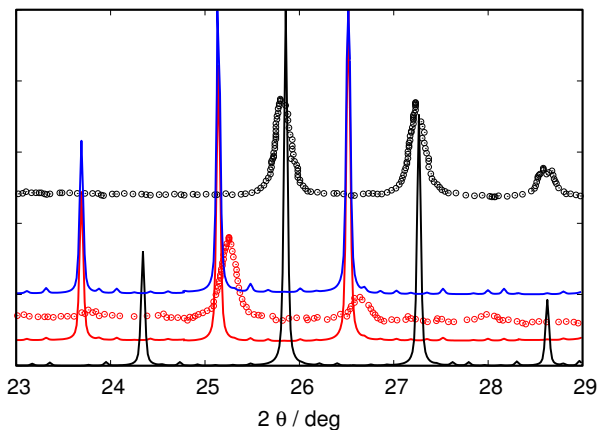


**Figure 3.4:** X-ray diffraction patterns using  $\text{CuK}\alpha$  radiation. Red circled dots ( $\odot$ ) correspond to an experimental determination attributed to space group  $Im\bar{3}m$ [89] and black circled dots ( $\odot$ ) to space group  $I\bar{4}3m$ . Red solid lines correspond to rescaled simulation structures at 11 K, black solid lines to the ones at 11 K, and blue dashed lines to the ones at 423 K.  $2\theta$  error bars are smaller than the line widths.

contain new structural information that enables the identification. To this end, the XRD pattern was recalculated using the cell lengths of the *other* space group (Figure A1 ). As a result, it is found that now the low-symmetry form is rather similar to the experimental high-symmetry form, and vice versa. So the cell lengths are clearly very important. However, the peak at 28-29° in  $I\bar{4}3m$  is missing when the real cell length, but the wrong symmetry is used.

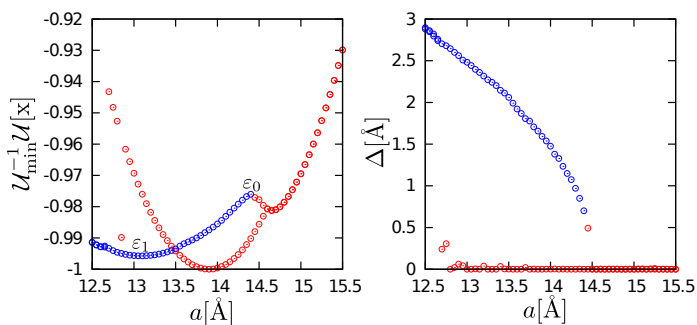


**Figure 3.5:** Equilibrium paths on the potential energy surface at 0 K  $u = -U_{\min}^{-1}U(a, \Delta)$  with  $k_B^{-1}U_{\min} = -6.77 \times 10^6$  K for Nicholas et al.'s force field. Systems with  $\Delta < 0.5$  Å in red and  $\Delta \geq 0.5$  Å in blue.

Furthermore, it is also possible to quantify directly the deformation of the structure

$\Delta$ . The energy of the structure was minimised at constant  $a$ . This calculation provides the equilibrium paths (at  $T = 0$  K) on the potential energy surface  $U = U(a, \Delta)$ . Two main potential wells were found: one at  $\Delta = 0$  and another at  $\Delta \neq 0$ . Figure shows two sections of the surface. It can be noted that with this force field,  $Im\bar{3}m$  is more stable at 0 K although the potential wells allow systems to get trapped in any of them at low enough temperature. The position of the minima is consistent with the calculations using NPT MD depicted in Figure 3.3. In Figure 3.5 (left), a data point at  $\simeq 12.7 \text{ \AA}$ ,  $u = -0.99$  has a deformation  $\Delta=0$  and seems to be an outlier. In fact, this is a significantly deformed window as can be seen in the snapshot obtained by minimisation of the  $Im\bar{3}m$  form at low volume (Figure 3.6). It would be interesting to see if this structure can be formed under high pressure conditions. At still lower volumes, the  $Im\bar{3}m$  form is converted to the  $I\bar{4}3m$  form, an observation in keeping with experimental findings [81].

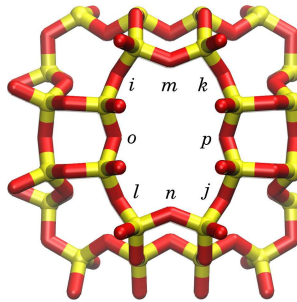


**Figure 3.6:** Minimized structure at low volume belonging to space group  $Pm\bar{3}$ .  $\Delta_{ijkl} = 0$  but  $\Delta_{mnop} = 0.92 \text{ \AA}$ .

The model reproduces also nicely the relationship between the amount of deformation  $\Delta$  in the windows and the cell length that was already observed by Parise and Prince:[82] for example, the structure responds to a  $0.7 \text{ \AA}$  shortening of its unit cell with a deformation  $\Delta \approx 1.8 \text{ \AA}$  and the downwards curvature is similar to the experimental one.

So far, the model of Nicholas et al. [83] has been used. In the next section, modifications on this model are studied to assess the sensitivity of the properties calculated hitherto on details of the force field. The first parameter modified was the set of partial charges.

### 3.3.2. Effect of charges

Electrostatic interactions are long-ranged and small modifications in charges can lead to relevant effects on the volume of the cell or on its symmetry. In order to assess the sensitivity of the structures on partial charges in the system, two modifications of Nicholas et al.'s[83] force field were tested: a zero-charge model and a model by

García-Sánchez et al. [93] This model uses the same intramolecular contributions as Nicholas et al.'s model, but charges and van der Waals contributions have been fitted for a more accurate reproduction of CO<sub>2</sub> adsorption in zeolites. Very roughly speaking, charges are reduced by around 40%. So in comparison with Nicholas et al.'s model, the models considered in this part weaken the electrostatic interactions.

With these new parameters, NPT MD calculations were repeated under the same conditions of pressure and temperatures as in Figure 3.3 (left). The time averaged values  $a_T$  at different temperatures have been added in Figures 3.7a and 3.7c for the corresponding model.

Energy minimisation calculations of the structure for García-Sánchez et al.'s model and the zero-charge model were performed and are shown in Figure 3.7.

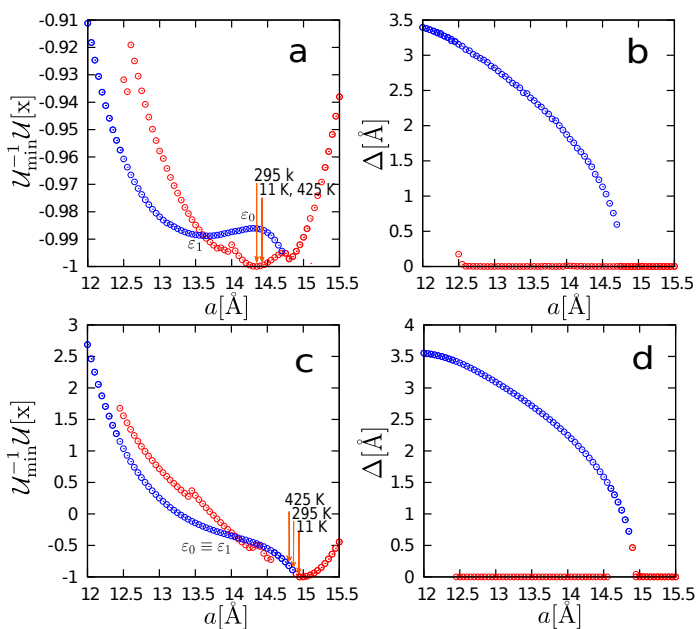


**Figure 3.7:** (a) Equilibrium paths on the potential energy surface  $u = U_{\min}^{-1}U(a, \Delta)$  and (b)  $\Delta$ -parameter for García-Sánchez et al.'s model, where  $k_B^{-1}U_{\min} = 3.46 \times 10^6 \text{ K}$ /unit cell, and corresponding plots for a zero-charge model (c and d) where  $k_B^{-1}U_{\min} = 1.51 \times 10^5 \text{ K}$ /unit cell. Systems with  $\Delta < 0.5 \text{ Å}$  in red and  $\Delta \geq 0.5 \text{ Å}$  in blue. The orange arrows indicate  $\langle a_T^{\pm} \rangle_t$  computed by NPT MD.

The simulations revealed that independently of the starting structure and of the model, the framework ended up in the high-symmetry,  $\Delta = 0$  structure since this is the lowest energy structure according to these models. How much thermal activation is required for the structure to be converted into the high-symmetry variant can be related qualitatively to barrier height  $\delta = \varepsilon_0 - \varepsilon_1$ . The variables represent the energy

$\varepsilon_0$  of the principal barrier and  $\varepsilon_1$  of the bottom of the well of  $\Delta \geq 0.5$  structures. These variables are marked in Figures 3.5 and 3.7. Nicholas et al.'s model predicts a difference of  $2\delta k_B^{-1}(3N - 6)^{-1} \simeq 633.8$  K, García-Sánchez et al.'s a difference of  $2\delta k_B^{-1}(3N - 6)^{-1} \simeq 44.3$  K, and the zero-charge model has no energy barrier for  $\Delta > 0$ .

However, with decreasing point charges, the length of the minimum-energy unit cell increases. For the centric structure, a decrease of the charges by 40% results in a unit cell length increase of  $\sim 0.54$  Å, while a decrease of charges by 100% involves an increase by  $\sim 1$  Å.

To conclude this section, the structure has been found to be very sensitive to a scaling of the point charges, both with respect to temperatures of conversion from asymmetric to symmetric structure and to the length of the unit cell.

### 3.3.3. Modifications of the rigidity of the lattice

It is interesting at this point to estimate just how dependent the findings are on details of the force field employed. While it may intuitively be easily understandable that the charges in the system should have a strong effect on the unit cell length vs. temperature graph, it is far less obvious how or whether a change in force constants of the lattice should affect this representation.

The contributions to potential energy given by bond stretching and bending are given by the set of equations (3.3).

$$\begin{aligned} U_{ij}(r_{ij}) &= k_r(r_{ij} - r_0)^2 \\ U_{ijk}(\theta_{ijk}) &= k_\theta(\theta_{ijk} - \theta_0)^2 \end{aligned} \quad (3.3)$$

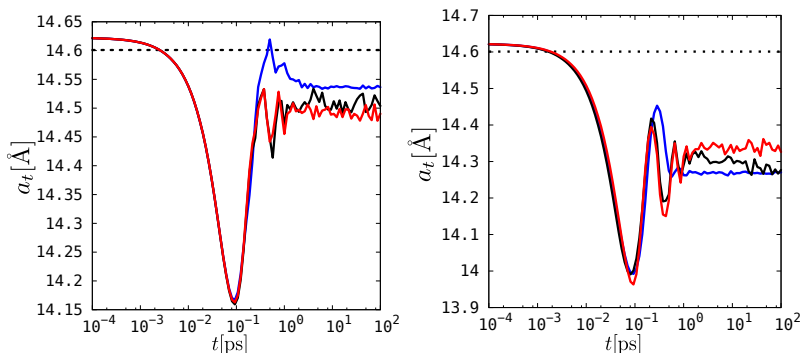


**Figure 3.8:** Length of unit cell  $a$  versus time  $t$  using  $k_r \rightarrow 2k_r$  and  $k_\theta \rightarrow \frac{k_\theta}{2}$  (left) and  $k_r \rightarrow \frac{k_r}{2}$  and  $k_\theta \rightarrow 2k_\theta$  (right) at 11 K (blue), 295 K (black), and 423 K (red).

In the previous section, it was found that over the temperature range 11-423 K no expansion or shrinkage of the unit cell was observed for the model of García-Sánchez

et al. In this section, systematic modifications of  $k_r$  and  $k_\theta$  by a factor of 1/2 or 2 were undertaken. In all cases, the frameworks formed had a  $\Delta$ -parameter of zero (see Figure 3.8). It was further found that the magnitude of  $k_r$  governs the absolute value of the unit cell length. A change by a factor two corresponds roughly to an increase of 0.1 Å. Moreover, the simultaneous halving of  $k_r$  and doubling of  $k_\theta$  force constants led to a positive thermal expansion, while on the contrary a doubling of  $k_r$  and halving of  $k_\theta$  led to a negative thermal expansion. This opens up the possibility in the development of a force field, of tuning the force constants to reproduce known thermal expansions

### 3.3.4. Other potentials

While in previous sections the model of Nicholas and modifications of this model have been investigated, in this section other popular approaches were tested. Probably the simplest force field one can imagine was proposed by Demontis et al. [86]. This force field is not stable in NPT-ensemble calculations, possibly due to the lack of Van der Waals and charge-charge long-range interactions (see Figure A2 in Appendix A). Oscillations and vibrations in the equilibrium introduce asymmetries in the structure, the lack of charges hinder their disappearance. This potential worked well in a number of applications in the NVT-ensemble in which it was developed, but folded unrealistically due to the lack of torsional, charges and other terms to restrain the movement of the atoms.

Similar graphics to Figure 3.5 can be constructed for the model by Hill and Sauer[85] and a further refinement of the latter that includes a core shell [87].

The results are shown in Figure 3.9 (top and bottom, respectively). Unit cell lengths at roughly 15 Å are in better agreement to experiment than Nicholas et al's model. However, as energy minimisations show, both the symmetric and asymmetric structure converge towards the same minimum and present no secondary minima. Hill and Sauer's model contains strong torsional force constants capable of maintaining the structure. Schröder and Sauer's model on the other side, based on a consistent force field, adapts a core shell to it. Normally, the fixed high symmetry in the structures tends to cancel out any small variation in charge [83]. But, if the volume and geometry of the unit cell are not fixed, the incidence of charges on the symmetry of the lattice is marked.

The simulations with Schröder and Sauer's core shell model increased the degrees of freedom, relaxing the system and thereby resulting in more realistic electrostatic interactions.

Figure 3.9-b, 3.9-d, and the corresponding representations in Figures 3.5 and 3.7 all show a downwards curvature in the ellipticity vs. unit cell length that is matched by the experiment. This behaviour that appears to be fairly universal is probably best understood in the context of flexing mechanically a structure with essentially rigid bond lengths gradually from a distorted geometry ( $I43m$  space group) towards a higher-symmetry geometry ( $Im\bar{3}m$  space group). It is the potential energy analysis discussed previously (Figures 9-a and 9-c) and the applied external pressure that

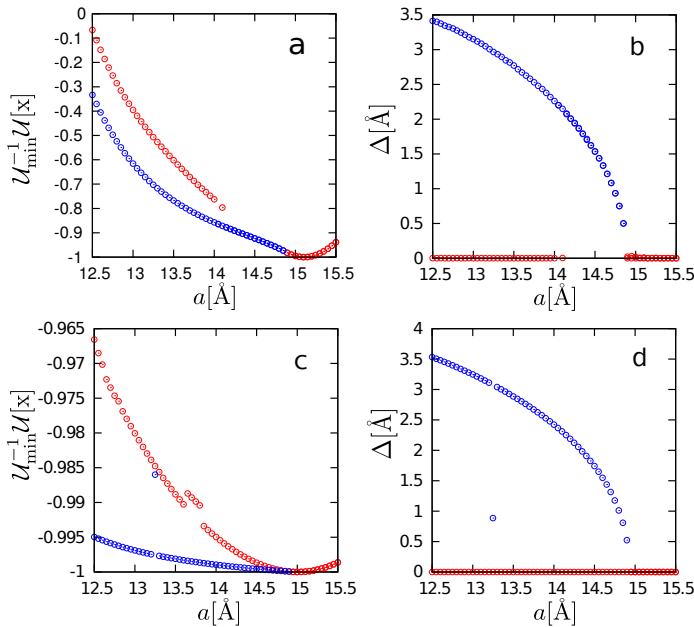


**Figure 3.9:** Equilibrium paths on the potential energy surface  $u = -U_{\min}^{-1}U(a, \Delta)$  for  $(a, b$  in plot) for Hill and Sauer’s force field, [84, 85] with  $k_B^{-1}U_{\min} = -1.077 \times 10^6$  K and  $(c, d$  in plot) for a core-shell model, [87] with  $k_B^{-1}U_{\min} = -7.25 \times 10^7$  K. Systems with  $\Delta < 0.5$  Å in red and  $\Delta \geq 0.5$  Å in blue.

determine ultimately how inevitable a falling back to the high symmetry model is.

### 3.4. Conclusions

Structural changes in zeolite RHO between  $\bar{I}43m$  and  $Im\bar{3}m$  space groups lead to a change in unit cell length. For this reason, flexible force fields for zeolites are worthwhile studying when the volume is not fixed.

In this work, it was found that the aluminium distribution does not seem to be the primary cause for the structural changes in flexible zeolite RHO. All framework models are unable to reproduce correctly the structural phase transition with use of energy minimisation and molecular dynamics techniques for the isothermal–isobaric ensemble. Energy minimisation results were consistent with molecular dynamics simulations.

However, a series of important conclusions could be drawn. Nicholas et al. [83]’s model was shown by X-ray diffraction and by recording the degree of ellipticity to reproduce the structural changes within the framework. The latter indicator correlates very well with changes in unit cell length in the exact way found experimentally.

The main drawback of Nicholas' model consists in too small unit cell lengths. A low volume structure belonging to space group  $Pm\bar{3}$  is predicted with this force field as an energetically competitive alternative to high ellipticity structures.

From the point of view of potential energy, decreasing the partial charges in the model reduces the barrier between structural phases and increases the volume of the unit cell. In this way, the study of modifications in the charges of the Nicholas model, in section 3.3.2, and the simulations with Demontis model in section 3.3.4, for the isothermal-isobaric ensemble, suggest that the role of the charges is notable. The Schröder and Sauer model with a core shell model, and Sauer and Hill model with strong torsions maintained the stability of the structure within NPT simulations, reproduced the experimental cell length well, but failed to account for the existence of  $I\bar{4}3m$  symmetry.

Thus, the potential of Nicholas et al. predicts for the pure silica zeolite RHO two stable structures ( $Im\bar{3}m$  and  $I\bar{4}3m$ ). The other potentials predict a single stable structure ( $Im\bar{3}m$ ) and predict a more realistic length of the unit cell.

Finally, it is worth highlighting the effects of modifying simultaneously the bond stretching and bending parameters in a framework model. These parameters drive the thermal expansion of the framework.



---

# Chapter 4

## Structural distortions by cation migration and hydration: RHO-type zeolite II

Molecular valves are nanostructured materials that are becoming popular, due to their potential use in bio-medical applications. However, little is known concerning their performance when dealing with small molecules, which are of interest in energy and environmental areas. It has been observed experimentally that zeolite RHO shows unique pore deformations upon changes in hydration, cation siting, cation type, and/or temperature-pressure conditions. By varying the level of distortion of double 8-rings it is possible to control the adsorption properties, which confers a molecular valve behaviour to this material. We have employed interatomic potentials-based simulations to obtain a detailed atomistic view of the structural distortion mechanisms of zeolite RHO, in contrast with the averaged and space group restricted information that can be retrieved from diffraction studies. We have modeled the pure silica zeolite RHO as well as four aluminosilicate structures, containing  $\text{Li}^+$ ,  $\text{Na}^+$ ,  $\text{K}^+$ ,  $\text{Ca}^{2+}$  and  $\text{Sr}^{2+}$  cations. It has been found that the distortions of the three zeolite rings are coupled, although the four-membered rings are rather rigid and both six- and eight-membered rings are largely flexible. A large dependence on the polarising power of the extra-framework cations and with the loading of water has been found for the minimum aperture of the eight-membered rings that control the nanovalve effect. The energy barriers needed to move the cations across the eight-membered rings are calculated to be very high, which explains the origin of the experimentally observed slow kinetics of the phase transition, as well as the appearance of metastable phases.

The publication related with this section can be found in:

- S. R. G. Balestra, S. Hamad, A. R. Ruiz-Salvador, V. Domínguez-García, P. J. Merklings, D. Dubbeldam and S. Calero. “Understanding Nanopore Window Distortions in the Revers-

ible Molecular Valve Zeolite RHO". *Chem. Mater.* 27, 5657–5667, 2015. DOI: 10.1021/acs.chemmater.5b02103. arXiv: 1605.06338.

## 4.1. Introduction

Molecular valves are a class of molecular devices that allow molecular transport in a controlled way through gate opening or trapdoor mechanisms. Valve action is typically performed by a molecule that is attached to the material, either by covalent bonds, hydrogen bonds or supramolecular interaction. In presence of external stimuli, such as temperature, pressure, pH, molecular or ion chemical potential, this molecule is able to change its configuration to allow the molecular flow. This ability has attracted huge attention during the last years, due to its impact in delivering medium and large size active molecules for medical applications [95–98].

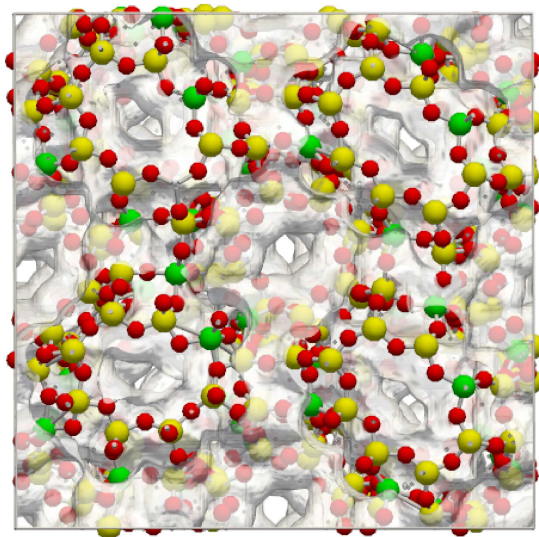


**Figure 4.1:** Snapshot of a distorted form of RHO-type zeolite obtained by Molecular Dynamics. An isoenergy surface is shown in translucent gray. Extra-framework cations are omitted for clarity.

However, for small molecules, such as carbon dioxide or small hydrocarbons, operating the molecular valve through an attached molecule is less suitable, as a higher structural control is required for this kind of molecules. In this context, zeolites and metal-organic frameworks (MOFs) appear as candidate materials, due to their crystalline nature and their smaller nanopore windows. As zeolites and MOFs exhibit molecular sieving properties, the conjunction of these properties with particular structural flexibility can give rise to molecular valve behaviour.

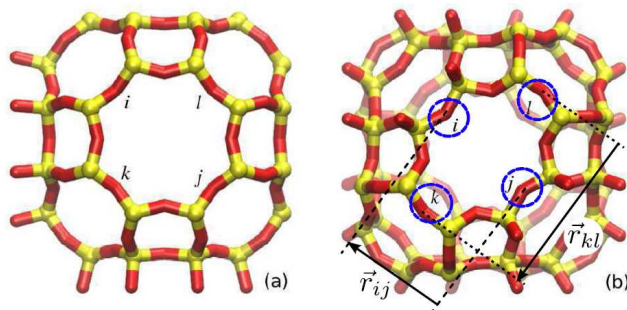


**Figure 4.2:** Zeolite RHO in the a)  $Im\bar{3}m$  and b)  $I\bar{4}3m$  space groups.  $r_{ij}$ , and  $r_{kl}$  are used for measuring the distortion parameter  $\Delta$  as defined in equation 4.1.

Kuznicki et al. [99] were pioneering in showing that efficient separation of small molecules can be achieved by exploiting framework flexibility. In these selected frameworks, pore window diameters can be tuned by means of temperature to separate  $O_2:N_2$ ,  $N_2:CH_4$ , and  $CH_4:C_2H_6$  mixtures. Zeolite RHO has a reversible operating mechanism, which can be controlled to smoothly switch from one stable form to another, by exposure to vacuum, dehydration, and changes in temperature [80, 100–105]. Its potential use in applications that make use of the molecular sieving of small molecules is huge, making this zeolite an excellent case for the study of thermally resistant and highly flexible materials (see Figure 4.1). Indeed, Lozinska et al. [106] studied recently  $CO_2$  adsorption and separation in several forms of univalent metal-exchanged zeolite RHO, and found that the Na-form is the best candidate for applications in selective kinetic gas separation of  $CO_2$ . They performed adsorption experiments, combined with crystallographic analysis, which showed that the observed molecular sieving behaviour is due to a molecular valve effect associated to the extra-framework cations that control the molecular passage through windows between cages. This is a key aspect, involved in the high selectivity of this material for  $CO_2:CH_4$  separation. In another recent paper, Palomino et al. [105] showed that in a mixed Na-Cs zeolite RHO, a reversible phase transition from  $I\bar{4}3m$  to  $Im\bar{3}m$ , and vice versa, can be driven by the presence of adsorbed  $CO_2$  molecules. They found that this zeolite exhibits the highest selectivity towards  $CO_2:CH_4$  separation, which was related to the polarity of the framework (ratio Si/Al = 4.5) and the pore opening due to the phase transition triggered by  $CO_2$  adsorption.

The aluminosilicate zeolite RHO, which adopts an  $Im\bar{3}m$  centric structure for temperatures above 300 K, undergoes a significant pore distortion at lower temperatures, resulting in the stabilisation of the  $I\bar{4}3m$  acentric form (Figure 4.2b). In order to quantify the degree of distortion, Parise and Prince [107] introduced a measure that relates the average value of the degree of ellipticity of the double 8-rings (D8R),

describing the pore opening windows, as shown in equation 4.1.

$$\Delta = \frac{1}{2} \langle |r_{ij} - r_{kl}| \rangle \quad (4.1)$$

where  $r_{ij} = \|\vec{r}_i - \vec{r}_j\|$  and  $i, j, k, l$  are defined in Figure 4.2.

It has been found that zeolite RHO, upon insertion of divalent cations, undergoes an abrupt structural change towards the acentric form [100], with 2-6% changes in the cell parameters and  $\Delta$  values  $\sim 2 \text{ \AA}$  in the acentric form. This is in contrast with the smoother behaviour found in the monovalent exchanged zeolite RHO, which exhibits changes in the cell parameters  $\sim 3 \%$  lower and has lower values of the  $\Delta$  parameter (circa  $1.5 \text{ \AA}$ ) [80]. It is worth noting that the appearance of framework distortions in deuterated zeolite RHO [103] suggests that this behaviour is inherent to the framework topology and that the extra-framework cations act as modulators. This observation is in agreement with our previous paper [76], in which we showed, by means of interatomic potential-based energy minimisations, that pure silica zeolite RHO has two stable forms (with  $\Delta = 0$  and  $\Delta \neq 0$ ) and it could experience a phase transition between them (from  $I43m$  to  $Im3m$  space group) at high temperatures. This result was supported by the calculations of X-ray Diffraction patterns.

The structural picture discussed above, which is also used to explain the molecular sieving properties of the mentioned works, rests on the averaged and space-group restricted information retrieved by diffraction techniques. Computer modelling offers the opportunity to overcome these limitations and hence to provide a deeper insight into the distortion mechanisms. In the present context this is of particular relevance, since the mechanism involved in the molecular valve behaviour in zeolites and related materials is still poorly understood.

In this work we carry out a detailed atomistic simulation study in order to gain a better understanding of the relationship between the nature of the extra-framework cations and the flexibility of the material, taking into account the concomitant impact on molecular sieving properties. Existing approaches for accurately modeling cation location and/or large variations of cell volumes in zeolites consider either poorly deformable frameworks [108–111], or those having low ratios between the cation number and their potentially accessible sites [112–114]. For all these reasons, in the early stage of this work we were unsuccessful in reproducing the crystal structure of several cation-forms of zeolite RHO by applying these methods. For the present study we have then developed a methodology for accurately modelling the structural behaviour of crystalline nanoporous solids undergoing large structural variations, which combines cycles of Monte Carlo (MC) calculations, energy minimisation (EM) and Molecular Dynamics (MD) simulations. In order to study the effect of the ionic polarising power *i.e.* the ionic charge/size ratio, five metal-forms ( $\text{Na}^+$ ,  $\text{Li}^+$ ,  $\text{K}^+$ ,  $\text{Ca}^{2+}$  and  $\text{Sr}^{2+}$ ) of zeolite RHO were considered. The behaviour of the pore windows deserves particular attention, as it is expected to be strongly associated with the nanovalve behaviour linked to three main phenomena, namely adsorption, separation and transport properties.

## 4.2. Computational Section

The methodology used here for the realistic structural modeling of zeolite RHO is inspired by the experience in modeling massively defective ionic solids [115, 116], in which large structural deformations occur. Since one of the results of this research has been the development of the new methodology, it is presented in the next section, along with the rest of the results. As anticipated above, several modeling cycles will be carried out, and therefore the use of first principles calculations is hindered by its CPU cost. Thus, interatomic potentials-based simulations are the method of choice. For the case of zeolite RHO, in particular to model the acentric phase, we noted that the shell model is required, in order to take into account the polarizability of the framework oxygen atoms. To check the importance of polarizability on the structure, several trial configurations of metal-forms of zeolite RHO having acentric  $I43m$  structures were modeled. While the acentric structure was kept during energy minimization, it changed to centric  $Im\bar{3}m$  when the shell constant is gradually increased to reach very high values. These high values of the shell constant would make the atoms to behave as non-polarizable atoms. In addition, we used the rigid-ion models of Van Beest et al. [117], Kramer et al. [118] and Ramsahye and Bell [119], for which the acentric structure is not stable either. Then, the well-known shell-model potentials of Sanders et al. [38] was used, as they provide accurate structures of complex zeolites. In connection with it,  $Li^+$ ,  $Na^+$ ,  $K^+$ ,  $Ca^{2+}$ , and  $Sr^{2+}$  cations were selected considering the existence of good quality interatomic potentials [39–41] that are compatible with the Sanders et al. [38] potentials.

At the experimental synthesis temperature RHO zeolites adopt the centric cubic  $Im\bar{3}m$  structure, with only one distinct tetrahedral site in the asymmetric unit cell [120, 121], which strongly suggests that a particular ordering of the Al atoms is not likely to occur. In addition, RHO zeolites are synthesized with monovalent cations, usually mixtures of  $Na^+$  and  $Cs^+$ . There is no need to introduce the close pairs Al-Al that would be required if divalent cations were used [122]. Therefore, like in the case of FAU zeolites [8], Al atoms in RHO zeolites are expected to stay as far as possible from each other, following Dempsey's rule [8], as was recently shown to be expected to hold in zeolites, unless framework anisotropy perturbs this behaviour [123]. In order to analyse the influence of Al location in the unit cell, we constructed two different configurations, distributing the Al atoms as follows: a) as far as possible in a  $2 \times 2 \times 2$  supercell, and b) as far as possible in a single unit cell, which was subsequently expanded to a  $2 \times 2 \times 2$  supercell.

Zeolites are known to contract upon dehydration, which in part is due to the loss of space filling molecules, but more importantly to the increased electrostatic attraction of the extra-framework cations (EFCs) [124]. In zeolite RHO experimental results have shown that the cell contraction caused by dehydration is accompanied by a phase transition from centric to acentric form [102, 107, 125]. Then, with the aim of determining whether the cell contraction *per se* causes the phase transition of the RHO zeolite framework, we modeled the effect of the externally applied pressure on the pure silica structure. Previous work has shown that the chosen potentials perform

very well on aluminosilicate zeolites subject to high pressures [126]. This is also a test for the applicability of the potentials to model the lower acentric symmetry of zeolite RHO.

Lozinska et al. [125] have found that, once dehydrated, the monovalent forms of zeolite RHO do not change from the acentric to the centric space group when increasing the temperature. In order to get a better atomistic insight into this interesting result, we have conducted three computational experiments. The first two concern the study of the influence of water and EFCs in the structural features of zeolites [124, 127]. In the first study, water was initially considered as a continuum dielectric medium that screens cation-zeolite Coulombic interactions, with the aim of understanding the structural features of complex zeolites upon progressive dehydration. In the second study, water molecules were treated explicitly using the shell-model potential of Higgins et al. [43]. Moreover, we calculated the energy barriers that the cations should surpass when travelling across the zeolite windows to go from one cationic site to another.

In order to quantify the degree of distortions we used the following parameters:

$$\delta_4^t = \frac{1}{2} |r_{ik}^t - r_{jl}^t| \quad (4.2)$$

$$\delta_6^t = \frac{1}{2} |\max(r_{il}^t, r_{jm}^t, r_{kn}^t) - \min(r_{il}^t, r_{jm}^t, r_{kn}^t)| \quad (4.3)$$

$$\delta_8^t = \frac{1}{2} \max(|r_{im}^t - r_{ko}^t|, |r_{jn}^t - r_{pl}^t|) \quad (4.4)$$

where  $r_{ij}^t = \|\vec{r}_i(t) - \vec{r}_j(t)\|$  and  $i, j, k, \dots, o, p$  are oxygen atoms labelled clockwise. These parameters are defined for each window (4, 6, and 8-rings) and time  $t$  (e.g. for 8-ring see Figure 4.2). Thus, we calculate average values for all windows and time:

$$\Gamma = \langle \delta_4 \rangle, \quad \Lambda = \langle \delta_6 \rangle, \quad \Delta \equiv \langle \delta_8 \rangle. \quad (4.5)$$

Equation 4.4 is a generalization of the degree of ellipticity of D8R, originally described as in Equation 4.1. This is motivated by a previous experimental work on zeolite LTA [128], where a complex behaviour for the window distortion was observed. Equation 4.4 was defined in a previous work [107], however Equation 4.2 and Equation 4.3 are first introduced in the present work. A state-of-the-art algorithm was used for the automatic non-trivial identification of all window-types [129], which is based on loops searching in empirical networks treating each zeolite window as a loop in a dynamic graph. In addition to the three distortion parameters ( $\Gamma$ ,  $\Lambda$ , and  $\Delta$ ), the average cell parameter allows us to monitor the geometry of the unit cell during the simulations. For computing the average values extracted from the simulations and reported below, ergodicity has been assumed, and therefore the average values are calculated as the corresponding ensemble average [51, 130]. In this way, the more stable configurations have a larger stability and contribute therefore more to the computed observables.

The MC simulations have been carried out using the code RASPA [55], while the EM and MD ones have been carried out using the GULP code [61]. Constant pressure MD simulations with isotropic volume fluctuations and fully flexible unit cells have been used to study the evolution of the system, and to produce the correct statistical

ensemble, (Nosé-Hoover thermostat with Rahman-Parrinello barostat [90]) since it allows for phase changes in the simulation. In the MD simulations, the pressure has been set to zero. The integration time step is 0.1 fs. Each MD step consisted on a 2.5 ps equilibration simulation, followed by a 2.5 ps production run. Electrostatic interactions are calculated using the Ewald summation [46, 48]. A cut-off radius of 12 Å is used for short-range interactions.

### 4.3. Results

In order to model a system that is comparable to those studied experimentally, we considered the inclusion of Al atoms. To do that, two crystalline configurations are set up, replacing 80 Si atoms by 80 Al atoms (per computational box, consisting of a  $2 \times 2 \times 2$  supercell). The Al atoms are placed in such a way that first, they obey Löwenstein's rule [7], and second, the Coulombic repulsions between Al-centered tetrahedron are minimised. The first configuration is labelled as C1, and has the Al atoms placed as far as possible in a  $2 \times 2 \times 2$  supercell. The average distance between Al atoms is  $\langle \text{Al}_i \text{Al}_j \rangle_{\text{C1}} = 14.49$  Å, and the average distance between the closest pairs of Al atoms is  $\langle \mathcal{C}(\text{Al}_i \text{Al}_j) \rangle_{\text{C1}} = 5.73$  Å. The second configuration (C2) is constructed by placing the Al atoms as far as possible in a single unit cell, which is subsequently expanded to build a  $2 \times 2 \times 2$  supercell. The average distance between Al atoms and between closest Al pairs are  $\langle \text{Al}_i \text{Al}_j \rangle_{\text{C2}} = 14.50$  Å, and  $\langle \mathcal{C}(\text{Al}_i \text{Al}_j) \rangle_{\text{C2}} = 5.64$  Å, respectively. C2 has a higher symmetry than C1, so the average distance between closest pairs of Al atoms is circa 0.1 Å higher. This is just a small increase, which suggests that it is not necessary to employ the larger unit cell to model the system correctly, since the small improvements that would be achieved by increasing Al-Al repulsions would be insufficient to compensate for the increase in simulation time. We will therefore use the configuration C1 for the rest of this work. The atomic coordinates of the framework atoms (Si, Al and O atoms) of both structures are provided in ESI.

The strong attractive interaction between the extra-framework cations and the oxygen atoms of the zeolite exerts a large force on the framework that is likely to be the cause of the phase transition from the centric  $\text{Im}\bar{3}\text{m}$  to the acentric  $\text{I43m}$  structure with the concomitant reduction of the cell volume and the increase of the pore window acentricity ( $\Delta$  parameter). In order to shed more light into this feature, we analysed the behaviour of the pure silica zeolite RHO in presence of an externally applied pressure. Figure 4.3-left shows that, indeed, framework volume decreases gradually until a step is found at 1 GPa. At this point the acentricity parameter is 0.25 Å, and the crystal structure adopts the acentric form. This explains the origin of the phase transition of zeolite RHO. In the remaining of the paper we will explore it to greater depths, as well as the structural features related to the cell deformation and its impact on the molecular nanovalve effects.

In a previous work it was shown that a qualitative picture of the role of the extra-framework cations in the zeolite structural deformation can be obtained by mimicking the screening effect of water by decreasing the charge of the extra-framework cations

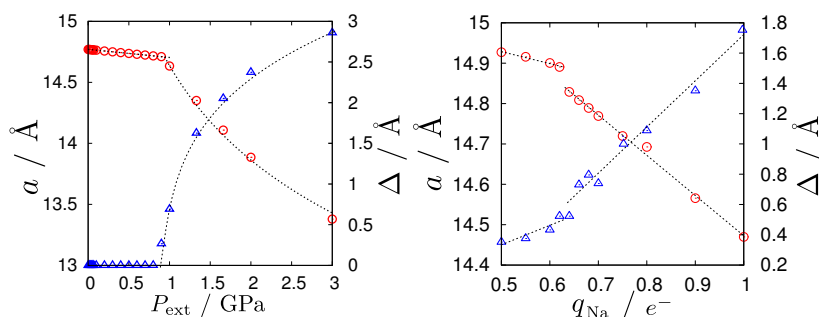


**Figure 4.3:** Left: cell parameter,  $a$  ( $\circ$ ), and 8MR window distortion  $\Delta$  ( $\triangle$ ), vs. applied external pressure. Right: cell parameter and 8MR window distortion vs. partial charge for sodium cations,  $q_{\text{Na}}$ . We observe a structural phase transition at 1 GPa and  $q_{\text{Na}} = 0.62 e^-$ , respectively. The errors are smaller than the size of the points. All regressions have  $r^2 > 0.99$ .

[124]. The curve displaying the variations of the cell parameter as a function of the charge of the cation is shown in Figure 4.3-right for Na-RHO. We observe again a gradual variation, followed by a step, where the acentricity parameter undergoes a large change. The symmetry also changes from the centric to the acentric space group. The decrease of the charge of the cations could be regarded as an increase in water content, and is accompanied by a reduction of cation-oxygen interactions, and consequently by larger interatomic distances [124]. This can cause the migration of cations, which indeed moved from Site I to Site II.

For a realistic modelling of highly-flexible porous nanoporous solids, we have used a methodology with which to achieve a step by step approach towards the most likely structure of these complex materials. Zeolite RHO, according to experimental evidences, is among those nanoporous materials where there are many available sites for cation siting and a close coupling exists between cation siting, cell parameters and crystal symmetry. In this case, it is not possible to find an initial structural model that leads to a realistic description of the zeolite through a single-step molecular simulation method (energy minimisation, Monte Carlo or Molecular Dynamics). This is a consequence of the very complex surface energy, and thus any random trial is likely to change the structure around the closest local minimum. To surmount this, we aimed to design a method that would be able to approach the structure in an adaptive way. This methodology combines MC, EM and MD in iterative cycles. A schematic view of the method is shown in Figure 4.4. This scheme shows the main feature of the method, which is the cyclic nature of the MC/EM/MD steps. The starting point is a stable framework structure, for instance the experimental structure (either solvated or desolvated), or a hypothetical structure. Ten trial MC runs are then performed, in order to locate the extra-framework species. In the present case these extra-framework species are extra-framework cations and/or water molecules. This is followed by a lattice EM for each MC configuration, keeping the cell parameters fixed as well as

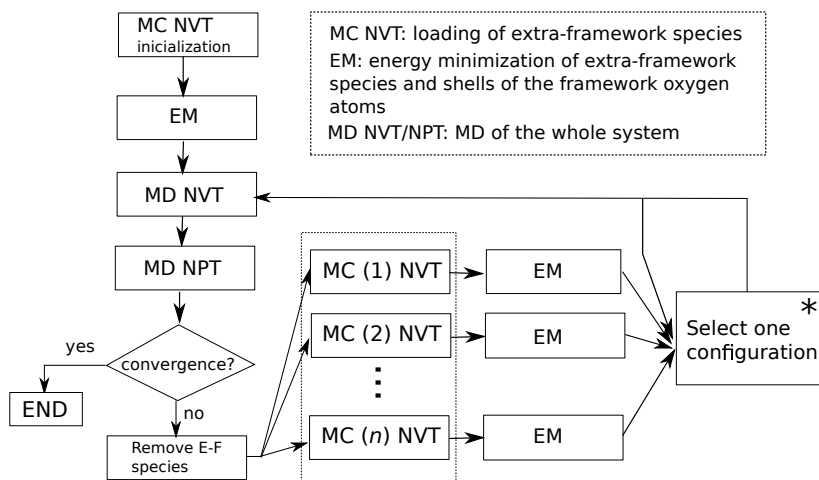


**Figure 4.4:** EM/MC/MD simulation scheme used in this work. (\*) We select the most stable configuration, according to their Boltzmann weights, among the previously accepted configuration and a new set of ten trial calculated systems.

the coordinates of the framework atoms. If the EM were performed allowing the cell parameters to vary, at constant pressure, the framework structure would change abruptly and it would be trapped in a local minimum with a large distortion, from which it would be very difficult to escape. At this stage the most important issue is to achieve the relaxation of the extra-framework species, to prevent unrealistic high forces at the beginning of the MD run, which would cause the collapse of the simulation. The energies of these ten configurations along with that accepted in the previous cycle are used to select one according to Boltzmann's weight as compared with a random probability. In this way, detailed balance is fulfilled [26, 51, 131].

Our aim is to provide a realistic description of the material, for which thermal and entropic contributions are relevant. Since in EM calculations, these are lacking, we decided to model the overall structural changes of the solid by means of MD simulations. Then, after performing the EMs, to further ensure that the MD can be performed in a reasonable way, a short run is first accomplished at fixed cell parameters, in the NVT ensemble, followed by a long run in the NPT ensemble, with a fully flexible cell. In the later run the cell parameters vary according to the effect of the extra-framework species and external conditions like temperature and hydrostatic external pressure. Since the coupling between the framework structure and the extra-framework species is quite strong, the MD simulation relaxes the structure primarily in accordance to the location of the extra-framework species. Moreover, in this MD stage some extra-framework species can surpass the local energy barriers and move to adjacent stable cation/adsorbate sites. This movement to other cation/adsorbate sites causes in turn changes in the framework and the overall structure of the material. After each MD

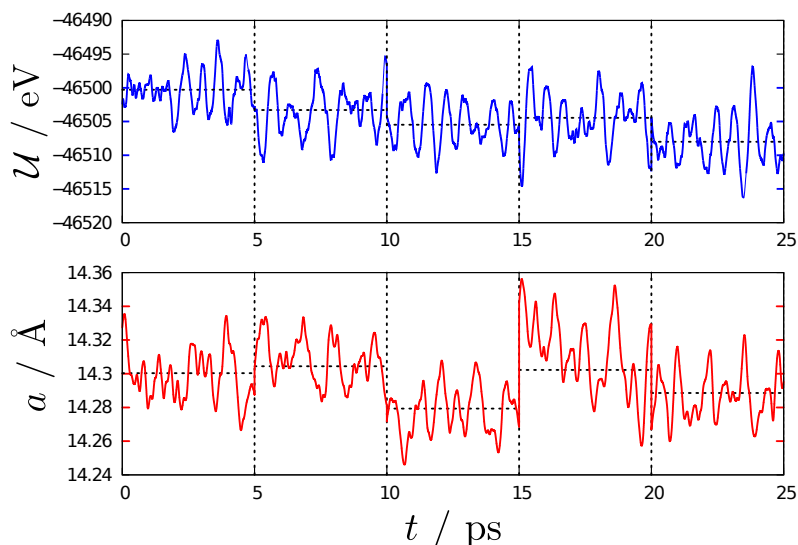


**Figure 4.5:** Variation of the potential energy (top) and cell size (bottom) with the number of MD simulation steps, for the first 5 MC/EM/MD cycles, for Sr-RHO. Horizontal dashed lines represent the average potential energy and cell size, respectively. Vertical dashed lines represent boundaries between cycles. The temperature is 300 K.

run, the obtained framework structure is taken for the new cycle, while the extra-framework atoms are removed and inserted back with the MC scheme step. This cyclic process is repeated iteratively, until the potential energy of the system is equilibrated.

Figure 4.5 shows the evolution of potential energy and cell size, as when the described method is employed to model zeolite RHO with  $\text{Sr}^{2+}$  cations. For clarity reasons, only the first five MD/EM/MC cycles are shown, and the complete curve is presented in the ESI (see Figure S4). At the beginning of each MC/EM/MD-cycle there is a sudden increase in the cell parameters, resulting from the repulsion induced by the extra-framework cations located in new sites with respect to their previous positions. The response of the whole system is to slightly increase cation-zeolite distances, while at the same time the structure is relaxed. During the transit along the MC/EM/MD cycles, the internal energy, i.e. the average of total potential energy, decreases and converges. We observe that the potential energy tends to decrease as the methodology proceeds. However the behaviour of the cell size is complex, which as a consequence of the structural variation of the system trying to gain stability upon relocation of the extra-framework cations in each MC step. In fact this is the core point of our methodology.

We have employed the MC/EM/MD algorithm to study the dependence with temperature of the cell size, for all cations. The results obtained in our simulations, as well as the available experimental data, are reported in Table 4.1. We have simulated zeolites containing 80 and 92 aluminium atoms per simulation cell, with Si/Al ra-

**Table 4.1:** Dependence with temperature of the average cell parameter,  $a$ , for silica and aluminosilicate forms of RHO-type zeolites.

Me-RHO <sub>n<sub>Al</sub></sub>	Na <sub>80</sub>		K <sub>80</sub>		Ca <sub>80</sub>		SiO <sub>2</sub>
$T_{\text{ext.}} / K$	$\langle a \rangle / \text{\AA}$ $\pm 0.001 \text{\AA}$	Exp.[Ref.]	$\langle a \rangle / \text{\AA}$ $\pm 0.001 \text{\AA}$	Exp.[Ref.]	$\langle a \rangle / \text{\AA}$ $\pm 0.001 \text{\AA}$	Exp.[Ref.]	$\langle a \rangle / \text{\AA}$
100	14.619		14.964		14.379		14.757
200	14.554		14.722		14.195		14.635
300	14.431	14.4139[106] 14.3771[125]	14.602	14.5951[106] 14.5959[125]	14.141		14.487
350	14.475		14.650		14.004		14.395
500	14.467		14.613		collapsed		14.438
600	14.423		14.805		collapsed		
		Li <sub>80</sub>		Sr <sub>80</sub>		Na <sub>92</sub>	
100	14.491		14.429		14.340		
200	14.330		14.388		14.103		
300	14.208	14.2448[106]	14.402		14.141		
350	14.102		14.352		14.004		
500	collapsed		14.173		collapsed		
600	collapsed		14.187		collapsed		
		K <sub>92</sub>		Ca <sub>92</sub>		Sr <sub>92</sub>	
100	14.747		14.340		14.382		
200	14.669		14.203	14.489	14.412		
300	14.607		14.058	14.45[100]	14.327	14.45[100]	
500	14.498		collapsed	14.01[100]	14.259	14.56[100]	
600	14.498		collapsed	14.07[100]	14.211	14.05[100] 13.98[100]	

tios of 3.8 and 3.17, respectively, in order to compare with experiments. We observe negative thermal expansion (NTE) in all cases, but unlike what Reisner et al. [102] reported, our results suggest that the negative thermal expansion is not associated to a gradual dehydration but to the intrinsic response of the dehydrated aluminosilicate to an increase of temperature. It is worth noting also that the pure silica hypothetical zeolite RHO shows NTE. In relation to this point, the collapse of the structures with high polarising powers occurs due to the limitation of the potentials, but the main picture is well described, as the same behaviour is observed experimentally but at higher temperatures. Finally, it is worth noting that the difference of the computed cell parameters with experiments is below 0.2 %. This is the first theoretical work that achieves such a close agreement with experimental data, in a highly flexible zeolite containing Al atoms and extra-framework cations.

In connection with the above results, here we address the EFCs location and the population of the different cationic sites, as obtained from our simulation. Experimentally three crystallographic sites are known for EFCs in zeolite RHO: (site I) inside a double 8-ring, (site II) at the center of a single 8-ring, and (site III) in front of the 6-ring (see Figure 4.6). In agreement with the experimental data [100, 101, 105, 106, 125], our MC/EM/MD methodology shows that most cations are distributed among the known cationic sites, while a small fraction was assigned elsewhere. This means that the latter were located outside of a 2 Å radius sphere from the reference sites,

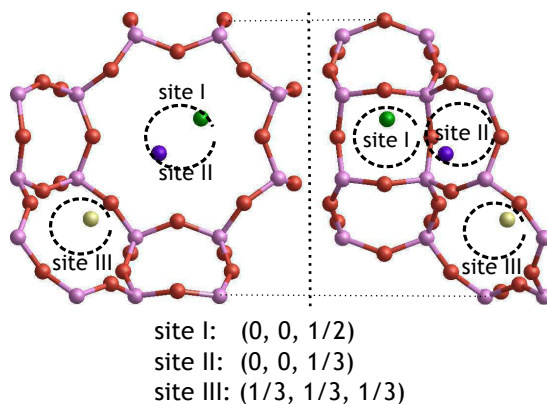


**Figure 4.6:** Atomistic view of the cationic sites in zeolite RHO sites I-III depicted as dashed spheres and its coordinates. The colored spheres represent cations in cationic sites.

which is mainly because EFCs are found moving from one stable site to another. The population of the sites is in good agreement with experimental results, when available, considering the uncertainties associated with the experimental data that can be extracted from diffraction (see Table 4.2). Note for example that the overall cation content determined in experiments varies from 80 to 95 % of the nominal EFCs content. The largest difference was found for  $\text{Li}^+$  with 10 cations per unit cell (80 cations per simulation cell), where experiments allocated 8 of these atoms to site III, whereas we found 5.3 atoms at this site, 2.7 at site II, 1.0 at site I and 1.0 elsewhere. The sum of the populations of sites II and III matches very well the experimental value obtained for the latter site. This is located near site II and, considering the large uncertainty that can be associated with the location of  $\text{Li}^+$  cations by X-Ray diffraction, we can conclude that the simulations provide a reasonable agreement with experiments. When the number of cations increases, concomitant with the increase of Al-atoms per unit cell from 10 to 11.5, we obtain that the occupation of site III increases for  $\text{Na}^+$  and  $\text{K}^+$ , while for the case of  $\text{Ca}^{2+}$  and  $\text{Sr}^{2+}$  this site depopulates in favor of site I. The success in reproducing both the cell parameter behaviour and the EFCs location provides confidence in the ability of our calculations to correctly describe the complex behaviour of zeolite RHO and analyse in detail the dynamical features of the pore window, and its connection to nanovalve effects.

Since the methodology does not impose any symmetry constraints other than the supercell, it is able to provide structural and dynamical data that are close to the behaviour of the materials. This can be exploited for increasing our understanding of this complex behaviour, in particular in materials with a large degree of flexibility, such as zeolite RHO. Previous simulation work [132, 133] has shown that, even for rather rigid zeolites, the size of the windows that delimit the pore opening has large

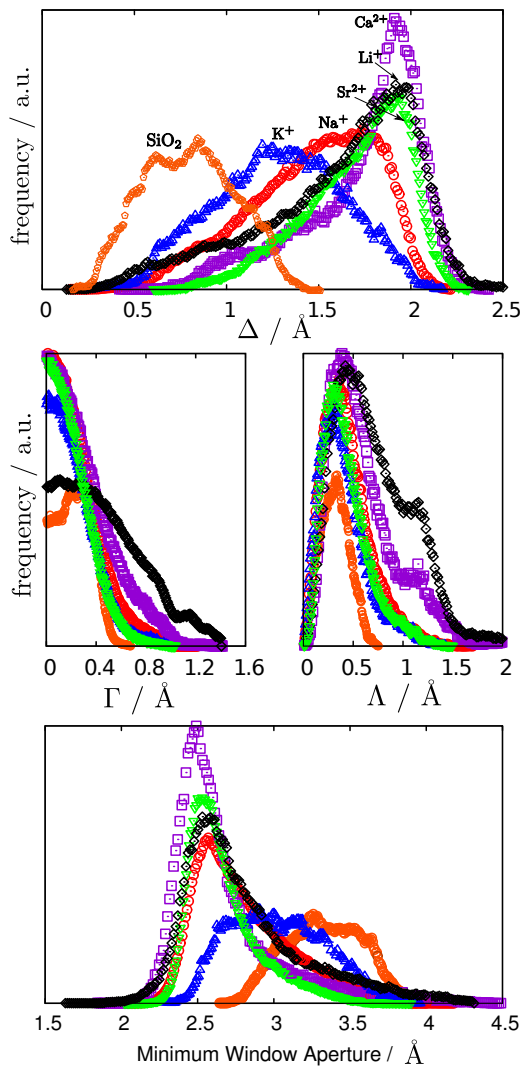
**Table 4.2:** Cation site populations in atoms / unit cell within a 2 Å radius from the cation sites at temperatures 300 K.<sup>a</sup>

cation	site I	site II	site III	elsewhere
Na <sub>80</sub>	1.64	6.55	1.61	0.08
Exp. [125]		6.48	3.00	
Na <sub>92</sub>	1.36	7.09	2.94	0.07
K <sub>80</sub>	2.06	5.54	2.36	0.09
Exp. [125]	2.06	6.85		
K <sub>92</sub>	2.08	5.91	3.39	0.10
Li <sub>80</sub>	1.04	2.68	5.28	1.03
Exp. [125]			8.00	
Li <sub>92</sub>	1.30	3.49	5.38	1.37
Ca <sub>80</sub>	2.00	1.99	0.75	0.26
Ca <sub>92</sub>	3.36	2.06	0.21	0.13
Sr <sub>80</sub>	1.91	2.24	0.74	0.11
Sr <sub>92</sub>	3.01	2.45	0.27	0.02

<sup>a</sup> Cation sites from: [101, 103, 105]

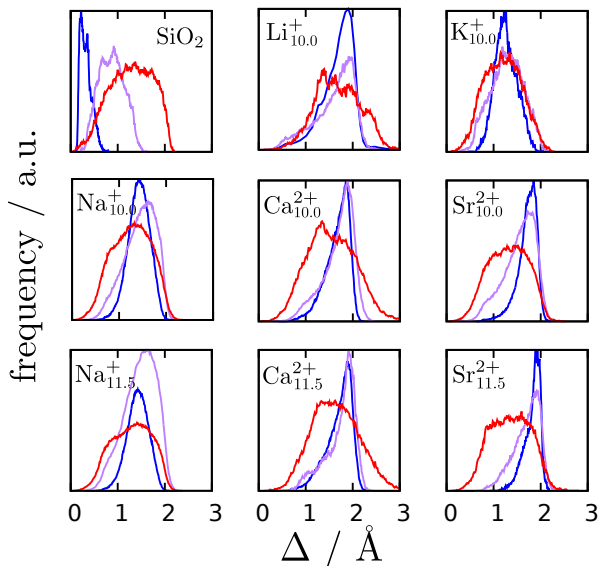
deviations (circa 0.4 Å), due to the thermal motion. Diffraction studies cannot capture this feature accurately due to the symmetry-averaged picture it provides, even by analyzing the information extracted from the Debye-Waller factors. In the present context, it is useful to note that despite the role that the flexibility of the windows plays in the transport properties of zeolites without EFCs [132, 133], how the windows flexibility is modified in the presence of EFCs remains unexplored. As we have shown above, we have confidence in the accuracy of the developed computational scheme to provide accurate structural data and therefore we can enter into the detailed analysis of the window deformations for the different metal-forms of zeolite RHO.

Figure 7.5 shows the window distortion profiles for pure silica and aluminosilicate forms (Li<sup>+</sup>, Na<sup>+</sup>, K<sup>+</sup>, Ca<sup>2+</sup> and Sr<sup>2+</sup>), by displaying the deformation parameters defined for the 4,6,8-rings ( $\Gamma$ ,  $\Lambda$ , and  $\Delta$ ). It is worth noting that the pure silica structure shows non-zero window distortion, which is due to the thermal motion and is a fact that cannot be directly inferred by diffraction methods. We have performed *Ab initio* Molecular Dynamic simulations that support these findings; details of which are provided in ESI. The distortions observed for this case can be regarded as those intrinsic to the topology and thus the deviations from them observed for the metal forms can be interpreted as being induced by the cations. 4-membered rings (4MRs) are kept mainly undistorted ( $\Gamma$  maximum population corresponds to  $\Gamma = 0$  Å, except for pure silica structures), due to their small size, although they exhibit relatively long tails, particularly Li<sup>+</sup> and Ca<sup>2+</sup>. Obviously, 4MRs do not directly contribute to molecular transport, but their deformation can couple to the deformation of larger windows, and could enhance the pore opening of these ones. The distortions of the 6MRs are not centered at zero, but circa at 0.5 Å for all forms, and they show a small dependence on the nature of the cations. This is also due to the small size of this type of window, although they have noticeably larger tails as well as a shoulder at around 1 Å for Li<sup>+</sup>



**Figure 4.7:** (Top and middle) Probability density of degree of distortion of the 4,6,8-rings ( $\Gamma$ ,  $\Lambda$ , and  $\Delta$ ) for pure silica and aluminosilicate forms ( $\text{Li}^+$ ,  $\text{Na}^+$ ,  $\text{K}^+$ ,  $\text{Ca}^{2+}$ , and  $\text{Sr}^{2+}$ ). (Bottom) Probability density of minimum window aperture of the 8-rings aluminosilicate forms ( $\text{Li}^+$ ,  $\text{Na}^+$ ,  $\text{K}^+$ ,  $\text{Ca}^{2+}$ , and  $\text{Sr}^{2+}$ ). The temperature is 300 K in both figures.

and  $\text{Ca}^{2+}$ . In the case of 8MRs a clear dependence of the  $\Delta$  parameter with the metal polarizing power is observed. Note that for this distortion there is a much larger de-



**Figure 4.8:** Probability density of degree of distortion of 8-rings for pure silica and aluminosilicate forms ( $\text{Li}^+$ ,  $\text{Na}^+$ ,  $\text{K}^+$ ,  $\text{Ca}^{2+}$ , and  $\text{Sr}^{2+}$ ) at different temperatures 100, 300 and 500 K (blue, purple and red, respectively) and Si/Al ratios (3.8 and 3.17).

parture from the behaviour of the pure silica zeolite. Going back to the smaller rings, *i.e.* 4 and 6MRs, it can be observed that indeed the effect of the polarising power in these cases.

These findings are consistent with the idea that distortions are coupled and cations produce distortions in all rings. On this basis it is possible to understand one interesting result of Lozinska et al. [106] who found, in their study of monovalent cation exchanged zeolite RHO, that despite not being located next to 8MR, the  $\text{Li}^+$  cation is the one that induces the largest values of the mean  $\Delta$  parameter. On the other hand, a direct relation between cation site occupancy and framework distortion has been found in divalent cation-exchanged zeolite RHO by Corbin et al. [100].

The behaviour of the distortions in 8MRs with temperature is dependent on the nature of the metal cation present in the zeolite, in a very distinct manner. For each structure with divalent cations the distortions are about the same at 100 K and 300 K, while at 500 K the position of the maximum of the curves are reduced circa 0.5 Å and the peak widths are doubled (Figure 4.8). The increase of the number of cations for these two metals has almost a negligible effect on the observed behaviour, which suggests that even at the lower number of cations, their interactions with the zeolite oxygen atoms are very strong. For the monovalent cations the influence of both the polarising power and the number of cations is clear.  $\text{Li}^+$  has the smallest cationic

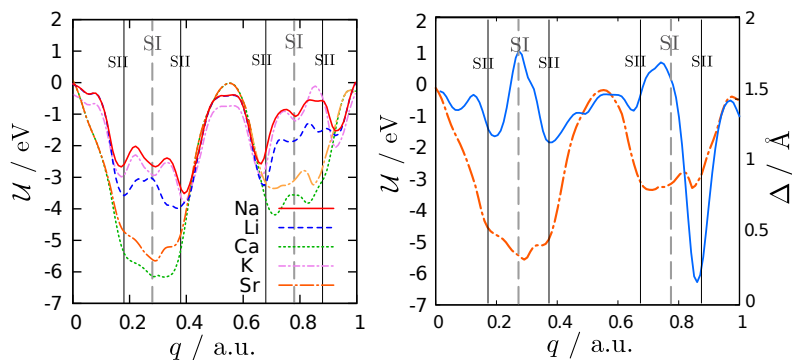


**Figure 4.9:** (Left) Potential energy landscape  $U$  vs. reaction coordinate (in the  $a$ -direction through the double 8-rings),  $q$ , for one or two aluminium atoms per unit cell. The position of the first aluminium atom is  $q = 0.37$  and the second (for the divalent cases) is  $q = 0.17$ . (Right) Potential energy landscape  $U$  and distortion parameter  $\Delta$  vs.  $q$  reaction coordinate for Sr-RHO form.

radius and thus the largest polarising power, and shows only a minor shift of the position of the maximum of the degree of distortion. The behaviour of the  $\text{Na}^+$  form shows variations with the number of cations and also with temperature. From 100 K to 300 K the distortions are larger, while they decrease at 500 K. In the case of  $\text{K}^+$ , which has the largest radius and lowest polarising power, very little variation of the maximum of the degree of distortion are observed, even at 500 K. As was more clearly shown in Figure 7.5-top, the positions of the peaks of the distortion distributions of the three metals with largest polarising power ( $\text{Ca}^{2+}$ ,  $\text{Li}^+$  and  $\text{Sr}^{2+}$ ) do not differ in a noticeable fashion, which together with the information gained from the analysis of the temperature dependence suggests that the largest window distortion that can occur in zeolite RHO under experimental conditions is about  $2 \text{ \AA}$ . The windows of pure silica zeolites exhibit increasing distortions with an increase in temperature. The overall analysis of Figure 4.8 reveals that at 500 K the thermal effect makes the behaviour of the window distortion independent of the nature of the cation and more dictated by the framework itself.

In agreement with Lozinska et al. [106], for the dehydrated metal containing zeolites we do not find a phase transition from the acentric  $I43m$  to the centric  $\text{Im}\bar{3}m$  form when increasing temperature. However, one would expect that such a phase transition might occur. In order to shed more light on the role of EFCs affecting the structural behaviour of RHO zeolites, we analysed the energy barrier for crossing an 8MR, by mapping the energy profile of the cations moving along a path traversing the zeolite following a line that crosses the 8MR (see Figure 4.9) and allowing the structure to relax *via* EM. The data in the middle of the zeolite has no physical meaning, as cations will not get into these sites in absence of adsorbed molecules, they will rather move along the pore surface. The attention should be focused on the regions close to

the zeolite windows, identified in the figure by vertical continuous lines. The centers of the D8R are represented by vertical dashed lines. We observe that the energy barriers are asymmetric, *i.e.* they are different for forward jumps and backward jumps, respect for D8R. Moreover, the relative well depth depends on the location of the Al in each case. The position of the first cation, for monovalent forms, is  $q = 0.37$ . For divalent forms a second cation is added at  $q = 0.17$ .

An important conclusion we can draw from the analysis of the values of the energy barriers is that, in the dehydrated state, the cations need to overcome very high energy barriers in order to jump from one site to another, suggesting that phase transitions induced by cation jumps will take very long times. This is a plausible explanation of the experimental observations of Bieniok and Baur [134] who observed that the high temperature structure Sr-RHO quenched to 90 K, and left in vacuum at room temperature, takes a week to recover the usual room temperature structure. It is interesting to note that the overall structure responds to the cation reaction coordinate, *i.e.* when the cation is in site I of the 8-ring closest to the cation ( $q = 0.27$ ) the degree of distortion is  $\delta_8 = 1.75$  (Equation 4.4). However, when the cation is in site II  $\delta_8 = 1.3$ . We have not measured the degree of ellipticity induced by cations in site III. For the second D8R,  $\delta_8$  is noticeably low, at less than 0.5 for a reaction coordinate of  $q = 0.85$ . This indicates that the local geometry is not so much affected by the presence of the cation as it is by the simultaneous presence of the extra-framework cation and the aluminum atom of the framework. Our result could also provide a rationalization for the experimental finding that, upon CO<sub>2</sub> adsorption in Cs-RHO, NaCs-RHO and K-RHO, two crystal phases appear over a considerable range of gas pressures, which is likely to be a consequence of the trapping of cations in long-lived sites [125].

In presence of molecules that have electrostatic interactions with the zeolite, like H<sub>2</sub>O and CO<sub>2</sub>, it has been experimentally found that zeolite RHO can undergo reversible phase transitions [103, 105]. In order to analyse how this process occurs, we have studied the behaviour of Na-RHO for 8 different water contents, from fully hydrated (36 molecules per unit cell) to completely dehydrated. We started from the fully hydrated structure and the appropriate number of water molecules was eliminated for each case. Then, the systems were equilibrated by MD simulations. The lattice parameter of the initially completely hydrated material remains almost unchanged by removing up to one quarter of the water molecules, reaching 24 molecules per unit cell (Figure 4.10-bottom). Further gradual dehydration is accompanied by a concomitant decrease of the cell parameter, until all water molecules are removed. Our simulations show that the variations of the cell parameters are related to variations of the population of the cationic sites (Figure 4.10). A remarkable result is that, at any water loading, the larger amount of cations are found in site II, whose occupation is at least two times larger than those of the other two sites. Three regions are clearly identified according to the behaviour of cation site population. One corresponds to high water loading, above 24 molecules per unit cell. Another region appears at low water loadings, between zero and 8 molecules per unit cell. Finally, an intermediate region is identified in between the other two. Sites I and III reach minimum occupations in the high water content region. In this case, site II is largely populated. In the inter-

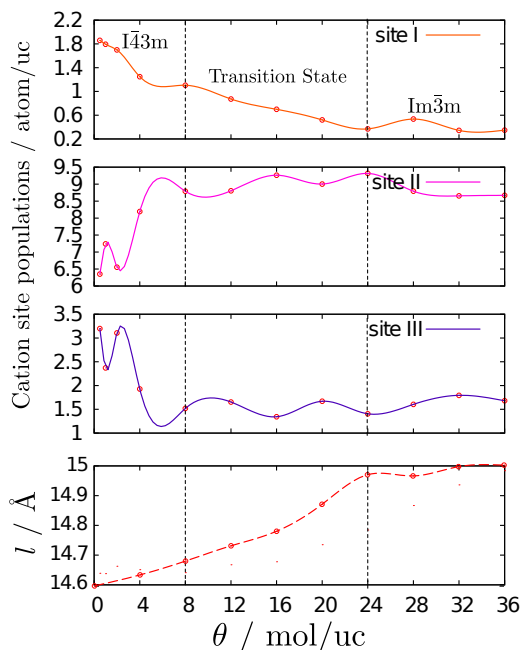


**Figure 4.10:** Top three panels: sodium site populations (at 300 K) vs. loading of water,  $\theta$ , for Na-RHO with 92 Na cations. Sodium site populations are measured in atoms per unit cell, within a 2 Å radius from the cation sites. Bottom panel: cell size vs. water loading of Na-RHO with 92 Na cations, at 300 K.

mediate region sites II and III largely maintain their occupancies, which are similar to those in the high water content region. In contrast, site I shows a gradual decrease in the intermediate region. In the absence of water, sites I and III have the largest occupation of Na cations, while the lowest occupation is observed for site II. Upon water adsorption, after the incorporation of 4 molecules per unit cell, the cationic site occupancies change rapidly and at 8 molecules, sites II and III already reach the levels that are kept about constant up to the full water loading. The observed changes of cell parameters and cationic site populations modify the symmetry of the zeolite, which has the centric  $Im\bar{3}m$  space group for 24 water molecules per cell up to full hydration, while adopting the acentric  $I\bar{4}3m$  space group for 8 water molecules and below.

The analysis of Figures 4.10 and 4.11 provides a more accurate view of the connection between changes in cell parameters and window distortions than that obtained earlier in this work in which water was modelled as a continuous dielectric (Figure 4.3-right). Figure 4.11 shows that the distortions of the smaller 4 and 6MRs are almost insensitive to the amount of water present, and are slightly lower than those of the fully dehydrated structure. In contrast, a very large dependence of the 8MR distortion parameter,  $\Delta$ , with the amount of water is observed for the interval delimited by 4

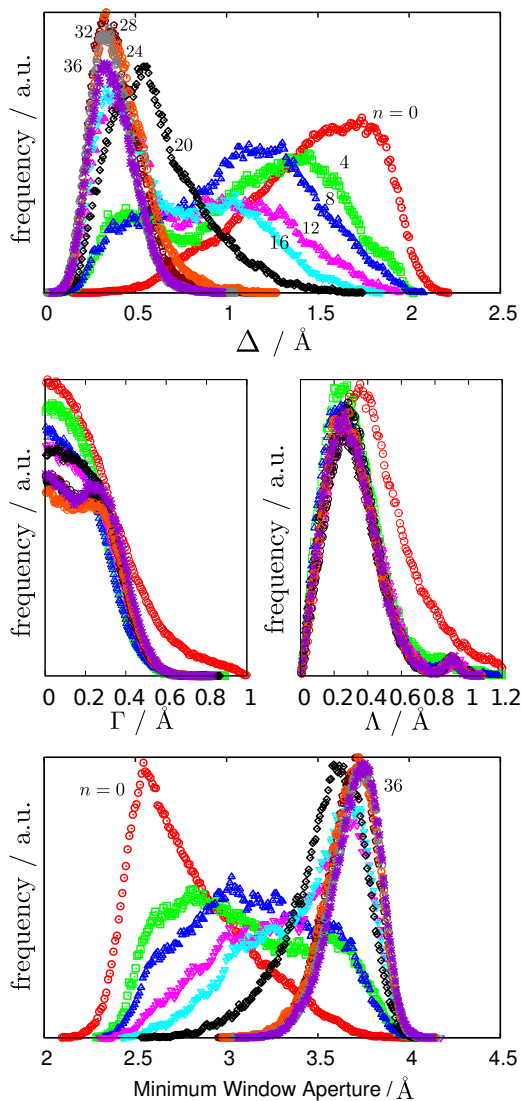


**Figure 4.11:** (Top and central) Probability density of the degree of distortion of the 4,6,8-rings ( $\Gamma$ ,  $\Lambda$ , and  $\Delta$ ) in presence of various amounts of water molecules and 92 Na cations, at 300 K. (Bottom) Probability density of minimum aperture of the 8-rings in the Na-RHO form in the same conditions.

and 48 water molecules per unit cell (Figure 4.11-top). From 24 water molecules per unit cell to full hydration (36 water molecules) the distortion of 8MR does not show

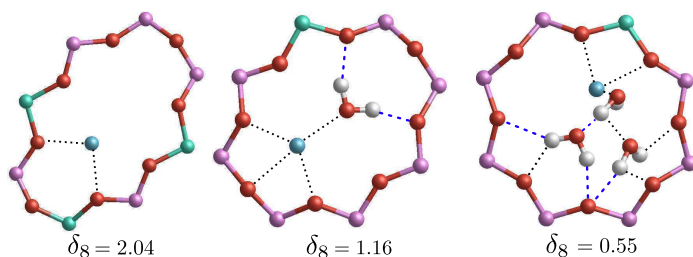


**Figure 4.12:** Snapshots of several 8MRs during simulations, when occupied by one  $\text{Na}^+$  cation (left), one  $\text{Na}^+$  cation and one water molecule (middle) and one  $\text{Na}^+$  cation and three water molecules (right). Note the gradual decrease of the instantaneous distortion parameter upon water presence. Blue dashed lines represent hydrogen bonds and black-dotted lines represent other strong interactions.

significant variations. This is in line with the behaviour of the cell parameter and the population of the cationic sites (Figure 4.10). Between 4 and 16 water molecules per unit cell the distribution of the  $\Delta$  distortion parameter is bimodal, suggesting that some pores are closed whereas others are open. The appearance of the double peak is due to the nucleation of water in specific sites, which is motivated by strong water-water interactions. This behaviour could not be predicted by the dielectric continuum model of water in Figure 4.3-right.

The structural changes occurring in an 8MR when a  $\text{Na}^+$  cation and varying amounts of water are presented is shown in Figure 4.12. We observe the large distortion of the 8MR when just one cation is present, which favors the stability of the acentric structure. The addition of water molecules induces a gradual opening of the window, leading eventually to the experimentally observed transitions to the centric form.

## 4.4. Conclusions

A detailed investigation has been conducted in order to reach a better understanding of the distortion mechanisms that take place in molecular valve zeolite RHO. To the best of our knowledge, this is the first study that has addressed the behaviour of zeolite molecular valves from a theoretical point of view. For this purpose, we have developed a new methodology based on cycles of Monte Carlo calculations, Energy Minimisation and Molecular Dynamics simulations to study both monovalent and divalent cation-containing zeolite RHO, and its evolution upon changes on the nature of extra-framework cations, temperature and adsorbed molecules. The explicit consideration of the polarisability of the oxygen atoms has been found to be necessary, and it has been taken into account by using the shell-model.

The analysis of the ring distortions shows that there is a close relationship between

the flexibility of the zeolite framework and the location of the extra-framework cations, as well as the water molecules, thus providing an atomistic insight that goes beyond the experimental information obtained by diffraction techniques, as no symmetry restrictions are considered. This finding is likely to have an influence on the further understanding of diffusion and separation processes, which are controlled by the molecular valve effect arising from the windows distortions. Previous theoretical works have stressed the relation between the effective diameter of the windows and the flexibility of the framework, in pure silica zeolites, but how the framework is affected by the presence of extra-framework cations had remained unexplored so far, being thus this work also pioneer in this respect. The analysis of the results obtained in our study enables us to draw the following conclusions concerning the structural features: *a*) the phase transition from the centric to the acentric form of zeolite RHO is due to the force exerted by the extra-framework cations, which has a similar effect to applying an external pressure, *b*) the newly developed method is accurate enough to provide the cell parameters within 0.07-0.2 % with respect to experimental values, *c*) the cation sites are not only well located by our computational approach but their populations are also in agreement with experiments, *d*) a clear dependence on the polarising power of the extra-framework cation has been found for the distortions of the 8MRs, as well as the minimum aperture of these rings that control the nanovalve effect, *e*) the distortions of 6MR and 8MR are connected, which explains the experimental observation that the largest distortion occurs for  $\text{Li}^+$ , *f*) the 8MR distortions follow a different behaviour with temperature, depending on the nature of the extra-framework cation, *g*) cations face large energy barriers in order to pass from one site to another when the zeolite is dehydrated, being particularly high in the case of divalent cations, *h*) the amount of water present in the zeolite controls the population of cationic sites, the size of the cell parameters and the symmetry of the zeolite, and *i*) the 8MR windows distortion and pore aperture can be systematically controlled by the loading of water, allowing a fine control of the nanovalve effect.

The calculated high energy barriers for cation hopping provide a rationalisation of the experimental finding that, upon  $\text{CO}_2$  adsorption in Cs-, NaCs- and K-RHO, two crystal phases appear over a considerable range of gas pressures, which according to our results is a consequence of the trapping of sets of cations in a range of configurations that lead to long-lived metastable structures. We have shown that polar molecules, in this case water, screen the large electrostatic interaction providing low energy paths for the structural change. The use of the methodology for other flexible materials is underway.



# Chapter 5

## Structure and stability of $\text{Ge}^{4+}/\text{Si}^{4+}$ bearing STW-type zeolites

### Note:

The publication incorporated in this section is unpublished. It is the product of a collaborative effort involving members of the Instituto de Ciencia de Materiales de Madrid from Consejo Superior de Investigaciones Científicas (ICMM-CSIC) and Pablo de Olavide University (UPO). The research carried out in this work is clearly separated in two parts, an experimental part, which has been developed and performed by Reus T. Tiago and Miguel A. Cambor, from the ICMM-CSIC and a second part, but with equal weight, which has been developed and performed by Salvador R.G. Balestra, Said Hamad, A. Rabdel Ruiz-Salvador and Sofía Calero from the UPO. This last part is the original contribution of the author of this dissertation. For ease of reading, a modified version of the entire paper have been included in this Chapter. In this context, it is worth to note that the experimental part of the collaborative work is not included in the body of this Thesis but has been added in the Appendix C. Due to the equal contribution of both parts to the whole research, an explicit mark has been added to the two first authors to declare that they have equally contribute to the paper. The complete details of the paper can be found as:

- R. T. Rigo, S. R. G. Balestra, S. Hamad, A. R. Ruiz-Salvador, S. Calero and M. A. Cambor. "The Si-Ge substitutional series in the chiral STW Zeolite Structure Type". submitted Chem. Mater., Manuscript ID: cm-2018-00786e. 2018

Only in order to provide support and a better understanding of the contribution of the author of this Thesis in the generation of structures with realist  $\text{Ge}^{4+}/\text{Si}^{4+}$  distributions and the analisis of the structural flexibility, two scientific works are listed below.

- R. Bueno-Pérez, S. R. G. Balestra, M. A. Cambor, J. G. Min, S. B. Hong, P. J. Merklng and S. Calero. “Influence of Flexibility on the Separation of Chiral Isomers in the STW-Type Zeolite”. *Chem.–Eur. J.*, **2018**. DOI: 10.1002/chem.201705627
- J. J. Gutiérrez-Sevillano, S. Calero, S. Hamad, R. Grau-Crespo, F. Rey, S. Valencia, M. Palomino, S. R. G. Balestra and A. R. Ruiz-Salvador. “Critical Role of Dynamic Flexibility in Ge-Containing Zeolites: Impact on Diffusion”. *Chem. Eur. J.* **22**, 10036–10043, **2016**. DOI: 10.1002/chem.201600983

Note that these points represent a secondary result in the original published researches. These works are included in the Theses of Bueno-Pérez [138] and Gutiérrez-Sevillano [139].

---

The  $\text{Ge}^{4+}/\text{Si}^{4+}$  cation distribution has been studied in the whole composition range from pure silica to pure germania in STW-type zeolites. The problem related to the colossal configuration space has been managed by the use of an Effective Hamiltonian, which has been parametrised based on calculations with interatomic potentials. The calculated free energy of formation has minimum values at the experimentally found maximum yield. The flexibility of the  $\text{GeO}_4$  tetrahedra explains the independence of the lattice parameters with the increase of Ge atoms at low Ge content. Density functional theory calculations provide a new assignment of the previously controversial  $^{19}\text{F}$  MAS NMR resonances for occluded fluoride, which is based not only in the number of Ge atoms in the double-4-ring units but also on the way they are associated (namely, no Ge, isolated Ge, Ge pairs or closed Ge clusters). While we found an overall good agreement between the experimental and theoretical trends in preferential occupation by Ge of different crystallographic sites, the theoretical models show more sharp and abrupt tendencies, likely due to limitations of the approach and to kinetic factors that allow metastable configurations to actually exist.

## 5.1. Introduction

Chiral zeolites are largely desired for their potential interest in chiral separations. A few years ago, the chiral zeolite SU-32 (IZA code STW) was synthesised by first time as a germanosilicate [140]. The 3D-channel system with interconnected ten and eight membered rings raised attention and the pure silica version was successfully performed [141, 142], on an effort to provide the zeolite more chemically and thermally stability. Every single crystal is homochiral but standard synthesis procedures using achiral organic SDA are expected to yield racemic conglomerates [140, 141, 143]. However, very recently it has been possible to prepare enantiomerically enriched scalemic conglomerates by using an enantiomerically pure chiral dication, and the materials proved to yield small but significant enantiomeric excess in both asymmetric catalysis and adsorption processes [144]. These syntheses produced germanosilicate and aluminogermanosilicates, but recent studies suggest homochiral STW silica phases may as well be possible [142]. These silica zeolites are expected to be not only much more stable but also more amenable to selective separations, since the larger flexibility of  $\text{GeO}_2$

**Table 5.1:** Details of the number of configurations used for each Ge content

Ge/Si substitutions	Total number of configurations	Number of inequivalent configurations
1	60	<b>5</b>
2	1770	<b>165</b>
3	34220	<b>2855</b>
4	487635	40890/ <b>1507<sup>a</sup></b>

<sup>a</sup> In bold type it is shown the number of considered configurations in the calculations.

frameworks appears to be detrimental to chiral recognition [136]. The experimental counter part of this work has been successfully in preparing STW-type zeolites for the whole compositional range ( $Ge_f = Ge/(Ge+Si) = 0$  to 1). They have found interesting results in terms of synthesis yield, the behaviour of the lattice parameters and the assignment of <sup>19</sup>F MAS NMR resonances for occluded fluoride. This Chapter is aimed to provide theoretical support and a better rationalisation of the experimental findings.

## 5.2. Methodology

The incorporation of heteroatoms in a zeolite framework might generate a large configurational space of possible atomic distribution. For simplicity, we will concern only on binary composition, for instance in the case of the present case Si-Ge distribution. Symmetry consideration, by using the SOD program,[145] allows us to map all non-equivalent configurations up to 4 Ge atoms by unit cell. Since the cell contains 60 tetrahedral sites and the symmetry of the pure silica STW zeolite framework is relatively low (space group # 178), with 4 Ge atoms by unit cell there are already more than 40 thousand configurations. Even by using interatomic potential based calculations, this is already a heavy computational effort. For larger increase of the minority element in the binary solid solution, the number of configurations increases exponentially and therefore it is not possible to compute their energy. To deal with this, we turn to the recently developed Effective Hamiltonian (EH) approach [146], which parametrise the atom-atom interaction in a simple numerical function. In this way, the energy of millions of configurations can be evaluated at a small computational cost. Nevertheless, the method implies an initial high cost, since all configurations having 2 Ge (for STW a total of 165) and 3 Ge (2855 configurations) are needed first to submit to full energy relaxation, including atomic coordinates and cell parameters. Since Ge atoms confers large structural flexibility to the framework, those configurations having 4 Ge atoms, with either 4 nearest Ge neighbours or 3 Ge neighbours plus a 4th Ge atom as second next nearest neighbour, were also considered for the parameterisation of the EH. The set of zeolites considered with 4 Ge atoms has 1507 configurations.

The EH is based on consideration that the entrance of a heteroatom can be treated as a defect. First the substitution energies for isolated Ge atoms in the five distinct T

sites are computed and after that, the interaction energies with the addition of new Ge atoms are computed. We therefore parameterise the effective Hamiltonian as follows:

1. Firstly, the perturbation energy to substitute a Ge atom,  $\Delta E(\vec{r}_i)$ , is calculated using the Mott-Littleton methodology [147], for each unique tetrahedral site  $\vec{r}_i$ .

$$\Delta E(\vec{r}_i) = E_i - E_0 \quad (5.1)$$

where  $E_0$  and  $E_i$  are the lattice energies computed with GULP using the interatomic potential of pure silica structures and structures with one Ge/Si substitutions.

2. We then consider a pair interaction energy denoted as  $\Delta E(\vec{r}_i, \vec{r}_j)$ , where  $\vec{r}_i$  and  $\vec{r}_j$  are two tetrahedral sites, and is computed as the difference in energy between the individual energies for placing Ge atoms at sites  $i$  and  $j$  (i.e.  $\Delta E(\vec{r}_i)$  and  $\Delta E(\vec{r}_j)$ ) from above) and the energy found when both sites are occupied in a periodic calculation. The perturbation energy is given by:

$$\Delta E(\vec{r}_i, \vec{r}_j) = E_{ij} - \Delta E(\vec{r}_i) - \Delta E(\vec{r}_j) - E_0 \quad (5.2)$$

where  $E_{ij}$  is the lattice energy of structures with two Ge/Si substitutions.

3. Idem for trios and quartets of atoms.

$$\begin{aligned} \Delta E(\vec{r}_i, \vec{r}_j, \vec{r}_k) &= E_{ijk} - \Delta E(\vec{r}_i, \vec{r}_j) - \Delta E(\vec{r}_i, \vec{r}_k) - \Delta E(\vec{r}_j, \vec{r}_k) - \\ &\quad - \Delta E(\vec{r}_i) - \Delta E(\vec{r}_j) - \Delta E(\vec{r}_k) - E_0 \end{aligned} \quad (5.3)$$

$$\begin{aligned} \Delta E(\vec{r}_i, \vec{r}_j, \vec{r}_k, \vec{r}_l) &= E_{ijkl} - \Delta E(\vec{r}_i, \vec{r}_j, \vec{r}_k) - \{ \dots \}^{ijk} - \Delta E(\vec{r}_j, \vec{r}_k, \vec{r}_l) - \\ &\quad - \Delta E(\vec{r}_i, \vec{r}_j) - \{ \dots \}^{ijkl} - \Delta E(\vec{r}_k, \vec{r}_l) - \\ &\quad - \Delta E(\vec{r}_i) - \Delta E(\vec{r}_j) - \Delta E(\vec{r}_k) - \Delta E(\vec{r}_l) - E_0 \end{aligned} \quad (5.4)$$

where  $\{ \dots \}^{ijk}$  and  $\{ \dots \}^{ijkl}$  represent all the summation terms, which are combinations of the  $ijk$  and  $ijkl$  indices, respectively.

Then, an effective approximate lattice energy of  $N$  Si/Ge substitutions is being calculated as:

$$\begin{aligned} \mathcal{H} &= E_0 + \sum_i \Delta E(\vec{r}_i) + \sum_{ij} \Delta E(\vec{r}_i, \vec{r}_j) + \sum_{ijk} \Delta E(\vec{r}_i, \vec{r}_j, \vec{r}_k) + \\ &\quad + \sum_{ijkl} \Delta E(\vec{r}_i, \vec{r}_j, \vec{r}_k, \vec{r}_l) + \mathcal{O}(\vec{r}^N) \end{aligned} \quad (5.5)$$

where  $i, j, k, l$ -indexes run on the total number of configurations. Is useful to adapt the Equation 5.5 with a *tensor* notation using the Einstein summation convention:

$$\mathcal{H}(N) = E_0 + \epsilon_i S^i + \rho_{ij} S^i S^j + \theta_{ijk} S^i S^j S^k + \phi_{ijkl} S^i S^j S^k S^l \quad (5.6)$$

where  $S^i$  are spin-type variables with 1 or 0 represent the presence or absence, respectively, of Ge atom in the crystallographic  $i$ -position,  $\epsilon := \{\Delta E(\vec{r}_i)\}$ ,  $\rho := \{\Delta E(\vec{r}_i, \vec{r}_j)\}$ ,  $\theta := \{\Delta E(\vec{r}_i, \vec{r}_j, \vec{r}_k)\}$  and  $\phi := \{\Delta E(\vec{r}_i, \vec{r}_j, \vec{r}_k, \vec{r}_l)\}$ . We can readapt the Equation 5.6 to sum on the inequivalent configurations using a dictionary,  $\delta$ , which connects each configuration with the calculated equivalent configuration.

$$\begin{aligned} \mathcal{H}(N) = E_0 + \epsilon_\alpha \delta_i^\alpha S^i + \frac{\rho_{\alpha\beta}}{N-1} \delta_{ij}^{\alpha\beta} S^i S^j + \frac{2\theta_{\alpha\beta\gamma}}{(N-2)(N-3)} \delta_{ijk}^{\alpha\beta\gamma} S^i S^j S^k + \\ + \frac{2\phi_{\alpha\beta\gamma\zeta}}{(N-3)(N-4)} \delta_{ijkl}^{\alpha\beta\gamma\zeta} S^i S^j S^k S^l \end{aligned} \quad (5.7)$$

For four Ge per unit cell, 40890 inequivalent configurations appear, which represented a heavy computational cost. We noted during the energy minimization with lower Ge content that the convergence of the calculations is rather slow, as compared to aluminosilicate zeolites due to the presence of multiple local minima on the total potential energy surface, which we identify as originated by the larger flexibility of the solids associated to the presence of Ge. Therefore, the lattice energy of ca. 3.68 % of the 4-Ge configurations were explicitly computed by standard atomistic methods and the remaining 96.31 % by using the EH. The selection of this 3.68 % was achieved by considering those relevant configurations having three neighbour Ge atoms and the fourth one as first or second neighbour of one of those three. A more spread distribution of Ge atoms causes a lower effect on the local structure and can therefore be accurately described by the EH. Once the EH was parameterized, it was used to compute the lattice energy of each configuration (see Equation 5.7). The atomistic calculations were performed with the GULP code [148], using Sastre and Gale interatomic potentials [149]. Short range Buckingham potential was evaluated within a cut-off of 16 Å, while the long-range Coulomb potential was calculated by the Ewald method [46]. Energy minimization was performed with the BFGS minimizer [150], switching to RFO method after a suitable progress of the structural relaxation to remove the existing imaginary vibrational modes, if any, and therefore providing true energy minima structures. This procedure has been proven to be particularly useful for modelling zeolitic materials [94, 151, 152].

To reduce the size-effect contribution in the error of averaged observables we have designed an ensemble of special quasirandom structures (SQS's)[153] that mimic the average in composition of the calculated structures and radial correlation functions of optimised structures for each molar fraction. The generation of these structures take into account the free energy of the unit cell for each Ge content and correlation functions. SQS's have been extensively used in substitutionally random  $A_xB_{1-x}$  solids in the past,[153–155] but never in nanoporous crystals, to our knowledge.

The use of the EH and SQS's allowed us to evaluate the free energy of formation of the zeolites in the complete range of Si/Ge content, by appropriate Boltzmann weighing and considering also the configurational entropic contribution. For each given number of Ge atoms per unit cell, we selected the 50 lowest energy configurations for the theoretical estimation of the structural features. They were subject to interatomic potentials full lattice energy minimisations using the same type of calcu-

lations described above. Since we are interested in understanding the behaviour of the cell parameters and volume as a function of the Ge molar fraction and the size constrains of our calculations leads to small variations of the hexagonal symmetry, we renormalised  $a$  and  $b$  parameters. For this, we take for each configuration the cell volume invariant given by the energy minimisation, as well as the cell parameters and force the cell angles to be  $\alpha = \beta = 90^\circ$  and  $\gamma = 120^\circ$ , while recalculating  $a$  and  $b$  cell parameters.

Density Functional Theory based calculations were conducted to compute the  $^{19}\text{F}$ -NMR chemical shift. We noted that calculations of the chemical shift in periodic models of this zeolite are very expensive. They were conducted using the linear response method,[156, 157] which requires the calculation of magnetic energy levels that are separated by very small gaps. This enforces the use of very tight minimization criteria for the structural relaxation. The combination of the size of the zeolite, the Pulay forces, inherent to the plane wave DFT calculation of periodic solids with varying cell volume, and the large flexibility caused by both the zeolite open framework and the presence of extra-framework species (fluor counteranion and template cation) are responsible for the large computational cost. For this purpose, eight configurations were manually created to include all possible composition and Si-Ge distribution within D4R units. Several works report the calculation of the chemical shift using non-periodic isolated D4R units having the F atom inside [158–160]. It is assumed then that the chemical shift is a local property depending only on the composition and Si-Ge distribution of a given D4R cube. To test this assumption, we used the same composition and Si-distribution in several cases among the 8-constructed structures. All DFT calculations were performed with the VASP program [161–164], using the PAW potentials [165], the PBE functional connected to the D3 van der Waals potential and 900 eV cut-off for both the geometry optimisation and the NMR data calculation. The calculations of the chemical shift on STW structures optimised using 600 eV cut-off did not converge in six cases, which caused the need to use the very expensive energy optimisation with 900 eV cut-off. All calculations were used with the gamma point only, allowed by the size of the unit cell.

### 5.3. Results and discussion

The experimental synthetic work found a maximum of yield at circa  $\text{Ge}_f = 0.35$  (see Figure C2 in Appendix C). Hence, in order to get a deeper understanding on the factors that influence the observed volcano-type curve of the synthesis yield, we calculated the free energy of formation of the zeolite, which is plotted in Figure 5.1 as a function of the Si/Ge molar fraction. It is also worth noting that the entropic contribution does not affect in a significant way the shape of the free energy curve, since the results are very similar for temperatures as different as 3 and 450 K. The increase of entropy produces a small shift in the minimum of the free energy towards to higher values of  $\text{Ge}_f$ , from 0.2 to 0.3. The later value is closer to the observed experimental maximum of the synthesis yield. The also close position of the minimum of

the free energy at 4 K suggests that the enthalpy contribution is the main factor driven to yield dependence as a function of the Ge content. Both the calculated free energy and the synthesis yield show clear asymmetric behaviour. This could be associated to the large structural relaxation that could take place at lower Ge content. The Si...O and Ge...O (1.60Å vs 1.74Å, respectively) which at low Ge atom number is expected to be solved by modification of bond angles. But after a certain value of Ge molar fraction are could be expected a saturation of the relaxation and then the ion size effect become dominant.

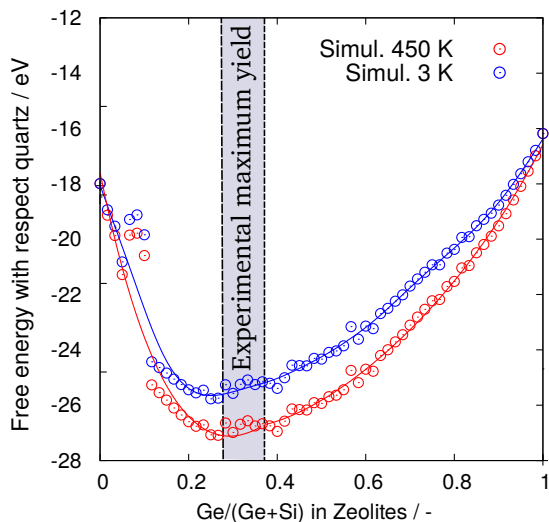


**Figure 5.1:** Free energy as a function of  $Ge_f$  at 450 K and 3 K, red and blue circles, respectively. Red and blue solid lines represents non-linear fittings of a potential function. The experimental maximum yield of solids is showed by coloured vertical bar at circa  $Ge_f = 0.35$ .

### 5.3.1. Structural characterisation

The lattice parameters of the experimental samples show a typical increase with the amount of Ge, as a consequence of the difference of the Si<sup>4+</sup> and Ge<sup>4+</sup> ion sizes, with an exception at very low Ge content. The cell parameters remain unchanged for  $Ge_f \leq 0.1$ . In order to understand the reasons for the observed changes in cell parameters and volume, we made use of simulations, which give us an atomistic insight into the system, in direct connection with the local structure. There are some limitations to the accuracy that our simulations can provide, associated mainly to the use of force fields, and the non-inclusion of factors such as temperature and the presence of SDAs in the structure. But despite those limitations, we found a relative good agreement between simulation and experimental data (see Figure 5.2), which gives us confidence in the atomistic behaviour of the simulated system.

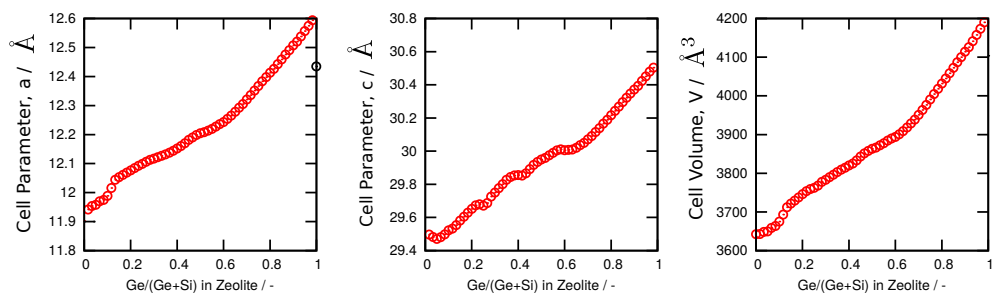


**Figure 5.2:** Cell parameters and volume vs.  $Ge_f$  computed with the Effective Hamiltonian.

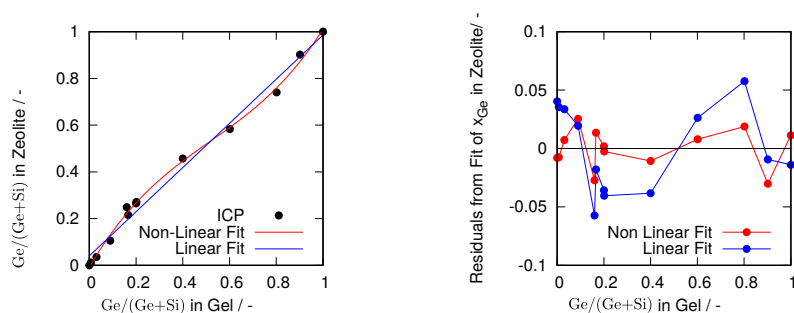


**Figure 5.3:** Molar fraction of Ge in the zeolites as a function of that in the gel.

To extract the relevant information, we plot the changes of T-T and T-O distances, as well as T-O-T angles, as a function of the Ge content. Since the  $Ge_f$  in the zeolite was close to that in the gel but not completely identical, we performed a non-linear fit of the data (see Figure 5.3) and represent the experimental cell values as a function of the calculated  $Ge_f$  in the zeolite. As we can see in Figure 5.4, the fact that, at low Ge contents, the cell volume remains constant (as observed in Figure 5.2), can be explained by the ability of a Ge tetrahedron to adapt to local deformations. In order to better understand the curves shown in Figure 5.4, we remind that the original unit cell has 60 Si atoms, so that the fully Ge-substituted system is achieved after the 60 additions represented by the 60 crosses of the figures. The first cross corresponds to the substitution of just one Ge atom. It is noticeable that, at very low Ge contents, both distances (Ge-O) and angles (O-Ge-O and Ge-O-T) show singularities, which can be understood as follows. The introduction of only one Ge in each of the six D4R cubes is easily accommodated by the structure, as the effect of the enlarged T-O distance is compensated by reducing the T-O-T angles, as shown in Figure C8. It is important to note that the presence of a F atom nearby the Ge atom causes larger distortions than those expected by the sole effect of the introduction of a Ge atom. While exploring the conformational space towards the global minimum energy, we noticed the presence of multiple local minima along with the deformation of the Ge bearing tetrahedra,

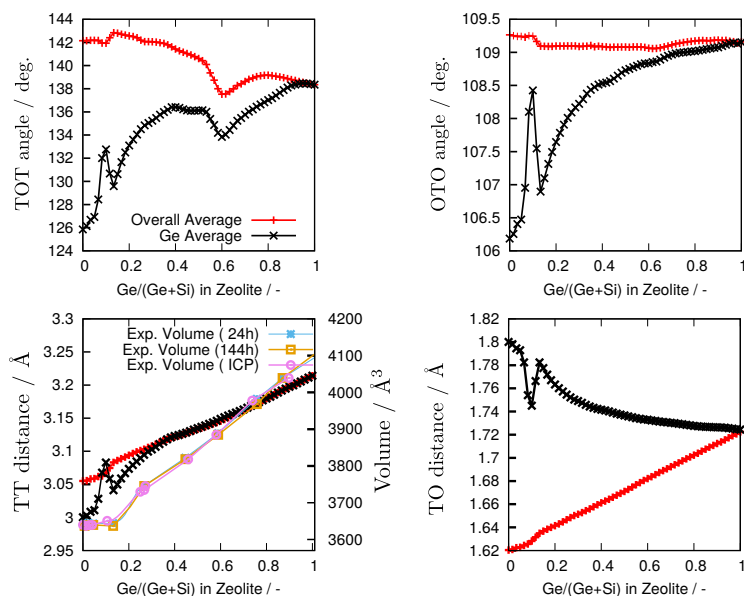


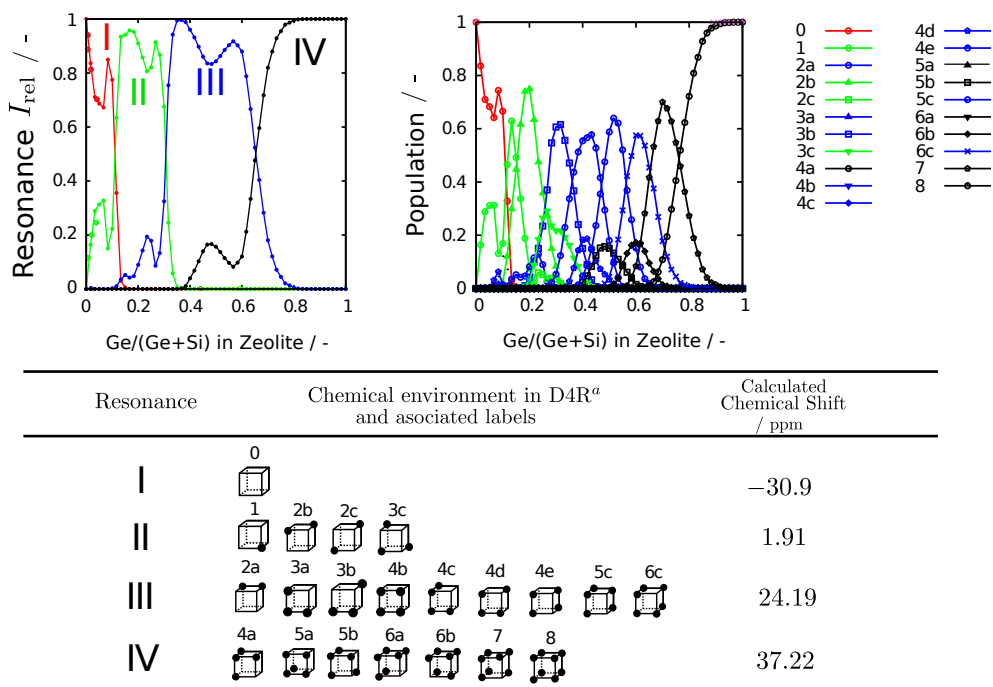
**Figure 5.4:** TT averaged distance (Bottom Left), TO average distance (Bottom Right), TOT average angle (Top Left), and OTO average angle (Top Right) versus  $Ge_f$ . Red and black points represent the overall average and average which involve tetrahedrons with Ge atoms, respectively.

indicating the presence of a complex potential energy surface. The small relative depth of the energy wells, served as an indication of metastable phases and of the probability of transitions, which suggests dynamic flexibility behavior, in agreement with previous findings.[15, 136, 137] This suggests that modelling the structural features of Ge containing zeolites, even with a static view, made provide means for predicting the flexibility, if any, of these materials. The addition of a second Ge atom in a D4R cube brings a large asymmetry into the local structure around the Ge atoms, since only one of the two Ge atoms is in close contact with the F atom (at ca. 1.82 Å), while the other is further away (ca. 2.75 Å). As a result, the former Ge atom behaves, from a local structure point of view, similarly to an isolated Ge-F pair, and the later behaves like an isolated Ge atom. We thus anticipate that the resilience to modify the cell upon a small extent of Si substitution by Ge may be a rather general behaviour for D4R-containing zeolites (we could not find relevant crystallographic data in the literature for this low  $Ge_f$  range, though).

### 5.3.2. Analysis of the Multinuclear NMR

NMR has been used for many years as a tool for determination of the Ge occupation in four membered rings [158, 166–168]. NMR resonances for pure silica and pure

germania zeolites are well established [166, 169–173], however the situation can be difficult for germanosilicates. In STW-type zeolites four resonances were found by Reus and Cambor, as shown in Figure C5. Those appears at -37/-40 and -9/-16 ppm, resonances I and IV, respectively, are easily assigned to pure silica and pure germania 4MR units, respectively. The other two -17.5 and -7.5 ppm resonances are difficult to assign (resonances II and II, respectively).



<sup>a</sup> Circles represent relative positions of Ge atoms in D4R

**Figure 5.5:** Top-Left: Relative intensities of the four resonances calculated in the  $^{19}\text{F}$  MAS NMR spectra of (Ge,Si)-STW zeolites as a function of the Ge fraction in the zeolites,  $\text{Ge}_f$ . The solid lines are the convolution of calculated populations of chemical environments in D4R, grouped by similar calculated chemical shift. Top-Right: Calculated population of chemical environments in D4R as a function of  $\text{Ge}_f$ . Bottom: Our proposed assignment of observed  $^{19}\text{F}$  MAS NMR resonances to chemical environments in D4R, with averaged calculated chemical shifts.

We made use of DFT calculations in an attempt to shed light on the origin of the four different resonances. It turned out (Figure 5.5) that the assignments are likely much more complicated than as described both above as well as in the prior literature. Our computed chemical shifts all fall in four well-defined ranges, which can be reasonably well matched to the observed  $^{19}\text{F}$  resonances. This results in an assignment that is not simply based on the number of Ge atoms in the D4R unit but mainly on how Ge atoms are or are not associated in that unit (please note that some

resonances correspond to more than one chemical environment, Figure 5.5, bottom). Based on this, we assign the four observed resonances to fluoride atoms occluded in D4R cages containing:

1. no Ge atoms (resonance I)
2. isolated Ge atoms, i.e. Ge atoms with three Si atoms as cage neighbours (resonance II). Thus, there may be 1-3 Ge atoms in the D4R.
3. Ge pairs not satisfying the conditions of type IV (resonance III). Here, up to nine different configurations with 2-6 Ge atoms are possible.
4. closed Ge clusters, i.t. configurations with at least one Ge possessing three Ge atoms as next nearest neighbours (resonance IV). There may be seven different such configurations with 4-8 Ge atoms.

Making use of the effective Hamiltonian, we have constructed the set of representative Ge configurations for each Ge content, covering the whole Ge-containing compositional range, i.e. from 1 to 60 Ge atoms per unit cell. We considered the configurations whose sum of occurrences of probability are at least 99.9 %. Taking into account the assignation of the DFT-computed NMR resonances, as well as the chemical environments identified, we recreated the theoretical population of the F-NMR resonances. The comparison between theoretical resonances and experimental intensities of the observed resonances is qualitatively good, as can be observed in Figure C6 in the Appendix C, top left, solid lines, which suggests that the distribution of chemical environments is reasonably well represented in the space of possible configurations that the effective Hamiltonian predicts (Figure 5.5, top right). Relatively large differences between experimental and theoretical chemical shifts might be expected, as has been reported earlier by several authors [174–176].

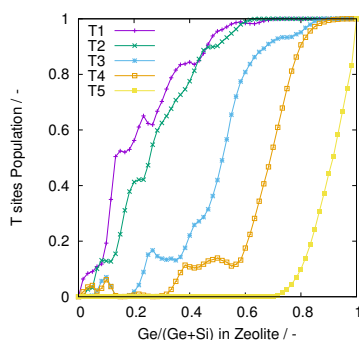


**Figure 5.6:** Variation of the populations of the different T sites, as a function of Ge content in zeolites,  $Ge_f$ , calculated with the EH.

We can also get an insight into the different preference of Ge (Si) to occupy the different crystallographic T-sites. Employing an effective Hamiltonian, we obtained the

population of each T site as a function of the  $Ge_f$ , as shown in Figure 5.6. According to these calculations, the Ge preferential occupation of sites goes in the order  $T1 > T2 > T3 > T4 > T5$ . Thus, as the Ge content increases, sites T1 and T2 are occupied first. Then site T3 followed by T4 start to be occupied at relatively low Ge contents but with a lower preference over T1 and T2. Finally, after sites T1 and T2 are fully occupied but before the rest of sites in the D4R units are occupied, site T5 begins to be occupied by Ge atoms.

## 5.4. Conclusions

Isomorphous substitution of Si by Ge in the synthesis of zeolite STW using 2-ethyl-1,3,4-trimethylimidazolium and fluoride affords the crystallization of the whole substitutional series from the pure  $SiO_2$  to the pure  $GeO_2$  end-members. A combined experimental-theoretical approach allowed us to get significant insight into the system, which may be of general interest for germanosilicate zeolites. As the Ge molar fraction increases, the yield of zeolite goes through a maximum and then severely drops at the  $GeO_2$  end member. Our calculation of the corresponding free energies matches well the inverse of the yield curve.

The isomorphous substitution of Si by Ge brings about an expansion of the structure that is roughly linear for most of the series. However, for low  $Ge_f$  ( $Ge_f \lesssim 0.1$ ) there is no expansion of the unit cell. This resilience to expansion is attributed to the local deformability around Ge atoms and the higher rigidity of  $SiO_2$ .

Similarly to previously published germanosilicate zeolites containing double 4-ring units (D4R), we observe up to four distinct resonances in the  $^{19}F$  MAS NMR spectra, depending on the Ge content. However, the assignment of these resonances is far more complicated than previously thought. Density functional theory calculations of the  $^{19}F$  chemical shifts of fluoride occluded in every possible configuration of every  $[Si_{(8-n)}Ge_n]$  D4R unit (with  $0 \leq n \leq 8$ ) reveals the resonances are not simply dependent on the number  $n$  of Ge atoms but also on the extension of Ge pairing. Thus, resonances are assigned to fluoride occluded in D4R with no Ge, with isolated Ge, with Ge pairs or with Ge in closed clusters.

Our modelling of these materials showed the presence of a complex energy surface with multiple shallow minima. We suggest that even static modelling of materials may thus provide means for predicting their flexibility.

Finally, we studied the preferential occupation of crystallographic sites by Ge both theoretically (for the whole series) and experimentally (by Rietveld refinement of structures with different  $Ge_f$  using synchrotron powder diffraction data). We found a good overall agreement but with a somewhat more abrupt and sharply distinct preferences in the models than in the experimental results. This is attributed to both the limitations of the theoretical approach and to kinetic factors allowing the real existence of metastable configurations not considered by the models.

## **Part II**

# **Metal–organic frameworks**



---

# Chapter 6

## Atomic charges for modelling metal-organic frameworks: Why and How

Atomic partial charges are parameters of key importance in the simulation of Metal-Organic Frameworks (MOFs), since Coulombic interactions decrease with the distance more slowly than van der Waals interactions. But despite its relevance, there is no method to unambiguously assign charges to each atom, since atomic charges are not quantum observables. There are several methods that allow the calculation of atomic charges, most of them starting from the wavefunction or the electronic density or the system, as obtained with quantum mechanical calculations. In this work, we describe the most common methods employed to calculate atomic charges in MOFs. In order to show the influence that even small variations of structure have on atomic charges, we present the results that we obtained for DMOF-1. We also discuss the effect that small variations of atomic charges have on the predicted structural properties IRMOF-1.

The publication related with this section can be found in:

- S. Hamad, S. R. G. Balestra, R. Bueno-Perez, S. Calero and A. R. Ruiz-Salvador. “Atomic charges for modeling metal–organic frameworks: Why and how”. *J. Solid State Chem.* 223, 144–151, 2015. DOI: 10.1016/j.jssc.2014.08.004. arXiv: 1802.08771.

### 6.1. Introduction

Metal-Organic Frameworks have emerged as front-edge materials, due to their potential impact on several types of applications, mainly those based on adsorption and separation (such as hydrogen storage [178], methane and carbon dioxide capture [179, 180], or hydrocarbon [181] and enantiomeric separation [181, 182]). Unlike traditional nanoporous solids, i.e. zeolites, carbons, and clays, MOFs do not only exhibit

enormous surface areas (beyond 5000 m<sup>2</sup> g<sup>-1</sup>), but also a huge structural and compositional diversity, resulting from the large amount of research carried out, which has recently reached over 2000 scientific papers by year. Obviously, it is very expensive and time consuming to carry out experimental studies on several different materials. But computer modelling is a useful tool, which can help guiding the experimental search into new and potentially interesting materials. It is possible, for example, to use computer simulations to devise viable routes for materials selection, via large screenings [183, 184]. Computer simulations can also provide a platform for understanding the material behavior at an atomic scale, which often leads to application-tailored materials design [185, 186].

Since the study of adsorption, separation and diffusion related phenomena involves the explicit consideration of hundreds, or even thousands of atoms (particularly in structures with large unit cells, such as MOFs) classical simulation methods are the first choice [187, 188]. It is worth noting that recently, quantum mechanics-based calculations have emerged as valuable tools in this field [189, 190], but in MOFs their computational cost still precludes its use for screenings of a larger number of materials, for the calculation of adsorption isotherms, diffusion of complex molecules, or the study of systems in which entropic effects are relevant, etc. In atomistic classical simulations the energy of the system can be written as:

$$E = E_{\text{bonding}} + E_{\text{non-bonding}} \quad (6.1)$$

where  $E_{\text{bonding}}$  involves contributions directly related to bonded atoms, and are described by the sum of bond, angles and dihedral terms, while  $E_{\text{non-bonding}}$  includes the interactions between non-bonded atoms and has the form:

$$E_{\text{non-bonding}} = E_{\text{van der Waals}} + E_{\text{Coulombic}} \quad (6.2)$$

The van der Waals interactions are usually described by the typical 12-6 Lennard-Jones potential:

$$E_{ij}^{\text{LJ}} = 4\epsilon_{ij} \left[ \left( \frac{\sigma_{ij}}{r_{ij}} \right)^{12} - \left( \frac{\sigma_{ij}}{r_{ij}} \right)^6 \right] \quad (6.3)$$

where  $\epsilon$  is the energy at the minimum and  $\sigma$  is the distance at which the energy is zero. The Coulombic interactions are calculated as follows:

$$E_{ij}^{\text{Coulombic}} = \frac{1}{4\pi\epsilon_0} \frac{q_i q_j}{r_{ij}} \quad (6.4)$$

where  $r_{ij}$  is the distance between atoms  $i$  and  $j$ ,  $q_i$  and  $q_j$  are the corresponding atomic partial charges and  $k_e = 1/4\pi\epsilon_0$  is the Coulomb's constant.

The parameters used for the calculation of bonded and van der Waals interactions are usually taken from generic force fields, such as Dreiding [30], UFF [31], OPLS [32], TraPPE [33–36] or AMBER [37]. Lennard–Jones van der Waals interactions between

different atoms are computed using the Lorentz-Berthelot [191] or the Jorgensen mixing rules [192]. When specific molecules force fields are used for modelling adsorbates, the atomic charges are usually taken from the force field used. In a number of cases, however, using the generic or specific force fields the experimental adsorption data are not reproduced, and hence transferable force field parameterization is required, via fitting of parameters to reproduce experimental data [193, 194] or via fitting to reproduce ab-initio surface energies [195–197]. The parameters that describe the van der Waals interactions and the interactions between bonded atoms are usually employed directly as taken from the generic force fields. But the atomic charges need to be calculated for each material. Since the atomic charges arise from the electronic density of the solids, even small chemical differences between related MOFs lead to differences in the charges, as was recently shown for functionalized imidazolates [198].

For the computation of the intermolecular interactions (MOF-adsorbate and adsorbate-adsorbate interactions), which control adsorption, diffusion and separation processes, it is important to keep in mind that they are of non-bonded nature, and consequently their correct description depends on achieving a balance between van der Waals and Coulombic contributions [199]. This implies that, if a generic force field is used, it is necessary to use charges that would be not very different from those employed during the parameterisation of the force field. For example, the parameters of the van der Waals interactions in the Dreiding and UFF force fields were fitted employing Gasteiger [200] and QEq charges [201], respectively. This seems to be one of the main reasons why calculated and experimental data do not agree, when generic force fields largely fail to model intermolecular interactions. As illustration, Babarao et al. [202] found that a good agreement with experimental CO<sub>2</sub> isotherms in ZIF-68 was obtained when ChelpG or Mulliken charges were used in conjunction with the Dreiding force field.

The effect of the choice of the atomic charges on computing adsorption and diffusion properties of MOFs has been a topic of increasing attention. A few years ago, Walton et al. [203] showed that the inclusion of the electrostatic interactions between adsorbate molecules and the framework was crucial in reproducing the step-like adsorption of CO<sub>2</sub> in IRMOF-1. Watanabe et al. [199] showed that even quadrupolar molecules, such as CO<sub>2</sub>, can interact very distinctly with MOFs, being the electrostatic interaction more or less relevant than the van der Waals interactions, depending on the atomic charges employed. They found that the influence of the charges on the adsorption properties is very material dependent, i.e. for some materials we observe the same adsorption behavior, for a wide range of atomic charges, but for other materials, slight changes in atomic charges produce large changes in the adsorption properties. They computed CO<sub>2</sub> adsorption isotherms up to 0.1 bar in IRMOF-1, ZIF-8, ZIF-90, and Zn(nicotinate)<sub>2</sub>, employing charges calculated by the REPEAT, DDEC, Hirshfeld and CBAC methods, and also without considering charges. These methods exhibit significant differences in the values of the charges that they predict, e.g. Zn charges calculated with the mentioned methods in IRMOF-1 are 1.2787, 1.2149, 0.4229 and 1.5955, respectively. However, the adsorption isotherms are very similar in Zn(nicotinate)<sub>2</sub>, less similar in IRMOF-1 and ZIF-8 and very different in ZIF-90.

In a study with 20 different MOFs with different topologies, pore sizes, and chemical characteristics, it was found that the guest–framework electrostatic interaction can account for 10–40% of the CO<sub>2</sub> uptake at very low pressure, and these values decrease at least by factor of 4 at high pressures, where guest–guest interactions dominate [204]. Sevillano et al. [198] used three sets of framework charges, changing in a range of 30% of their values, to examine its effect on the adsorption of CO<sub>2</sub> in ten ZIFs of different functionalities, and found that, while adsorption heats are almost the same for ZIF-8 and small differences are observed for ZIF-96, the effect of varying framework charges on ZIF-3, -7, -93 and -97 is large. The hydrophobic character of ZIF-8 seems to be responsible for the negligible effect that the choice of charges has on the values of CO<sub>2</sub> adsorption heats, which is supported by the results of Zhang et al. [205], who found that simulated methanol adsorption in ZIF-8 is not affected by the framework charges.

When modelling water in MOFs, the choice of the charges is much more relevant. Castillo et al. [206] studied water adsorption in HKUST, and found that, in order to reproduce the experimental adsorption isotherms in the low pressure range, the *ab-initio* derived framework charges needed to be scaled up by 25 %. And Salles et al. [207] studied the adsorption in the hydrophobic MIL- 47, finding that the previously used *ab-initio* charges for modelling CO<sub>2</sub> adsorption needed to be scaled down by 30%, in order to reproduce water adsorption behaviour.

The influence of the MOF framework charges on molecular diffusion has been a topic of less research. The calculated self-diffusion coefficients for CO<sub>2</sub> in ZIF-8 using charges obtained with the CBAC, REPEAT, and DDEC, and ESP methods show significant differences [208]. The latter set of charges provides results in good agreement with experimental values, but the other three sets overestimate the diffusion coefficient between 1.5 and 20 times. Liu and Zhong [209] used a different set of charges (as well as different Lennard-Jones potentials), and the calculated self-diffusion coefficient of CO<sub>2</sub> in ZIF-8 was two times larger than in the previous cited work. Since in a number of MOFs the proper choice of the framework charges is of key importance to model correctly the adsorption and diffusion behaviour, it is natural that the simulation of molecular separation would be also markedly influenced by the electrostatic interactions. For instance, the simulated CO<sub>2</sub>/CH<sub>4</sub> selectivity in HKUST shows reverse behaviors when charges are not considered at all than when there is a fully account of both host-guest and guest-guest electrostatic interactions [210]. For quadrupolar molecules, such as CO<sub>2</sub> and N<sub>2</sub>, it has been observed that the atomic charges produce an electric field inside the nanopores that largely enhances the selectivity due to the difference in quadrupole moments [211].

In the following section we will present a brief description of the most used methods for calculating atomic charges in MOFs, referring the reader to the relevant references for a more in-depth description. Then, we will present the results of the calculations we have carried out, to illustrate the influence of the structure on the charge calculation of DMOF-1. We will also show how the different sets of framework charges predict different thermal behaviors of IRMOF-1.

## 6.2. Methods for calculating atomic charges in MOFs

There are several methods with which to calculate atomic charges. They are always developed with the aim of providing the most realistic description of the system. But we have to take into account the fact that atomic charges are not quantum observables. Electron density can be easily calculated and studied, but, there are no operators to unambiguously determine the charges associated to each atom. This makes the calculation of charges almost a matter of choice. Nevertheless, there are several methods that can provide atomic charges which can be used to model porous materials with reasonable accuracy. We will describe the most widely used methods to calculate atomic charges, employing quantum mechanical calculations. Methods a) and b) are based on the population analysis of the wavefunction, methods c), d), e), and f) are based on the partition of the electron density, methods g), h), and i) are based on the fitting of the electrostatic potential around the molecule, and methods i) and j) are semiempirical approaches, the first based on electronegativity equalisation and the other on bond connection sequences.

### 6.2.1. Mulliken Charges

Mulliken charges are obtained from the Mulliken Population Analysis [212]. The first step in the calculation of these charges is to obtain the wavefunction. Like in other methods, the partial charge of atom  $A$  ( $q_A$ ) can be calculated as:

$$q_A = Z_A - \int_{V_A} \rho_A(r) dr \quad (6.5)$$

where  $Z_A$  is the charge of the positively charge atom core, and  $\rho_A(r)$  is the electron density surrounding the core, associated to that atom. This seemingly simple equation becomes very complex when we want to know which part of the total electron density (which can be easily calculated with any quantum mechanical calculation) is associated to that particular atom. And here is where each method makes a different choice. In the Mulliken method the charge is calculated as:

$$q_A = Z_A - G_A \quad (6.6)$$

where  $G_A$  is the gross atom population for atom  $A$ , which is calculated as the sum of the population of all orbitals belonging to atom  $A$ . The population matrix is constructed by assigning half the electron density to each of the two atoms that share electrons in a bond, regardless of the electronegativity of the atoms.

Mulliken charges have been widely used, mainly due to the simplicity and computational speed with which they can be obtained. For these reason they have been widely used in MOFs [21, 213–221]. There are two main problems with the Mulliken charges. Firstly, they are very dependent on the molecular geometry and the basis set, so that small changes in either the geometry or the basis sets give rise to large differences in the calculated charges [222]. And secondly, they do not provide a good description of the degree of covalency in bonds.

### 6.2.2. Natural Population Analysis charges

In order to overcome the problems associated with the Mulliken method, Reed et al. [223] developed the Natural Population Analysis (NPA). NPA charges are calculated using a set of orthonormal orbitals called natural atomic orbitals (NAOs), which are generated from the atomic orbitals that form the basis set. NAOs are used to calculate another set of orthonormal orbitals, called natural bond orbitals (NBOs), which are then used to perform the population analysis that provides the NPA charges. NPA charges usually provide charges that are not very dependent on the molecular conformation or the basis set, but they have not been developed to be calculated on periodic systems, so that the cluster approach (see section g) must be used if the charges of a periodic system need to be calculated. That is one of the main reasons why they have not been used often in the study of MOFs. Nevertheless there are some studies in which they have been used [198, 220, 224, 225].

### 6.2.3. Bader charges

These charges are calculated using Bader's atoms-in-molecules (AIM) theory. In this theory it is possible to partition the electron density and assign the density to each atom, by analysing the gradient and the Laplacian of the electron density. The electron density must be obtained first, using any quantum mechanical method (HF, post-HF, DFT, etc.). Once we have the electron density, we look for critical points in the middle of each bond, which are the points along the line between two atoms at which the electron density is minimal. From that point a surface is created by moving along the direction given by the gradient vector (that points to the direction of fastest electron density decrease). This gradient vector will create a surface that encloses a certain volume, which will be the volume associated to the atom enclosed. The integral of the electron density within that volume will provide the negative charge of the atom, and the partial charge is the atom can be calculated just by subtracting that negative charge to the positive charge of the nucleus.

Despite being useful to provide atomic partial charges, this method has been more frequently used to get information about the changes on the electron density that take place upon adsorption [226] or the differences in electron density when the metals sites of MOFs are changed [227]. Direct use of Bader charges in MOFs is not found very often [226, 228–232].

### 6.2.4. Density Derived Electrostatic and Chemical (DDEC) charges

This method (developed by Manz and Sholl [233]), is based on the atoms-in-molecules method described above, but there are two main differences: it is designed to incorporate spherical averaging to minimise atomic multipole magnitudes (in order to get a better description of the electrostatic potential) and it uses reference ion densities to enhance the transferability and chemical meaning of the charges.

These charges are better suited to model porous materials than Bader charges, because the latter do not give a correct description of the electrostatic potential (be-

cause they predict too large atomic multipole moments [234]). This method has been used to study the adsorption of water in Cu-BTC [235], N<sub>2</sub>/CO<sub>2</sub> separation in a large number of MOFs [236], CO<sub>2</sub>/CH<sub>4</sub>, CO<sub>2</sub>/N<sub>2</sub> and H<sub>2</sub>/CO<sub>2</sub> separations in several MOFs [237] and separation in Zr-Based MOFs [238].

### 6.2.5. Hirshfeld charges

In the Hirshfeld method [239] the population of each atom is calculated by assuming that the charge density at each point is shared among the surrounding atoms in direct proportion to their free-atom densities at the corresponding distances from the nuclei. There have been several improvements upon the original Hirshfeld scheme, such as the Iterative Hirshfeld [240] method (HI), Fractional Occupation Hirshfeld-I method (FOHI-D) [241], and the Extended Hirshfeld method (HE) [242], which has been proved to provide good results for periodic materials [243]. Hirshfeld charges has been used for the development of MIL-53(Al) force field [20] and modelling functionalizing effects in MIL-47 [244], among other works.

### 6.2.6. Charge Model 5 (CM5) charges

This method was developed by Marenich et al. [245] and it uses the charges obtained from a Hirshfeld population analysis (of a wavefunction obtained with density functional calculations) as a starting point. The charges are then varied, using a set of parameters derived by fitting to reference values of the gas-phase dipole moments of 614 molecular structures. CM5 charges have been successfully used to study hydrocarbon separation [246] and N<sub>2</sub>/CH<sub>4</sub> separation in MOF-74 with various types of metal atoms [247]. These charges can also be used to study the hydration of molecules in aqueous solutions, obtaining the best results when the charges are scaled by the factor 1.27 [248].

One drawback of this method is that it is implemented as a script that uses the output from the Gaussian09 code as the input for calculating the charges. This means that only non-periodic systems can be studied, and the calculation of charges of periodic systems must be performed making use of the cluster approach, which is explained in the following method.

### 6.2.7. Electrostatic Potential (ESP) derived charges

The first step is the calculation of the electrostatic potential around the molecule of interest, using any quantum mechanical method. Once this potential is known for each point of space, a set of initial atomic charges is assigned to each atom. With these initial charges, the potential on a grid of points placed in a surface around the molecule is calculated, and an iterative method is followed with which to fit the atomic partial charges that minimise the difference between the quantum mechanical ESP and the one calculated with the atomic partial charges. There are various methods to calculate ESP charges (differing in the choice of the points at which to calculate the potential),

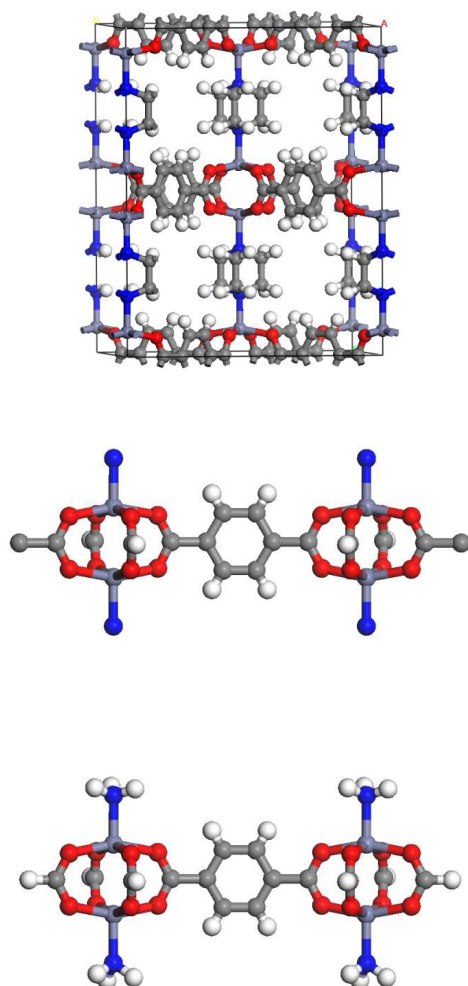


**Figure 6.1:** Top) Ball and stick representation of the atoms of the unit cell of DMOF-1 (Zn, O, N, C, and H atoms are represented as light blue, red, dark blue, grey and white atoms respectively). Middle) Cluster created by cutting directly a piece of framework. This cluster cannot be used to model the environment of the BDC ligand and calculate its charges, since there are cleaved bonds that will have very different electronic structures than in the bulk structure. Bottom) Same cluster shown in b), although the cleaved bonds have been saturated with H atoms in order to achieve electronic structures in the terminal N and C atoms that are similar to those in the crystal structure.

such as CHELPG (CHarges from Electrostatic Potentials using a Grid- based method [249]) and Merz-Kollman [250]. The main drawback of these methods is that they allow the calculation of charges for non-periodic systems. For crystals these methods cannot be applied, since the electrostatic potential in periodic systems is not uniquely determined, because there is a constant shift at each point of space. This problem has been circumvented by using the so-called cluster approach (see Figure 6.1). This approach consists in using a cluster model of the crystal, i.e. cutting a piece of crystal bulk, in the hope that the ESP derived charges for this cluster model will be the same than for the bulk. This approximation works better for larger clusters, so usually the charges are calculated for clusters of different sizes, until convergence is achieved. There is another drawback for these methods, which is the fact that when the crystal is cut to create the cluster model, there will be several bonds cleaved, leaving dangling bonds.

They are usually saturated with H atoms or with methyl groups. But these species are not part of the original crystal, and they might have an influence on the fitted charges. Nevertheless, ESP derived charges, have been the most widely used methods to obtain atomic partial charges, with large success in modelling MOFs [20–22, 220, 251–257]. Only in the last few years they have been gradually replaced by other methods better suited for studying periodic systems.

### 6.2.8. Repeating Electrostatic Potential Extracted Atomic (REPEAT) charges

This method is similar to the ESP based methods described above. It was developed by Campaná et al. [258], with the aim of solving the problems that ESP methods presented in the study of periodic systems. The key point is the introduction of an error functional which acts on the relative differences of the potential and not on its absolute values. For non-periodic systems the REPEAT method provides charges that are very similar to those obtained with the CHELPG method, and for periodic systems the charges it provides are chemically sound. Another advantage of REPEAT charges is that it predicts similar charges when different codes (such as CPMD, VASP or SIESTA) are employed. This method is becoming very popular to model MOFs [238, 259–263].

### 6.2.9. Density Derived Atomic Point (DDAP) charges

This method was developed by Blöchl [264]. It is based on the use of plane-waves to calculate the density of a molecule. Atom-centered Gaussians are used to decouple the density of the molecule (or each portion of the structure) from its periodic images, and the Ewald summation is used to calculate their interaction energy. Finally, the charge density is modelled with a set of atomic point charges. Although these charges can be used to study MOFs, its main use has been in the study of ionic liquids [265–267].

### 6.2.10. Extended Charge Equilibration (EQEq) charges

This method is based on the Charge Equilibration (QEq) method of Rappe and WA [201]. In the QEq method the charges are calculated using a set of experimental data, namely atomic ionisation potentials, electron affinities, and atomic radii, with which an atomic chemical potential is obtained (taking also into account shielded electrostatic interactions between all the atomic charges). These charges are iteratively changed, until the equilibrium is found, when the chemical potentials are equal in all atoms. The EQEq method [268] uses less fitting parameters, while maintaining the accuracy. One important aspect in the charge equilibration methods is that they do not require the calculation of wavefunction of electron densities; the only data needed are the positions of the atoms and their atomic number. For this reason, these are the fastest methods in terms of computation time, which makes them very useful for performing screenings of a large number of materials [268–270]. Recent reparametrisations of the Qeq method have been carried out by Haldoupis et al. [236] and by Kadantsev et al. [271].

### 6.2.11. Connectivity-based atom contribution (CBAC) charges

In this method (developed by Xu and Zhong [272]) there is no need to perform quantum calculations, as happened in the EQEq method. The basis of this method was the assumption that atoms with same bonding connectivity have identical charges in different MOFs. They first obtained the charges of a set of 30 MOFs, using the ChelpG method (with the cluster approach) from the electron density calculated with unrestricted B3LYP calculations. The basis set employed is LANL2DZ for the metal atoms and 6-31+G\* for the rest. The average charges for similar atoms were calculated and tabulated. It is therefore possible to obtain the charges of any MOFs, as long as it has the same types of atoms that were studied in the set of 30 MOFs (plus 16 COFs with which the database was subsequently expanded [273]). There is one small drawback associated with the wide range of MOFs that can be studied with this method, which is that in some cases the structures are not charge neutral. Nevertheless, it is very easy to calculate charges with this method, and they usually provide good results, so they are frequently used to model adsorption in MOFs [274, 275].

## 6.3. Learning from two examples

Here we show two examples chosen to illustrate two different aspects related to the charges, i.e. (a) influence of the framework geometries on the calculated charges and (b) influence of the chosen charges on structural properties, namely the negative thermal expansion of IRMOF-1.

### 6.3.1. Influence of the framework geometries on the calculated charges

We have calculated atomic charges of DMOF-1, which exhibits breathing-like flexibility [276]. The dabco pillars are disordered along the fourfold crystallographic axis. Such disorder precludes the direct use of the structure for calculating the charges, due to the atoms overlap. Thus, the reported crystal structure in the  $I4/mcm$  (# 140) space group needs to be fixed for its description without symmetry (using a P1 space group). The obtained P1 structure has a number of constrained bonds that can be relaxed using a generic force field (we employed the UFF force field in our case). This structure is labelled as DMOF-1-ini. We have labelled as DMOF-1-opt1 the structure after an optimisation has been carried out at the DFT-D level, with the VASP code [161, 162]. The dabco unit has a complex structure and their atoms in the DMOF-1-ini structure are slightly disordered, the optimisation leads to a configuration with a relatively high energy. For that reason, we carried out an additional optimisation, in which we first adjusted the symmetry of the system, and then we reoptimise it with VASP. We called this third structure DMOF-1-opt2. All the VASP calculations are carried out employing the PAW potentials [165], with the PBE exchange-correlation functional [72], and a cut-off energy of 500 eV. Due to the large sizes of the unit cells ( $a = 15.0630$  Å and  $c = 19.2470$  Å) only the gamma point was used. The framework of DMOF-1 is shown in Figure 1.3a, while the atom labels used for reporting the charges are shown in Figure 6.2.

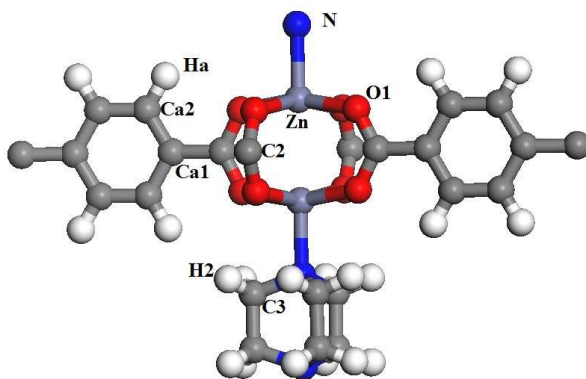


**Figure 6.2:** Atom labels of DMOF-1 (see Tables 1, 2, and 3 for charges associated to the C3, Zn, and H2 atoms respectively).

The calculations with the VASP code permit the calculation of the REPAT and Bader charges, for which we use the codes provided by Campaná et al. [258] and Tang et al. [277] respectively. We also calculated the Mulliken and DDAP charges for the same structures, using the cp2k code [278] and the PBE exchange-correlation functional. Finally, we also calculated the EQeq charges, with the code provided by Wilmer et al.

[269]. We report, in Table 6.1, the range of variation of the charges of the C3 atom, for the three studied structures. We can see that, overall, the values of the calculated charges vary in a very wide range. For a given structure, each method provides different charges, ranging for instance the charge of the C3 atom, in the DMOF-1-*ini* structure, from  $-0.299$  to  $+0.128$  when calculated with the REPEAT method, while when the DDAP method is used the range of variation goes from  $+0.224$  to  $0.240$ . This is not surprising, since we have mentioned the intrinsic subjectivity associated to the process of assigning the electronic density to each atom. The smaller range of variation is observed for the Mulliken method, while the Bader charges are the ones that show a larger range of variation. A similar behavior is observed for the Zn and H<sub>2</sub> atoms, as can be seen in Tables 6.2 and 6.3. The large range of variation of the charges in structures DMOF-1-*ini* and DMOF-1-*opti1* indicates that the obtained charges will not be able to be used in force field-based simulations, since atoms that should have the same chemical behavior are predicted to have very different charges. It is worth noticing that three of the methods (Bader, DDAP and EQeq) predicted a negative charge for the H<sub>2</sub> hydrogen atom (see Table 6.3).

**Table 6.1:** Range of variation of the atomic partial charges for atom C3, calculated for the structures DMOF-1-*ini*, DMOF-1-*opti1* and DMOF-1-*opti2*, using 5 different methods, namely REPEAT, Bader, Mulliken, DDAP, and EQeq.

Method	DMOF-1- <i>ini</i>	DMOF-1- <i>opti1</i>	DMOF-1- <i>opti2</i>
REPEAT	-0.299; 0.128	-0.573; 0.308	-0.363; 0.137
Bader	-0.03; 0.443	0.176; 0.543	0.187; 0.598
Mulliken	-0.052; -0.049	-0.052; -0.042	-0.040; -0.036
DDAP	0.224; 0.240	0.148; 0.233	0.194; 0.223
EQeq	-0.119; 0.093	0.098; 0.161	-0.047; -0.033

**Table 6.2:** Range of variation of the atomic partial charges for atom Zn, calculated for the structures DMOF-1-*ini*, DMOF-1-*opti1* and DMOF-1-*opti2*, using 5 different methods, namely REPEAT, Bader, Mulliken, DDAP, and EQeq.

Method	DMOF-1- <i>ini</i>	DMOF-1- <i>opti1</i>	DMOF-1- <i>opti2</i>
REPEAT	0.962; 0.968	0.881; 0.926	0.920; 0.922
Bader	1.251; 1.269	1.258; 1.285	1.074; 1.082
Mulliken	0.516; 0.519	0.502; 0.505	0.565; 0.568
DDAP	0.855; 0.856	0.810; 0.831	0.806; 0.809
EQeq	1.092; 1.143	1.072; 1.144	1.131; 1.132

We have discussed the influence of the method for calculating charges, but even more interesting is the influence that the geometry of the framework has on the charges. When the same method is employed, the slight variations of the framework geometry that exist between the three structures induce significant differences in atomic charges. For example, in Table 6.1 we see that the charge of atom C3 calculated

**Table 6.3:** Range of variation of the atomic partial charges for atom H2, calculated for the structures DMOF-1-ini, DMOF-1-opti1 and DMOF-1-opti2, using 5 different methods, namely REPEAT, Bader, Mulliken, DDAP, and EQeq.

Method	DMOF-1-ini	DMOF-1-opti1	DMOF-1-opti2
REPEAT	0.048; 0.126	0.024; 0.202	0.047; 0.147
Bader	-0.158; 0.112	-0.258; 0.052	-0.236; 0.081
Mulliken	0.067; 0.073	0.064; 0.080	0.063; 0.070
DDAP	-0.086; -0.036	-0.090; 0.004	-0.087; -0.029
EQeq	-0.030; 0.083	-0.039; 0.112	0.035; 0.038

with the EQeq method can vary from  $-0.119$  to  $0.093$  for the DMOF-1-ini structure, but for the DMOF-1-opti1 there are no negatively charged C3 atoms. This is a weak point of the force field-based calculations, which rely upon the validity of the charges to provide an adequate description of the electrostatic interactions. The influence of the geometry on the calculated charges is more marked for the Bader and REPEAT methods, while the Mulliken method seems to be the one that minimises the spread of charges for atoms that are symmetrically equivalent. The DDAP method also shows an acceptable spread of charges, and if we take into account both the advantages and drawbacks of the two methods, discussed in the previous section, we would suggest using these charges for the calculation of atomic partial charges. If a screening of a large number of structures will be performed the use of DDAP charges is unfeasible. In that case, the EQeq method provides reasonably good charges, at a low computational cost, so that method would be the method of choice.

## 6.4. Influence of the chosen charges on structural properties

The effect of the charges on the calculation of adsorption heats, diffusion constants and separation properties has already been treated in the literature, as shown in section 1. Here we discuss how charges affect the structural behavior of MOFs. To do this, we have selected IRMOF-1, which is known to show a negative thermal expansion [42, 279]. The atomic charges reported by Dubbeldam et al. [42] were scaled by 0.95 and 1.05, and the thermal behavior was studied by means of molecular dynamics. The framework has been modelled by molecular dynamics simulations in the isothermal-isobaric (NPT) ensemble (fully flexible cell, using Nosé-Hoover thermostat and Parrinello-Rahman barostat). Intramolecular interactions were taken into account employing the force field developed by Dubbeldam et al. [42]. The external pressure is set to zero. The simulations have been run for 5 ns, using an integration step of 0.5 fs. Ewald summation was used to calculate the electrostatic energy in the crystalline framework, and a cut-off radius of 12 Å was used for short-range interactions. We have used the RASPA code to carry out the simulations [55].

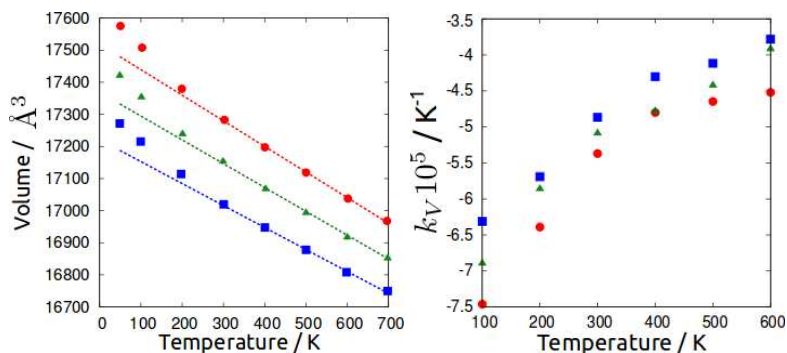


**Figure 6.3:** Left: Dependence of the cell volume with the temperature, for IRMOF-1. Right: Dependence of the thermal expansion coefficient with the temperature, for IRMOF-1.

In Figure 6.3-Left, we show the dependence with temperature of the cell volume, in IRMOF-1, for three different sets of charges. Since the charges are homogeneously changed in the whole unit cell, and the charges do not affect the bond strengths, it is somewhat surprising that the small changes introduced in the charges (5%) produce a significant modification in the (negative) thermal expansion of IRMOF-1. For each temperature, it is observed that there is an inverse dependence of the cell volume with the amount of charge scaling, which is an evidence of the role of long range (Coulombic) interactions in the overall structure of MOFs. However, the rate of the structural changes with temperature has a direct dependence with the charges, as revealed by the behavior of the thermal expansion coefficient (Figure 6.3-Right). This is probably due to a balance between the elastic and the entropic effects, as long range forces compete with the bonding interactions that are not modified by the charges.

## 6.5. Conclusions

We have reviewed the different methods available to calculate atomic partial charges in MOFs, and we have also presented two examples of materials in which the choice of charges has a big influence on the results obtained. The decision about what method is the best is not a simple one, and the choice will depend on factors such as the knowledge and experience of the researcher, the codes that he or she has access to, the type of systems that will be studied, etc. Once a method has been chosen, it is important to check carefully that all charges are chemically sound. And, if possible, it is desirable to compare the charges obtained with more than one method. We also suggest charge calculations on structures optimized by different approaches, as small structural differences might have a large impact on the resulting atomic charges. We have also shown that not only molecular adsorption, separation and diffusion are affected by the choice of the charges, but also the structural properties, which is

particularly relevant for modeling systems with at least certain degree of flexibility.



---

# Changes in thermal expansion in a rigid MOF: MOF-5

Controlling thermal expansion is an important, not yet resolved, and challenging problem in materials research. A conceptual design is introduced here for the first time, for the use of MOFs as platforms for controlling thermal expansion devices that can operate in the negative, zero and positive expansion regimes. A detailed computer simulation study, based on molecular dynamics, is presented to support the targeted application. MOF-5 has been selected as model material along with three molecules of similar size and known differences in terms of the nature of host–guest interactions. It has been shown that adsorbate molecules can control, in a colligative way, the thermal expansion of the solid, so that changing the adsorbate molecules induces the solid to have positive, zero or negative thermal expansion. We analyse in-depth the distortion mechanisms, beyond the ligand metal junction to cover the ligand distortions, and the energetic and entropic effect on the thermo-structural behavior. We provide an unprecedented atomistic insight on the effect of adsorbates on the thermal expansion of MOFs, as a basic tool towards controlling the thermal expansion.

The publication related with this section can be found in:

- S. R. G. Balestra, R. Bueno-Perez, S. Hamad, D. Dubbeldam, A. R. Ruiz-Salvador and S. Calero. “Controlling Thermal Expansion: A Metal–Organic Frameworks Route”. *Chem. Mater.* 28, 8296–8304, 2016. DOI: 10.1021/acs.chemmater.6b03457. arXiv: 1610.08122.

## 7.1. Introduction

Thermal expansion (TE) mismatch is at the core of common mechanical failures in a wide range of systems [281–284]. This is an intriguing problem that needs to be solved for the development of new applications in advanced industries, such as

aerospace and microelectronics. To overcome this problem, it is desirable to have materials with controlled thermal expansion (CTE), a topic that has been of high interest over decades [281, 283, 285, 286]. Currently, the most frequently used choice is composite materials, whose TE can be controlled by adjusting the amount of components having positive (PTE) and negative thermal expansion (NTE), in such a way that the overall behavior fits the targeted necessities [285]. Composite materials, however, have a high concentration of interfaces, which are weak points, not only from a mechanical but also from a chemical point of view, mainly at medium and high temperatures [287, 288]. There is therefore a great interest in finding systems where the control of the thermal expansion can be achieved, without resorting to composite materials.

Recently, Tallentire et al. [286] successfully prepared cubic  $Zr_{1-x}Sn_xMo_2O_8$  solids, and found an unprecedented level of chemical control of the thermal expansion (negative, zero and positive) in a single phase, over a very wide range of temperatures [286]. They started from the known fact that oxide frameworks, such as cubic  $ZrW_2O_8$ , show NTE Mary et al. [289], while the analogous  $SnMo_2O_8$  is unique in showing PTE. Shortly after, Carey et al. [290] studied the TE of dehydrated  $Li^+$ ,  $Na^+$ ,  $K^+$ ,  $Rb^+$ ,  $Cs^+$  and  $Ag^+$  exchanged zeolite A and their purely siliceous analogue ITQ-29 [290]. They found that, in dehydrated state, NTE dominates in most cases, except for Li- and Ag-forms, which show a small PTE. On the other hand, PTE is observed in the presence of water. These approaches stimulate the search for materials that can be easily prepared and readily tuned to obtain ad hoc thermal expansion coefficients. Since a number of Metal-Organic Frameworks (MOFs) are known to show NTE Carey et al. [290], Collings et al. [291], Lock et al. [292] and Peterson et al. [293], it is interesting to investigate whether MOFs can be used to develop systems with controlled thermal expansion. This is also stimulated by the recent study of Yot et al. [294] that shows that MOFs can be used as a shock absorber. In this context, exploiting the mechanical properties of MOFs emerges as a fascinating new branch in MOFs applications horizon.[295]

There are theoretical and experimental studies that show that MOFs exhibit interesting TE features. Dubbeldam et al. [42] predicted exceptional NTE in MOF-5 using molecular simulations, achieving a good agreement with the experimental behavior of the material loaded with  $CO_2$ ,  $N_2$ , and Ar [296], results that were later validated experimentally for the empty framework [279]. Yang et al. [297] found a MOF that undergoes PTE when desolvated, but it contracts in the presence of  $N_2$  at temperatures below 119 K, while it expands at higher temperatures. Joo et al. [298] predicted a cell volume contraction due to van der Waals interactions of guest  $H_2$  molecules in MOF-5. Lock et al. [292] found experimentally that the NTE observed in MOF-5 decreases with the amount of loaded helium.

In addition, cell contraction in the breathing MOF MIL-53, induced by attractive host-guest interactions, has been identified [19, 299]. And Grobler et al. [300] observed that the extent of positive thermal expansion in an anisotropic MOF can be tuned by the adsorption of molecules, and that the size of the molecules is correlated with the induced change of the CTEs. All these findings suggest the hypothesis that

MOFs can be tuned to be materials with CTE coefficients. In this study, we show at a theoretical level that controlling the nature and amount of adsorbed molecules in a MOF, the TE coefficient can be finely tuned to desirable behavior (PTE, NET or ZET, i.e. Zero TE). Note that large deformable MOFs, like MIL-53 [301] or soft coordination polymer [302], are not likely to be relevant solids for CTE, as their volume changes usually largely exceed the required adjustment of the TE-induced size mismatch.

As a model material we have selected MOF-5[11], considering that not only it is an archetypal MOF, but most importantly, that molecular simulation methods perform very well in modelling its thermal behavior, including the NTE [42]. The adsorption of polar molecules, in MOF-5 [303], is known to occur in the proximity of the metal oxocluster. Since the formation of water clusters in this material provokes chemical instability [303], we have chosen an alcohol molecule, isopropanol (IPA), to study the influence of polar adsorbate–metal oxocluster interactions in its thermal behavior. Similarly, but for comparative purposes, we have also studied benzene (BEN) to observe the behavior associated to non-polar adsorbate–ligand interactions, as the role of the ligands in adsorption in MOF-5 has been identified to be of the same order than this of the oxocluster [304]. Experimental results have shown that the ligands in MOF-5 also act as adsorption sites [296]. Other authors, using molecular simulation, found similar conclusions with regards to the presence of an adsorption site next to the ligands [305, 306]. A large discussion of the effect of metals and ligands on the adsorption properties of MOFs can be found in a recent review by Andirova et al. [307]. In the present case, since benzene as adsorbate can interact with the benzene ring of the ligand via  $\pi$ – $\pi$  interactions[308], it is interesting to consider also a linear alkane, propane (PRO), as non-polar adsorbate with no particular interaction with the MOF. The overall behavior of MOF-5 when guest molecules are adsorbed is expected to be the result of a balance between three factors, namely the attractive host–guest interactions, the vibrational modes of the MOF structure (taking into account that they are likely to be affected by the adsorbates), and the repulsive contributions from adsorbate–framework collisions, which are more relevant at higher temperatures. We noted that MOF-5 collapses at relatively low external pressures[309], which precludes its use at high mechanical stresses. Nevertheless, this system has other advantages. the material is an appropriate model system, considering the available experimental and theoretical literature on its thermal behavior, and on the other hand it can be used for controlling TE in small devices, such as those required in microelectronics.

## 7.2. Conceptual Design, Methods and Computational Details

In this work, we introduce a new concept in MOFs applications: their use as materials for controlling thermal expansion, in the three regimes, namely negative, zero and positive. As described in the introduction, there is a large amount of published studies accounting for interesting thermo–structural behaviors of MOFs, including changes of the thermal expansion with adsorbed molecules, which support the devised applica-

tion. Our approach consists in the design of coatings made by MOFs, which are loaded with a certain amount of adsorbate molecules. These MOFs can have a desired, specific thermal expansion, covering all the range of behaviors, i.e. negative, zero and positive expansions. It is well known that a number of MOFs suffer damage upon desolvation, even leading to loss of crystallinity and structural collapse or amorphization [310]. The presence of guest molecules in a MOF can enhance its mechanical resistance against framework collapse [311]. Therefore, a careful selection of the MOF and the adsorbate molecules is essential. Nowadays there are several robust MOFs that have been proven to withstand cycles of solvation and desolvation, such as those studied by Khutia et al. [312] on MIL-101, and Begum et al. [313]. Chemical stabilization of certain MOFs, which are known to collapse otherwise, can be achieved, by applying solvent exchange to remove the pristine molecules in the pores resulting from the synthetic procedure. Such molecules might exert large capillary forces on desolvation, leading to collapse, but an exchange with weak-interacting solvents can prevent it [314]. We have paid attention to the known fact that the equilibrium loading of adsorbate molecules in a porous material depends on temperature, pressure, and the nature of the molecules. In this regard, since the planned application involves variations of external temperature, and implicitly also of external pressure, the device used for controlling thermal expansion must be operated without molecular exchange with the environment.

Simulations were performed with the RASPA code [55]. The isosteric heats of adsorption of the guest molecules were computed after 500,000 sampling steps using the Widom Insertion Particle Method [315]. Adsorbate–adsorbent interactions were modeled with Lennard–Jones (LJ) pairwise interatomic potentials, plus coulombic interactions. The values of the LJ parameters were calculated through Lorentz–Berthelot mixing rules, for which the force field parameters of the atom of the MOF were taken from UFF force field [31], and those of isopropanol, propane, and benzene molecules were taken from the OPLS-aa force field [32, 316]. The LJ interactions were computed in the real space within a cut-off of 12 Å, while the coulomb interactions were handled using the Ewald summation method [46, 317]. The atomic charges used for the molecules are the assigned by the selected force field, and the atomic charges for the MOF were taken from Dubbeldam et al. [42].

The overall thermostructural behavior is expected to depend, particularly at high adsorbate loadings, on the adsorbate–adsorbate interactions, as well as on the framework properties and framework–adsorbate interactions. Therefore, we did not only pay careful attention to the force field used for the framework but also that of the adsorbates. The force fields employed to model guest–guest interactions have been proven to model accurately the liquid phase of the compounds [318–320], so that we can rely on its validity modelling the dense phases within the pores.

Monte Carlo (MC) simulations in the Canonical (NVT) ensemble were conducted initially with one adsorbate molecule, in order to compute average occupational density profiles of each adsorbate. This was used as a tool for localizing the adsorption sites, and to calculate the binding energies of the adsorbates on the preferential sites. The maximum loading capacities were extracted from the saturation of the adsorption

isotherms computed in the Grand Canonical ( $\mu$ VT) ensemble. To insert successfully the molecules in the system, the Configurational Bias Monte Carlo (CBMC) technique was used [51]. NVT MC simulations were conducted with 20, 40, 60 and 80 % of saturation of adsorbate molecules as starting configurations for the subsequent molecular dynamics simulations. MC simulations were run with 80,000 and 1,000,000 equilibration and production steps, respectively.

Molecular Dynamics (MD) simulations were performed in the Isothermal-Isobaric ensemble, (NPT), with isotropic cell fluctuations, using the fully flexible force field reported by Dubbeldam et al. [42] for the description of the thermo-structural properties of MOF-5 with and without adsorbate molecules. The integration of the equations of motion that generate the NPT ensemble was performed following the scheme of Martyna et al. [52] and Tuckerman et al. [53]. A short time step of 0.5 fs was used to avoid the generation of abnormally large interatomic forces that might eventually induce partial collapse of the framework. A total of 200,000 steps (100 ps) were used for the equilibration of the systems and 10,000,000 steps (5 ns) for the production run. The adsorbate–adsorbent interactions were computed in the same way as used for the computation of the heats of adsorption. The structural data, acquired from the MD simulations, were analyzed with a home-made code, explicitly written for this purpose, which allows partitioning the cell length deformations among the different geometrical units composing the material.

### 7.3. Results and Discussion

We first present some introductory results that are useful on the one hand for validating the theoretical methods, and on the other hand to describe the host–guest interactions between MOF-5 and the selected guest molecules. The closest available experimental results with which we can compare, regarding the variation of the thermal expansion of MOF-5 produced by changes in the amount of adsorbed molecules, are those reported by Lock et al. [292]. They employed helium flows at different rates to vary the amount of adsorbate molecules. We have therefore simulated this system to show the reliability of our computer simulation protocol, though it is worth mentioning that only qualitative comparisons can be established, as an accurate, quantitative estimation of the resident helium atoms inside the MOF in gas-flow operando experimental conditions is not possible. To obtain the best possible estimation, we calculate the number of helium atoms in the GCMC simulations at the pressures used to set the helium fluxes in the experiments of Lock et al. [292]. In Figure 7.1 we plot the dependence of the cell volume of MOF-5 with temperature, for different amounts of helium atoms, (below 10% of saturation capacity). It shows reasonable agreement with the experimental results [292], since the correct NTE behavior is present, while there is an increase of cell parameters as the number adsorbed helium molecules increases. We did not get a decreasing behavior of the NTE coefficient as the number of guest molecules increases, since the number of flowing helium atoms per unit cell in the experiments is likely to be much higher than that we obtain for the equilibrium

**Table 7.1:** Calculated isosteric heats of adsorption,  $\Delta H$ , adsorption entropies,  $\Delta S$ , binding energies,  $\Delta U$ , binding energies at minimum energy configuration,  $\Delta U_{\min}$ , and Henry coefficients,  $K_H$  of benzene, isopropanol, and propane in MOF-5, at 300 and 500 K.

	$T / \text{K}$	$\Delta H / \text{kJ mol}^{-1}$	$\Delta U / \text{kJ mol}^{-1}$	$\Delta U_{\min} / \text{kJ mol}^{-1}$	$T\Delta S / \text{kJ mol}^{-1}$	$K_H / \text{mol kg}^{-1} \text{Pa}^{-1}$
Benzene	300.0	-32.34	-29.85	-40.80	-10.87	$1.381 \times 10^{-3}$
	500.0	-28.16	-24.0	-	-10.35	$1.082 \times 10^{-5}$
Isopropanol	300.0	-27.16	-24.66	-41.84	-10.26	$2.174 \times 10^{-4}$
	500.0	-22.52	-18.36	-	-8.66	$4.18 \times 10^{-6}$
Propane	300.0	-21.41	-8.91	-31.11	-7.45	$6.7 \times 10^{-5}$
	500.0	-19.46	-15.3	-	-7.59	$2.587 \times 10^{-6}$

calculation (ca. 10% of saturation) through GCMC. Below, we show that by increasing the number of adsorbate molecules, the NTE coefficient can indeed be tuned.

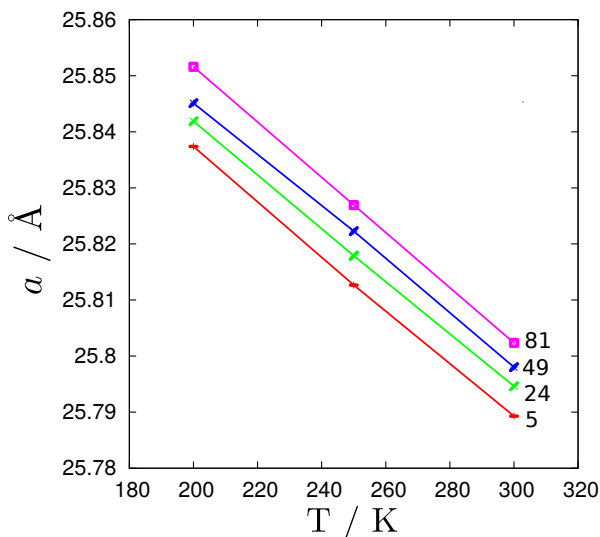


**Figure 7.1:** Variation of the cell parameter,  $a$ , of MOF-5 with temperature,  $T$ . The MOF was loaded with 5, 24, 49 and 81 helium molecules per unit cell (red, green, blue and pink lines, respectively).

Using the selected probe molecules, we will provide a rationalisation on the behavior found in Figure 7.1. As stated above, the nature and strength of the interactions of the guest molecules with the material are expected to play an important role in its overall thermo-structural behavior. Accordingly, MC simulations were used to study the adsorbate-adsorbent interactions for the selected three molecules. The heats of ad-

sorption, adsorption entropies, Henry coefficients, and binding energies are reported in Table 7.1. The strength of the host-guest interactions, as expected, increases with the number of non-H atoms. In general, single adsorbate molecules are preferentially located near the zinc atom of the oxocluster, in a corner also delimited by the adjacent atoms of the three benzene rings (Figure 7.2). In the MOF-5 structure there are two types of cages, big and small, with different degrees of rotation of the benzene rings in the linker. Our results show that the three guest molecules studied occupy mainly the big cages in first place. The distribution of molecules around the oxocluster is different between benzene, which spreads up to the benzene rings in the linkers, and isopropanol and propane, which are rather concentrated around the oxocluster. Likewise, the different nature of the adsorption of isopropanol and propane is shown in the wider area that the latter occupies around the oxocluster. This is also supported by the different behavior found in the adsorption isotherms (Figure D2).

Along with the density profiles, the heats of adsorption and binding energies reveal that dispersive van der Waals interactions represent an important contribution to host-guest interactions. It is also noticeable that the stronger electrostatic interaction of isopropanol increases its binding energy. In the case of benzene, the  $\pi$ - $\pi$  interactions are responsible for the high binding energy. Nevertheless, the large porosity and heterogeneity of binding sites of this material lead to a much lower average interaction strength. This is also reflected in the entropy and Henry coefficients and from a structural point of view, this is revealed by slight changes of the atomic density near the oxocluster: isopropanol is more concentrated than propane at the corner of the oxocluster and benzene is also likely to occupy an intermediate position between the oxocluster and the benzene ring in the linker. We noted that at high loading conditions the sites in the small cages are also occupied by guest molecules (Figure D1).

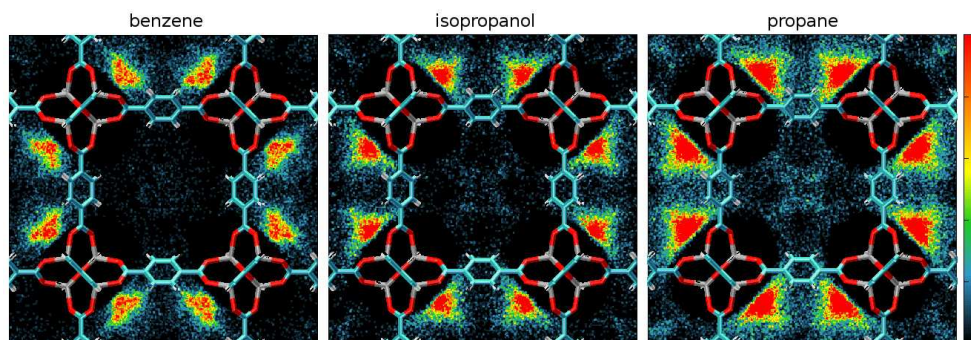


**Figure 7.2:** Average occupational density profiles of the center of mass of adsorbate molecules (benzene, isopropanol, and propane), in an  $xy$ -view. The cages located at the center and the corners of each snapshot correspond to the small cage. The framework atoms are superimposed to get a better understanding of the density profiles. The color code of the framework atoms is: carbon, blue; oxygen, red; hydrogen, white; zinc, grey respectively.

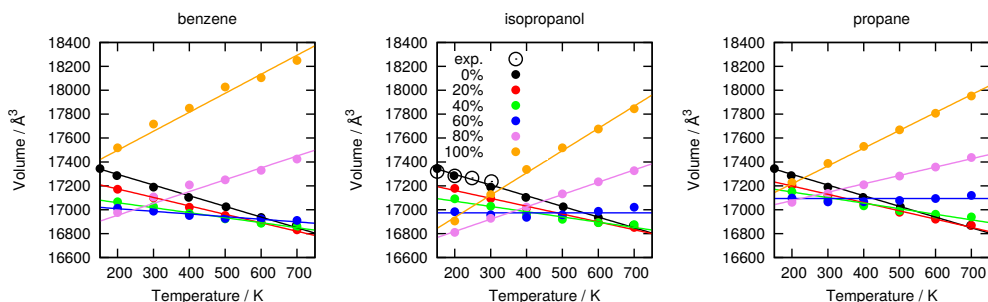


**Figure 7.3:** Cell volume as a function of temperature, for several loadings (in % of saturation) of benzene, isopropanol, and propane. Experimental data are taken from references[11, 179]. Solid lines represent linear regressions ( $r^2 > 0.9$ ). The color code is the same for the three figures.

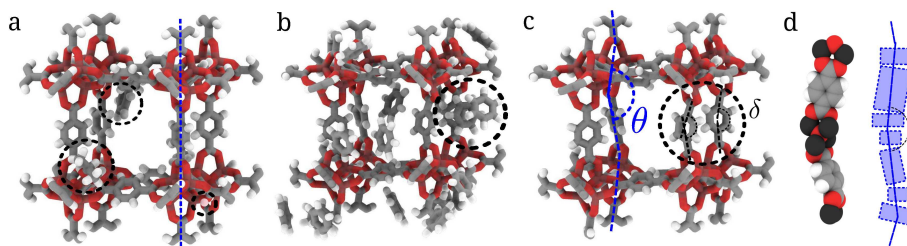


**Figure 7.4:** (a) Structure of idealized undistorted MOF-5 with the guest molecules in their corresponding binding sites. (b) Snapshot of the structure with 20% of saturation of benzene. We show benzene molecules interacting with a benzene molecule of the linker via  $\pi$ - $\pi$  interactions. (c) Distorted structure. Dashed blue lines represent a schematic view of the string of atoms crossing the cell, with different degrees of distortions  $\theta$ , and  $\delta$  represents small distortions in the BDC linker. (d, left) String of atoms crossing the cell. (d, right) Schematic view of the line distorted string.

The adsorption saturation capacities in MOF-5, as calculated by GCMC at high pressure, are 86, 98 and 105 molecules per unit cell, for benzene, isopropanol and propane, respectively. As expected when we selected the molecules with similar molecular sizes, differences in the number of molecules do not exceed 20%. Note that a cell volume change of the MOF should lead to a variation in the number of molecules in saturation conditions. However, the variation of volume is tiny, compared with the total volume, and consequently the largest deviation in number of molecules is less than 3.2%. We note that the comparison of the computed saturation capacity with experiments is only possible with benzene [179, 321], as for the other two molecules there are not

available published data. The difference between the two experimental values available differ by 12.66% (8.95 mol kg<sup>-1</sup> and 10.24 mol kg<sup>-1</sup>, Shim et al. [321] and Eddaoudi et al. [179], respectively), which is no surprising considering that defects and residual dimethylformamide from the synthesis might alter the otherwise ideal adsorption capacity. This is also relevant that both experiments are conducted only to relatively low pressure values (less than 10 kPa). Our simulations are conducted in defect-free, completely desolvated frameworks, and the computed loading value at the pressure where adsorption saturation is observed (ca. 1 kPa) is within 15% (11.96 mol kg<sup>-1</sup>) of the experimental data, which is a reasonable good agreement. In addition, as an important point for practical applications, it is useful to see that 98% of adsorption is reached at experimentally accessible pressures (Figure D2).

Once the basic introductory data has been presented, we will carry out the analysis of the thermal expansion. The wide range of thermal expansion behaviors of MOF-5 loaded with benzene (BEN-MOF-5), isopropanol (IPA-MOF-5) and propane (PRO-MOF-5) is displayed in Figure 7.3. MOF-5 has a cubic space group and therefore we only plot the cell volume. Three regimes are clearly observed: NTE, PTE, and ZTE. We found that the simulated thermal behavior of the bare framework is in fair agreement with experimental data. We found that the simulated thermal behavior of the bare framework is in fair agreement with the experimental data. This was also observed in a previous work [42]. It is worth noting that while the variation of the cell parameter of the mixed oxide solution of Tallentire et al. [286] is of the order of 0.5%, in this system we find a larger variation, of 2.7%, i.e. a range of variation five times larger.

A remarkable conclusion that can be drawn from Figure 3 is that the system shows a colligative behavior, as the qualitative behavior of the material does not depend on the choice of the adsorbed molecule. This is somehow surprising, as we noted that the interaction energies of the molecules with the framework as single entities (Table 7.1) are different. Nevertheless, it is clear that the nature of the molecules allows a fine tuning of the volume variation, but the overall behavior is qualitatively the same for the three types of adsorbed molecules. The appearance of colligative behavior has not yet been reported in MOFs or coordination polymers. The key point in controlling the thermal dependence of the cell volume is the degree of guest loading. As shown in Figure 7.3, below 40% the NTE regime is observed, and PTE appears above 80%, while ZTE appears between these two values. In order to rationalise this interesting behavior it is instructive to focus firstly at very low temperatures. In this situation, the influence of the attractive host-guest interactions on the structure contraction is large. This is evidenced by cell volume values below saturation at 200 K that are lower than that of the bare structure. For instance, benzene molecules are attracted by the aromatic rings of the linkers, as shown in the snapshot of MOF-5 at 300 K, and a benzene loading of 20% (Figure 7.4.b). In a second stage, it is interesting to pay attention to the behavior at loadings close to saturation, where the guest-induced molecular pressure on the framework is dominant, leading to cell volume increases, and the display of the PTE regime. As anticipated above, it is apparent that two effects compete in directing the thermal behavior: host-guest attraction and guest-induced pressure. The calculated TE coefficients systematically increase with a rise of the

number of adsorbate molecules present in the structure. For the three molecules, at loadings of 20% of saturation, the TE coefficients are around  $-40 \times 10^{-6} \text{ K}^{-1}$ , they are nearly zero at 60% loading, and the saturation values are  $80 \times 10^{-6} \text{ K}^{-1}$  for BEN and PRO, and  $107 \times 10^{-6} \text{ K}^{-1}$  for IPA. Details are given in the Appendices (Figure D3 and Table D2).

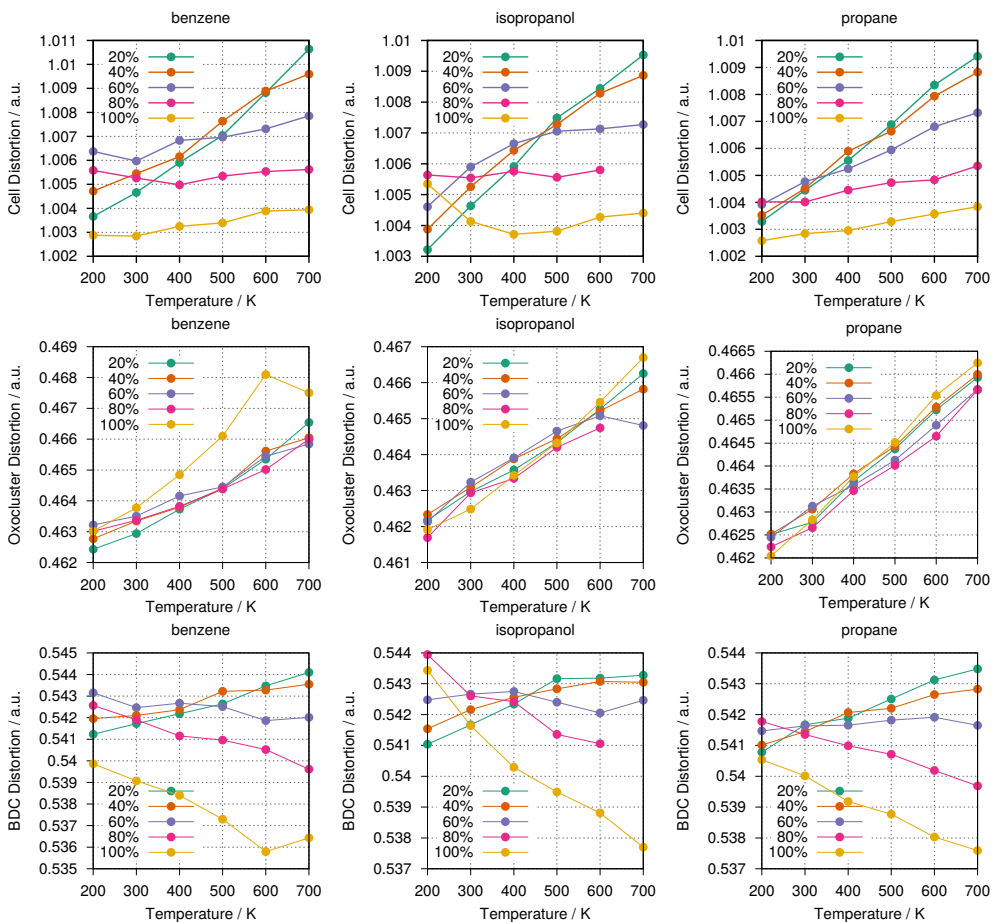


**Figure 7.5:** Variation as a function of temperature of (top) the cell distortion, (middle) the oxocluster distortion, and (bottom) benzenedicarboxylate (BDC) distortion, for benzene, isopropanol and propane. The distortions are defined in the text and in the Appendices (Equation D8). Note that oxocluster plus BDC distortion sum about 1.

To obtain further insights into the thermal behavior of the system we analyze the relationship between molecular interactions, local deformations, and TE. From previous work, it is known that the NTE observed in MOF-5 is not associated with a concerted

rotation of the oxocluster [42], as it would be expected from the behavior in inorganic porous materials [322–324]. Although several studies have addressed this point [279, 292, 325–327], the question remains still open, particularly when guest molecules are present. Here we perform a real space analysis of the system in order to get a better picture of the effect of the adsorbates over the structural behavior. As expected, in all cases the bonds of the solid elongate as temperature increases (Figure S5). Therefore a rationalisation of the peculiar TE should be provided by the analysis of the collective behavior.

Using lattice dynamics DFT calculations Zhou et al. [279], found that a number of low energy modes are associated with deformation of BDC ligands [279]. They did not identify them as a likely source of the observed NTE behavior, but they considered the BDC ligands as rigid units, as well as the oxocluster, and only linked the NTE with the junction flexibility. Further understanding was obtained by combining diffraction studies and cluster DFT calculations of the empty framework MOF-5 [326]. They suggested that the motions associated to low energy modes, which are responsible of NTE, are not only linked to the flexibility of connecting junctions, but also to intra-unit (ligand and oxocluster) motions [326]. Since our study comprises periodic MD simulations, which for structural dynamics studies is benefited by the absent of symmetry constrains within the unit cell [94], here we focus on both the junction units and intra-unit deformations, as well as into their relation to the observed complex thermostructural behavior. It is worth noting that this analysis can provide knowledge that will be useful for achieving control of the thermal expansion.

The structure of MOF-5 can be described as a 3-D grid structure, built up by strings that cross the cell, parallel to the axes (dashed blue line, in Figure 7.4.a). There is a degree of flexibility along the rods composing the strings, and it is easy to visualise that the further away the strings of atoms are from a perfect line (a schematic view in Figure 7.4.c,d), the shorter the corresponding cell axis will be. The rods represent the segments between the midpoints of the pair of oxygen atoms of each carboxylate group, and are depicted by blue bars in the schematic view of Figure 7.4.d. More details are given in the Appendix D (Figure D4). In order to quantify the structural changes, we have plotted the ratio between the sum of the length of four rods and the length of the cell axis parallel to each line. We called this value "cell distortion", and it is displayed in Figure 7.5 (top) and in Equation D8. Two different regimes are found: an almost linear increase, at loadings below 80%, and no variation, at higher loadings. The dominant role of the guest-induced pressure over the framework, at higher loadings, is evident from the figure, as the strings tend to expand as much as possible. Deviations from 1.0 are caused by thermal noise. At lower loadings, the collisions of these molecules with the framework are not enough to keep the strings extended. The most relevant effects are, instead, the flexibility of the rods junctions, and the internal deformations of the rods. The collisions play a key role in deforming the lines, as can be inferred by the rise of the line deformation parameter with an increase of temperature (Figure 7.4.c). The ZTE behavior (curves at ca. 60% loadings) is then the result of the compensating effect between the increase of the atomic line deformation, i.e. the relatively smaller geometric line length, and the natural increase

of the length of the bonds.

The central and bottom panels of Figure 7.5 show the relative size of the oxocluster and BDC, with respect to the cell size. The behavior of the oxocluster unit shows a monotonous variation with temperature, it is mostly independent of loading, for the three molecules. However, we observed that the effects of the loading on the shape and size of the BDC unit are radically different. At low loading, the relative distortion of the BDC unit increases with the increase of temperature and at high loadings, the relative distortion decreases. This is related to the ability of the BDC unit to be distorted. This observation is further supported by the analysis of the angle formed by the average points of the oxygen atoms in the carboxylic groups and the carbon atoms in the benzene ring (top panel Figure S7).

One important conclusion arisen from the structural analysis, in connection to the TE, is related to the flexibility of MOFs, particularly to the flexibility and deformations of both, the junctions between molecular units and the units themselves. There is an accepted understanding that flexibility in MOFs can be depicted in a mechanical view, based on the flexibility of the junctions connecting rigid units [328]. However, this mechanical approach fails to explain the flexibility behavior for the isostructural MOFs MIL-47 and MIL-53, being the first rigid and the second flexible [329]. Our results indicate, moreover, that besides the primary source of flexibility associated to the units junctions, the nature of the units is also essential, and the deformations inside the units also contribute to the overall flexibility of the materials. A detailed description of the intra- and inter-units deformations in terms of relevant angles, distances and distortions parameters can be found in the Appendix in the Figures D5, D6 and D7.

In our investigation of routes to control thermal expansion, we have shown that there is a clear connection between adsorbate loading, local and long range distortions, and thermo-structural behavior. We have shown that the material can be regarded as assembled by relatively rigid units, such as the oxoclusters and benzene rings, and by units with some degree of flexibility, such as the fragments composed by the acid groups with the connecting carbon atom from the benzene ring, and flexible junctions. Focusing on the strings of atoms (Figure 7.4.d), a large number of degrees of freedom can be associated to this particular structural motif, although their motions are constrained by the 3-D architecture of the network. In addition, the internal motion of each grid is restricted by the presence of atomic rings and clusters. The NTE thermal behavior of the empty framework can then be easily interpreted in terms of the Rigid Unit Modes (RUM) formalism [323, 330], which supports the presence of cooperative modes. They generate disorder, making the atomic string to deviate more from the ideal line as temperature increases, as can be observed in Figure 7.5 bottom. In presence of adsorbates, host-guest attraction causes a degree of coordination between the movement of the adsorbate molecules and the flexible constituents of the material. This explains the observed behavior: At low loading the adsorbate molecules have large local mobility therefore increasing the NTE coefficients. And at high loading, the average position of the center of mass the adsorbate molecules is rather static due to the lack of available space, consequently ruling out the appearance of cooperative modes responsible of NTE. In the latter case, the close intermolecular distances

provoke rocking motions that result in PTE.

On this basis, it is easy to rationalize why, at low loading, the qualitative behavior of the thermal expansion is similar for a wide range of temperatures. We observe that guest molecules are localized around certain positions, and have negligible impact on the host-host interactions that are associated to the NTE regime. Conversely, at high loading, there are "steric shielding effects" on the thermal expansion behavior, i.e. host-host interactions are seemingly weakened by the high number of guest molecules. From a materials design point of view, we know that long range coulombic interactions can finely modulate the intrinsic TE properties of a MOF [177]. It is known that the charge distribution in a MOF can be tailored by changing the chemical composition [331–335]. For example, in a combined experimental and computational work, it was shown that varying the metal nature in  $M_2(m\text{-dobdc})$  ( $\{M = \text{Mg, Mn, Fe, Co, Ni}\}$  and  $m\text{-dobdc}(4-) = 4,6\text{-dioxido-1,3-benzenedicarboxylate}$ ) MOFs the polarity is systematically changed [331]. On the other hand, we show here that despite the colligative behavior found for the thermo-structural properties, the nature of the molecules influences the change of the cell volume at given loadings. Overall, we advance that exploiting the modulation of TE given by long-range, coulombic interactions, in connection with the guest-assisted control shown in this work, it is possible to achieve a large versatility in controlling the thermal expansion characteristics of the material.

## 7.4. Conclusions

In summary, we devised an approach with which it is possible to create systems with fine-tuned thermal expansion coefficients, thanks to the structural properties of Metal-Organic Frameworks. We found a complex interplay between competing effects, which permits the control of the thermal expansion. The attractive host-guest interactions induce the cell to contract, particularly at low loading. In these conditions, upon an increase of temperature, the thermal disorder increases and thus the coupled host-guest movements largely distort the atomic strings, which reduce the cell parameters, expressed as NTE. With increasing loading, the collisions of the guest molecules to the framework tend to direct the atomic strings to straight lines, and therefore inducing an increase of the cell parameter. At about 60% of loading this effect is not enough yet to produce PTE, which, combined with the natural increase of bond distances, results in ZTE. At higher loadings, the increasing number of collisions leads to significant effects on the framework dynamics, much larger than the volume-reducing effect of the attractive host-guest interactions, so PTE is observed. In summary, we have found a surprising colligative behavior of the system, which determines the thermal expansion of MOF-5, featured by a general behavior that, for these similarly sized molecules, is not particularly dependent on the nature of the adsorbed molecule.



# Conclusions

The **main finding** in this thesis is that it is possible to obtain molecular insights into flexibility of soft nanoporous crystals by descending to atomic level. As we assume in the hypothesis, there is strong interplay between structural changes and sorption and transport properties on nanoporous crystals. Molecular simulation can be an extremely useful tool: calculating and predicting observables which can be compared with experimental findings, to obtain knowledge on the nature of the flexibility of these materials.

The  $\text{Al}^{+3}/\text{Si}^{4+}$  cation distribution has minor impact on the phase transition associated to the flexibility of zeolite RHO. Therefore, pure silica structure provides an initial model for the study of the phase transition between acentric and centric space groups. The role of point charges and atom polarisability is crucial to describe the structural distortion, the volume, cell size and cell shape. The main conclusion in Chapter 3 is that interatomic potentials from molecular mechanics (those that involve an appreciable sort of interactions for bonds, bendings, and torsion) are unable to correctly reproduce the structure because they try to linearise a strictly energetic non-linear problem. The use of a polarisable force field and anharmonic potentials in Chapter 4, like the shell model for instance that stabilises low-symmetry structures, is mandatory for this purpose.

A novel method, based on cycles of the combined use of Monte Carlo, Energy Minimisation and Molecular Dynamics methods, has been proposed for the study of structural changes of high flexible nanoporous materials that are associated to the effect of temperature or guest molecules. The method provides crystallographic-quality structures (0.07-0.2% deviation from experimental values) of zeolite RHO exchanged with different extra-framework cations and different water content. A close relation was found between the polarising power of the extra-framework cations and the effective pore windows. The amount of water also modulates the effective pore windows. By choosing the right combination of extra-framework cations and water content, one can design the size of the effective pore windows for targeted molecular separations.

The  $\text{Ge}^{4+}/\text{Si}^{4+}$  cation distribution has a huge impact on the associated flexibility and stability of STW-type germanosilicate. This is a consequence of the difference in the deformability and size of silicon and germanium tetrahedra. An effective Hamiltonian has been performed to successfully study the colossal number of configurations in the whole compositional range ( $\text{Ge}_f = \text{Ge}/(\text{Ge} + \text{Si}) = 0$  to 1). As the Ge molar fraction increases, the free energy of zeolite goes through a minimum and then severely rise at the  $\text{GeO}_2$  end member. Our modelling of these materials showed the presence of a

complex energy surface with multiple shallow minima which is an explanation of the structural flexibility of the Ge bearing zeolites. Density functional theory calculations of the  $^{19}\text{F}$  chemical shifts of fluoride occluded in every possible configuration of every  $[\text{Si}_{(8-n)}\text{Ge}_n]$  D4R unit (with  $0 \geq n \geq 8$ ) reveals the configurations of every D4R unit which contribute to the experimentally observed four distinct resonances in the  $^{19}\text{F}$  MAS NMR spectra. These resonances are not simply dependent on  $n_{\text{Ge}}$  atoms but also on the extension of Ge pairing. Resonances are assigned to fluoride occluded in D4R with no Ge, with isolated Ge, with Ge pairs or with Ge in closed clusters.

The most common methods for calculating atomic charges of metal organic frameworks are discussed, emphasising the need of the appropriate selection of the method in connection to the intermolecular force field that would be used to compute host-guest interactions. The use of DMOF-1 as model system for the evaluation of different methods for calculating charges shows that careful geometry optimisation is necessary for reliable calculations of the atomic charges. It was also shown that not only molecular adsorption, separation and diffusion are affected by the choice of the charges, but also the structural properties. This is particularly relevant for modelling systems with at least certain degree of flexibility.

A new conceptual design was introduced by predicting the use of MOF as system for controlling thermal expansion. It was shown that by varying the number of molecules within the pores of MOF-5, the thermal expansion coefficient can be tuned to be negative, zero and positive. At low temperature the host-guest interactions dominate and the cell parameters are reduced due to small deformations of the bond angles, while at high temperatures the guest-guest repulsion induced effective pressure on the framework increasing the cell parameters. The analysis of the effect of loading shows that at low values the thermal disorder increases with temperature and thus the coupled host-guest movements largely distort the bond angles, which reduce the cell parameters, expressed as negative thermal expansion. With increasing loading, the collisions of guest molecules with the framework tend to enlarge the angles, and therefore inducing an increase of the cell parameter. At about 60% of loading this effect is not enough yet to produce positive thermal expansion. This, combined with the natural increase of bond distances, results in zero thermal expansion. At higher loadings, the increasing number of collisions leads to significant effects on the framework dynamics, much larger than the volume-reducing effect of the attractive host-guest interactions, so positive thermal expansion is observed. It was found a surprising colligative behaviour of the system, which determines the thermal expansion of MOF-5, featured by a general behaviour that is not particularly dependent on the nature of the adsorbed molecule that are similar in size.

# Conclusiones

La **principal conclusión** de esta tesis es que es posible obtener una visión molecular de la flexibilidad de cristales blandos nanoporosos al descender a un nivel atómico. Como suponemos en la hipótesis, existe una fuerte interacción entre los cambios estructurales y las propiedades de adsorción y transporte en cristales nanoporosos: cada fenómeno actúa retroalimentando, positiva o negativamente, a los otros fenómenos. La simulación molecular ha sido una herramienta extremadamente útil de esta manera: el cálculo y la predicción de observables contrastables con los hallazgos experimentales, con el fin de obtener un conocimiento más profundo de la naturaleza de la flexibilidad de estos materiales.

La distribución de Si/Al tiene un impacto menor en la transición de fase asociada a la flexibilidad de la zeolita RHO de lo supuesto inicialmente. Por tanto, el material pura sílice proporciona un modelo inicial para el estudio de la transición de fase entre los grupos espaciales acéntricos y céntricos. El papel de las cargas y la polarizabilidad del átomo es crucial para describir estas distorsiones estructurales, cambios de volumen, y los tamaños y formas de la celda unidad. La principal conclusión en el Capítulo 3 es que los potenciales interatómicos que provienen de la mecánica molecular (aquellos que implican un número apreciable de interacciones para enlaces, flexiones y torsiones) no pueden reproducir correctamente la estructura porque intentan linealizar un problema energético estrictamente no lineal. El uso de un potencial interatómico polarizable en el Capítulo 4, como el modelo de núcleo–corteza, estabiliza las estructuras de baja simetría y es obligatorio para este tipo de cálculos.

Se ha propuesto un método basado en ciclos combinados de métodos Monte Carlo, minimizaciones energéticas y dinámicas moleculares para el estudio de los cambios estructurales que ocurren en materiales nanoporosos altamente flexibles asociados al efecto de la temperatura o adsorbatos. Este método proporciona estructuras de alta calidad cristalográfica (desviaciones del 0.07-0.2 % respecto a valores experimentales) de la zeolita tipo RHO intercambiada con diferentes cationes libres y diferente contenido de agua. Se encontró una relación entre el poder de polarización de los cationes libre y la apertura de las ventanas del poro. La cantidad de agua también modula la apertura de las ventanas. Eligiendo una combinación específica de cationes libres y contenido de agua, es posible diseñar y modular la apertura de estas ventanas para una separación molecular específica.

La distribución de cationes  $\text{Ge}^{4+}/\text{Si}^{4+}$  tiene un impacto importante en la estabilidad y flexibilidad asociada de las zeolitas tipo STW. Esto es una consecuencia de la diferente deformabilidad y tamaño de los tetraedros de germanio y silicio. Un hamiltoniano efectivo fue desarrollado y diseñado con éxito para estudiar el enorme número

de configuraciones en todo el intervalo de fracciones molares ( $Ge_f = Ge/(Ge+Si) =$  de 0 a 1). A medida que la fracción molar de Ge aumenta, la energía libre desciende a un mínimo y luego aumenta súbitamente hasta la composición pura de Ge. Nuestro estudio de modelización ha mostrado la compleja presencia de múltiples mínimos poco profundos en la hipersuperficie de energía, lo cual es una explicación de la flexibilidad estructural de las zeolitas que contienen germanio. Cálculos DFT de los desplazamientos químicos del  $^{19}F$  para los átomos de fluor atrapados en todas las posibles configuraciones de D4R con  $[Si_{(8-n)}Ge_n]$  (siendo  $0 \geq n \geq 8$ ) revelaron las configuraciones que contribuyen a los cuatro tipos de resonancias detectadas experimentalmente en el espectro de  $^{19}F$  MAS NMR. Estas resonancias no dependen simplemente del número de Ge si no también de cómo están distribuidos en el D4R. Las resonancias son asignadas a átomos de fluor ocluidos en D4R sin Ge, con Ge aislados, con Ge conectados como primeros vecinos y Ge formando clústers.

Se discuten los métodos más comunes para calcular las cargas atómicas de las estructuras metalorgánicas, haciendo especial énfasis en la selección correcta del método de cálculo, relacionándolo con el campo de fuerza intermolecular que se usaría para calcular las interacciones adsorbato–adsorbente. El uso de DMOF-1 como modelo para la evaluación de diferentes métodos de cálculo de cargas eléctricas muestra que la optimización de geometría es necesaria para obtener un resultado fiable cargas atómicas obtenidas. También se demostró que, no solo la adsorción molecular, la separación y la difusión se ven afectadas por la elección de las cargas, sino también las propiedades estructurales, lo que es particularmente relevante para sistemas de modelado con cierto grado de flexibilidad.

Se presenta un nuevo diseño conceptual al predecir el uso de MOFs como sistema para controlar la expansión térmica. Se demuestra que, variando el número de moléculas dentro de los poros de MOF-5, el coeficiente de expansión térmica puede ajustarse para ser negativo, cero y positivo. A baja temperatura, las interacciones adsorbente–adsorbato dominan y los parámetros de la célula se reducen debido a pequeñas deformaciones de los ángulos de enlace (principalmente en las juntas entre nodos y ligandos del framework), mientras que a altas temperaturas la presión molecular efectiva inducida por el adsorbato sobre los ligandos de la estructura da como resultado un aumento de los parámetros de la célula. El análisis sobre el efecto que tiene la cantidad adsorbida de moléculas muestra que a valores bajos, aumentando la temperatura, el desorden atómico aumenta y, por tanto, el acoplamiento adsorbato–adsorbente distorsiona cierto enlaces y ángulos que permiten crear fonones capaces de mover el clúster y el anillo aromático como unidades rígidas sin deformarlas), lo que se expresa en una expansión térmica negativa. A medida que aumenta el número de moléculas adsorbidas, las colisiones de éstas con la estructura y, más concretamente, con los ligandos, destruyen estos modos de vibración induciendo un aumento del parámetro de celda. Aproximadamente al 60% de la saturación en la adsorción, este efecto todavía no es suficiente para generar una expansión térmica positiva, pero que, combinado con el aumento natural de las distancias de enlace al aumentar la temperatura, sí generan una expansión térmica nula. A mayor número de adsorbato, el aumento de las colisiones produce efectos significativos en la dinámica de la estructura, superan-

do al efecto de la reducción de volumen provocado por las interacciones atractivas adsorbato-adsorbente, y expresándose en una expansión térmica positiva. Se encontró un sorprendente comportamiento coligativo del sistema: el comportamiento general de expansión térmica de MOF-5 no depende de la naturaleza de las moléculas si no sólo de su tamaño.



# Bibliography

- [1] S. Horike, S. Shimomura and S. Kitagawa. "Soft porous crystals". *Nat. Chem.* 1, 695–704, **2009**. DOI: 10.1038/nchem.444. (Cit. on pp. 9, 14).
- [2] W. H. Taylor. "The structure of analcite (NaAlSi<sub>2</sub>O<sub>6</sub>H<sub>2</sub>O)". *Zeitschrift für Kristallographie - Crystalline Materials* 74, 1–19, **1930**. DOI: 10.1524/zkri.1930.74.1.1. (Cit. on p. 9).
- [3] L. Pauling. "The structure of some sodium and calcium aluminosilicates". *Proc. Natl. Acad. Sci. U.S.A.* 16, 453–459, **1930**. ISSN: 0027-8424. (Cit. on p. 9).
- [4] W. L. Bragg. "The Structure of Silicates". *Nature* 125, 510–511, **1930**. DOI: 10.1038/125510a0. (Cit. on p. 9).
- [5] W. H. Taylor. "The Nature and Properties of Aluminosilicate Framework Structures". *Proceedings of the Royal Society A: Mathematical, Physical and Engineering Sciences* 145, 80–103, **1934**. DOI: 10.1098/rspa.1934.0083. (Cit. on p. 9).
- [6] C. Baerlocher, L. B. McCusker and D. H. Olson. *Atlas of zeolite framework types*. Elsevier, 2007. (Cit. on p. 9).
- [7] W. Loewenstein. "The distribution of aluminum in the tetrahedra of silicates and aluminates". *Am. Mineral.* 39, 92–96, **1954**. (Cit. on pp. 11, 57).
- [8] E. Dempsey, G. H. Kuehl and D. H. Olson. "Variation of the lattice parameter with aluminum content in synthetic sodium faujasites. Evidence for ordering of the framework ions". *J. Phys. Chem.* 73, 387–390, **1969**. DOI: 10.1021/j100722a020. (Cit. on pp. 11, 55).
- [9] D. H. Olson and P. T. Reischman. "Structure-related paraffin sorption in ZSM-5". *Zeolites* 17, 434–436, **1996**. DOI: 10.1016/s0144-2449(96)00087-5. (Cit. on p. 11).
- [10] O. M. Yaghi and H. Li. "Hydrothermal Synthesis of a Metal-Organic Framework Containing Large Rectangular Channels". *J. Am. Chem. Soc.* 117, 10401–10402, **1995**. DOI: 10.1021/ja00146a033. (Cit. on p. 11).
- [11] H. Li, M. Eddaoudi, M. O’Keeffe and O. M. Yaghi. "Design and synthesis of an exceptionally stable and highly porous metal-organic framework". *Nature* 402, 276–279, **1999**. (Cit. on pp. 11, 105, 110).
- [12] S. S. Chui. "A Chemically Functionalizable Nanoporous Material [Cu<sub>3</sub>(TMA)2(H<sub>2</sub>O)3]n". *Science* 283, 1148–1150, **1999**. DOI: 10.1126/science.283.5405.1148. (Cit. on p. 11).
- [13] S. Kitagawa and R. Matsuda. "Chemistry of coordination space of porous coordination polymers". *Coord. Chem. Rev.* 251, 2490–2509, **2007**. DOI: 10.1016/j.ccr.2007.07.009. (Cit. on p. 11).
- [14] H. Furukawa, K. E. Cordova, M. O. Koeffe and O. M. Yaghi. "The Chemistry and Applications of Metal-Organic Frameworks". *Science* 341, 1230444–1230444, **2013**. DOI: 10.1126/science.1230444. (Cit. on p. 13).
- [15] E. Verheyen, L. Joos, C. Martineau, C. J. Dawson, C. Weidenthaler, W. Schmidt, R. Yuan, E. Breynaert, V. V. Speybroeck, M. Waroquier, F. Taulelle, M. M. J. Treacy, J. A. Martens and C. E. A. Kirschhock. "Flexibility versus rigidity: what determines the stability of zeolite frameworks? A case study". *Mater. Horiz.* 1, 582–587, **2014**. DOI: 10.1039/c4mh00127c. (Cit. on pp. 14, 81).
- [16] A. Schneemann, V. Bon, I. Schwedler, I. Senkovska, S. Kaskel and R. A. Fischer. "Flexible metal-organic frameworks". *Chem. Soc. Rev.* 43, 6062–6096, **2014**. DOI: 10.1039/c4cs00101j. (Cit. on pp. 14, 15).
- [17] A. Schneemann, P. Vervoorts, I. Hante, M. Tu, S. Wannapaiboon, C. Sternemann, M. Paulus, D. C. F. Wieland, S. Henke and R. A. Fischer. "Different Breathing Mechanisms in Flexible Pillared-Layered Metal-Organic Frameworks: Impact of the Metal Center". *Chemistry of Materials*, **2018**. DOI: 10.1021/acs.chemmater.7b05052. (Cit. on p. 14).

- [18] C. R. A. Catlow, V. Van Speybroeck and R. van Santen. *Modelling and Simulation in the Science of Micro-and Meso-porous Materials*. Elsevier, 2017. (Cit. on p. 14).
- [19] A. Boutin, F.-X. Coudert, M.-A. Springuel-Huet, A. V. Neimark, G. Férey and A. H. Fuchs. “The behavior of flexible MIL-53 (Al) upon CH<sub>4</sub> and CO<sub>2</sub> adsorption”. *J. Phys. Chem. C* 114, 22237–22244, **2010**. (Cit. on pp. 15, 104).
- [20] L. Vanduyfhuys, T. Verstraelen, M. Vandichel, M. Waroquier and V. V. Speybroeck. “Ab Initio Parametrized Force Field for the Flexible Metal-Organic Framework MIL-53(Al)”. *J. Chem. Theory Comput.* 8, 3217–3231, **2012**. DOI: 10.1021/ct300172m. (Cit. on pp. 15, 21, 93, 95).
- [21] N. A. Ramsahye, G. Maurin, S. Bourrelly, P. Llewellyn, T. Loiseau and G. Férey. “Charge distribution in metal organic framework materials: transferability to a preliminary molecular simulation study of the CO<sub>2</sub> adsorption in the MIL-53 (Al) system”. *Phys. Chem. Chem. Phys.* 9, 1059–1063, **2007**. DOI: 10.1039/b613378a. (Cit. on pp. 15, 91, 95).
- [22] J. S. Grosch and F. Paesani. “Molecular-Level Characterization of the Breathing Behavior of the Jungle-Gym-type DMOF-1 Metal-Organic Framework”. *J. Am. Chem. Soc.* 134, 4207–4215, **2012**. DOI: 10.1021/ja2100615. (Cit. on pp. 15, 95).
- [23] J.-P. Zhang, H.-L. Zhou, D.-D. Zhou, P.-Q. Liao and X.-M. Chen. “Controlling flexibility of metal-organic frameworks”. *National Science Review*, **2017**. DOI: 10.1093/nsr/nwx127. (Cit. on p. 15).
- [24] F. R. Gantmakher. *Lectures in analytical mechanics*. Mir, URSS Ed., 1970. (Cit. on pp. 17, 20).
- [25] H. Goldstein. *Mecánica Clásica*. Reverté, 1987. ISBN: 978-84-291-4306-5. (Cit. on p. 17).
- [26] D. Chandler. *Introduction to modern statistical mechanics*. 1. Oxford University Press, 1987. ISBN: 978-0-19-504277-1. (Cit. on pp. 17, 59).
- [27] M. E. Tuckerman, Y. Liu, G. Ciccotti and G. J. Martyna. “Non-Hamiltonian molecular dynamics: Generalizing Hamiltonian phase space principles to non-Hamiltonian systems”. *J. Chem. Phys.* 115, 1678–1702, **2001**. (Cit. on pp. 17, 20, 39).
- [28] J. J. Brey, J. de la Rubia Pacheco and J. de la Rubia Sánchez. *Mecánica estadística*. Universidad Nacional de Educación a Distancia, 2001. ISBN: 84-362-4572-5. (Cit. on p. 20).
- [29] H. Chalmers. *Non-Euclidean Geometry*. Miskatonic University Press, 1922. (Cit. on p. 20).
- [30] S. Mayo, B. Olafson and W. Goddard. “DREIDING: a generic force field for molecular simulations”. *J. Phys. Chem.* 94, 8897, **1990**. (Cit. on pp. 21, 88).
- [31] A. K. Rappé, C. J. Casewit, K. Colwell, W. Goddard III and W. Skiff. “UFF, a full periodic table force field for molecular mechanics and molecular dynamics simulations”. *J. Am. Chem. Soc.* 114, 10024–10035, **1992**. (Cit. on pp. 21, 88, 106).
- [32] W. L. Jorgensen and J. Tirado-Rives. “The OPLS [optimized potentials for liquid simulations] potential functions for proteins, energy minimizations for crystals of cyclic peptides and crambin”. *J. Am. Chem. Soc.* 110, 1657–1666, **1988**. (Cit. on pp. 21, 88, 106).
- [33] M. Martin and J. Siepmann. “Transferable potentials for phase equilibria. 1. United-atom description of n-alkanes”. *J. Phys. Chem. B* 102, 2569, **1998**. (Cit. on pp. 21, 88).
- [34] B. Chen and J. Siepmann. “Transferable potentials for phase equilibria. 3. Explicit-hydrogen description of normal alkanes”. *J. Phys. Chem. B* 103, 5370, **1999**. (Cit. on pp. 21, 88).
- [35] S. JM, P. JJ and S. JI. “Transferable potentials for phase equilibria. 6. United-atom description for ethers, glycols, ketones, and aldehydes”. *J. Phys. Chem. B* 108, 17596, **2004**. (Cit. on pp. 21, 88).
- [36] M. Martin and J. Siepmann. “Novel configurational-bias Monte Carlo method for branched molecules. Transferable potentials for phase equilibria. 2. United-atom description of branched alkanes”. *J.*

- Phys. Chem. B* 103, 4508, **1999**. (Cit. on pp. 21, 88).
- [37] W. Cornell, P. Cieplak, C. Bayly, I. Gould, K. Merz, D. Ferguson, D. Spellmeyer, T. Fox, J. Caldwell and P. Kollman. "A second generation force field for the simulation of proteins, nucleic acids and organic molecules". *J. Am. Chem. Soc.* 117, 5179, **1992**. (Cit. on pp. 21, 88).
- [38] M. J. Sanders, M. Leslie and C. R. A. Catlow. "Interatomic potentials for SiO<sub>2</sub>". *J. Chem. Soc., Chem. Commun.* 1271–1273, **1984**. DOI: 10.1039/C39840001271. (Cit. on pp. 21, 55).
- [39] R. A. Jackson, R. G. Bell and C. R. Catlow. "Computer Simulation Studies of Zeolite Structure and Stability". In: *Recent Advances in Zeolite Science Proceedings of the 1989 Meeting of the British Zeolite Association*. Ed. by J. Klinowski and P. J. Barrie. 52. Studies in Surface Science and Catalysis. Elsevier, 1989. 203–208. (Cit. on pp. 21, 55).
- [40] R. A. Jackson and C. R. A. Catlow. "Computer Simulation Studies of Zeolite Structure". *Mol. Simul.* 1, 207–224, **1988**. DOI: 10.1080/08927028808080944. (Cit. on pp. 21, 55).
- [41] J. Kučera and P. Nachtigall. "Coordination of alkali metal ions in ZSM-5: A combined quantum mechanics/interatomic potential function study". *Phys. Chem. Chem. Phys.* 5, 3311–3317, **2003**. (Cit. on pp. 21, 55).
- [42] D. Dubbeldam, K. S. Walton, D. E. Ellis and R. Q. Snurr. "Exceptional negative thermal expansion in isorecticular metal–organic frameworks". *Angew. Chem. Int. Edn.* 119, 4580–4583, **2007**. DOI: 10.1002/ange.200700218. (Cit. on pp. 21, 99, 104–107, 111, 113).
- [43] F. M. Higgins, N. H. de Leeuw and S. C. Parker. "Modelling the effect of water on cation exchange in zeolite A". *J. Mater. Chem.* 12, 124–131, **2001**. DOI: 10.1039/b104069n. (Cit. on pp. 21, 56).
- [44] L. Jansen, L. Chandran and R. Block. "On the concept of "bond valence sums" and its applicability in solid state chemistry and physics". *Journal of Molecular Structure: THEOCHEM* 260, 81–98, **1992**. DOI: 10.1016/0166-1280(92)87036-y. (Cit. on p. 21).
- [45] V. S. Urusov. "Semi-empirical groundwork of the bond-valence model". *Acta Crystallographica Section B Structural Science* 51, 641–649, **1995**. DOI: 10.1107/S0108768195003417. (Cit. on pp. 21, 22).
- [46] P. P. Ewald. "Die Berechnung optischer und elektrostatischer Gitterpotentiale". *Ann. Phys.* 369, 253–287, **1921**. (Cit. on pp. 22, 57, 77, 106).
- [47] A. Aguado and P. Madden. "Ewald summation of electrostatic multipole interactions up to the quadrupolar level". *J. Chem. Phys.* 119, 7471, **2003**. (Cit. on p. 22).
- [48] D. Adams. "On the use of the Ewald summation in computer-simulation". *J. Chem. Phys.* 78, 2585, **1983**. (Cit. on pp. 22, 57).
- [49] F. London. "Zur Theorie und Systematik der Molekularkräfte". *Zeitschrift für Physik* 63, 245–279, **1930**. ISSN: 0044-3328. DOI: 10.1007/BF01421741. (Cit. on p. 22).
- [50] B. G. Dick and A. W. Overhauser. "Theory of the Dielectric Constants of Alkali Halide Crystals". *Phys. Rev.* 112, 90–103, **1958**. DOI: 10.1103/physrev.112.90. (Cit. on p. 25).
- [51] D. Frenkel and B. Smit. "Understanding Molecular Simulation. Academic Press". San Diego, **1996**. (Cit. on pp. 27, 33, 56, 59, 107).
- [52] G. L. Martyna, D. J. Tobias and M. L. Klein. "Constant pressure molecular dynamics algorithms". *J. Chem. Phys.* 101, 4177, **1994**. (Cit. on pp. 28, 39, 107).
- [53] M. E. Tuckerman, J. Alejandre, R. López-Rendón, A. L. Jochim and G. J. Martyna. "A Liouville-operator derived measure-preserving integrator for molecular dynamics simulations in the isothermal-isobaric ensemble". *J. Phys. A: Math. Gen.* 39, 5629–5651, **2006**. (Cit. on pp. 28, 39, 107).
- [54] D. Dubbeldam, D. C. Ford, D. E. Ellis and R. Q. Snurr. "A new perspective on the order-n-algorithm for computing correlation functions". *Mol. Simul.* 35, 1084–1097, **2009**. DOI: 10.1080/08927020902818039. (Cit. on p. 28).
- [55] D. Dubbeldam, S. Calero, D. E. Ellis and R. Q. Snurr. "RASPA: molecular simulation software for adsorption and diffusion in flexible nanoporous materials". *Mol. Simul.* 0, 1–21, **0**. DOI: 10.1080/08927022.2015.1010082. (Cit. on pp. 28, 31, 56, 99, 106).

- [56] D. Sheppard, R. Terrell and G. Henkelman. "Optimization methods for finding minimum energy paths". *J. Chem. Phys.* 128, 134106, **2008**. DOI: 10 . 1063 / 1 . 2841941. (Cit. on p. 29).
- [57] W. H. Press, S. A. Teukolsky, W. T. Vetterling and B. P. Flannery. *Numerical Recipes in Fortran 90 (2Nd Ed.): The Art of Parallel Scientific Computing*. New York, NY, USA: Cambridge University Press, 1996. ISBN: 0-521-57439-0. (Cit. on p. 29).
- [58] E. Polak and G. Ribière. "Note sur la convergence de méthodes de directions conjuguées". *Revue française d'informatique et de recherche opérationnelle, série rouge* 3, 35–43, **1969**. (Cit. on p. 30).
- [59] J. Nocedal and S. J. Wright. *Numerical optimization 2nd*. 2006 (cit. on p. 30).
- [60] R. H. Byrd, J. C. Gilbert and J. Nocedal. "A trust region method based on interior point techniques for nonlinear programming". *Math. Program.* 89, 149–185, **2000**. DOI: 10.1007/s100011391. (Cit. on p. 30).
- [61] J. D. Gale and A. L. Rohl. "The General Utility Lattice Program (GULP)". *Mol. Simul.* 29, 291–341, **2003**. DOI: 10.1080/0892702031000104887. (Cit. on pp. 30, 31, 56).
- [62] J. Baker. "An algorithm for the location of transition states". *J. Comput. Chem.* 7, 385–395, **1986**. ISSN: 1096-987X. DOI: 10.1002/jcc.540070402. (Cit. on pp. 30, 39).
- [63] A. Banerjee, N. Adams, J. Simons and R. Shepard. "Search for stationary points on surfaces". *J. Phys. Chem.* 89, 52–57, **1985**. DOI: 10 . 1021 / j100247a015. (Cit. on p. 30).
- [64] D. Dubbeldam, R. Krishna and R. Q. Snurr. "Method for Analyzing Structural Changes of Flexible Metal-Organic Frameworks Induced by Adsorbates". *J. Phys. Chem. C* 113, 19317–19327, **2009**. DOI: 10.1021/jp906635f. (Cit. on p. 31).
- [65] S. Plimpton. "Fast Parallel Algorithms for Short-Range Molecular Dynamics". *J. Comput. Phys.* 117, 1–19, **1995**. DOI: 10.1006/jcph.1995.1039. (Cit. on p. 31).
- [66] V. Fock. "Näherungsmethode zur Lösung des quantenmechanischen Mehrkörperproblems". *Zeitschrift für Physik* 61, 126–148, **1930**. (Cit. on p. 31).
- [67] D. Hartree. "DR Hartree and W. Hartree, Proc. Roy. Soc.(London) A149, 210 (1935)". In: *Proc. Roy. Soc.(London)*. 149. 1935. 210. (Cit. on p. 31).
- [68] J. C. Slater. "Note on Hartree's Method". *Phys. Rev.* 35, 210–211, **1930**. DOI: 10 . 1103/physrev.35.210.2. (Cit. on p. 31).
- [69] J. C. Slater. "A Simplification of the Hartree-Fock Method". *Phys. Rev.* 81, 385–390, **1951**. DOI: 10 . 1103/physrev.81.385. (Cit. on p. 31).
- [70] J. Thijssen. *Computer Physics*. 1999 (cit. on p. 31).
- [71] P. Hohenberg and W. Kohn. "Inhomogeneous Electron Gas". *Phys. Rev.* 136, B864–B871, **1964**. DOI: 10.1103/physrev.136.b864. (Cit. on p. 31).
- [72] J. P. Perdew, K. Burke and M. Ernzerhof. "Generalized Gradient Approximation Made Simple". *Phys. Rev. Lett.* 77, 3865–3868, **1996**. DOI: 10.1103/PhysRevLett.77.3865. (Cit. on pp. 32, 97).
- [73] S. Grimme, J. Antony, S. Ehrlich and H. Krieg. "A consistent and accurate *ab initio* parametrization of density functional dispersion correction (DFT-D) for the 94 elements H-Pu". *J. Chem. Phys.* 132, 154104, **2010**. DOI: 10.1063/1.3382344. (Cit. on p. 32).
- [74] N. Metropolis, A. W. Rosenbluth, M. N. Rosenbluth, A. H. Teller and E. Teller. "Equation of State Calculations by Fast Computing Machines". *J. Chem. Phys.* 21, 1087–1092, **1953**. DOI: 10 . 1063 / 1 . 1699114. (Cit. on p. 32).
- [75] D.-Y. Peng and D. B. Robinson. "A New Two-Constant Equation of State". *Ind. Eng. Chem. Fundamen.* 15, 59–64, **1976**. DOI: 10.1021/i1600057a011. (Cit. on p. 34).
- [76] S. R. G. Balestra, J. J. Gutierrez-Sevillano, P. J. Merklings, D. Dubbeldam and S. Calero. "Simulation Study of Structural Changes in Zeolite RHO". *J. Phys. Chem. C* 117, 11592–11599, **2013**. DOI: 10 . 1021 / jp4026283. (Cit. on pp. 37, 54, 187).
- [77] V. Kapko, C. Dawson, M. M. J. Treacy and M. F. Thorpe. "Flexibility of ideal zeolite frameworks". *Phys. Chem. Chem. Phys.* 12, 8531–8541, **2010**. (Cit. on p. 38).

- [78] D. R. Corbin, L. Abrams, G. A. Jones, M. M. Eddy, W. T. A. Harrison, G. D. Stucky and D. E. Cox. "Flexibility of the zeolite RHO framework: in situ x-ray and neutron powder structural characterization of divalent cation-exchanged zeolite RHO". *J. Am. Chem. Soc.* 112, 4821–4830, **1990**. (Cit. on p. 38).
- [79] J. B. Parise and D. E. Cox. "Structural changes occurring upon dehydration of zeolite Rho. A study using neutron powder diffraction and distance-least-squares structural modeling". *J. Phys. Chem.* 88, 1635–1640, **1984**. (Cit. on p. 38).
- [80] J. B. Parise, L. Abrams, T. E. Gier, D. R. Corbin, J. D. Jorgensen and E. Prince. "Flexibility of the framework of zeolite Rho. Structural variation from 11 to 573 K. A study using neutron powder diffraction data". *J. Phys. Chem.* 88, 2303–2307, **1984**. (Cit. on pp. 38, 41, 53, 54).
- [81] Y. Lee, J. A. Hriljac, T. Vogt, J. B. Parise, M. J. Edmondson, P. A. Anderson, D. R. Corbin and T. Nagai. "Phase Transition of Zeolite RHO at High-Pressure". *J. Am. Chem. Soc.* 123, 8418–8419, **2001**. (Cit. on pp. 38, 44).
- [82] J. B. Parise and E. Prince. "The structure of cesium-exchanged zeolite-RhO at 293K and 493K determined from high resolution neutron powder data". *Mater. Res. Bull.* 18, 841–852, **1983**. ISSN: 0025-5408. (Cit. on pp. 38, 44).
- [83] J. B. Nicholas, A. J. Hopfinger, F. R. Trouw and L. E. Iton. "Molecular modeling of zeolite structure. 2. Structure and dynamics of silica sodalite and silicate force field". *J. Am. Chem. Soc.* 113, 4792–4800, **1991**. (Cit. on pp. 38, 39, 44, 47, 48).
- [84] J. R. Hill and J. Sauer. "Molecular mechanics potential for silica and zeolite catalysts based on ab initio calculations. 1. Dense and microporous silica". *J. Phys. Chem.* 98, 1238–1244, **1994**. (Cit. on pp. 38, 48).
- [85] J. R. Hill and J. Sauer. "Molecular Mechanics Potential for Silica and Zeolite Catalysts Based on ab Initio Calculations. 2. Aluminosilicates". *J. Phys. Chem.* 99, 9536–9550, **1995**. (Cit. on pp. 38, 47, 48).
- [86] P. Demontis, G. B. Suffritti, S. Quartieri, E. S. Fois and A. Gamba. "Molecular dynamics studies on zeolites. 3. Dehydrated zeolite A". *J. Phys. Chem.* 92, 867–871, **1988**. DOI: 10.1021/j100315a003. (Cit. on pp. 38, 47).
- [87] K.-P. Schröder and J. Sauer. "Potential Functions for Silica and Zeolite Catalysts Based on ab Initio Calculations. 3. A Shell Model Ion Pair Potential for Silica and Aluminosilicates". *J. Phys. Chem.* 100, 11043–11049, **1996**. (Cit. on pp. 38, 47, 48).
- [88] R. Bueno-Perez, S. Calero, D. David, C. O. Ania, J. B. Parra, A. P. Zaderenko and P. J. Merkling. "Zeolite Force Fields and Experimental Siliceous Frameworks in a Comparative Infrared Study". *J. Phys. Chem. C* 116, 25797–25805, **2012**. (Cit. on p. 39).
- [89] M. Palomino, A. Corma, J. L. Jorda, F. Rey and S. Valencia. "Zeolite Rho: a highly selective adsorbent for CO<sub>2</sub>/CH<sub>4</sub> separation induced by a structural phase modification". *Chem. Commun.* 48, 215–217, **2012**. (Cit. on pp. 39, 40, 42, 43).
- [90] M. Parrinello and A. Rahman. "Polymorphic transitions in single crystals: A new molecular dynamics method". *J. Appl. Phys.* 52, 7182–7190, **1981**. DOI: 10.1063/1.328693. (Cit. on pp. 39, 57).
- [91] W. Miller, C. W. Smith, D. S. Mackenzie and K. E. Evans. "Negative thermal expansion: a review". *J. Mater. Sci.* 44, 5441–5451, **2009**. DOI: 10.1007/s10853-009-3692-4. (Cit. on p. 41).
- [92] T. Carey, A. Corma, F. Rey, C. C. Tang, J. A. Hriljac and P. A. Anderson. "The effect of extra framework species on the intrinsic negative thermal expansion property of zeolites with the LTA topology". *Chem. Commun.* 48, 5829–5831, **2012**. DOI: 10.1039/C2CC30582H. (Cit. on p. 42).
- [93] A. García-Sánchez, C. O. Ania, J. B. Parra, D. Dubbeldam, T. J. H. Vlught, R. Krishna and S. Calero. "Transferable Force Field for Carbon Dioxide Adsorption in Zeolites". *J. Phys. Chem. C* 113, 8814–8820, **2009**. (Cit. on p. 45).
- [94] S. R. G. Balestra, S. Hamad, A. R. Ruiz-Salvador, V. Domínguez-García, P. J. Merkling, D. Dubbeldam and S. Calero. "Understanding Nanopore Window Distortions in the Reversible Molecular Valve

- Zeolite RHO". *Chem. Mater.* 27, 5657–5667, **2015**. DOI: 10.1021/acs.chemmater.5b02103. arXiv: 1605.06338. (Cit. on pp. 51, 77, 113, 187).
- [95] H. Meng, M. Xue, T. Xia, Y.-L. Zhao, F. Tamanoi, J. F. Stoddart, J. I. Zink and A. E. Nel. "Autonomous in Vitro Anticancer Drug Release from Mesoporous Silica Nanoparticles by pH-Sensitive Nanovalves". *J. Am. Chem. Soc.* 132, 12690–12697, **2010**. DOI: 10.1021/ja104501a. (Cit. on p. 52).
- [96] Y.-W. Yang. "Towards biocompatible nanovalves based on mesoporous silica nanoparticles". *Med. Chem. Commun.* 2, 1033–1049, **2011**. DOI: 10.1039/C1MD00158B. (Cit. on p. 52).
- [97] Q. Yuan, Y. Zhang, T. Chen, D. Lu, Z. Zhao, X. Zhang, Z. Li, C.-H. Yan and W. Tan. "Photon-Manipulated Drug Release from a Mesoporous Nanocontainer Controlled by Azobenzene-Modified Nucleic Acid". *ACS Nano* 6, 6337–6344, **2012**. DOI: 10.1021/nl3018365. (Cit. on p. 52).
- [98] A. Bernardos, L. Mondragón, E. Aznar, M. D. Marcos, R. Martínez-Máñez, F. San- cenón, J. Soto, J. M. Barat, E. Pérez-Payá, C. Guillem and P. Amorós. "Enzyme-Responsive Intracellular Controlled Release Using Nanometric Silica Mesoporous Supports Capped with Saccharides". *ACS Nano* 4, 6353–6368, **2010**. DOI: 10.1021/nn101499d. (Cit. on p. 52).
- [99] S. M. Kuznicki, V. A. Bell, S. Nair, H. W. Hillhouse, R. M. Jacubinas, C. M. Braunbarth, B. H. Toby and M. Tsapatsis. "A titanosilicate molecular sieve with adjustable pores for size-selective adsorption of molecules". *Nature* 412, 720–724, **2001**. DOI: 10.1038/35089052. (Cit. on p. 53).
- [100] D. R. Corbin, L. Abrams, G. A. Jones, M. M. Eddy, W. T. A. Harrison, G. D. Stucky and D. E. Cox. "Flexibility of the zeolite RHO framework: in situ x-ray and neutron powder structural characterization of divalent cation-exchanged zeolite RHO". *J. Am. Chem. Soc.* 112, 4821–4830, **1990**. (Cit. on pp. 53, 54, 61, 65).
- [101] J. B. Parise, X. Liu and D. R. Corbin. "Flexibility of the zeolite RHO framework; relocation of cadmium accompanying transformation of the unit cell at high temperatures". *J. Chem. Soc., Chem. Commun.* 162–163, **1991**. DOI: 10.1039/C39910000162. (Cit. on pp. 53, 61, 63).
- [102] B. A. Reisner, Y. Lee, J. C. Hanson, G. A. Jones, J. B. Parise, D. R. Corbin, B. H. Toby, A. Freitag, J. Z. Larese and V. Kahlenberg. "Understanding negative thermal expansion and 'trap door' cation relocations in zeolite rho". *Chem. Commun.* 2221–2222, **2000**. DOI: 10.1039/B006929I. (Cit. on pp. 53, 55, 61).
- [103] J. B. Parise and D. E. Cox. "Structural changes occurring upon dehydration of zeolite Rho. A study using neutron powder diffraction and distance-least-squares structural modeling". *J. Phys. Chem.* 88, 1635–1640, **1984**. (Cit. on pp. 53, 54, 63, 67).
- [104] Y. Lee, J. A. Hriljac, T. Vogt, J. B. Parise, M. J. Edmondson, P. A. Anderson, D. R. Corbin and T. Nagai. "Phase Transition of Zeolite RHO at High-Pressure". *J. Am. Chem. Soc.* 123, 8418–8419, **2001**. (Cit. on p. 53).
- [105] M. Palomino, A. Corma, J. L. Jorda, F. Rey and S. Valencia. "Zeolite Rho: a highly selective adsorbent for CO<sub>2</sub>/CH<sub>4</sub> separation induced by a structural phase modification". *Chem. Commun.* 48, 215–217, **2012**. (Cit. on pp. 53, 61, 63, 67).
- [106] M. Lozinska, E. Mangano, J. Mowat, A. Shepherd, R. Howe, S. Thompson, J. Parker, S. Brandani and P. Wright. "Understanding Carbon Dioxide Adsorption on Univalent Cation Forms of the Flexible Zeolite Rho at Conditions Relevant to Carbon Capture from Flue Gases". *J. Am. Chem. Soc.* 134, 17628–17642, **2012**. ISSN: 0002-7863. (Cit. on pp. 53, 61, 65, 66).
- [107] J. B. Parise and E. Prince. "The structure of cesium-exchanged zeolite-RhO at 293K and 493K determined from high resolution neutron powder data". *Mater. Res. Bull.* 18, 841–852, **1983**. ISSN: 0025-5408. (Cit. on pp. 53, 55, 56).
- [108] C. Mellot and J. Lignieres. "Monte Carlo Simulations of N<sub>2</sub> and O<sub>2</sub> Adsorption in Silicalite and CaLSX Zeolites". *Mol. Sim.* 18, 349–365, **1997**. DOI: 10.1080/08927029708024130. (Cit. on p. 54).

- [109] G. Vitale, C. F. Mellot, L. M. Bull and A. K. Cheetham. "Neutron Diffraction and Computational Study of Zeolite NaX: Influence of SIII Cations on Its Complex with Benzene". *J. Phys. Chem. B* 101, 4559–4564, **1997**. DOI: 10.1021/jp970393x. (Cit. on p. 54).
- [110] G. Maurin, P. Llewellyn, T. Poyet and B. Kuchta. "Influence of Extra-Framework Cations on the Adsorption Properties of X-Faujasite Systems: Microcalorimetry and Molecular Simulations". *J. Phys. Chem. B* 109 PMID: 16850994, 125–129, **2005**. DOI: 10.1021/jp0461753. (Cit. on p. 54).
- [111] D. F. Plant, G. Maurin, H. Jobic and P. L. Llewellyn. "Molecular Dynamics Simulation of the Cation Motion upon Adsorption of CO<sub>2</sub> in Faujasite Zeolite Systems". *J. Phys. Chem. B* 110 PMID: 16854144, 14372–14378, **2006**. DOI: 10.1021/jp062381u. (Cit. on p. 54).
- [112] A. R. Ruiz-Salvador, D. W. Lewis, J. Rubayo-Soneira, G. Rodriguez-Fuentes, L. R. Sierra and C. R. A. Catlow. "Aluminum distribution in low Si/Al zeolites: dehydrated Naclinoptilolite". *J. Phys. Chem. B* 102, 8417–8425, **1998**. (Cit. on p. 54).
- [113] A. R. Ruiz-Salvador, A. Gómez, D. W. Lewis, G. Rodriguez-Fuentes and L. Montero. "Silicon–aluminium distribution in dehydrated calcium heulandite". *Phys. Chem. Chem. Phys.* 1, 1679–1685, **1999**. (Cit. on p. 54).
- [114] E. Fois, A. Gamba, G. Tabacchi, S. Quartieri and G. Vezzolini. "On the collective properties of water molecules in one-dimensional zeolitic channels". *Phys. Chem. Chem. Phys.* 3, 4158–4163, **2001**. DOI: 10.1039/B102231H. (Cit. on p. 54).
- [115] N. L. Allan, G. D. Barrera, J. A. Purton, C. E. Sims and M. B. Taylor. "Ionic solids at elevated temperatures and/or high pressures: lattice dynamics, molecular dynamics, Monte Carlo and ab initio studies". *Phys. Chem. Chem. Phys.* 2, 1099–1111, **2000**. DOI: 10.1039/A908622F. (Cit. on p. 55).
- [116] A. Rabdel Ruiz-Salvador, M. F. Garcia-Sanchez, M. O'Reilly-Lukin, D. W. Lewis and A. Gomez. "Approaching the structure of heavily defective ionic oxides through atomistic modeling". *Phys. Statu. Sol. C* 2, 3521–3524, **2005**. ISSN: 1610-1642. DOI: 10.1002/pssc.200461708. (Cit. on p. 55).
- [117] B. W. Van Beest, G. J. Kramer and R. A. Van Santen. "Force fields for silicas and aluminophosphates based on ab initio calculations". *Phys. Rev. Lett.* 64, 1955, **1990**. (Cit. on p. 55).
- [118] G. J. Kramer, N. P. Farragher, B. W. Van Beest and R. A. Van Santen. "Interatomic force fields for silicas, aluminophosphates, and zeolites: Derivation based on ab initio calculations". *Phys. Rev. B* 43, 5068, **1991**. (Cit. on p. 55).
- [119] N. A. Ramsahye and R. G. Bell. "Cation Mobility and the Sorption of Chloroform in Zeolite NaY: A Molecular Dynamics Study". *J. Phys. Chem. B* 109 PMID: 16851556, 4738–4747, **2005**. DOI: 10.1021/jp046958o. (Cit. on p. 55).
- [120] H. E. Robson, D. P. Shoemaker, R. A. Ogilvie and P. C. Manor. "Synthesis and crystal structure of zeolite rho - a new zeolite related to Linde Type A". *Adv. Chem. Ser.* 121, 106–115, **1973**. (Cit. on p. 55).
- [121] L. B. McCusker and C. Baerlocher. "The effect of dehydration upon the crystal structure of zeolite rho". In: *Proc. 6th Int. Zeolite Conf.* 1984. 812–822. (Cit. on p. 55).
- [122] L. Gomez-Hortiguera, A. B. Pinar, F. Cora and J. Perez-Pariente. "Dopant-siting selectivity in nanoporous catalysts: control of proton accessibility in zeolite catalysts through the rational use of templates". *Chem. Commun.* 46, 2073–2075, **2010**. DOI: 10.1039/B920648E. (Cit. on p. 55).
- [123] A. R. Ruiz-Salvador, R. Grau-Crespo, A. E. Gray and D. W. Lewis. "Aluminium distribution in ZSM-5 revisited: The role of Al–Al interactions". *J. Solid State Chem.* 198, 330–336, **2013**. ISSN: 0022-4596. (Cit. on p. 55).
- [124] A. R. Ruiz-Salvador, N. Almora-Barrios, A. Gómez and D. W. Lewis. "Interplay of water, extra-framework cations and framework atoms in the structure of low-silica zeolites: the case of the natural zeolite Goosecreekite as studied by computer simulation". *Phys. Chem. Chem. Phys.* 9, 521–532, **2007**. DOI: 10.1039/B607030B. (Cit. on pp. 55, 56, 58).

- [125] M. M. Lozinska, J. P. S. Mowat, P. A. Wright, S. P. Thompson, J. L. Jorda, M. Palomino, S. Valencia and F. Rey. "Cation Gating and Relocation during the Highly Selective Trapdoor Adsorption of CO<sub>2</sub> on Univalent Cation Forms of Zeolite RHO". *Chem. Mater.* 26, 2052–2061, **2014**. DOI: 10.1021/cm404028f. (Cit. on pp. 55, 56, 61, 63, 67).
- [126] C. L. White, A. R. Ruiz-Salvador and D. W. Lewis. "Pressure-Induced Hydration Effects in the Zeolite Laumontite". *Angew. Chem.* 116, 475–478, **2004**. (Cit. on p. 56).
- [127] A. R. Ruiz-Salvador, A. Gómez, B. N. Diaz, O. Y. and D. W. Lewis. "Si atoms in SAPO-31: A computational study". In: *Recent Advances in the Science and Technology of Zeolites and Related Materials Part B Proceedings of the 14th International Zeolite Conference*. Ed. by M. C. E. van Steen and L. H. Callanan. 154, Part B. Studies in Surface Science and Catalysis. Elsevier, 2004. 1439–1447. (Cit. on p. 56).
- [128] J. L. Jordá, F. Rey, G. Sastre, S. Valencia, M. Palomino, A. Corma, A. Segura, D. Errandonea, R. Lacombe, F. J. Manjón, Ó. Gomis, A. K. Kleppe, A. P. Jephcoat, M. Amboage and J. A. Rodríguez-Velamazán. "Synthesis of a Novel Zeolite through a Pressure-Induced Reconstructive Phase Transition Process". *Angew. Chem. Int. Edn.* 52, 10458–10462, **2013**. ISSN: 1521-3773. DOI: 10.1002/anie.201305230. (Cit. on p. 56).
- [129] V. Domínguez-García, S. Pigolotti and M. A. Muñoz. "Inherent directionality explains the lack of feedback loops in empirical networks". *Sci. Rep.* 4, **2014**. (Cit. on p. 56).
- [130] L. D. Landau, E. M. Lifshitz, J. B. Sykes and J. Kearsley. *Statistical Physics*. Course of Theoretical Physics. Elsevier Science, 1980. ISBN: 978-0-7506-3372-7. (Cit. on p. 56).
- [131] L. D. Landau and E. M. Lifshitz. *Course of Theoretical Physics*. Elsevier, 2013. (Cit. on p. 59).
- [132] R. V. Awati, P. I. Ravikovitch and D. S. Sholl. "Efficient and Accurate Methods for Characterizing Effects of Framework Flexibility on Molecular Diffusion in Zeolites: CH<sub>4</sub> Diffusion in Eight Member Ring Zeolites". *J. Phys. Chem. C* 117, 13462–13473, **2013**. DOI: 10.1021/jp402959t. (Cit. on pp. 62, 63).
- [133] G. Sastre. "Computational study of diffusion of propane in small pore acidic zeotypes AFX and AEI". *Catal. Today* 226 Acid-Base Catalysis Advanced Sciences and Spreading Applications to Solutions of Environmental, Resources and Energy Issues: ABC-7, 7th International Symposium on Acid-Base Catalysis, Tokyo, May 12-15, 2013, 25–36, **2014**. ISSN: 0920-5861. DOI: 10.1016/j.cattod.2013.07.021. (Cit. on pp. 62, 63).
- [134] A. Bieniok and W. H. Baur. "A large volume contraction accompanies the low- to high-temperature phase transition of zeolite Srho". *J. Solid State Chem.* 90, 173–177, **1991**. ISSN: 0022-4596. (Cit. on p. 67).
- [135] R. T. Rigo, S. R. G. Balestra, S. Hamad, A. R. Ruiz-Salvador, S. Calero and M. A. Cambor. "The Si-Ge substitutional series in the chiral STW Zeolite Structure Type". submitted *Chem. Mater.*, Manuscript ID: cm-2018-00786e. 2018 (cit. on pp. 73, 188).
- [136] R. Bueno-Pérez, S. R. G. Balestra, M. A. Cambor, J. G. Min, S. B. Hong, P. J. Merklung and S. Calero. "Influence of Flexibility on the Separation of Chiral Isomers in the STW-Type Zeolite". *Chem.–Eur. J.* **2018**. DOI: 10.1002/chem.201705627. (Cit. on pp. 74, 75, 81, 187).
- [137] J. J. Gutiérrez-Sevillano, S. Calero, S. Hamad, R. Grau-Crespo, F. Rey, S. Valencia, M. Palomino, S. R. G. Balestra and A. R. Ruiz-Salvador. "Critical Role of Dynamic Flexibility in Ge-Containing Zeolites: Impact on Diffusion". *Chem. Eur. J.* 22, 10036–10043, **2016**. DOI: 10.1002/chem.201600983. (Cit. on pp. 74, 81, 188).
- [138] R. Bueno-Pérez. "Separation Of Structural and Chiral Isomers in Nanoporous Materials". PhD thesis. Seville, Andalusia, Spain: Pablo de Olavide University, 2018. (Cit. on p. 74).
- [139] J. J. Gutiérrez-Sevillano. "Computational techniques applied to the study and development of nanoporous materials". PhD thesis. Seville, Andalusia, Spain: Pablo de Olavide University, 2013. (Cit. on p. 74).
- [140] L. Tang, L. Shi, C. Bonneau, J. Sun, H. Yue, A. Ojuva, B.-L. Lee, M. Kritikos, R. G. Bell, Z. Bacsik, J. Mink and X. Zou. "A zeolite family with chiral and achiral structures built from the same building layer". *Nat.*

- Mater.* 7, 381–385, **2008**. DOI: 10.1038/nmat2169. (Cit. on p. 74).
- [141] A. Rojas and M. A. Cambor. “A Pure Silica Chiral Polymorph with Helical Pores”. *Angew. Chem. Int. Ed.* 51, 3854–3856, **2012**. DOI: 10.1002/anie.201108753. (Cit. on p. 74).
- [142] P. Lu, L. Gomez-Hortiguera, L. Xu and M. A. Cambor. “Synthesis of STW zeolites using imidazolium-based dications of varying length”. *J. Mater. Chem. A* 6, 1485–1495, **2018**. DOI: 10.1039/C7TA10002G. (Cit. on p. 74).
- [143] J. E. Schmidt, M. W. Deem and M. E. Davis. “Synthesis of a Specified, Silica Molecular Sieve by Using Computationally Predicted Organic Structure-Directing Agents”. *Angew. Chem. Int. Ed.* 53, 8372–8374, **2014**. DOI: 10.1002/anie.201404076. (Cit. on p. 74).
- [144] S. K. Brand, J. E. Schmidt, M. W. Deem, F. Daeyaert, Y. Ma, O. Terasaki, M. Orazov and M. E. Davis. “Enantiomerically enriched, polycrystalline molecular sieves”. *P. Natl. Acad. Sci. USA* 114, 5101–5106, **2017**. DOI: 10.1073/pnas.1704638114. (Cit. on p. 74).
- [145] R. Grau-Crespo, S. Hamad, C. R. A. Catlow and N. H. de Leeuw. “Symmetry-adapted configurational modelling of fractional site occupancy in solids”. *J. Phys.: Condens. Matter* 19, 256201, **2007**. DOI: 10.1088/0953-8984/19/25/256201. (Cit. on p. 75).
- [146] J. Arce-Molina, R. Grau-Crespo, D. W. Lewis and A. R. Ruiz-Salvador. “Screening Heteroatom Distributions in Zeotype Materials Using an Effective Hamiltonian Approach: The Case of Aluminogermanate PKU-9”. submitted *J. Phys. Chem. C*, Manuscript ID: jp-2018-01601p (cit. on p. 75).
- [147] C. R. A. Catlow, M. Dixon and W. C. Mackrodt. “Interionic potentials in ionic solids”. In: *Computer Simulation of Solids*. Springer-Verlag. 130–161. DOI: 10.1007/bfb0017937. (Cit. on p. 76).
- [148] J. D. Gale. “GULP – a computer program for the symmetry adapted simulation of solids”. *J. Chem. Soc., Faraday Trans.* 93, . **1997**. (Cit. on p. 77).
- [149] G. Sastre and J. D. Gale. “Derivation of an Interatomic Potential for Germanium- and Silicon-Containing Zeolites and Its Application to the Study of the Structures of Octadecasil, ASU-7, and ASU-9 Materials”. *Chem. Mater.* 15, 1788–1796, **2003**. DOI: 10.1021/cm021262y. (Cit. on p. 77).
- [150] W. H. Press, S. A. Teukolsky, W. T. Vetterling and B. P. Flannery. *Numerical Recipes 3rd Edition: The Art of Scientific Computing*. 3rd ed. New York, NY, USA: Cambridge University Press, 2007. ISBN: 0-521-88068-8. (Cit. on p. 77).
- [151] N. Almora-Barrios, A. R. Ruiz-Salvador, A. Gómez, M. Mistry and D. W. Lewis. “Understanding Si/Al distributions in Al-rich zeolites: the role of water in determining the structure of Goosecreekite”. *Chem. Commun.* 531–532, **2001**. DOI: 10.1039/b009623g. (Cit. on p. 77).
- [152] D. W. Lewis, A. R. Ruiz-Salvador, N. Almora-Barrios, A. Gómez and M. Mistry. “Modelling of hydrated Ca-rich zeolites”. *Mol. Simul.* 28, 649–661, **2002**. DOI: 10.1080/08927020210871. (Cit. on p. 77).
- [153] A. Zunger, S.-H. Wei, L. G. Ferreira and J. E. Bernard. “Special quasirandom structures”. *Phys. Rev. Lett.* 65, 353–356, **1990**. DOI: 10.1103/physrevlett.65.353. (Cit. on p. 77).
- [154] A. Urban, I. Matts, A. Abdellahi and G. Ceder. “Computational Design and Preparation of Cation-Disordered Oxides for High-Energy-Density Li-Ion Batteries”. *Adv. Energy Mater.* 6, 1600488, **2016**. DOI: 10.1002/aenm.201600488. (Cit. on p. 77).
- [155] V. Saltas, D. Horlait, E. N. Sgourou, F. Vallianatos and A. Chroneos. “Modelling solid solutions with cluster expansion, special quasirandom structures, and thermodynamic approaches”. *Applied Physics Reviews* 4, 041301, **2017**. DOI: 10.1063/1.4999129. (Cit. on p. 77).
- [156] C. J. Pickard and F. Mauri. “All-electron magnetic response with pseudopotentials: NMR chemical shifts”. *Phys. Rev. B* 63, **2001**. DOI: 10.1103/physrevb.63.245101. (Cit. on p. 78).
- [157] J. R. Yates, C. J. Pickard and F. Mauri. “Calculation of NMR chemical shifts for extended systems using ultrasoft pseudopotentials”. *Phys. Rev. B* 76, **2007**. DOI: 10.1103/physrevb.76.024401. (Cit. on p. 78).

- [158] G. Sastre, J. A. Vidal-Moya, T. Blasco, J. Rius, J. L. Jordá, M. T. Navarro, F. Rey and A. Corma. "Preferential Location of Ge Atoms in Polymorph C of Beta Zeolite (ITQ-17) and Their Structure-Directing Effect: A Computational, XRD, and NMR Spectroscopic Study". *Angew. Chem. Int. Ed.* 41, 4722–4726, **2002**. DOI: 10.1002/anie.200290028. (Cit. on pp. 78, 81).
- [159] A. Pulido, G. Sastre and A. Corma. "Computational Study of <sup>19</sup>F NMR Spectra of Double Four Ring-Containing Si/Ge-Zeolites". *ChemPhysChem* 7, 1092–1099, **2006**. DOI: 10.1002/cphc.200500634. (Cit. on p. 78).
- [160] A. Rojas, L. Gómez-Hortigüela and M. A. Cambor. "Zeolite Structure Direction by Simple Bis (methylimidazolium) Cations: The Effect of the Spacer Length on Structure Direction and of the Imidazolium Ring Orientation on the <sup>19</sup>F NMR Resonances". *J. Am. Chem. Soc.* 134, 3845–3856, **2012**. DOI: 10.1021/ja210703y. (Cit. on p. 78).
- [161] G. Kresse and J. Hafner. "Ab initio molecular dynamics for liquid metals". *Phys. Rev. B* 47, 558–561, **1993**. DOI: 10.1103/physrevb.47.558. (Cit. on pp. 78, 97).
- [162] G. Kresse and J. Hafner. "Ab initio molecular-dynamics simulation of the liquid-metal / amorphous-semiconductor transition in germanium". *Phys. Rev. B* 49, 14251–14269, **1994**. DOI: 10.1103/physrevb.49.14251. (Cit. on pp. 78, 97).
- [163] G. Kresse and J. Furthmüller. "Efficient iterative schemes for *ab initio* total-energy calculations using a plane-wave basis set". *Phys. Rev. B* 54, 11169–11186, **1996**. DOI: 10.1103/PhysRevB.54.11169. (Cit. on p. 78).
- [164] G. Kresse and J. Furthmüller. "Efficiency of *ab-initio* total energy calculations for metals and semiconductors using a plane-wave basis set". *Comput. Mater. Sci.* 6, 15–50, **1996**. DOI: 10.1016/0927-0256(96)00008-0. (Cit. on p. 78).
- [165] G. Kresse and D. Joubert. "From ultrasoft pseudopotentials to the projector augmented-wave method". *Phys. Rev. B* 59, 1758–1775, **1999**. DOI: 10.1103/PhysRevB.59.1758. (Cit. on pp. 78, 97).
- [166] L. A. Villaescusa, P. Lightfoot and R. E. Morris. "Synthesis and structure of fluoride-containing GeO<sub>2</sub> analogues of zeolite double four-ring building units". *Chem. Commun.* 2220–2221, **2002**. DOI: 10.1039/b207374a. (Cit. on pp. 81, 82).
- [167] T. Blasco, A. Corma, M. J. Díaz-Cabañas, F. Rey, J. A. Vidal-Moya and C. M. Zicovich-Wilson. "Preferential Location of Ge in the Double Four-Membered Ring Units of ITQ-7 Zeolite". *J. Phys. Chem. B* 106, 2634–2642, **2002**. DOI: 10.1021/jp013302b. (Cit. on p. 81).
- [168] K. Wang, J. Yu, C. Li and R. Xu. *Inorg. Chem.* 42, 4597–4602, **2003**. (Cit. on p. 81).
- [169] P. Caullet, J. Guth, J. Hazm, J. Lamblin and H. Gies. "Synthesis, Characterization, and Crystal Structure of the New Clathrasil Phase Octadecasil". *Eur. J. Sol. State Inor.* 22, 345–361, **1991**. (Cit. on p. 82).
- [170] L. A. Villaescusa, P. A. Barrett and M. A. Cambor. "ITQ-7: A New Pure Silica Polymorph with a Three-Dimensional System of Large Pore Channels". *Angew. Chem. Int. Ed.* 38, 1997–2000, **1999**. ISSN: 1521-3773. DOI: 10.1002/(SICI)1521-3773(19990712)38:13/14<1997::AID-ANIE1997>3.0.CO;2-U. (Cit. on p. 82).
- [171] M. A. Cambor, P. A. Barrett, M.-J. Díaz-Cabañas, L. A. Villaescusa, M. Puche, T. Boix, E. Pérez and H. Koller. "High silica zeolites with three-dimensional systems of large pore channels". *Microporous Mesoporous Mater.* 48, 11–22, **2001**. DOI: 10.1016/S1387-1811(01)00325-0. (Cit. on p. 82).
- [172] P. A. Barrett, T. Boix, M. Puche, D. H. Olson, E. Jordan, H. Koller and M. A. Cambor. "ITQ-12: a new microporous silica polymorph potentially useful for light hydrocarbon separations". *Chem. Commun.* 2114, **2003**. DOI: 10.1039/b306440a. (Cit. on p. 82).
- [173] A. Rojas, O. Arteaga, B. Kahr and M. A. Cambor. "Synthesis, Structure, and Optical Activity of HPM-1, a Pure Silica Chiral Zeolite". *J. Am. Chem. Soc.* 135, 11975–11984, **2013**. DOI: 10.1021/ja405088c. (Cit. on p. 82).

- [174] A. Sadoc, M. Biswal, M. Body, C. Legein, F. Boucher, D. Massiot and F. Fayon. "NMR parameters in column 13 metal fluoride compounds (AlF<sub>3</sub>, GaF<sub>3</sub>, InF<sub>3</sub> and TlF) from first principle calculations". *Solid State Nucl. Magn. Reson.* 59–60, 1–7, **2014**. DOI: 10.1016/j.ssnmr.2014.01.001. (Cit. on p. 83).
- [175] A. Zheng, S.-B. Liu and F. Deng. "19F Chemical Shift of Crystalline Metal Fluorides: Theoretical Predictions Based on Periodic Structure Models". *J. Phys. Chem. C* 113, 15018–15023, **2009**. DOI: 10.1021/jp904454t. (Cit. on p. 83).
- [176] C. Martineau, M. Allix, M. R. Suchomel, F. Porcher, F. Vivet, C. Legein, M. Body, D. Massiot, F. Taulelle and F. Fayon. "Structure determination of Ba<sub>5</sub>AlF<sub>13</sub> by coupling electron, synchrotron and neutron powder diffraction, solid-state NMR and ab initio calculations". *Dalton Trans.* 45, 15565–15574, **2016**. DOI: 10.1039/c6dt02454h. (Cit. on p. 83).
- [177] S. Hamad, S. R. G. Balestra, R. Bueno-Perez, S. Calero and A. R. Ruiz-Salvador. "Atomic charges for modeling metal-organic frameworks: Why and how". *J. Solid State Chem.* 223, 144–151, **2015**. DOI: 10.1016/j.jssc.2014.08.004. arXiv: 1802.08771. (Cit. on pp. 87, 115, 187).
- [178] M. P. Suh, H. J. Park, T. K. Prasad and D.-W. Lim. "Hydrogen Storage in Metal-Organic Frameworks". *Chem. Rev.* 112, 782–835, **2011**. DOI: 10.1021/cr200274s. (Cit. on p. 87).
- [179] M. Eddaoudi, J. Kim, N. Rosi, D. Vodak, J. Wachter, M. O'Keeffe and O. M. Yaghi. "Systematic design of pore size and functionality in isorecticular MOFs and their application in methane storage". *Science* 295, 469–472, **2002**. (Cit. on pp. 87, 110, 111).
- [180] K. Sumida, D. L. Rogow, J. A. Mason, T. M. McDonald, E. D. Bloch, Z. R. Herm, T.-H. Bae and J. R. Long. "Carbon dioxide capture in metal-organic frameworks". *Chem. Rev.* 112, 724–781, **2011**. (Cit. on p. 87).
- [181] J.-R. Li, J. Sculley and H.-C. Zhou. "Metal-organic frameworks for separations". *Chem. Rev.* 112, 869–932, **2011**. (Cit. on p. 87).
- [182] K. A. Cychosz, R. Ahmad and A. J. Matzger. "Liquid phase separations by crystalline microporous coordination polymers". *Chem. Sci.* 1, 293, **2010**. DOI: 10.1039/c0sc00144a. (Cit. on p. 87).
- [183] C. E. Wilmer, M. Leaf, C. Y. Lee, O. K. Farha, B. G. Hauser, J. T. Hupp and R. Q. Snurr. "Large-scale screening of hypothetical metal-organic frameworks". *Nat. Chem.* 4, 83–89, **2011**. DOI: 10.1038/nchem.1192. (Cit. on p. 88).
- [184] D. Dubbeldam, R. Krishna, S. Calero and A. Ö. Yazaydin. "Computer-Assisted Screening of Ordered Crystalline Nanoporous Adsorbents for Separation of Alkane Isomers". *Angew. Chem. Int. Edn.* 124, 12037–12041, **2012**. DOI: 10.1002/ange.201205040. (Cit. on p. 88).
- [185] A. W. Thornton, D. Dubbeldam, M. S. Liu, B. P. Ladewig, A. J. Hill and M. R. Hill. "Feasibility of zeolitic imidazolate framework membranes for clean energy applications". *Energy & Environmental Science* 5, 7637, **2012**. DOI: 10.1039/c2ee21743k. (Cit. on p. 88).
- [186] K. R. and van Baten JM. "Comment on comparative molecular simulation study of CO<sub>2</sub>/N<sub>2</sub> and CH<sub>4</sub>/N<sub>2</sub> separation in zeolites and metal-organic frameworks". *Langmuir* 26, 2975, **2010**. (Cit. on p. 88).
- [187] T. Düren, Y.-S. Bae and R. Q. Snurr. "Using molecular simulation to characterise metal-organic frameworks for adsorption applications". *Chem. Soc. Rev.* 38, 1237, **2009**. DOI: 10.1039/b803498m. (Cit. on p. 88).
- [188] S. Calero. *Adsorption in Metal-Organic Frameworks*. 2nd Edition. From Elements to Applications. Elsevier, 2013. ISBN: 978-0-08-097774-4. (Cit. on p. 88).
- [189] D. Yu, A. O. Yazaydin, J. R. Lane, P. D. C. Dietzel and R. Q. Snurr. "A combined experimental and quantum chemical study of CO<sub>2</sub> adsorption in the metal-organic framework CPO-27 with different metals". *Chem. Sci.* 4, 3544, **2013**. DOI: 10.1039/c3sc51319j. (Cit. on p. 88).
- [190] K. Sillar, A. Hofmann and J. Sauer. "Ab initio study of hydrogen adsorption in MOF-5". *J. Am. Chem. Soc.* 131, 4143–4150, **2009**. (Cit. on p. 88).

- [191] M. P. Allen and D. J. Tildesley. *Computer simulation of liquids*. Oxford university press, 2017. (Cit. on p. 89).
- [192] W. Jorgensen. “Optimized intermolecular potential functions for liquid alcohols”. *J. Phys. Chem.* 90, 1276, **1986**. (Cit. on p. 89).
- [193] S. Calero, D. Dubbeldam, R. Krishna, B. Smit, T. J. H. Vlugt, J. F. M. Denayer, J. A. Martens and T. L. M. Maesen. “Understanding the Role of Sodium during Adsorption: A Force Field for Alkanes in Sodium-Exchanged Faujasites”. *J. Am. Chem. Soc.* 126, 11377–11386, **2004**. DOI: 10.1021/ja0476056. (Cit. on p. 89).
- [194] A. Martin-Calvo, F. D. Lahoz-Martin and S. Calero. “Understanding Carbon Monoxide Capture Using Metal–Organic Frameworks”. *J. Phys. Chem. C* 116, 6655–6663, **2012**. DOI: 10.1021/jp211563e. (Cit. on p. 89).
- [195] H. Fang, H. Demir, P. Kamakoti and D. S. Sholl. “Recent developments in first-principles force fields for molecules in nanoporous materials”. *J. Mater. Chem. A* 2, 274–291, **2014**. DOI: 10.1039/c3ta13073h. (Cit. on p. 89).
- [196] L.-C. Lin, K. Lee, L. Gagliardi, J. B. Neaton and B. Smit. “Force-Field Development from Electronic Structure Calculations with Periodic Boundary Conditions: Applications to Gaseous Adsorption and Transport in Metal–Organic Frameworks”. *J. Chem. Theory Comput.* 10, 1477–1488, **2014**. DOI: 10.1021/ct500094w. (Cit. on p. 89).
- [197] S. Bureekaew, S. Amirjalayer, M. Tafipolsky, C. Spickermann, T. K. Roy and R. Schmid. “MOF-FF - A flexible first-principles derived force field for metal-organic frameworks”. *physica status solidi (b)* 250, 1128–1141, **2013**. DOI: 10.1002/pssb.201248460. (Cit. on p. 89).
- [198] J. J. G. Sevilla, S. Calero, C. O. Ania, J. B. Parra, F. Kapteijn, J. Gascon and S. Hamad. “Toward a Transferable Set of Charges to Model Zeolitic Imidazolate Frameworks: Combined Experimental–Theoretical Research”. *J. Phys. Chem. C* 117, 466–471, **2012**. DOI: 10.1021/jp3107167. (Cit. on pp. 89, 90, 92).
- [199] T. Watanabe, T. Manz and D. Sholl. “Accurate treatment of electrostatics during molecular adsorption in nanoporous crystals without assigning point charges to framework atoms”. *J. Phys. Chem. C* 115, 4824, **2011**. (Cit. on p. 89).
- [200] J. Gasteiger and M. Marsili. “Iterative partial equalization of orbital electronegativity – a rapid access to atomic charges”. *Tetrahedron* 36, 3219, **1980**. (Cit. on p. 89).
- [201] A. Rappe and G. WA. “Charge equilibration for molecular dynamics simulations”. *J. Phys. Chem.* 95, 3358, **1991**. (Cit. on pp. 89, 96).
- [202] R. Babarao, S. Dai and D.-e. Jiang. “Effect of Pore Topology and Accessibility on Gas Adsorption Capacity in Zeolitic-Imidazolate Frameworks: Bringing Molecular Simulation Close to Experiment”. *J. Phys. Chem. C* 115, 8126–8135, **2011**. DOI: 10.1021/jp1117294. (Cit. on p. 89).
- [203] K. S. Walton, A. R. Millward, D. Dubbeldam, H. Frost, J. J. Low, O. M. Yaghi and R. Q. Snurr. “Understanding Inflections and Steps in Carbon Dioxide Adsorption Isotherms in Metal-Organic Frameworks”. *J. Am. Chem. Soc.* 130, 406–407, **2008**. DOI: 10.1021/ja076595g. (Cit. on p. 89).
- [204] C. Zheng, D. Liu, Q. Yang, C. Zhong and J. Mi. “Computational Study on the Influences of Framework Charges on CO<sub>2</sub> Uptake in Metal-Organic Frameworks”. *Ind. Eng. Chem. Res.* 48, 10479–10484, **2009**. DOI: 10.1021/ie901000x. (Cit. on p. 90).
- [205] K. Zhang, L. Zhang and J. Jiang. “Adsorption of C1–C4 Alcohols in Zeolitic Imidazolate Framework-8: Effects of Force Fields, Atomic Charges, and Framework Flexibility”. *J. Phys. Chem. C* 117, 25628–25635, **2013**. DOI: 10.1021/jp409869c. (Cit. on p. 90).
- [206] J. M. Castillo, T. J. H. Vlugt and S. Calero. “Understanding Water Adsorption in Cu-BTC Metal-Organic Frameworks”. *J. Phys. Chem. C* 112, 15934–15939, **2008**. DOI: 10.1021/jp806363w. (Cit. on p. 90).
- [207] F. Salles, S. Bourrelly, H. Jobic, T. Devic, V. Guillermin, P. Llewellyn, C. Serre, G. Ferey and G. Maurin. “Molecular Insight into the Adsorption and Diffusion of Water in the Versatile Hydrophilic/Hydrophobic Flexible MIL-53(Cr) MOF”. *J. Phys. Chem.*

- C 115, 10764–10776, **2011**. DOI: 10.1021/jp202147m. (Cit. on p. 90).
- [208] B. Zheng, M. Sant, P. Demontis and G. B. Suffritti. “Force Field for Molecular Dynamics Computations in Flexible ZIF-8 Framework”. *J. Phys. Chem. C* 116, 933–938, **2012**. DOI: 10.1021/jp209463a. (Cit. on p. 90).
- [209] D. Liu and C. Zhong. “Understanding gas separation in metal–organic frameworks using computer modeling”. *J. Mater. Chem.* 20, 10308, **2010**. DOI: 10.1039/c0jm01045f. (Cit. on p. 90).
- [210] Q. Yang and C. Zhong. “Electrostatic-Field-Induced Enhancement of Gas Mixture Separation in Metal-Organic Frameworks: A Computational Study”. *ChemPhysChem* 7, 1417–1421, **2006**. DOI: 10.1002/cphc.200600191. (Cit. on p. 90).
- [211] Q. Yang, C. Xue, C. Zhong and J.-F. Chen. “Molecular simulation of separation of CO<sub>2</sub> from flue gases in Cu-BTC metal-organic framework”. *AIChE Journal* 53, 2832–2840, **2007**. DOI: 10.1002/aic.11298. (Cit. on p. 90).
- [212] R. S. Mulliken. “Electronic Population Analysis on LCAO–MO Molecular Wave Functions. I”. *J. Chem. Phys.* 23, 1833–1840, **1955**. DOI: 10.1063/1.1740588. (Cit. on p. 91).
- [213] K. C. Szeto, C. Prestipino, C. Lamberti, A. Zecchina, S. Bordiga, M. Bjørgen, M. Tilset and K. P. Lillerud. “Characterization of a New Porous Pt-Containing Metal-Organic Framework Containing Potentially Catalytically Active Sites: Local Electronic Structure at the Metal Centers”. *Chem. Mater.* 19, 211–220, **2007**. DOI: 10.1021/cm0616432. (Cit. on p. 91).
- [214] T. Watanabe, S. Keskin, S. Nair and D. S. Sholl. “Computational identification of a metal organic framework for high selectivity membrane-based CO<sub>2</sub>/CH<sub>4</sub> separations: Cu(hfipbb)(H<sub>2</sub>hfipbb)<sub>0.5</sub>”. *Phys. Chem. Chem. Phys.* 11, 11389, **2009**. DOI: 10.1039/b918254n. (Cit. on p. 91).
- [215] J. Rydén, S. Öberg, M. Heggie, M. Rayson and P. Briddon. “Hydrogen storage in the manganese containing metal–organic framework MOF-73”. *Microporous Mesoporous Mater.* 165, 205–209, **2013**. DOI: 10.1016/j.micromeso.2012.08.024. (Cit. on p. 91).
- [216] P. N. Gaponik, M. M. Degtyarik, A. S. Lyakhov, V. E. Matulis, O. A. Ivashkevich, M. Quesada and J. Reedijk. “Bis(2-methyltetrazole)dichlorocopper(II) is a layered coordination polymer built from dinuclear chloro-bridged Cu units linked by bridging tetrazoles. The first structurally and magnetically characterized complex of 2-monosubstituted tetrazoles”. *Inorg. Chim. Acta* 358, 3949–3957, **2005**. DOI: 10.1016/j.ica.2005.06.029. (Cit. on p. 91).
- [217] C. B. Messner, M. R. Mirza, M. Rainer, O. M. D. Lutz, Y. Güzel, T. S. Hofer, C. W. Huck, B. M. Rode and G. K. Bonn. “Selective enrichment of phosphopeptides by a metal–organic framework”. *Anal. Methods* 5, 2379, **2013**. DOI: 10.1039/c3ay40308d. (Cit. on p. 91).
- [218] Z. Bao, S. Alnemrat, L. Yu, I. Vasiliev, Q. Ren, X. Lu and S. Deng. “Adsorption of Ethane, Ethylene, Propane, and Propylene on a Magnesium-Based Metal–Organic Framework”. *Langmuir* 27, 13554–13562, **2011**. DOI: 10.1021/1a2030473. (Cit. on p. 91).
- [219] O. Khvostikova, B. Assfour, G. Seifert, H. Hermann, A. Horst and H. Ehrenberg. “Novel experimental methods for assessment of hydrogen storage capacity and modelling of sorption in Cu-BTC”. *Int. J. Hydrogen Energy* 35, 11042–11051, **2010**. DOI: 10.1016/j.ijhydene.2010.07.089. (Cit. on p. 91).
- [220] R. Xiong, D. J. Keffer, M. Fuentes-Cabrera, D. M. Nicholson, A. Michalkova, T. Petrova, J. Leszczynski, K. Odbadrakh, B. L. Doss and J. P. Lewis. “Effect of Charge Distribution on RDX Adsorption in IRMOF-10”. *Langmuir* 26, 5942–5950, **2010**. DOI: 10.1021/1a9039013. (Cit. on pp. 91, 92, 95).
- [221] L.-M. Yang. “Quantum chemistry investigation of rigid A-IRMOF-MO series (A=zinc, cadmium, and alkaline-earth metals) on crystal structure, electronic structure, formation energy, chemical bonding, and optical properties”. *Microporous Mesoporous Mater.* 183, 218–233, **2014**. DOI: 10.1016/j.micromeso.2013.09.031. (Cit. on p. 91).
- [222] F. Martin and H. Zipse. “Charge distribution in the water molecule. A comparison of methods”. *J. Comput. Chem.* 26, 97–105, **2004**. DOI: 10.1002/jcc.20157. (Cit. on p. 91).

- [223] A. E. Reed, R. B. Weinstock and F. Weinhold. "Natural population analysis". *J. Chem. Phys.* 83, 735–746, **1985**. DOI: 10.1063/1.449486. (Cit. on p. 92).
- [224] S. Choomwattana, T. Maihom, P. Khongpracha, M. Probst and J. Limtrakul. "Structures and Mechanisms of the Carbonyl-ene Reaction between MOF-11 Encapsulated Formaldehyde and Propylene: An ONIOM Study". *J. Phys. Chem. C* 112, 10855–10861, **2008**. DOI: 10.1021/jp8021437. (Cit. on p. 92).
- [225] S.-i. Noro, D. Tanaka, H. Sakamoto, S. Shimomura, S. Kitagawa, S. Takeda, K. Uemura, H. Kita, T. Akutagawa and T. Nakamura. "Selective Gas Adsorption in One-Dimensional, Flexible CuII Coordination Polymers with Polar Units". *Chem. Mater.* 21, 3346–3355, **2009**. DOI: 10.1021/cm9012969. (Cit. on p. 92).
- [226] L.-M. Yang, P. Ravindran, P. Vajeeston, S. Svelle and M. Tilset. "A quantum mechanically guided view of Cd-MOF-5 from formation energy, chemical bonding, electronic structure, and optical properties". *Microporous Mesoporous Mater.* 175, 50–58, **2013**. DOI: 10.1016/j.micromeso.2013.03.020. (Cit. on p. 92).
- [227] P. Canepa, C. A. Arter, E. M. Conwill, D. H. Johnson, B. A. Shoemaker, K. Z. Soliman and T. Thonhauser. "High-throughput screening of small-molecule adsorption in MOF". *J. Mater. Chem. A* 1, 13597, **2013**. DOI: 10.1039/c3ta12395b. (Cit. on p. 92).
- [228] L.-M. Yang, P. Ravindran, P. Vajeeston and M. Tilset. "Ab initio investigations on the crystal structure, formation enthalpy, electronic structure, chemical bonding, and optical properties of experimentally synthesized isoreticular metal-organic framework-10 and its analogues: M-IRMOF-10 (M = Zn, Cd, Be, Mg, Ca, Sr and Ba)". *RSC Adv.* 2, 1618–1631, **2012**. DOI: 10.1039/c1ra00187f. (Cit. on p. 92).
- [229] M. R. V. Jørgensen, S. Cenedese, H. F. Clausen, J. Overgaard, Y.-S. Chen, C. Gatti and B. B. Iversen. "Experimental and Theoretical Charge Densities of a Zinc-Containing Coordination Polymer, Zn(HCOO)<sub>2</sub>(H<sub>2</sub>O)<sub>2</sub>". *Inorg. Chem.* 52, 297–305, **2012**. DOI: 10.1021/ic301918x. (Cit. on p. 92).
- [230] L. Tabrizi, H. Chiniforoshan, P. McArdle, H. Tavakol, B. Rezaei and M. M. Dehcheshmeh. "Selective gas sorption and electrochemical properties of a dicyanamide coordination polymer: Insight from experimental and theoretical study". *Polyhedron* 69, 84–89, **2014**. DOI: 10.1016/j.poly.2013.11.029. (Cit. on p. 92).
- [231] C. Zhou, L. Cao, S. Wei, Q. Zhang and L. Chen. "A first principles study of gas adsorption on charged CuBTC". *Comput. Theor. Chem.* 976, 153–160, **2011**. DOI: 10.1016/j.comptc.2011.08.018. (Cit. on p. 92).
- [232] J. Park, H. Kim, S. S. Han and Y. Jung. "Tuning Metal-Organic Frameworks with Open-Metal Sites and Its Origin for Enhancing CO<sub>2</sub> Affinity by Metal Substitution". *J. Phys. Chem. Lett.* 3, 826–829, **2012**. DOI: 10.1021/jz300047n. (Cit. on p. 92).
- [233] T. A. Manz and D. S. Sholl. "Improved Atoms-in-Molecule Charge Partitioning Functional for Simultaneously Reproducing the Electrostatic Potential and Chemical States in Periodic and Nonperiodic Materials". *J. Chem. Theory Comput.* 8, 2844–2867, **2012**. DOI: 10.1021/ct3002199. (Cit. on p. 92).
- [234] T. A. Manz and D. S. Sholl. "Chemically Meaningful Atomic Charges That Reproduce the Electrostatic Potential in Periodic and Nonperiodic Materials". *J. Chem. Theory Comput.* 6, 2455–2468, **2010**. DOI: 10.1021/ct100125x. (Cit. on p. 93).
- [235] J. Zang, S. Nair and D. S. Sholl. "Prediction of Water Adsorption in Copper-Based Metal-Organic Frameworks Using Force Fields Derived from Dispersion-Corrected DFT Calculations". *J. Phys. Chem. C* 117, 7519–7525, **2013**. DOI: 10.1021/jp310497u. (Cit. on p. 93).
- [236] E. Haldoupis, S. Nair and D. S. Sholl. "Finding MOFs for Highly Selective CO<sub>2</sub>/N<sub>2</sub> Adsorption Using Materials Screening Based on Efficient Assignment of Atomic Point Charges". *J. Am. Chem. Soc.* 134, 4313–4323, **2012**. DOI: 10.1021/ja2108239. (Cit. on pp. 93, 96).
- [237] I. Erucar, T. A. Manz and S. Keskin. "Effects of electrostatic interactions on gas adsorption and permeability of MOF membranes". *Mol. Simul.* 40, 557–570, **2014**. DOI: 10.

- 1080 / 08927022 . 2013 . 829219. (Cit. on p. 93).
- [238] H. Jasuja, J. Zang, D. S. Sholl and K. S. Walton. "Rational Tuning of Water Vapor and CO<sub>2</sub> Adsorption in Highly Stable Zr-Based MOFs". *J. Phys. Chem. C* 116, 23526–23532, **2012**. DOI: 10 . 1021 / jp308657x. (Cit. on pp. 93, 95).
- [239] F. L. Hirshfeld. "Bonded-atom fragments for describing molecular charge densities". *Theor. Chim. Acta* 44, 129–138, **1977**. DOI: 10.1007/bf00549096. (Cit. on p. 93).
- [240] P. Bultinck, C. V. Alsenoy, P. W. Ayers and R. Carbó-Dorca. "Critical analysis and extension of the Hirshfeld atoms in molecules". *J. Chem. Phys.* 126, 144111, **2007**. DOI: 10.1063/1.2715563. (Cit. on p. 93).
- [241] D. Geldof, A. Krishtal, F. Blockhuys and C. V. Alsenoy. "FOHI-D: An iterative Hirshfeld procedure including atomic dipoles". *J. Chem. Phys.* 140, 144104, **2014**. DOI: 10.1063/1.4870498. (Cit. on p. 93).
- [242] T. Verstraelen, P. W. Ayers, V. V. Speybroeck and M. Waroquier. "Hirshfeld-E Partitioning: AIM Charges with an Improved Trade-off between Robustness and Accurate Electrostatics". *J. Chem. Theory Comput.* 9, 2221–2225, **2013**. DOI: 10.1021/ct4000923. (Cit. on p. 93).
- [243] D. E. P. Vanpoucke, P. Bultinck and I. V. Driessche. "Extending Hirshfeld-I to bulk and periodic materials". *J. Comput. Chem.* 34, 405–417, **2012**. DOI: 10.1002/jcc.23088. (Cit. on p. 93).
- [244] S. Biswas, D. E. P. Vanpoucke, T. Verstraelen, M. Vandichel, S. Couck, K. Leus, Y.-Y. Liu, M. Waroquier, V. V. Speybroeck, J. F. M. Denayer and P. V. D. Voort. "New Functionalized Metal–Organic Frameworks MIL-47-X (X = -Cl, -Br, -CH<sub>3</sub>, -CF<sub>3</sub>, -OH, -OCH<sub>3</sub>): Synthesis, Characterization, and CO<sub>2</sub> Adsorption Properties". *J. Phys. Chem. C* 117, 22784–22796, **2013**. DOI: 10.1021/jp406835n. (Cit. on p. 93).
- [245] A. V. Marenich, S. V. Jerome, C. J. Cramer and D. G. Truhlar. "Charge Model 5: An Extension of Hirshfeld Population Analysis for the Accurate Description of Molecular Interactions in Gaseous and Condensed Phases". *J. Chem. Theory Comput.* 8, 527–541, **2012**. DOI: 10.1021/ct200866d. (Cit. on p. 93).
- [246] P. Verma, X. Xu and D. G. Truhlar. "Adsorption on Fe-MOF-74 for C1-C3 Hydrocarbon Separation". *J. Phys. Chem. C* 117, 12648–12660, **2013**. DOI: 10.1021/jp402884h. (Cit. on p. 93).
- [247] K. Lee, W. C. Isley, A. L. Dzubak, P. Verma, S. J. Stoneburner, L.-C. Lin, J. D. Howe, E. D. Bloch, D. A. Reed, M. R. Hudson, C. M. Brown, J. R. Long, J. B. Neaton, B. Smit, C. J. Cramer, D. G. Truhlar and L. Gagliardi. "Design of a Metal–Organic Framework with Enhanced Back Bonding for Separation of N<sub>2</sub> and CH<sub>4</sub>". *J. Am. Chem. Soc.* 136, 698–704, **2013**. DOI: 10.1021/ja4102979. (Cit. on p. 93).
- [248] J. Z. Vilseck, J. Tirado-Rives and W. L. Jorgensen. "Evaluation of CM5 Charges for Condensed-Phase Modeling". *J. Chem. Theory Comput.* 10, 2802–2812, **2014**. DOI: 10.1021/ct500016d. (Cit. on p. 93).
- [249] C. M. Breneman and K. B. Wiberg. "Determining atom-centered monopoles from molecular electrostatic potentials. The need for high sampling density in formamide conformational analysis". *J. Comput. Chem.* 11, 361–373, **1990**. DOI: 10.1002/jcc.540110311. (Cit. on p. 95).
- [250] U. C. Singh and P. A. Kollman. "An approach to computing electrostatic charges for molecules". *J. Comput. Chem.* 5, 129–145, **1984**. DOI: 10.1002/jcc.540050204. (Cit. on p. 95).
- [251] T. Sagara, J. Klassen and E. Ganz. "Computational study of hydrogen binding by metal-organic framework-5". *J. Chem. Phys.* 121, 12543, **2004**. DOI: 10.1063/1.1809608. (Cit. on p. 95).
- [252] M. Tafipolsky, S. Amirjalayer and R. Schmid. "Ab initio parametrized MM3 force field for the metal-organic framework MOF-5". *J. Comput. Chem.* 28, 1169–1176, **2007**. DOI: 10.1002/jcc.20648. (Cit. on p. 95).
- [253] Y. Chen and J. Jiang. "A Bio-Metal–Organic Framework for Highly Selective CO<sub>2</sub> Capture: A Molecular Simulation Study". *ChemSusChem* 3, 982–988, **2010**. DOI: 10.1002/cssc.201000080. (Cit. on p. 95).

- [254] Z. Zhang, Z. Li and J. Li. “Computational Study of Adsorption and Separation of CO<sub>2</sub>, CH<sub>4</sub>, and N<sub>2</sub> by an rht-Type Metal-Organic Framework”. *Langmuir* 28, 12122–12133, **2012**. DOI: 10 . 1021 / 1a302537d. (Cit. on p. 95).
- [255] X. Sun, C. D. Wick, P. K. Thallapally, B. P. McGrail and L. X. Dang. “Computational Study of Hydrocarbon Adsorption in Metal-Organic Framework Ni<sub>2</sub>(dhtp)”. *J. Phys. Chem. B* 115, 2842–2849, **2011**. DOI: 10 . 1021/jp1115299. (Cit. on p. 95).
- [256] Y. Ma and P. B. Balbuena. “Window effect on CO<sub>2</sub>/N<sub>2</sub> selectivity in metal organic framework materials”. *Chem. Phys. Lett.* 552, 136–140, **2012**. DOI: 10 . 1016 / j . cplett.2012.09.069. (Cit. on p. 95).
- [257] Z. Qiao, A. Torres-Knoop, D. Dubbeldam, D. Fairen-Jimenez, J. Zhou and R. Q. Snurr. “Advanced Monte Carlo simulations of the adsorption of chiral alcohols in a homochiral metal-organic framework”. *AIChE Journal* 60, 2324–2334, **2014**. DOI: 10.1002/aic.14415. (Cit. on p. 95).
- [258] C. Campaná, B. Mussard and T. K. Woo. “Electrostatic Potential Derived Atomic Charges for Periodic Systems Using a Modified Error Functional”. *J. Chem. Theory Comput.* 5, 2866–2878, **2009**. DOI: 10 . 1021/ct9003405. (Cit. on pp. 95, 97).
- [259] K. G. Ray, D. Olmsted, N. He, Y. Houndonoubo, B. B. Laird and M. Asta. “van der Waals density functional study of CO<sub>2</sub> binding in zeolitic imidazolate frameworks”. *Phys. Rev. B* 85, **2012**. DOI: 10 . 1103 / physrevb . 85 . 085410. (Cit. on p. 95).
- [260] R. Vaidhyanathan, S. S. Iremonger, G. K. H. Shimizu, P. G. Boyd, S. Alavi and T. K. Woo. “Direct Observation and Quantification of CO<sub>2</sub> Binding Within an Amine-Functionalized Nanoporous Solid”. *Science* 330, 650–653, **2010**. DOI: 10 . 1126 / science.1194237. (Cit. on p. 95).
- [261] W. Morris, B. Leung, H. Furukawa, O. K. Yaghi, N. He, H. Hayashi, Y. Houndonoubo, M. Asta, B. B. Laird and O. M. Yaghi. “A Combined Experimental-Computational Investigation of Carbon Dioxide Capture in a Series of Isoreticular Zeolitic Imidazolate Frameworks”. *J. Am. Chem. Soc.* 132, 11006–11008, **2010**. DOI: 10.1021/ja104035j. (Cit. on p. 95).
- [262] W. Morris, N. He, K. G. Ray, P. Klonowski, H. Furukawa, I. N. Daniels, Y. A. Houndonoubo, M. Asta, O. M. Yaghi and B. B. Laird. “A Combined Experimental-Computational Study on the Effect of Topology on Carbon Dioxide Adsorption in Zeolitic Imidazolate Frameworks”. *J. Phys. Chem. C* 116, 24084–24090, **2012**. DOI: 10.1021/jp307170a. (Cit. on p. 95).
- [263] A. Sutrisno, V. V. Terskikh, Q. Shi, Z. Song, J. Dong, S. Y. Ding, W. Wang, B. R. Provost, T. D. Daff, T. K. Woo and Y. Huang. “Characterization of Zn-Containing Metal-Organic Frameworks by Solid-State <sup>67</sup>Zn NMR Spectroscopy and Computational Modeling”. *Chem. –Eur. J.* 18, 12251–12259, **2012**. DOI: 10 . 1002 / chem . 201201563. (Cit. on p. 95).
- [264] P. E. Blöchl. “Electrostatic decoupling of periodic images of plane-wave-expanded densities and derived atomic point charges”. *J. Chem. Phys.* 103, 7422–7428, **1995**. DOI: 10 . 1063 / 1 . 470314. (Cit. on p. 95).
- [265] J. Schmidt, C. Krekeler, F. Dommert, Y. Zhao, R. Berger, L. D. Site and C. Holm. “Ionic Charge Reduction and Atomic Partial Charges from First-Principles Calculations of 1, 3-Dimethylimidazolium Chloride”. *J. Phys. Chem. B* 114, 6150–6155, **2010**. DOI: 10.1021/jp910771q. (Cit. on p. 95).
- [266] F. Dommert and C. Holm. “Refining classical force fields for ionic liquids: theory and application to [MMIM][Cl]”. *Phys. Chem. Chem. Phys.* 15, 2037–2049, **2013**. DOI: 10.1039/c2cp43698a. (Cit. on p. 95).
- [267] Y. Zhang and E. J. Maginn. “A Simple AIMD Approach to Derive Atomic Charges for Condensed Phase Simulation of Ionic Liquids”. *J. Phys. Chem. B* 116, 10036–10048, **2012**. DOI: 10 . 1021 / jp3037999. (Cit. on p. 95).
- [268] C. Wilmer, K. Kim and R. Snurr. “An extended charge equilibration method”. *J. Phys. Chem. Lett.* 3, 2506, **2012**. (Cit. on p. 96).
- [269] C. E. Wilmer, O. K. Farha, Y.-S. Bae, J. T. Hupp and R. Q. Snurr. “Structure–property relationships of porous materials for carbon dioxide separation and capture”. *Energy & Environmental Science* 5, 9849, **2012**. DOI: 10.1039/c2ee23201d. (Cit. on pp. 96, 97).

- [270] M. C. Bernini, D. Fairen-Jimenez, M. Pasinetti, A. J. Ramirez-Pastor and R. Q. Snurr. "Screening of bio-compatible metal-organic frameworks as potential drug carriers using Monte Carlo simulations". *J. Mater. Chem. B* 2, 766–774, **2014**. DOI: 10.1039/c3tb21328e. (Cit. on p. 96).
- [271] E. S. Kadantsev, P. G. Boyd, T. D. Daff and T. K. Woo. "Fast and Accurate Electrostatics in Metal Organic Frameworks with a Robust Charge Equilibration Parameterization for High-Throughput Virtual Screening of Gas Adsorption". *J. Phys. Chem. Lett.* 4, 3056–3061, **2013**. DOI: 10.1021/jz401479k. (Cit. on p. 96).
- [272] Q. Xu and C. Zhong. "A General Approach for Estimating Framework Charges in Metal-Organic Frameworks". *J. Phys. Chem. C* 114, 5035–5042, **2010**. DOI: 10.1021/jp910522h. (Cit. on p. 96).
- [273] C. Zheng and C. Zhong. "Estimation of Framework Charges in Covalent Organic Frameworks Using Connectivity-Based Atom Contribution Method". *J. Phys. Chem. C* 114, 9945–9951, **2010**. DOI: 10.1021/jp102409a. (Cit. on p. 96).
- [274] A. L. Robinson, V. Stavila, T. R. Zeitler, M. I. White, S. M. Thornberg, J. A. Greathouse and M. D. Allendorf. "Ultrasensitive Humidity Detection Using Metal-Organic Framework-Coated Microsensors". *Anal. Chem.* 84, 7043–7051, **2012**. DOI: 10.1021/ac301183w. (Cit. on p. 96).
- [275] W. Zhuang, D. Yuan, D. Liu, C. Zhong, J.-R. Li and H.-C. Zhou. "Robust Metal-Organic Framework with An Octatopic Ligand for Gas Adsorption and Separation: Combined Characterization by Experiments and Molecular Simulation". *Chem. Mater.* 24, 18–25, **2011**. DOI: 10.1021/cm2008889. (Cit. on p. 96).
- [276] D. N. Dybtsev, H. Chun and K. Kim. "Rigid and Flexible: A Highly Porous Metal-Organic Framework with Unusual Guest-Dependent Dynamic Behavior". *Angew. Chem. Int. Edn.* 116, 5143–5146, **2004**. DOI: 10.1002/ange.200460712. (Cit. on p. 97).
- [277] W. Tang, E. Sanville and G. Henkelman. "A grid-based Bader analysis algorithm without lattice bias". *J. Phys.: Condens. Matter* 21, 084204, **2009**. DOI: 10.1088/0953-8984/21/8/084204. (Cit. on p. 97).
- [278] T. Laino, F. Mohamed, A. Laio and M. Parrinello. "An Efficient Linear-Scaling Electrostatic Coupling for Treating Periodic Boundary Conditions in QM/MM Simulations". *J. Chem. Theory Comput.* 2, 1370–1378, **2006**. DOI: 10.1021/ct6001169. (Cit. on p. 97).
- [279] W. Zhou, H. Wu, T. Yildirim, J. R. Simpson and A. H. Walker. "Origin of the exceptional negative thermal expansion in metal-organic framework-5 Zn<sub>4</sub>O (1,4-benzenedicarboxylate)<sub>3</sub>". *Phys. Rev. B* 78, 054114, **2008**. DOI: 10.1103/physrevb.78.054114. (Cit. on pp. 99, 104, 113).
- [280] S. R. G. Balestra, R. Bueno-Perez, S. Hamad, D. Dubbeldam, A. R. Ruiz-Salvador and S. Calero. "Controlling Thermal Expansion: A Metal-Organic Frameworks Route". *Chem. Mater.* 28, 8296–8304, **2016**. DOI: 10.1021/acs.chemmater.6b03457. arXiv: 1610.08122. (Cit. on pp. 103, 187).
- [281] B. Han, M. Chopra, S. Park, L. Li and K. Verma. "Effect of substrate CTE on solder ball reliability of flip-chip PBGA package assembly". *Journal of Surface Mount Technology* 9, 43–52, **1996**. (Cit. on pp. 103, 104).
- [282] R. Darolia. "Thermal barrier coatings technology: critical review, progress update, remaining challenges and prospects". *Int. Mater. Rev.* 58, 315–348, **2013**. (Cit. on p. 103).
- [283] E. Della Gaspera, R. Tucker, K. Star, E. H. Lan, Y. S. Ju and B. Dunn. "Copper-based conductive composites with tailored thermal expansion". *ACS applied materials & interfaces* 5, 10966–10974, **2013**. (Cit. on pp. 103, 104).
- [284] B. Hu, Y. Zhang, W. Chen, C. Xu and Z. L. Wang. "Self-heating and External Strain Coupling Induced Phase Transition of VO<sub>2</sub> Nanobeam as Single Domain Switch". *Adv. Mater.* 23, 3536–3541, **2011**. (Cit. on p. 103).
- [285] A. Kelly, R. Stearn and L. McCartney. "Composite materials of controlled thermal expansion". *Compos. Sci. Technol.* 66, 154–159, **2006**. (Cit. on p. 104).
- [286] S. E. Tallentire, F. Child, I. Fall, L. Vella-Zarb, I. R. Evans, M. G. Tucker, D. A. Keen, C. Wilson and J. S. Evans. "Systematic and Controllable Negative, Zero, and Positive Thermal Expansion in Cubic Zr<sub>1-x</sub>Sn<sub>x</sub>

- Mo<sub>2</sub>O<sub>8</sub>". *J. Am. Chem. Soc.* 135, 12849–12856, **2013**. (Cit. on pp. 104, 111).
- [287] L. Banks-Sills. "50th anniversary article: review on interface fracture and delamination of composites". *Strain* 50, 98–110, **2014**. (Cit. on p. 104).
- [288] S. Sethi and B. C. Ray. "Environmental effects on fibre reinforced polymeric composites: Evolving reasons and remarks on interfacial strength and stability". *Adv. Colloid Interface Sci.* 217, 43–67, **2015**. (Cit. on p. 104).
- [289] T. Mary, J. Evans, T. Vogt and A. Sleight. "Negative thermal expansion from 0.3 to 1050 Kelvin in ZrW<sub>2</sub>O<sub>8</sub>". *Science* 272, 90, **1996**. (Cit. on p. 104).
- [290] T. Carey, C. C. Tang, J. A. Hriljac and P. A. Anderson. "Chemical control of thermal expansion in cation-exchanged zeolite A". *Chem. Mater.* 26, 1561–1566, **2014**. (Cit. on p. 104).
- [291] I. E. Collings, M. G. Tucker, D. A. Keen and A. L. Goodwin. "Geometric switching of linear to area negative thermal expansion in uniaxial metal–organic frameworks". *CrytEngComm* 16, 3498–3506, **2014**. (Cit. on p. 104).
- [292] N. Lock, M. Christensen, C. J. Kepert and B. B. Iversen. "Effect of gas pressure on negative thermal expansion in MOF-5". *Chem. Commun.* 49, 789–791, **2012**. (Cit. on pp. 104, 107, 113).
- [293] V. K. Peterson, G. J. Kearley, Y. Wu, A. J. Ramirez-Cuesta, E. Kemner and C. J. Kepert. "Local Vibrational Mechanism for Negative Thermal Expansion: A Combined Neutron Scattering and First-Principles Study". *Angew. Chem. Int. Ed.* 49, 585–588, **2010**. (Cit. on p. 104).
- [294] P. G. Yot, Z. Boudene, J. Macia, D. Granier, L. Vanduyffhuys, T. Verstraelen, V. Van Speybroeck, T. Devic, C. Serre, G. Férey et al. "Metal–organic frameworks as potential shock absorbers: the case of the highly flexible MIL-53 (Al)". *Chem. Commun.* 50, 9462–9464, **2014**. (Cit. on p. 104).
- [295] W. Li, S. Henke and A. K. Cheetham. "Research Update: Mechanical properties of metal-organic frameworks—Influence of structure and chemical bonding". *APL Mater.* 2, 123902, **2014**. (Cit. on p. 104).
- [296] J. L. Rowsell, E. C. Spencer, J. Eckert, J. A. Howard and O. M. Yaghi. "Gas adsorption sites in a large-pore metal-organic framework". *Science* 309, 1350–1354, **2005**. (Cit. on pp. 104, 105).
- [297] C. Yang, X. Wang and M. A. Omary. "Crystallographic observation of dynamic gas adsorption sites and thermal expansion in a breathable fluorinated metal–organic framework". *Angew. Chem. Int. Edn.* 121, 2538–2543, **2009**. (Cit. on p. 104).
- [298] J. Joo, H. Kim and S. S. Han. "Volume shrinkage of a metal–organic framework host induced by the dispersive attraction of guest gas molecules". *Phys. Chem. Chem. Phys.* 15, 18822–18826, **2013**. (Cit. on p. 104).
- [299] A. V. Neimark, F.-X. Coudert, C. Triguero, A. Boutin, A. H. Fuchs, I. Beurroies and R. Denoyel. "Structural transitions in MIL-53 (Cr): View from outside and inside". *Langmuir* 27, 4734–4741, **2011**. (Cit. on p. 104).
- [300] I. Grobler, V. J. Smith, P. M. Bhatt, S. A. Herbert and L. J. Barbour. "Tunable Anisotropic Thermal Expansion of a Porous Zinc (II) Metal–Organic Framework". *J. Am. Chem. Soc.* 135, 6411–6414, **2013**. (Cit. on p. 104).
- [301] C. Serre, F. Millange, C. Thouvenot, M. Nogués, G. Marsolier, D. Louër and G. Férey. "Very Large Breathing Effect in the First Nanoporous Chromium (III)-Based Solids: MIL-53 or Cr(III) (OH)·(O<sub>2</sub>C-C<sub>6</sub>H<sub>4</sub>-CO<sub>2</sub>)·(HO<sub>2</sub>C-C<sub>6</sub>H<sub>4</sub>-CO<sub>2</sub>H)<sub>x</sub>·H<sub>2</sub>O<sub>y</sub>". *J. Am. Chem. Soc.* 124, 13519–13526, **2002**. (Cit. on p. 105).
- [302] R. Matsuda, R. Kitaura, S. Kitagawa, Y. Kubota, T. C. Kobayashi, S. Horike and M. Takata. "Guest shape-responsive fitting of porous coordination polymer with shrinkable framework". *J. Am. Chem. Soc.* 126, 14063–14070, **2004**. (Cit. on p. 105).
- [303] L. Bellarosa, J. M. Castillo, T. Vlught, S. Calero and N. López. "On the Mechanism Behind the Instability of Isoreticular Metal–Organic Frameworks (IRMOFs) in Humid Environments". *Chem.–Eur. J.* 18, 12260–12266, **2012**. (Cit. on p. 105).

- [304] R. A. Sarmiento-Perez, L. M. Rodriguez-Albelo, A. Gomez, M. Autie-Perez, D. W. Lewis and A. R. Ruiz-Salvador. "Surprising role of the BDC organic ligand in the adsorption of CO<sub>2</sub> by MOF-5". *Microporous Mesoporous Mater.* 163, 186–191, **2012**. (Cit. on p. 105).
- [305] K. G. Ray, D. Olmsted, N. He, Y. Houndougbo, B. B. Laird and M. Asta. "van der Waals density functional study of CO<sub>2</sub> binding in zeolitic imidazolate frameworks". *Phys. Rev. B* 85, 085410, **2012**. (Cit. on p. 105).
- [306] H.-c. Guo, F. Shi, Z.-f. Ma and X.-q. Liu. "Molecular simulation for adsorption and separation of CH<sub>4</sub>/H<sub>2</sub> in zeolitic imidazolate frameworks". *J. Phys. Chem. C* 114, 12158–12165, **2010**. (Cit. on p. 105).
- [307] D. Andirova, C. F. Cogswell, Y. Lei and S. Choi. "Effect of the structural constituents of metal organic frameworks on carbon dioxide capture". *Microporous Mesoporous Mater.* 219, 276–305, **2016**. (Cit. on p. 105).
- [308] W.-W. He, G.-S. Yang, Y.-J. Tang, S.-L. Li, S.-R. Zhang, Z.-M. Su and Y.-Q. Lan. "Phenyl Groups Result in the Highest Benzene Storage and Most Efficient Desulfurization in a Series of Isostructural Metal–Organic Frameworks". *Chem.–Eur. J.* 21, 9784–9789, **2015**. (Cit. on p. 105).
- [309] Y. H. Hu and L. Zhang. "Amorphization of metal-organic framework MOF-5 at unusually low applied pressure". *Phys. Rev. B* 81, 174103, **2010**. (Cit. on p. 105).
- [310] L. Ma, A. Jin, Z. Xie and W. Lin. "Freeze Drying Significantly Increases Permanent Porosity and Hydrogen Uptake in 4,4-Connected Metal–Organic Frameworks". *Angew. Chem. Int. Edn.* 121, 10089–10092, **2009**. (Cit. on p. 106).
- [311] T. Bennett, J. Sotelo, J.-C. Tan and S. Moggach. "Mechanical properties of zeolitic metal–organic frameworks: mechanically flexible topologies and stabilization against structural collapse". *CrystEngComm* 17, 286–289, **2015**. (Cit. on p. 106).
- [312] A. Khutia, H. U. Rammelberg, T. Schmidt, S. Henninger and C. Janiak. "Water sorption cycle measurements on functionalized MIL-101Cr for heat transformation application". *Chem. Mater.* 25, 790–798, **2013**. (Cit. on p. 106).
- [313] S. Begum, S. Horike, S. Kitagawa and H. Krautscheid. "Water stable triazolyl phosphonate MOFs: steep water uptake and facile regeneration". *Dalton Trans.* 44, 18727–18730, **2015**. (Cit. on p. 106).
- [314] J. E. Mondloch, M. J. Katz, N. Planas, D. Semrouni, L. Gagliardi, J. T. Hupp and O. K. Farha. "Are Zr<sub>6</sub>-based MOFs water stable? Linker hydrolysis vs. capillary-force-driven channel collapse". *Chem. Commun.* 50, 8944–8946, **2014**. (Cit. on p. 106).
- [315] B. Widom. "Some topics in the theory of fluids". *J. Chem. Phys.* 39, 2808–2812, **1963**. (Cit. on p. 106).
- [316] W. L. Jorgensen, D. S. Maxwell and J. Tirado-Rives. "Development and testing of the OPLS all-atom force field on conformational energetics and properties of organic liquids". *J. Am. Chem. Soc.* 118, 11225–11236, **1996**. (Cit. on p. 106).
- [317] M. P. Tosi. "Cohesion of ionic solids in the Born model". *Solid state physics* 16, 1–120, **1964**. (Cit. on p. 106).
- [318] W. L. Jorgensen, E. R. Laird, T. B. Nguyen and J. Tirado-Rives. "Monte Carlo simulations of pure liquid substituted benzenes with OPLS potential functions". *J. Comput. Chem.* 14, 206–215, **1993**. (Cit. on p. 106).
- [319] A. Nemkevich, H.-B. Bürgi, M. A. Spackman and B. Corry. "Molecular dynamics simulations of structure and dynamics of organic molecular crystals". *Phys. Chem. Chem. Phys.* 12, 14916–14929, **2010**. (Cit. on p. 106).
- [320] C. Caleman, P. J. van Maaren, M. Hong, J. S. Hub, L. T. Costa and D. van der Spoel. "Force field benchmark of organic liquids: density, enthalpy of vaporization, heat capacities, surface tension, isothermal compressibility, volumetric expansion coefficient, and dielectric constant". *J. Chem. Theory Comput.* 8, 61–74, **2011**. (Cit. on p. 106).
- [321] W.-G. Shim, K.-J. Hwang, J.-T. Chung, Y.-S. Baek, S.-J. Yoo, S.-C. Kim, H. Moon and J.-W. Lee. "Adsorption and thermodesorption characteristics of benzene in nanoporous metal organic framework MOF-5". *Adv. Powder Technol.* 23, 615–619, **2012**. (Cit. on pp. 110, 111).

- [322] P. Welche, V. Heine and M. Dove. "Negative thermal expansion in beta-quartz". *Phys. Chem. Miner.* 26, 63–77, **1998**. (Cit. on p. 113).
- [323] A. K. Pryde, K. D. Hammonds, M. T. Dove, V. Heine, J. D. Gale and M. C. Warren. "Origin of the negative thermal expansion in  $ZrW_2O_8$  and  $ZrV_2O_7$ ". *J. Phys.: Condens. Matter* 8, 10973, **1996**. (Cit. on pp. 113, 114).
- [324] G. Barrera, J. Bruno, T. Barron and N. Allan. "Negative thermal expansion". *J. Phys.: Condens. Matter* 17, R217, **2005**. (Cit. on p. 113).
- [325] N. Lock, M. Christensen, Y. Wu, V. K. Peterson, M. K. Thomsen, R. O. Piltz, A. J. Ramirez-Cuesta, G. J. McIntyre, K. Norén, R. Kutteh et al. "Scrutinizing negative thermal expansion in MOF-5 by scattering techniques and *ab initio* calculations". *Dalton Trans.* 42, 1996–2007, **2013**. (Cit. on p. 113).
- [326] N. Lock, Y. Wu, M. Christensen, L. J. Cameron, V. K. Peterson, A. J. Bridgeman, C. J. Kepert and B. B. Iversen. "Elucidating negative thermal expansion in MOF-5". *J. Phys. Chem. C* 114, 16181–16186, **2010**. (Cit. on p. 113).
- [327] H. Fang, M. T. Dove and A. E. Phillips. "Common origin of negative thermal expansion and other exotic properties in ceramic and hybrid materials". *Phys. Rev. B* 89, 214103, **2014**. (Cit. on p. 113).
- [328] L. Sarkisov, R. L. Martin, M. Haranczyk and B. Smit. "On the flexibility of metal-organic frameworks". *J. Am. Chem. Soc.* 136, 2228–2231, **2014**. (Cit. on p. 114).
- [329] S. Devautour-Vinot, G. Maurin, F. Henn, C. Serre, T. Devic and G. Férey. "Estimation of the breathing energy of flexible MOFs by combining TGA and DSC techniques". *Chem. Commun.* 2733–2735, **2009**. (Cit. on p. 114).
- [330] K. D. Hammonds, V. Heine and M. T. Dove. "Insights into zeolite behaviour from the rigid unit mode model". *Phase Transitions* 61, 155–172, **1997**. (Cit. on p. 114).
- [331] M. T. Kapelewski, S. J. Geier, M. R. Hudson, D. Stück, J. A. Mason, J. N. Nelson, D. J. Xiao, Z. Hulvey, E. Gilmour, S. A. FitzGerald et al. " $M_2(m\text{-dobdc})(M = \text{Mg, Mn, Fe, Co, Ni})$  Metal–Organic Frameworks Exhibiting Increased Charge Density and Enhanced  $H_2$  Binding at the Open Metal Sites". *J. Am. Chem. Soc.* 136, 12119–12129, **2014**. (Cit. on p. 115).
- [332] D. Gygi, E. D. Bloch, J. A. Mason, M. R. Hudson, M. I. Gonzalez, R. L. Siegelman, T. A. Darwish, W. L. Queen, C. M. Brown and J. R. Long. "Hydrogen Storage in the Expanded Pore Metal–Organic Frameworks  $M_2(\text{dobpd}) (M = \text{Mg, Mn, Fe, Co, Ni, Zn})$ ". *Chem. Mater.* 28, 1128–1138, **2016**. (Cit. on p. 115).
- [333] T. Pham, K. A. Forrest, R. Banerjee, G. Orcajo, J. Eckert and B. Space. "Understanding the  $H_2$  Sorption Trends in the M-MOF-74 Series ( $M = \text{Mg, Ni, Co, Zn}$ )". *J. Phys. Chem. C* 119, 1078–1090, **2014**. (Cit. on p. 115).
- [334] M. H. Rosnes, M. Opitz, M. Frontzek, W. Lohstroh, J. P. Embs, P. A. Georgiev and P. D. Dietzel. "Intriguing differences in hydrogen adsorption in CPO-27 materials induced by metal substitution". *J. Mater. Chem. A* 3, 4827–4839, **2015**. (Cit. on p. 115).
- [335] T. Pham, K. A. Forrest, J. Eckert and B. Space. "Dramatic Effect of the Electrostatic Parameters on  $H_2$  Sorption in an M-MOF-74 Analogue". *Crystal Growth & Design* 16, 867–874, **2015**. (Cit. on p. 115).
- [336] J. Sánchez-Láinez, A. Veiga, B. Zornoza, S. R. G. Balestra, S. Hamad, A. R. Ruiz-Salvador, S. Calero, C. Téllez and J. Coronas. "Tuning the separation properties of zeolitic imidazolate framework core-shell structures via post-synthetic modification". *J. Mater. Chem. A* 5, 25601–25608, **2017**. DOI: 10.1039/c7ta08778k. (Cit. on p. 187).
- [337] A. Sławek, J. M. Vicent-Luna, B. Marszałek, S. R. G. Balestra, W. Makowski and S. Calero. "Adsorption of n-Alkanes in MFI and MEL: Quasi-Equilibrated Thermodesorption Combined with Molecular Simulations". *J. Phys. Chem. C* 120, 25338–25350, **2016**. DOI: 10.1021/acs.jpcc.6b06957. (Cit. on p. 187).

- [338] P. Gómez-Álvarez, J. Perez-Carbajo, S. R. G. Balestra and S. Calero. "Impact of the Nature of Exchangeable Cations on LTA-Type Zeolite Hydration". *J. Phys. Chem. C* 120, 23254–23261, **2016**. DOI: 10.1021/acs.jpcc.6b06916. (Cit. on p. 188).
- [339] A. Torres-Knoop, S. R. G. Balestra, R. Krishna, S. Calero and D. Dubbeldam. "Entropic Separations of Mixtures of Aromatics by Selective Face-to-Face Molecular Stacking in One-Dimensional Channels of Metal-Organic Frameworks and Zeolites". *ChemPhysChem* 16, 532–535, **2014**. DOI: 10.1002/cphc.201402819. (Cit. on p. 188).
- [340] S. Rodriguez-Gomez. "El metodo Monte Carlo". *MoleQla* 5, 133–135, **2012**. ISSN: 2173-0903. (Cit. on p. 188).
- [341] S. Rodriguez-Gomez. "Diagrama de fases de un sistema de esferas duras". *MoleQla* 6, 161–162, **2012**. ISSN: 2173-0903. (Cit. on p. 188).
- [342] S. R. G. Balestra, R. Bueno-Perez and S. Calero. *Genetic Algorithm IAST*. 2016. DOI: 10.5281/zenodo.165844 (cit. on p. 188).
- [343] J. G. Min, A. Luna-Triguero, Y. Byun, S. R. G. Balestra, J. M. Vicent-Luna, S. Calero, S. B. Hong and M. Cambor. "Stepped Propane Adsorption in Pure-Silica ITW Zeolite". submitted *Langmuir*, Manuscript ID: la-2018-00628f. 2018 (cit. on p. 188).



# Appendices



---

# Appendix

# A

## Chapter 3

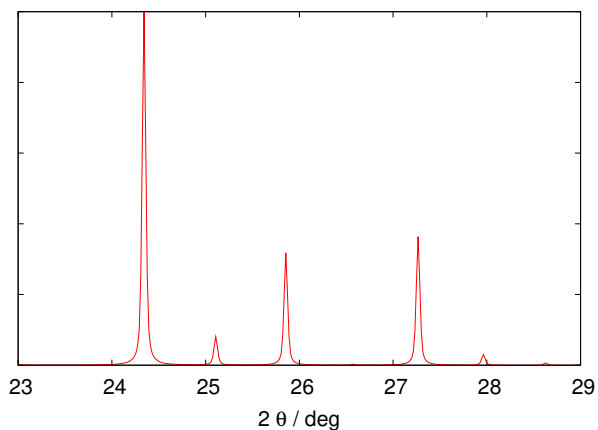


**Figure A1:** X-ray diffraction patterns using  $\text{CuK}\alpha$  radiation for the  $\text{Pm}\bar{3}$  structure. Atomic positions were collected from an energy minimisation calculation from  $\text{Im}\bar{3}\text{m}$  structure (Figure 5 in the main text). We do not know the real size of this hypothetical structure and we have rescaled the lattice size by the length of the unit cell of the experimental structure  $\text{I}\bar{4}\bar{3}\text{m}$   $a = 14.62\text{\AA}$ .

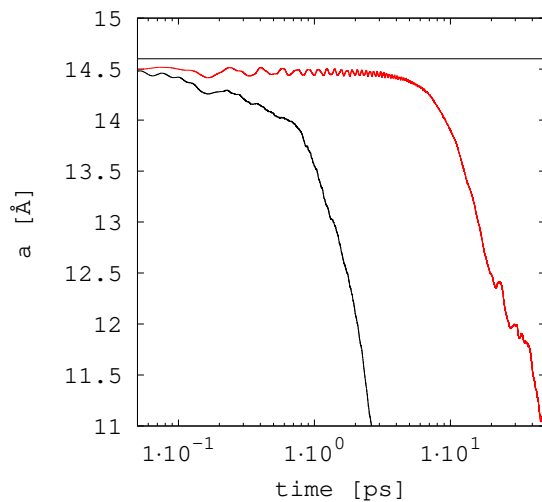


**Figure A2:** Length of unit cell  $a$  versus time  $t$  using the force field of Demontis (non-charged model). Red line represents the lattice size for 11 K and black line for 295 K. MD NPT was used to study the evolution of the lattice size using an integration time step of  $\tau = 5 \times 10^{-4}$  ps. This force field is not stable in NPT-ensemble calculations and always collapsed.

# Appendix

# B

## Chapter 4

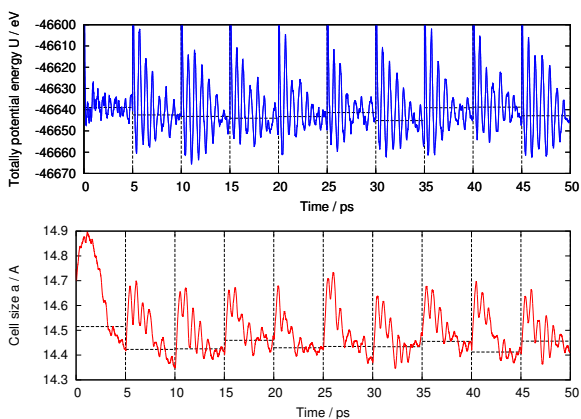


**Figure B1:** Variation of the potential energy (top) and cell size (bottom) with the number of MD simulation steps, for ten MC/EM/MD cycles, for Na-RHO. Horizontal dashed lines represent the average potential energy and cell size, respectively. Vertical dashed lines represent boundaries between cycles. The average cell parameter is  $\langle a \rangle = 14.43 \text{ \AA}$ . Only the last 1 ps for each step are used to calculate the average value.

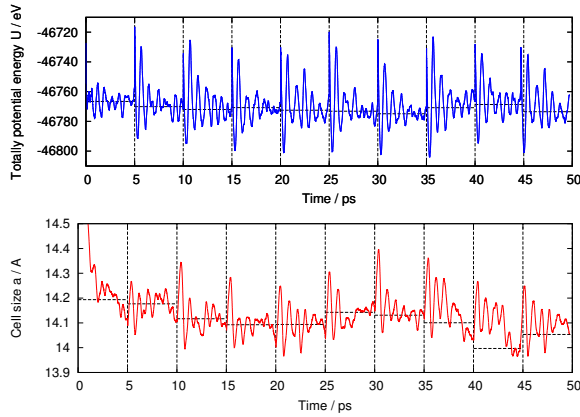


**Figure B2:** Variation of the potential energy (top) and cell size (bottom) with the number of MD simulation steps, for ten MC/EM/MD cycles, for Li-RHO. The average cell parameter is  $\langle a \rangle = 14.43 \text{ \AA}$ .

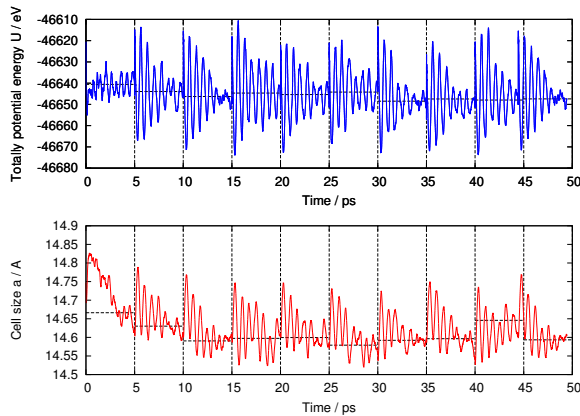


**Figure B3:** Variation of the potential energy (top) and cell size (bottom) with the number of MD simulation steps, for ten MC/EM/MD cycles, for K-RHO. The average cell parameter is  $\langle a \rangle = 14.43 \text{ \AA}$ .

The Quickstep program [1], from the CP2K package [2], was used for the *ab-initio* Molecular Dynamics. simulations. The PBE exchange-correlation functional was used [3], and the inclusion of van der Waals interactions was improved by using D3 Grimme's dispersion corrections [4]. The basis set were triple-zeta, of the Goedecker-Teter-Hutter (GTH) type, with the corresponding pseudopotentials [5]. NVT simulations of 50 ps were performed at 300 K, using a time step of 0.5 fs.

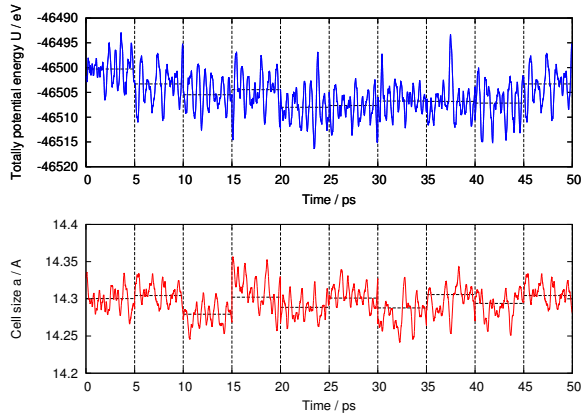


**Figure B4:** Variation of the potential energy (top) and cell size (bottom) with the number of MD simulation steps, for ten MC/EM/MD cycles, for Sr-RHO. The average cell parameter is  $\langle a \rangle = 14.43 \text{ \AA}$ .

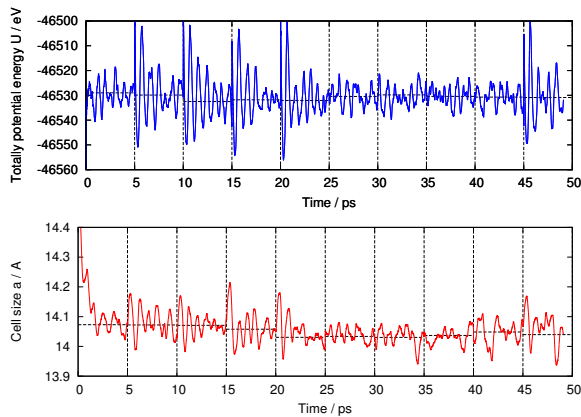


**Figure B5:** Variation of the potential energy (top) and cell size (bottom) with the number of MD simulation steps, for ten MC/EM/MD cycles, for Ca-RHO. The average cell parameter is  $\langle a \rangle = 14.43 \text{ \AA}$ .



---

## Chapter 5

### C.1. Introduction

Zeolites find an extraordinarily wide commercial applicability,[6] and this in turn fosters further research aimed to the synthesis of zeolites with new structures and compositions [7]. Among the many factors determining the phase that crystallizes in a zeolite synthesis [8], the organic structure directing agents (SDA) [9], fluoride anions [10] and framework elements other than Si and Al (Ge, Zn, Be, Ga . . . ) may afford the discovery of new zeolite structures [11]. In particular, Germanium, specially when used together with fluoride, tend to produce structures with double 4-ring units (D4R).[12–14] Despite the low stability of Ge-zeolites upon both calcination,[15] and hydrolysis by ambient moisture of the calcined materials,[16] the discovery of new Zeolite Framework Types (ZFT)[17], even if unstable, is still of interest. In fact, the weakness of Ge-zeolites has been advantageously used to derive new materials from them through the assembly-disassembly-organisation-reassembly strategy (ADOR), which has so far produced several interesting zeolites that are, in addition, more stable than the parent one [18–21]. These derived zeolites may be *unfeasible* to obtain by the conventional hydrothermal routes, adding interest to Ge-zeolites [22]. On the other hand, Ge-zeolites may be stabilized by postsynthetic treatments by substituting Ge by Si or Al [16, 23–25]. Finally, unstable but structurally interesting zeolites discovered by using Ge, such as the chiral zeolite STW [26], can become a target for the synthesis of more stable materials with the same structure, as was the case for the STW pure silica version, HPM-1 [27, 28].

STW was first realized as a germanosilicate [26]. Its interest relies on its chiral nature and the presence of a helicoidal medium pore channel. Every single crystal is homochiral but standard synthesis procedures using achiral organic SDA are expected to yield racemic conglomerates [26–28]. However, very recently it has been possible to prepare enantiomerically enriched scalemic conglomerates by using an enantiomerically pure chiral dication, and the materials proved to yield small but sig-

nificant enantiomeric excess in both asymmetric catalysis and adsorption processes [29]. These syntheses produced germanosilicate and aluminogermanosilicates, but recent studies suggest homochiral STW silica phases may as well be possible [30]. These silica zeolites are expected to be not only much more stable but also more amenable to selective separations, since the larger flexibility of  $\text{GeO}_2$  frameworks appears to be detrimental to chiral recognition [31]. Here we report that substitution of Si by Ge in the chiral D4R-containing zeolite structure STW can be attained for any value of the Ge molar fraction ( $\text{Ge}_f = \text{Ge}/(\text{Ge} + \text{Si})$ ). By combining experiment and theory we have been able to get significant insight into that system, particularly on the energetics of the zeolite, the unit cell expansion, which is buffered at the low  $\text{Ge}_f$  side, the previously controversial assignment of  $^{19}\text{F}$  MAS NMR resonances, and the differential occupation of crystallographic sites as  $\text{Ge}_f$  increases.

## C.2. Methodology

### C.2.1. Synthesis

All the zeolite syntheses were done using equimolar amounts of hydrofluoric acid and 2-ethyl-1,3,4-trimethylimidazolium (2E134TMI) hydroxide. 2E134TMI was synthesized as iodide salt and exchanged to the hydroxide form as previously reported.[32] The synthesis mixture was prepared by adding (if required) first tetraethylorthosilicate (TEOS, 98% Aldrich) and then (if required) germanium dioxide (99.998% Aldrich) to a concentrated solution of 2E134TMI hydroxide. The mixture was stirred at room temperature allowing evaporation of ethanol (if TEOS was used) and water, until the desired composition was reached. Evaporation was monitored by weight. Then, hydrofluoric acid (48 wt%, Sigma–Aldrich) was added to the gel and stirred with a spatula for approximately 15 minutes. The obtained gel was transferred to Teflon vessels inside stainless steel autoclaves, which were heated in an oven at a temperature of 175 °C while tumbling at 60 rpm. At preselected times (generally close to 24, 48, 144 and 240 hours), the autoclaves were removed from the oven and quenched and the product filtered on paper or centrifuged, washed with deionized water and dried at 100 °C. The final composition of the gel was:  $(1 - x)\text{SiO}_2 : x\text{GeO}_2 : 0.5 \text{ 2E134TMIOH} : 0.5 \text{ HF} : 4\text{H}_2\text{O}$ , where  $x = \text{Ge}/(\text{Si} + \text{Ge})$  is the molar fraction of germanium oxide, which will be expressed in the following as  $\text{Ge}_f$ .

### C.2.2. Characterization

Power X-ray diffraction was performed using a Bruker D8 Advance diffractometer, with  $\text{Cu } K_\alpha$  radiation in the 3.5–45 °  $2\theta$  range. The unit cell of HPM-1 samples with varying  $\text{Ge}_f$  were refined by a least squares regression procedure using the program UnitCell and 16 reflections uniquely indexed in space group  $\text{P6}_122$ , covering the 8–30 °  $2\theta$  range.[33] Synchrotron X-ray powder diffraction data were collected at the SpLine BM25A at the ESRF, Grenoble, in capillary mode (0.8 mm diameter) using monochromatic radiation ( $\lambda = 0.56383 \text{ \AA}$ ) for the samples synthesized with  $\text{Ge}_f = 0.4, 0.6$  and

1.0. Rietveld refinement was performed using GSAS,[34] under the EXPGUI graphical interface.[35] C,N,H analyses were performed with a LECO CHNS-932 instrument. Ge and Si chemical analysis were performed by Inductively Couple Plasma–Mass Spectrometry (ICP-MS) using an ICP-MS NexION 300XX equipment.  $^{19}\text{F}$ ,  $^{29}\text{Si}$ ,  $^1\text{H}$  and  $^{13}\text{C}$  MAS NMR experiments were recorded on a Bruker AV 400WB, as described elsewhere.[36] Field emission scanning electron microscopy (FE-SEM) images were obtained with a FEI NOVA NANOSEM 230 without metal coating. Thermogravimetric analyses were obtained with an SDT Q600 from TA Instruments at a heating rate  $10^\circ\text{C min}^{-1}$  under an air flow of 100 mL/min.

## C.3. Results and discussion

### C.3.1. Synthesis

The use of 2E134TMI and fluoride allows the synthesis of HPM-1 (STW) zeolites in the whole 0-1 range of  $\text{Ge}_f$  molar fractions (see Table C2). The robustness of this type of synthesis that combines the structure directing effects of both 2E134TMI and fluoride ions is revealed not only by the full Si-Ge substitutional range attainable but also by the fact that STW is the only zeolite that crystallized within a relatively wide range of crystallization times. This clearly reveals the superior structure-directing effect of 2E134TMI compared to the original organic SDA (diisopropylamine), which produced a mixture of phases,[26] or a more recent SDA (N,N-diethylethylendiamine) which produced a pure STW phase in a limited range of conditions (particularly regarding the  $\text{Ge}_f$  compositional range).[37] For another recent SDAs based in the imidazolium ring (pentamethylimidazolium), only the synthesis of either pure silica STW or of intermediate germanosilicates and germanoaluminosilicates have been so far reported.[28–30] We also point out that the synthesis of pure  $\text{GeO}_2$ -STW had never been described before.

The combined structure-directing ability of 2E134TMI and  $\text{F}^-$  is likely helped up to some extent by the tendency of Ge to produce zeolites containing D4R (a structure-direction tendency shared with fluoride). However, and somehow surprisingly, the crystallization of the pure Ge-end member appears to be the less favorable one within the series, since only in that case we observed noticeable deviations from the noted crystallization of STW (see last five entries in Table C2): at short times (27 hours) we collected no solids by filtration or centrifugation, while at long times (over 100 hours) a dense quartz-like phase, and latter an argutite-like phase, started to compete. We also observed some reproducibility problems at  $\text{Ge}_f=1$ , since in two different runs we obtained either a very small yield of pure HPM-1 at 113 hours or HPM-1 with some quartz-like  $\text{GeO}_2$  in a higher yield at 96 and 102 h.

At the more siliceous side of the series, STW is the only crystalline phase produced and its crystallization markedly accelerates when Ge substitutes for Si even in very small fractions (compare entries 1, 5 and 9 in Table C2). It is interesting that, for any of the crystallization times producing STW, the yield of zeolite goes through a

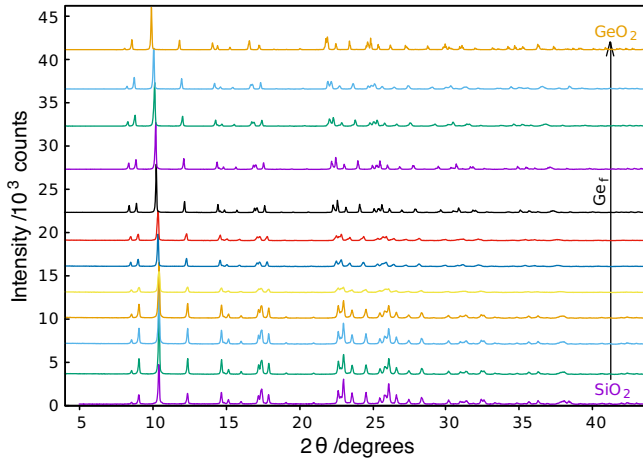


**Figure C1:** Powder XRD of the (Ge,Si)-HPM-1 series with varying germanium molar fractions in the gel (from bottom to top)  $Ge_f = 0.00, 0.009, 0.019, 0.032, 0.09, 0.167, 0.20, 0.40, 0.60, 0.80, 0.90$  and 1.00. All the samples were crystallized at  $175^\circ\text{C}$  for 144 hours, except the top one, pure  $\text{GeO}_2$ -HPM-1, which was crystallized for 113 h.

maximum as  $Ge_f$  increases and then decreases significantly, so that the value for the pure germanate material is much lower than for the pure silicate end member, Figure 5.1. The oxide-based yield shows even stronger differences: the value for the Ge-end member is less than half that of the Si-end member and less than a quarter of the maximum at  $Ge_f \approx 0.4$ ).

### C.3.2. Characterisation

The powder XRD patterns of the STW samples, Figure C1, display clear changes in the positions of the different reflections as the composition changes. This is, in principle, as expected because of the Ge substitution for Si and the different size and different T-O lengths of Si and Ge. There are abundant examples in the literature of close to linear changes of unit cell parameters as a function of T-atom substitution, [38–40] although at least one exception showing a reversal of the expected trend also exists. [41]

In the case of Si,Ge-STW, the overall trend is the expected expansion as the Ge fraction increases and the correlation is indeed close to linear, specially for  $Ge_f > 0.2$ , for both the unit cell edges size and volume. However, a careful inspection at the high silica side of the series shows little, if any, noticeable change in the bottom five traces of Figure C1. In fact, the refined unit cells do not change appreciably for small substitutions of Si by Ge ( $Ge_f < 0.2$ ). As seen in Figure C3 the overall increase in  $a$ ,  $c$  and  $V$  from the pure silica to the pure germania end members is of around 4.4, 3.3

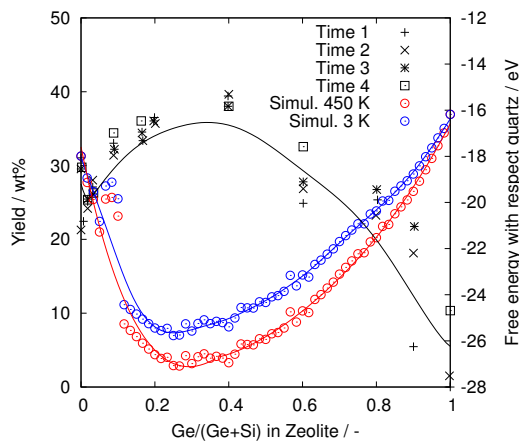


**Figure C2:** Yield of solids as a function of the Ge molar fractions in the zeolites (black dots). At any given  $Ge_f$  different data markers refer to different crystallisation times. Bézier black curve fitted from experimental points is shown in the figure as a guide to the eye.

and 12.6%. However, in the  $Ge_f$  range from 0 to 0.1 there are essentially no changes, instead of the expected increase in unit cell to around  $a = 11.95 \text{ \AA}$ ,  $b = 29.78 \text{ \AA}$  and  $V = 3690 \text{ \AA}^3$  if the overall trend were followed.

We propose that, since the  $[\text{GeO}_{4/2}]$  tetrahedron is larger but also more flexible than the  $[\text{SiO}_{4/2}]$  tetrahedron, small amounts of Ge can enter the framework without significantly altering the unit cell size. This buffering effect appears to occur in the 0-0.1 range and contrasts with the relatively large changes in the  $^{29}\text{Si}$  and specially  $^{19}\text{F}$  spectra of the same samples (see below). This could be related to a preferential sitting of one Ge atom in each D4R in this  $Ge_f$  range, see below. In contrast, in Ge-MFI, lacking D4R, Kosslick et al. found a significant increase in the cell parameters in the 0-0.13  $Ge_f$  range [42].

The infrared spectra of a series of as-made STW zeolites prepared from gels with different  $Ge_f$  are shown in Figure C9. Apparently, the overall effect of the presence of Ge is to cause a new set of vibrational bands at lower wavenumbers, rather than simply redshifting the bands.

Figure C10 shows that as the  $Ge_f$  increases the crystal habit changes in the sense of gradually reducing the prismatic faces. Thus, the 'double tip pencil' habit (i.e. hexagonal prisms ending in hexagonal pyramids) characteristic of pure silica and very high silica HPM-1 almost completely disappears for  $Ge_f \geq 0.2$ , which consists of hexagonal bipyramids.

The thermogravimetric analyses of HPM-1 solids prepared at different  $Ge_f$  ratios are provided in the supplementary information (Figure C11). As the Ge fraction increases the weight losses decrease, as expected for the larger atomic mass of Ge compared to Si. Further, the temperature of the main weight loss also increases and,

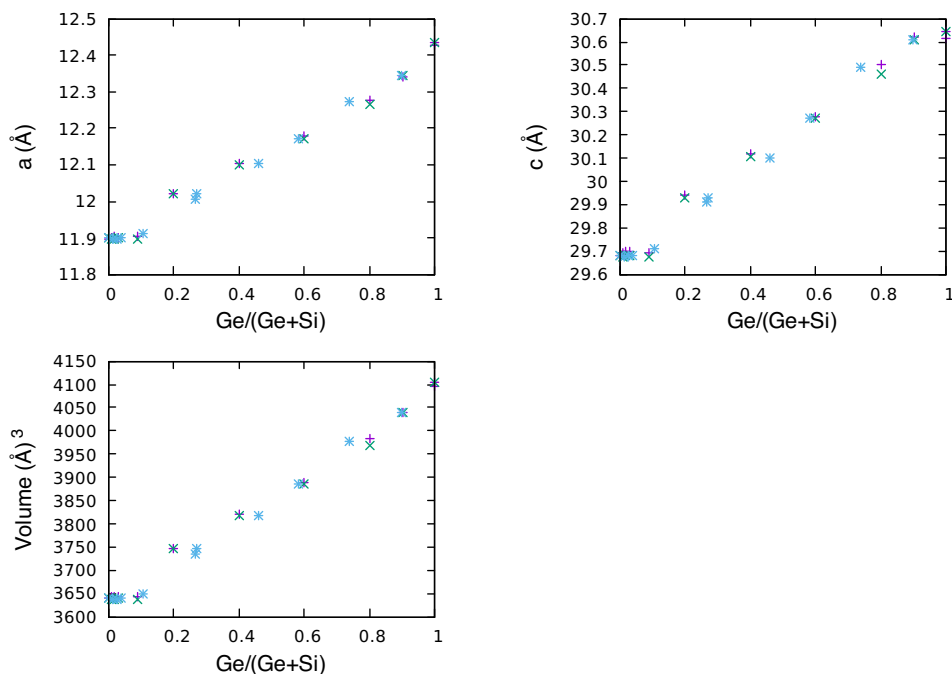


**Figure C3:** Variation of the unit cell edge  $a$  (top), the unit cell edge  $c$  (middle), and the volume  $V$  (bottom) of (Ge,Si)-STW as a function of the Ge fraction in the gel. Blue asterisks correspond to  $Ge_f$  experimentally measured by ICP.

for the higher  $Ge_f$  values, several weight gain events are clearly observed (starting mainly around 700 °C and again around 900 °C), both effects likely resulting from the complex nature of oxidation–reduction processes that Ge-containing zeolites typically undergo (notably including framework  $GeO_2$  reduction and reoxidation) as very recently reported.[15]

### C.3.3. Multinuclear NMR

$^{13}C$  and  $^1H$  MAS NMR spectra (not shown) demonstrate the organic SDA is occluded intact in the zeolites. The  $^{29}Si$  CP MAS NMR spectra of several relevant germanosilicate HPM-1 samples are shown in Figure C4. The lower trace in the figure is the direct irradiation  $^{29}Si$  MAS NMR spectrum of the pure silica material, which shows two clear resonances at -106.2 and -113.6 ppm, with a relative intensity ratio close to 4:1, assigned to Si in crystallographic sites  $T_{1-4}$  and  $T_5$ , respectively.[32] These correspond to sites in and out of D4R, respectively. Interestingly, introduction of Ge causes a new resonance to appear at lower fields (ca. -103.2 ppm for a  $Ge_f=0.167$ ). If Ge shows a preference to occupy sites within D4R units, see below, the new res-

onance at -103.2 ppm may be ascribed to  $\text{Si}(\text{OSi})_3\text{OGe}$  sites in D4R. Schmidt et al. found a similar downfield shift for  $\text{Si}(\text{Si}_3\text{Ge})$  (-102 ppm) compared to  $\text{Si}(\text{Si}_4)$  resonances (-108 ppm) in silicogermanate LTA zeolite.[43] For  $\text{Ge}_f=0.20$  all the resonances experience a small upfield shift (to 103.7, -107.5 and -114.9 ppm, respectively). Upon a further increase in the level of Ge for Si substitution to  $\text{Ge}_f=0.40$ , the lower field signal is the dominant one and clearly consists of several resonances, while the high field side of the spectrum consists of at least three heavily overlapped resonances (-108.4, -111.8 and -114.9 ppm, respectively), suggesting site T5, not belonging to D4R, may be now populated by  $\text{Si}(\text{OSi})_2(\text{OGe})_2$  and  $\text{Si}(\text{OSi})_3\text{OGe}$  and  $\text{Si}(\text{OSi})_4$ , respectively. This is not unexpected if the fraction of Ge in D4R sites is significant. As the Si content decreases further, the spectra becomes much broader, blurry and noisy. We cannot perform a more quantitative analysis of the spectra because the intensities in the CP spectra depend on the proximity to protons and the direct irradiation  $^{29}\text{Si}$  MAS NMR spectra require prohibitively long recycle delays to achieve spectra with decent signal to noise ratios (see Figure C12).

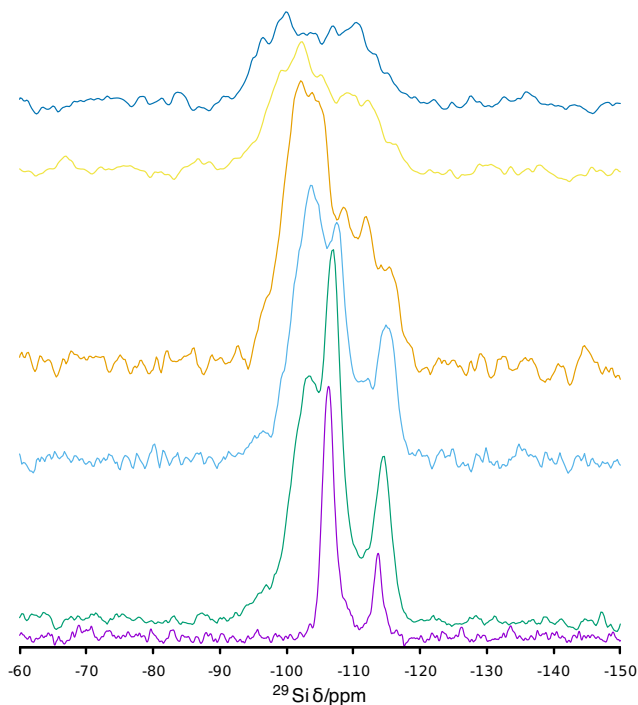


**Figure C4:**  $^{29}\text{Si}$  MAS spectra of (Ge,Si)-STW with  $\text{Ge}_f = 0.00, 0.166, 0.20, 0.40, 0.60$  and  $0.80$  (from bottom to top). The lower trace is a direct irradiation spectrum while the rest were collected under cross polarization.

More interesting for a better understanding of these materials is the  $^{19}\text{F}$  MAS

NMR spectroscopy (Figure C5), which is much sensitive to the type of cavity in which fluoride resides and to its kind of interaction with framework atoms. In the case of zeolites containing D4R, fluoride is typically occluded within this small cavity, and its chemical shift depends on the composition of the D4R. The pure silica HPM-1 material displays a single resonance at around -35.7 ppm, that we will call here resonance 'I'. The assignment of resonance I to  $F^-$  occluded in purely siliceous D4R (i.e., 8Si,0Ge D4R) is well established for several pure silica zeolites,[44–47] as well as for pure silica STW,[32] despite it appears quite downfield shifted compared to more typical values (-37/-40ppm). When Ge is introduced in the synthesis mixture, even in minute amounts ( $Ge_f = 0.009$ ), a new resonance appears around -16.6ppm (resonance 'II'). As more Ge is introduced, this resonance first increases, then decreases in intensity, while it experiences an upfield shift (up to -17.5 ppm). Upon increasing the Ge content above  $Ge_f = 0.032$  a broad resonance ('III') appears around -7.5 ppm and increases in intensity while shifts to lower field up to  $Ge_f = 0.4$ . Then, an apparent upfield shift starts, while the resonance becomes narrower. This apparent change in shift, the narrowing of the band, and prior literature reports on other zeolites lead us think that there is a fourth resonance (IV, around -10/-11 ppm), rather than one that first moves downfield then jumps upfield, and that at intermediate Ge fractions resonances III and IV severely overlap. Since the pure germanate end-member displays a single, relatively narrow and pretty symmetrical resonance IV at -11.0 ppm, we can safely assign it to  $F^-$  occluded in D4R built only of Ge and O (i.e., 0Si,8Ge D4R) (literature values vary roughly in the -9 to -16 ppm).[48]

The assignment of the remaining  $^{19}F$  resonances, II and III, is intriguing and has been the subject of debate. There are typically four types of resonances in the  $^{19}F$  MAS NMR spectra of (Si,Ge)-zeolites containing D4R, despite the fact that, in principle, there may be up to nine different Ge contents in a D4R unit (from 0 to 8) and for several of these contents there may be a number of different configurations of Si and Ge within the D4R. The scarce number of resonances could be just due to resonance overlapping, to some configurations being prohibited or scarce or to an insensitiveness of  $^{19}F$  to certain differences among configurations and compositions. Sastre et al. assigned resonances at -38, -20 and -8ppm in silicogermanates ITQ-17 and ITQ-7 to  $F^-$  in nD4R with, respectively, 8, 7, and either 5 or 6 Si atoms, being more favorable to 5.[49, 50] Wang et al. studied octadecasil silicogermanates synthesized with three different SDA cations, covering for two of them the whole range of  $Ge_f$  from 0 to 1. The pure silica and pure germania end members present resonances at around -38 and -15 ppm, which are thus assigned to  $F^-$  in D4R with 8 and 0 Si, respectively. For intermediate compositions resonances around -8 and -19 ppm were assigned to the presence of 4 and 6 Si per D4R, respectively, and the authors concluded there is an ordered pattern of Ge insertion in the D4R units in which Ge-Ge pairing tend to be avoided.[52] To complicate things, each one of these resonances may change position depending on the  $Ge_f$ ,[51] or occluded SDA cation.[53]

Latter on, Sastre et al. suggested that there may exist direct covalent Ge-F bonds in D4R units, with expansion of the coordination of the involved Ge to 5.[54] The same authors calculated the chemical shifts of fluoride occluded in different configurations

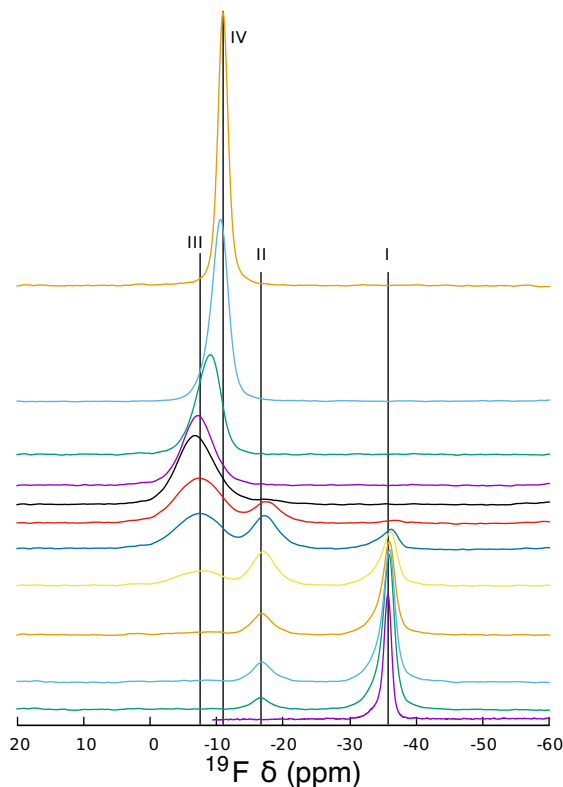


**Figure C5:**  $^{19}\text{F}$  MAS NMR spectra of (Ge,Si)-STW with  $\text{Ge}_f = 0.00, 0.009, 0.019, 0.032, 0.09, 0.166, 0.20, 0.40, 0.60$  and  $0.80, 0.9$  and  $1.00$  (from bottom to top). The four types of resonances found are marked with the vertical lines I-IV, placed at the position where they appear at lower  $\text{Ge}_f$  (except line IV, placed at the resonance of the pure germanate.)

of D4R units containing 0, 1, 2, 3, 4 or 8 Ge atoms (but not 5,6,7, for undisclosed reasons) and concluded that, due to the displacement of fluoride out of the cage center and towards a corner, the main factor determining the chemical shift of fluoride was the nature of the 4 closest T, i.e., the  $n$  number of closest Si and  $m$  number of closest Ge, with  $n + m = 4$ . [55] Thus, the chemical shift of fluoride increased (values more positive) when the number  $m$  of Ge atoms closer to F increased. This could explain that fluoride in D4R containing  $4\text{Si}4\text{Ge}$  would resonate at a similar chemical shift as those in  $5\text{Si}3\text{Ge}$ . This view differs significantly from that of Wang et al. described above, [52] because if Ge-Ge pairings were avoided the  $4\text{Si}4\text{Ge}$  D4R unit would have  $m = 0$  Ge as closest neighbours to F.

After deconvolution of the assumed III+IV resonance in the spectra of materials with  $\text{Ge}_f$  in the 0.6–1.0 range, the evolution of the four resonances as a function of

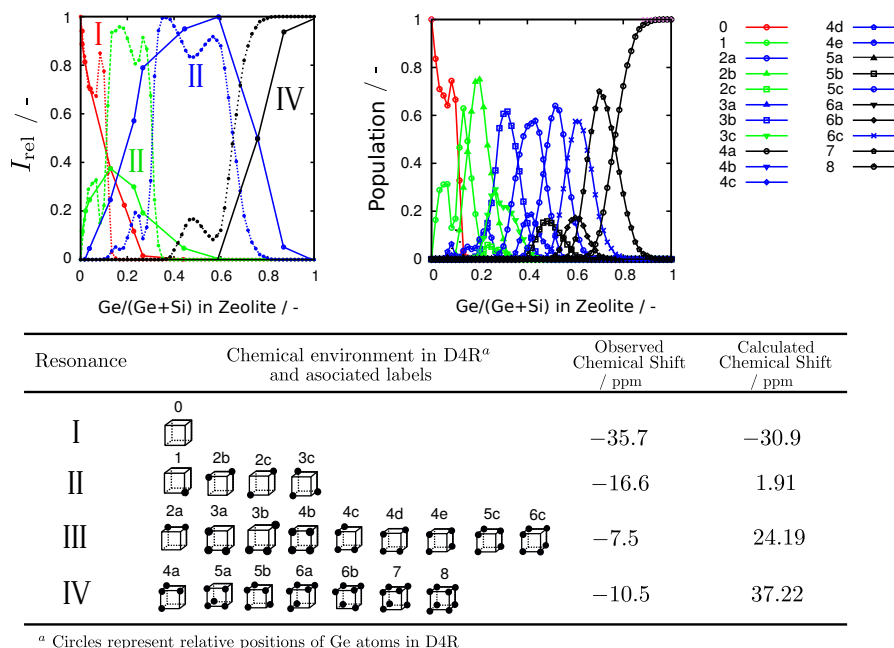


**Figure C6:** Top-Left: Relative intensities of the four resonances observed in the  $^{19}\text{F}$  MAS NMR spectra of (Ge,Si)-STW zeolites as a function of the Ge fraction in the zeolites,  $\text{Ge}_f$  (Solid lines: experimental; Dotted lines: convolution of calculated populations of chemical environments in D4R, grouped by similar calculated chemical shift). Top-Right: Calculated population of chemical environments in D4R as a function of  $\text{Ge}_f$ . Bottom: Our proposed assignment of observed  $^{19}\text{F}$  MAS NMR resonances to chemical environments in D4R, with experimental and averaged calculated chemical shifts.

the Ge content in the gel is shown in Figure C6, top left, solid lines. It is worth noting that, at the high silica side of the substitutional series, the  $^{19}\text{F}$  resonances change very drastically as the  $\text{Ge}_f$  increases. The sharp decrease of resonance I, which is replaced for resonance II and then III occurs in a range of  $\text{Ge}_f$  that, as discussed above, shows essentially no variation in unit cell parameters. For a  $\text{Ge}_f$  of 0.09 the spectrum consists of resonances I, II and III with roughly similar intensities ( $\approx 37:38:25$ ), while the unit cell shows essentially no variation in dimensions.

At first sight, there would be little question about the assignments of resonances I, II and IV. In the case of resonances I and IV the assignment gets strong support from the spectra of the pure  $\text{SiO}_2$  and  $\text{GeO}_2$  end members, respectively, in which resonances I and IV have no other possible assignment. In the case of II, its appearance at very low  $\text{Ge}_f$  together with its fast grow and decay as  $\text{Ge}_f$  increases, also supports the assignment to 7Si1Ge-D4R. Resonance III is, obviously, the problem, and the fact that there is only one such resonance implies that either there is a very ordered pattern of Ge introduction (as proposed by Wang et al.) [52] or the resonance actually consists

of several resonances overlapped (as suggested by Pulido et al.).[55]

### C.3.4. Rietveld refinement

The starting model for Rietveld refinement of samples prepared with  $Ge_f = 0.4, 0.6$  and 1 was the refined structure of pure silica HPM-1,[32] in space group  $P6_122$  modified to have the unit cell dimensions determined from conventional powder XRD data and a Ge occupation of all crystallographic positions initially set at 0.4, 0.6 and 1.0, respectively (Si occupancies of 0.6, 0.4 and 0.0, respectively). Although the sample with  $Ge_f = 1$  appeared as phase-pure in the conventional XRD pattern, synchrotron radiation showed the presence of small traces of quartz-like  $GeO_2$ , and the corresponding regions were excluded from the refinement. A Lobanov and Alte da Veiga absorption correction was applied.[34] Scale factor, unit cell and profile parameters were refined, with a shifted Chebyshev function initially with 16 fixed parameters to simulate the background. Then, the Ge, Si, O and F atoms were allowed to move, initially with soft restraints on T-O and O-O distances and with Ge and Si in each crystallographic site constrained to move together. Then, the position and orientation of the organic SDA was refined as a rigid body consisting of the imidazolium ring with the three methyl substituents as a rigid unit plus the ethyl group as a satellite that could freely rotate along the C2-C9 bond. The hydrogen atoms were omitted but the fractional occupancies of the C atoms were adjusted to account for the electrons of the bonded H. The weight of the distance restraints was gradually reduced and eventually eliminated. In the final stages of the refinements, atom displacement factors (grouped by atom type), background and fractional occupancies of Ge and Si in each crystallographic site (constrained to amount to a full occupancy of each site) were included in the refinement. Final crystallographic data are summarised in Tables C3, the final Rietveld plots are given in Figures C13, C14 and C15.

The final refined structures have reasonable bond distances and angles (see Table C4 and all show the fluoride anions slight off the center of the D4R cages and closer to T1 than to any other tetrahedral atom in the framework. The refined occupancies of Ge and Si in the  $Ge_f = 0.4$  and 0.6 samples are close to the nominal values (0.40 and 0.57, respectively) and both show a distinct preference for Si rather than Ge to occupy T5 (the non-D4R site) and a Ge preference to occupy preferentially sites T1 and T2 over T3 and T4 (see Table C1). The site occupancies observed in these samples roughly agree with the order of preferential occupations determined from our calculations (see Figure 5.6). In both cases, as the amount of Ge increases, T1 and T2 are populated before T3 and T4, which in turn get occupied preferentially over T5. There are, however, quantitative discrepancies between both results. The first one is that the differences in occupations between sites T1 and T2 and between sites T3 and T4 are larger in our calculations than in the experiments. And the second discrepancy is that experimentally T5 starts being slightly populated at  $Ge_f = 0.4$ , and at  $Ge_f = 0.6$  its population is already roughly one third of either one of T3 and T4, while at that point T1 and T2 are not fully occupied by Ge yet. This is in clear contrast with the predicted values, which show that T5 does not start being populated by Ge

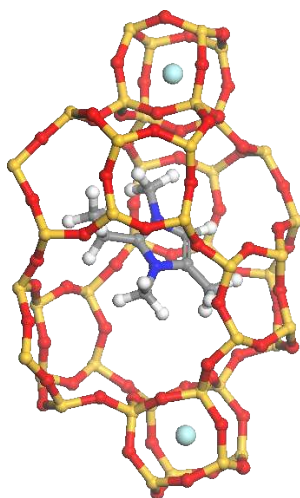


**Figure C7:** The organic SDA cation inside the large  $[4^6 5^8 8^2 10^2]$  cage (only one of the two symmetrical cations is shown) and the fluoride anion inside the small  $[4^6]$  cage of Ge-HPM-1.

until all other sites are filled. Roughly speaking, our calculations predict more strict preferential occupations and, hence, more abrupt changes in population trends. There are mainly two possible explanations for these discrepancies. First, we could ascribe the differences to inaccuracies of the energy calculation employed, which might be making T5 sites too unstable compared with the other sites. While this might be the case, it is also possible that we are neglecting some factors in our calculations. Namely, our calculations are based on the analysis of the thermodynamic properties of the system in equilibrium. But it is well known that kinetic factors play a relevant role in the formation of zeolites, i.e. the system might have a mixture of metastable configurations, and configurations that appear purely for kinetic reasons, and we are missing all of those in our analysis. These kinetic factors would smooth the tendencies observed in the calculations. But apart from these discrepancies, both sets of data provide the same general view, consisting in the similar population of sites T1 and T2, followed by T3 and T4, and finally T5.

**Table C1:** Refined Ge occupancies of T sites in Ge,Si-HPM-1

	Overall $Ge_f = 0.4$	Overall $Ge_f = 0.6$
Ge in $T_1$	0.552	0.748
Ge in $T_2$	0.555	0.735
Ge in $T_3$	0.388	0.584
Ge in $T_4$	0.393	0.591
Ge in $T_5$	0.092	0.215

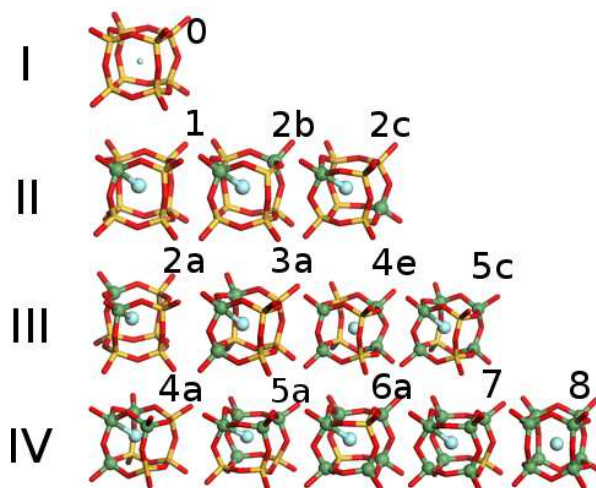


**Figure C8:** Some of the energy-minimised D4Rs configurations. They are classified according to the resonance. Some structural distortions are distinguishable with respect to the configuration of pure silica.

## C.4. Supporting Information

### C.4.1. Rietveld details

The starting model for Rietveld refinement of samples prepared with  $Ge_f = 0.4, 0.6$  and 1 was the refined structure of pure silica HPM-1,[32] in space group  $P6_122$  modified to have the unit cell dimensions determined from conventional powder XRD data and a Ge occupation of all crystallographic positions initially set at 0.4, 0.6 and 1.0, respectively (Si occupancies of 0.6, 0.4 and 0.0, respectively). Although the sample with  $Ge_f = 1$  appeared as phase-pure in the conventional XRD pattern, synchrotron radiation showed the presence of small traces of quartz-like  $GeO_2$ , and the corresponding regions were excluded from the refinement. A Lobanov and Alte da Veiga absorption correction was applied.[34] Scale factor, unit cell and profile parameters were refined, with a shifted Chebyshev function initially with 16 fixed parameters to simulate the background. Then, the Ge, Si, O and F atoms were allowed to move, initially with soft restraints on T-O and O-O distances and with Ge and Si in each crystallographic site constrained to move together. Then, the position and orientation of the organic SDA was refined as a rigid body consisting of the imidazolium ring with the three methyl substituents as a rigid unit plus the ethyl group as a satellite that could freely rotate along the C2-C9 bond. The hydrogen atoms were omitted but the fractional occupancies of the C atoms were adjusted to account for the electrons of the bonded H. The weight of the distance restraints was gradually reduced and eventually eliminated. In the final stages of the refinements, atom displacement factors (grouped

**Table C2:** Summary of synthesis results at 175 °C

Ge <sub>f</sub>	Time (hours)	Yield (wt. %)	Phase <sup>a</sup>
0	27	31.1	amorphous (+ HPM-1)
0	48	21.2	HPM-1
0	143	29.7	HPM-1
0	264	29.6	HPM-1
0.009	25	22.5	HPM-1 + amorphous
0.009	48	23.7	HPM-1
0.009	144	23.7	HPM-1
0.009	240	24.1	HPM-1
0.019	25	25.1	HPM-1
0.019	48	24.1	HPM-1
0.019	144	25.4	HPM-1
0.019	240	25.4	HPM-1
0.032	25	27.1	HPM-1
0.032	48	27.9	HPM-1
0.032	144	26.16	HPM-1
0.032	240	26.3	HPM-1
0.09	25	33.1	HPM-1
0.09	48	31.4	HPM-1
0.09	144	32.2	HPM-1
0.09	240	34.4	HPM-1
0.166	25	34.4	HPM-1
0.166	48	34.5	HPM-1
0.166	144	33.3	HPM-1
0.166	237	36.1	HPM-1
0.2	25	36.4	HPM-1
0.2	48	35.7	HPM-1
0.2	144	36.1	HPM-1
0.2	240	35.5	HPM-1
0.4	25	39.3	HPM-1
0.4	48	39.7	HPM-1
0.4	144	38.0	HPM-1
0.4	240	37.9	HPM-1
0.6	25	24.9	HPM-1
0.6	48	26.8	HPM-1
0.6	144	27.6	HPM-1
0.6	240	32.5	HPM-1
0.8	25	25.4	HPM-1
0.8	48	23.3	HPM-1
0.8	144	26.6	HPM-1
0.9	25	5.5	HPM-1
0.9	48	18.1	HPM-1
0.9	144	21.8	HPM-1
1	27	0	- <sup>b</sup>
1	113	1.7	HPM-1
1	200	2.6	Q+Arg (+HPM-1) <sup>c</sup>
1	96	10.4	HPM-1 (+Q) <sup>c,d</sup>
1	102	9.5	HPM-1 + Q <sup>c,d</sup>

<sup>a</sup> Major phases are listed first, very minor phases appear between parentheses. <sup>b</sup> No solids could be collected. <sup>c</sup> Q is the Quartz-like and Arg is the Argutite-like GeO<sub>2</sub> phases. <sup>d</sup> The last two entries correspond to a different synthesis run in the same nominal conditions as the preceding ones.

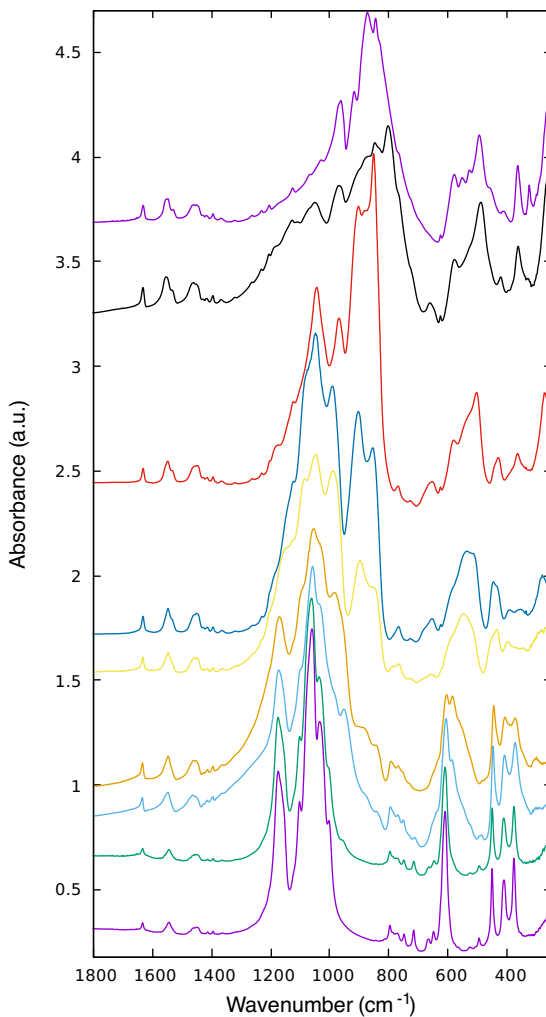


**Figure C9:** Infrared species of STW zeolites obtained from gels with  $Ge_f = 0, 0.01, 0.09, 0.17, 0.4, 0.6, 0.8, 0.9$  and 1 (from bottom to top)

by atom type), background and fractional occupancies of Ge and Si in each crystallographic site (constrained to amount to a full occupancy of each site) were included in the refinement. Final crystallographic data are summarized in Tables C3, the final Rietveld plots are given in Figures C13, C14 and C15.

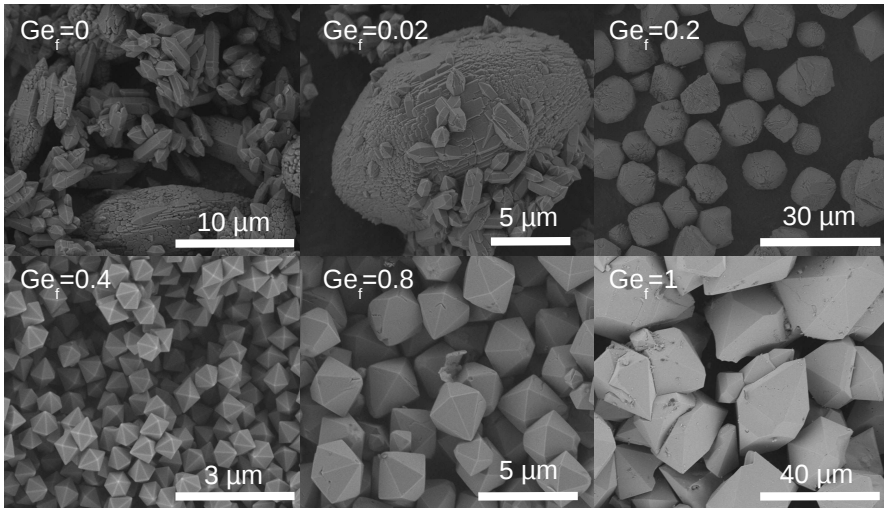


Figure C10: FESEM images of HPM-1 zeolites prepared at different  $Ge_f$  levels.

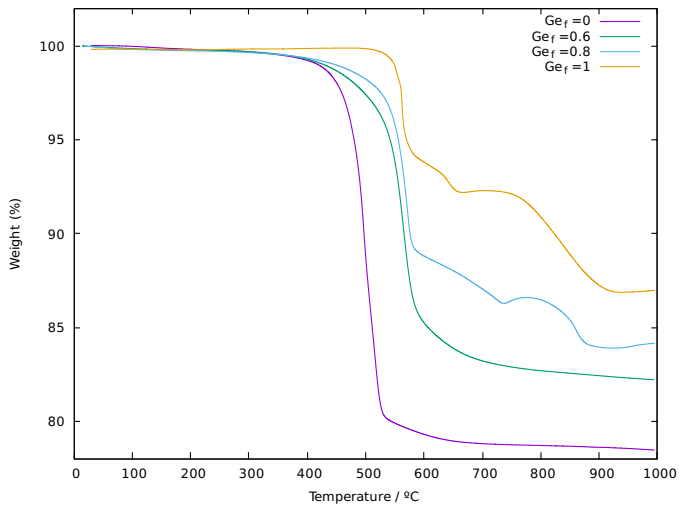
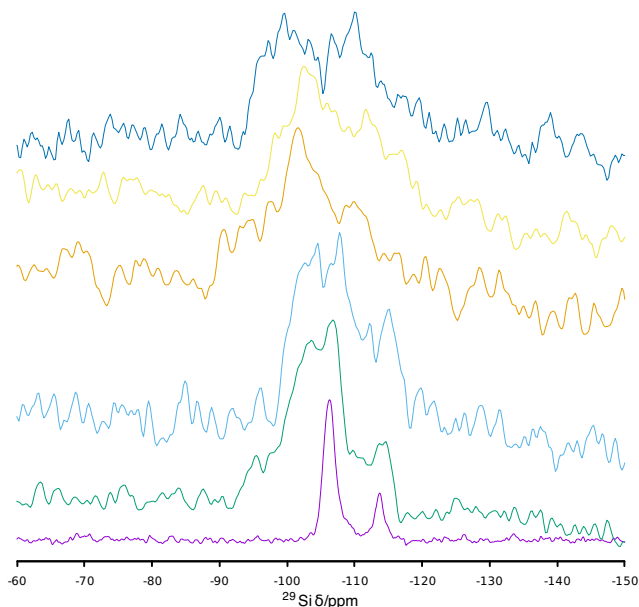


Figure C11: Thermograms of HPM-1 zeolites prepared at different  $Ge_f$  levels.



**Figure C12:** Direct irradiation  $^{29}\text{Si}$  MAS spectra of (Ge,Si)-STW with  $Ge_f = 0.00, 0.166, 0.20, 0.40, 0.60$  and  $0.80$  (from bottom to top). For every spectra 2048 scans were acquired. Recycle delays are 60s for the pure silica sample and 180s for the rest.

**Table C3:** Crystallographic and Experimental Parameters for the Rietveld Refinement of as-made Ge,Si-HPM-1 phases (wavelength:  $0.56383 \text{ \AA}$ , Temperature 293K)

Nominal $Ge_f$	0.4	0.6	1
Refined $Ge_f$	0.396	0.574	-
$2\theta$ range	2.00-38.32	2.00-33.97	2.50-44.9
no. of data points	3733	3198	4241
no. of reflections	1327	977	1792
Space Group	$P6_122$	$P6_122$	$P6_122$
unit cell parameters ( $\text{\AA}$ )			
$a, b$	12.09289(16)	12.16714(17)	12.42671(11)
$c$	30.0839(5)	30.2519(6)	30.6310(5)
Cell volume ( $\text{\AA}^3$ )	3810.01(12)	3878.46(13)	4096.41(8)
Residuals			
$R_{wp}$	3.06%	2.82%	3.66%
$R_p$	2.36%	2.23%	2.65%
$R_{F^2}$	7.76%	7.53%	10.58%
reduced $\chi^2$	2.513	2.527	3.98

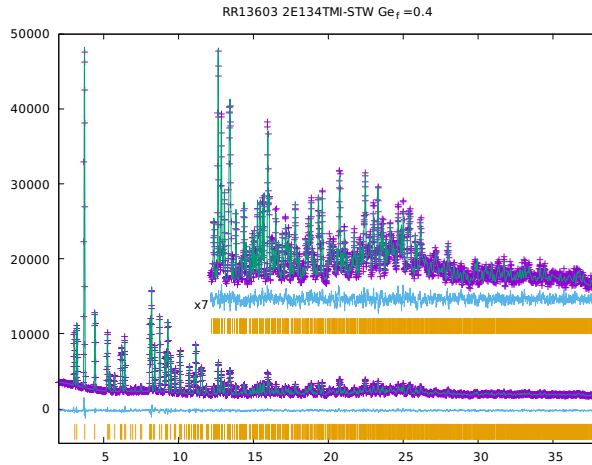


**Figure C13:** Observed (+) and calculated (solid line) powder X-ray diffractograms for as-made Ge<sub>f</sub>Si<sub>1-f</sub>-HPM-1 with  $Ge_f = 0.4$  refined in space group  $P6_122$ . Vertical tic marks indicate the positions of allowed reflections. The lower trace is the difference plot.  $\lambda=0.56383 \text{ \AA}$ .

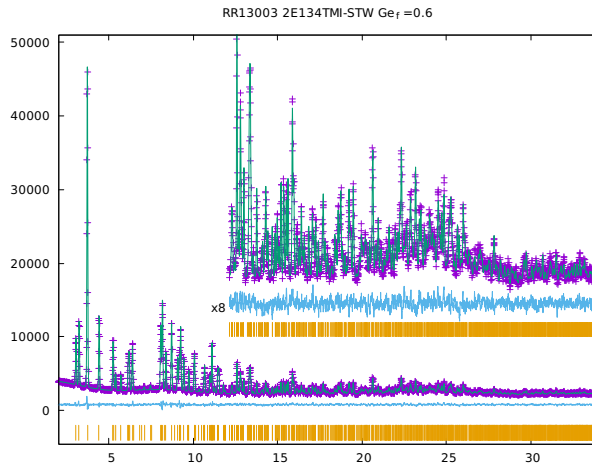


**Figure C14:** Observed (+) and calculated (solid line) powder X-ray diffractograms for as-made Ge<sub>f</sub>Si<sub>1-f</sub>-HPM-1 with  $Ge_f = 0.6$  refined in space group  $P6_122$ . Vertical tic marks indicate the positions of allowed reflections. The lower trace is the difference plot.  $\lambda=0.56383 \text{ \AA}$ .

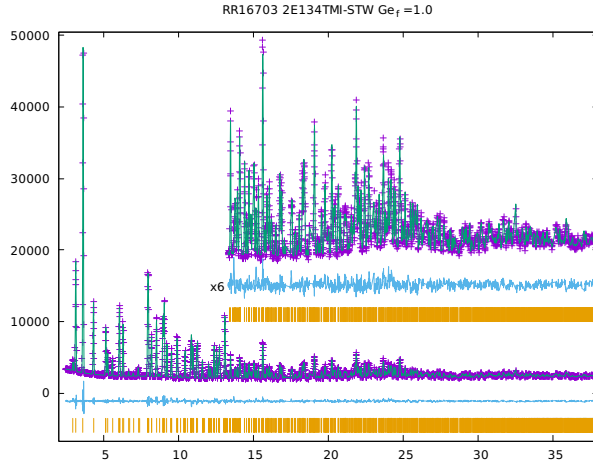


**Figure C15:** Observed (+) and calculated (solid line) powder X-ray diffractograms for as-made Ge-HPM-1 ( $Ge_f = 1.0$ ) refined in space group  $P6_122$ . Vertical tic marks indicate the positions of allowed reflections. The lower trace is the difference plot.  $\lambda = 0.56383 \text{ \AA}$ .

**Table C4:** Average bond distances and angles in Ge,Si-HPM-1 phases

Average distance ( $\text{\AA}$ )	$Ge_f = 0.4$	$Ge_f = 0.6$	$Ge_f = 1$
T1-O	1.654	1.662	1.668
T2-O	1.656	1.670	1.714
T3-O	1.637	1.647	1.706
T4-O	1.667	1.689	1.724
T5-O	1.635	1.642	1.724
T1-F	2.57	2.63	2.57
T2-F	2.79	2.76	2.89
T3-F	2.70	2.71	2.72
T4-F	2.74	2.75	2.75
Average angle ( $^\circ$ )			
O-T1-O	109.3	109.2	109.2
O-T2-O	109.4	109.4	109.3
O-T3-O	109.1	109.0	109.4
O-T4-O	109.4	109.4	109.2
O-T5-O	109.4	109.4	109.6



## Chapter 7

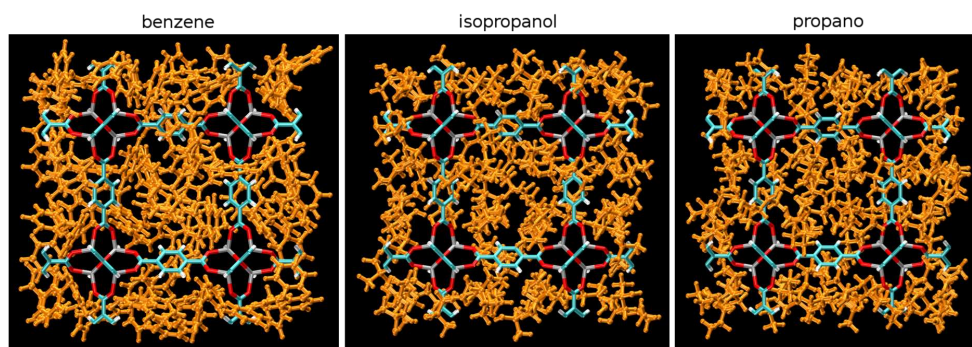


**Figure D1:** Snapshots of the structure of the MOF-5 framework and the adsorbed molecules (benzene, isopropanol and propane), at saturation.

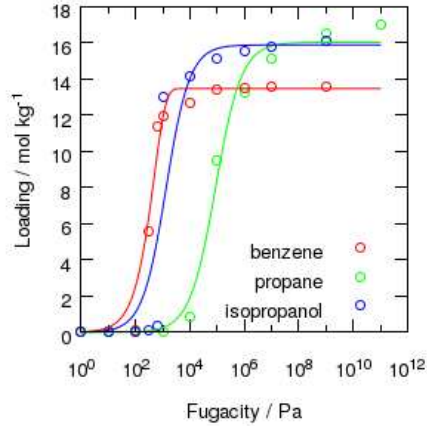


**Figure D2:** Adsorption isotherms were performed at 300 K, obtained using MC simulations in the grand-canonical ensemble ( $\mu VT$ ), i.e. maintaining constant  $\mu$ . In this ensemble, the volume  $V$ , temperature  $T$ , and chemical potential  $\mu$  are kept constant. The chemical potential is imposed with the fugacity, which is the effective thermodynamic pressure. We converted the fugacity to the corresponding pressure, using the Peng–Robinson equation of state [56]. Solid lines correspond with fitted models of the calculated isotherms, using with the models of Jovanović [57], Langmuir-Freundlich or Sips [58] and Langmuir [59] for benzene, propane and isopropanol, respectively. The experimental values for the saturation adsorption of benzene is 10.24 mol/kg in reference [60] and 8.95 mol/kg in reference [61], and the pressure at which the saturation is attained is around 1 kPa.

**Table D1:** Relation between loading (in molecules per unit cell), loading in % of saturation, and fugacities (in Pa). A volume change should lead to a variation in the number of molecules in saturation conditions. However, the variation of volume is small, compared with the total volume, and the larger error in the number of molecules is less than 3.2 %.

Loading / % in saturation	Loading / molecules per unit cell			Corresponding Fugacity / Pa		
	Benzene	Isopropanol	Propane	Benzene	Isopropanol	Propane
20	17	20	21	$1.24 \times 10^2$	$3.72 \times 10^2$	$2.04 \times 10^4$
40	34	39	42	$2.52 \times 10^2$	$9.19 \times 10^2$	$6.54 \times 10^4$
60	52	59	63	$4.81 \times 10^2$	$1.99 \times 10^3$	$1.72 \times 10^5$
80	69	78	84	$8.61 \times 10^2$	$5.61 \times 10^3$	$5.17 \times 10^5$
100	86	98	105	$1.12 \times 10^2$	$1.07 \times 10^7$	$3.4 \times 10^9$

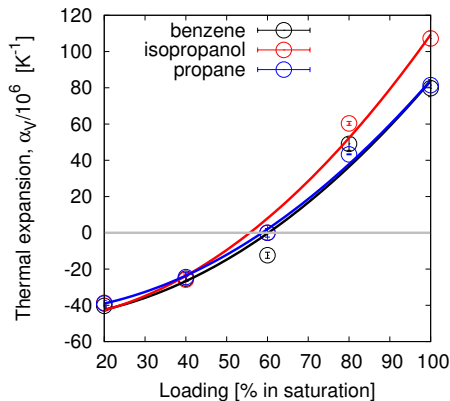


**Figure D3:** Thermal expansion coefficients vs. loading in IRMOF-1, when adsorbing benzene, isopropanol and propane. Zero Thermal Expansion (ZTE) is observed at 60 % of saturation.

**Table D2:** Relation between loading (in molecules per unit cell), loading in % of saturation, and fugacities (in Pa). A volume change should lead to a variation in the number of molecules in saturation conditions. However, the variation of volume is small, compared with the total volume, and the larger error in the number of molecules is less than 3.2 %.

Loading / % in saturation	Thermal expansion coefficient, $\beta / 10^{-6} K^{-1}$		
	Benzene	Isopropanol	Propane
20	$-40.2 \pm 0.1$	$-38.6 \pm 0.5$	$-39.0 \pm 1$
40	$-25.3 \pm 0.5$	$-25 \pm 1$	$-24 \pm 1$
60	$-12.3 \pm 1$	$0 \pm 1^a$	$0 \pm 1$
80	$49 \pm 1$	$60.3 \pm 0.5$	$43.2 \pm 0.5$
100	$79 \pm 1$	$107 \pm 1$	$81 \pm 1$

<sup>a</sup> The error is larger than the measurement.

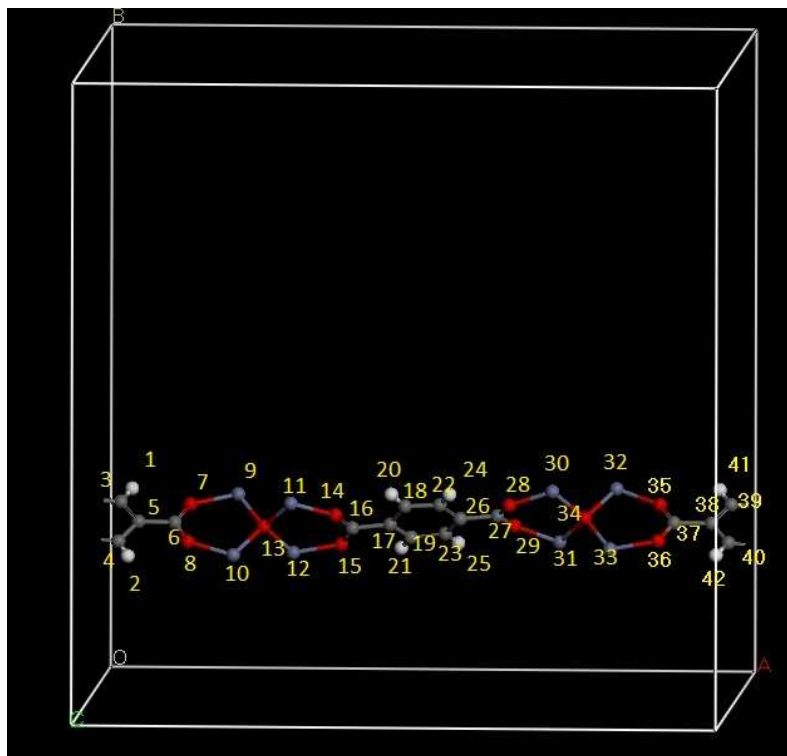


**Figure D4:** Single string of atoms going across the whole cell of IRMOF-1. The numbers will be used to perform an analysis of the geometric measurements. The results of this analysis will be shown in the following figures. We show the time average distances, angles and distortions units between atoms, and IRMOF-1 units. Note that the material is composed by 12 strings of atoms, like the one shown here.

Atoms list:

1 H left, 2 H left, 3 CbenzH left, 4 CbenzH left, 5 CbenznoH left 10 Zn left, 6 Cacid left left 11 Zn left, 7 Oacid left left 12 Zn left, 8 Oacid left left, 9 Zn left, 10 Zn left, 11 Zn left, 12 Zn left, 13 Ooxide left, 14 Oacid left right, 15 Oacid left right, 16 Cacid left right, 17 CbenznoH center left, 18 CbenzH center left ,19 CbenzH center, left, 20 H center left, 21 H center left, 22 CbenzH center, 23 CbenzH center right, 24 H center right, 25 H center right, 26 CbenznoH center right, 27 Cacid right left, 28 Oacid right left, 29 Oacid right left, 30 Zn right, 31 Zn right, 32 Zn right, 33 Zn right, 34 Ooxide right, 35 Oacid right right, 36 Oacid right right, 37 Cacid right right, 38 CbenznoH right, 39 CbenzH right, 40 CbenzH right, 41 H right, AND 42 H right.

Atom-atom bond distances:

1 CacidCbenznoH, 2 CbenzHCbenzH, 3 CbenzHHatom, 4 CbenznoHCbenzH, 5 OacidCacid, 6 ZnOacid, AND 7 ZnOoxide Unit-unit angles:

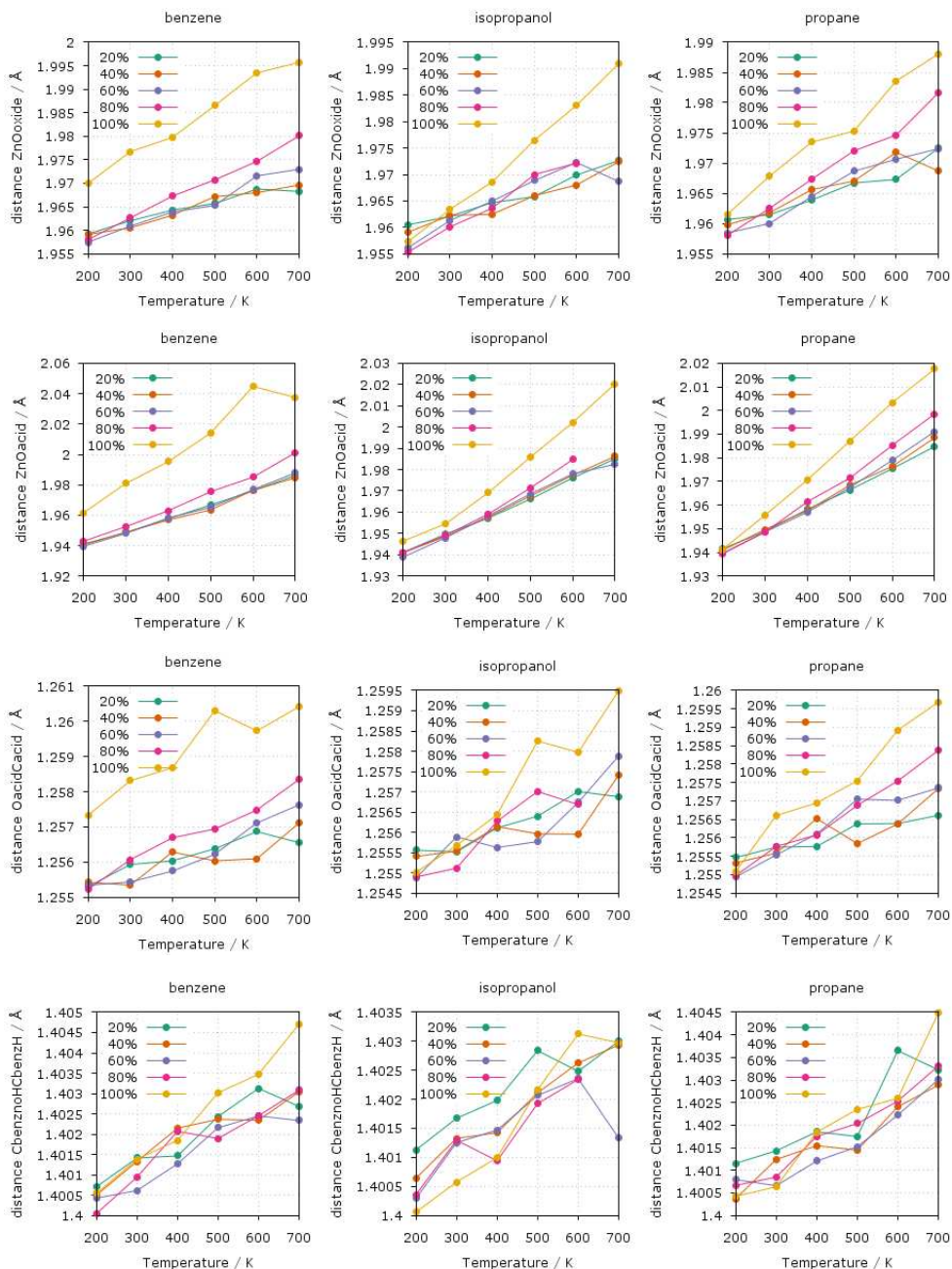
8 BenzenePlusAcid, 9 BenzeneRing, 10 CacidCbenznoHCRing, 11 OacidCacidCbenznoH, 12 OacidOoxideOacidLig, 13 OoxideOacidCRing, 14 OoxideZnOacid, AND 15 ZnOoxideZn.

Unit-unit distances:

16 BenzenePlusAcid, 17 BenzeneRing, AND 18 ZnOcluster

Distortion parameters:

19 cell, 20 OacidOacid, 21 OacidOacidClus, 22 OoxideCRing.



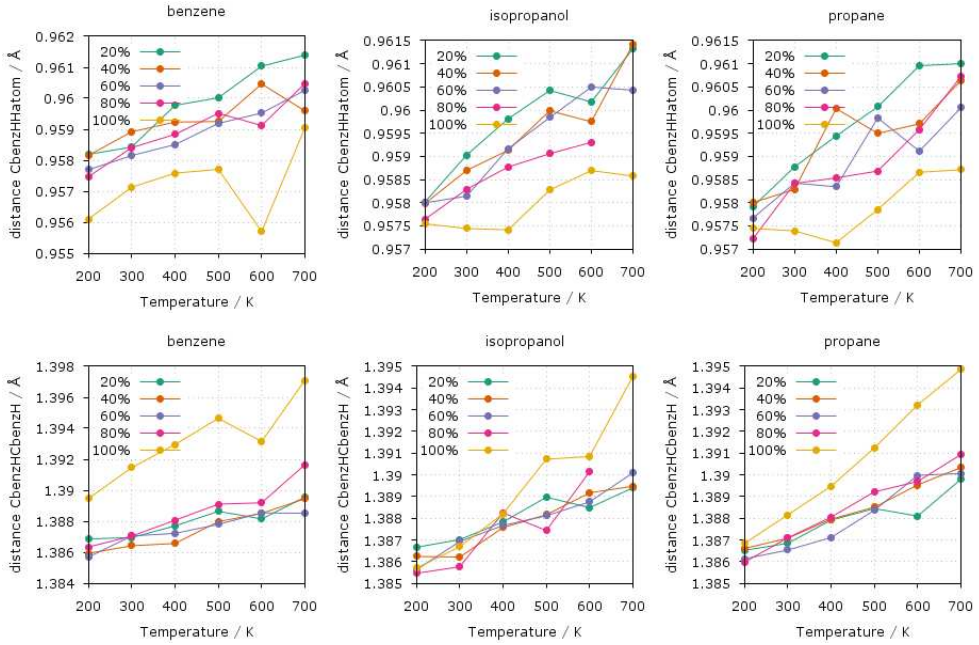
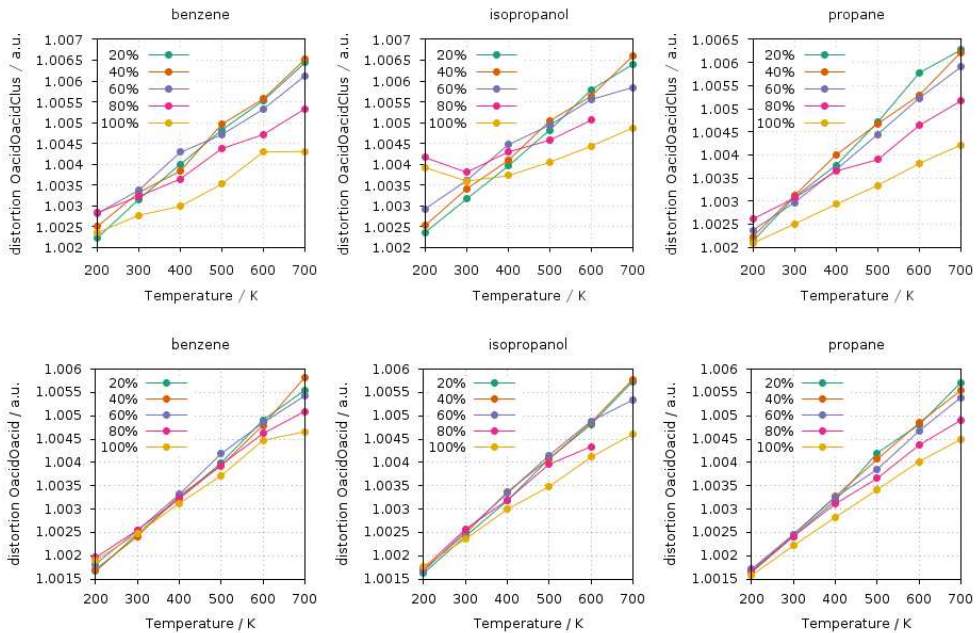


Figure D5: Temperature dependence of the bond distances. See Figure D4 for labels.



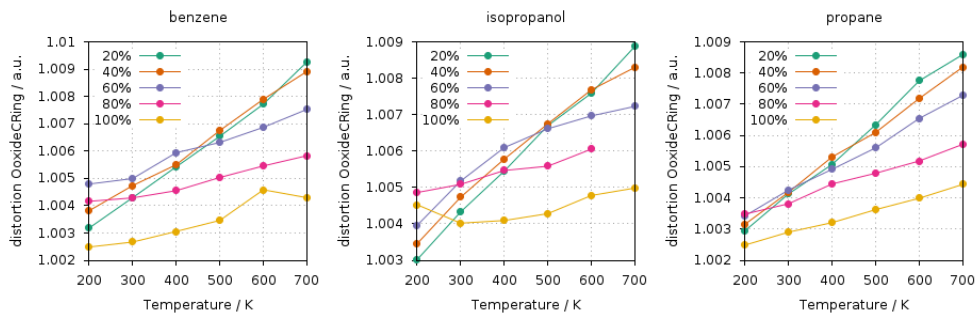
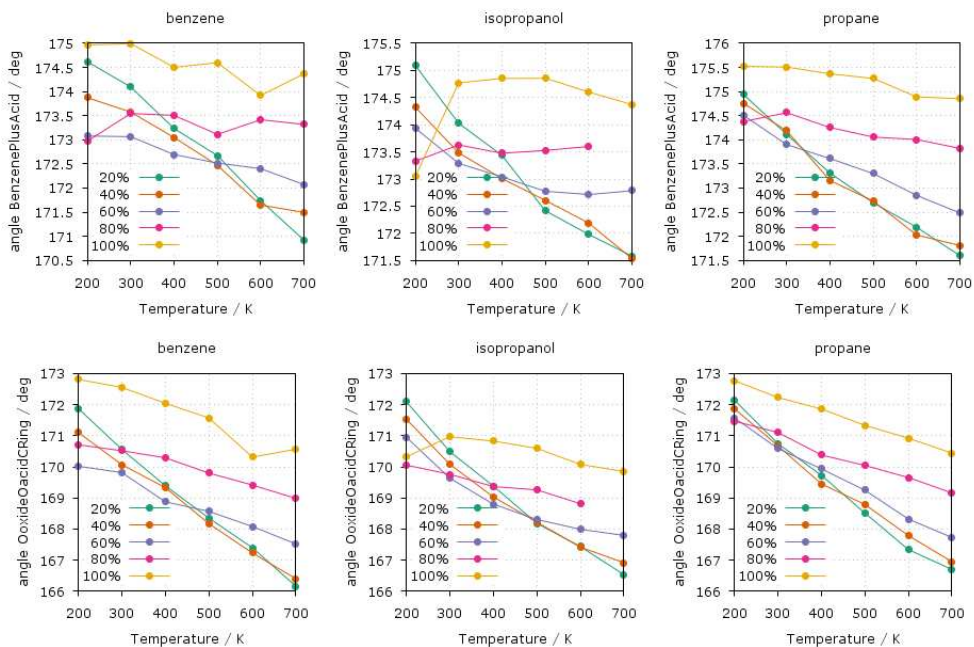
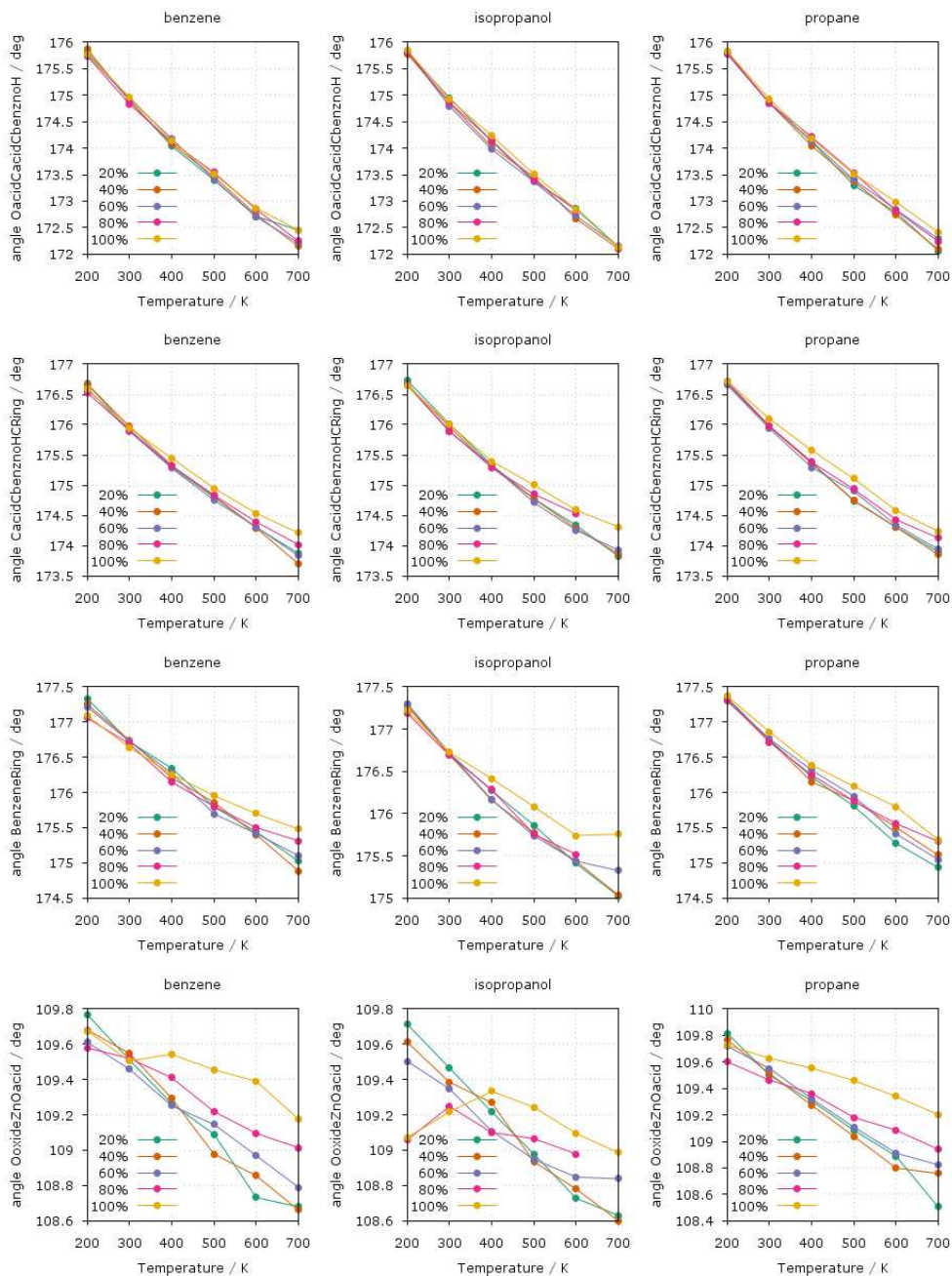
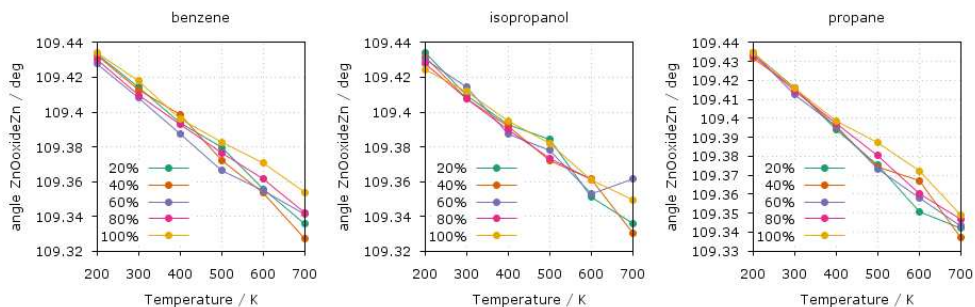


Figure D6: Temperature dependence of the distortion parameters. See Figure D4 for labels.

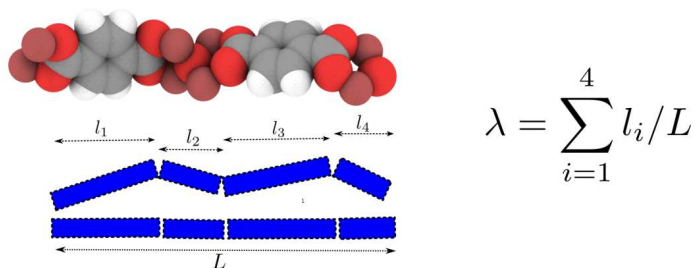






**Figure D7:** Temperature dependence of the relevant unit–unit angles. See Figure D4 for labels.

**Figure D8:** Definition of cell distortion,  $\lambda(l_i)$  represents the instantaneous length of the sub-elements of a single string of atoms going across the whole cell of IRMOF-1.  $L$  is the cell parameter. Other distortion parameters are defined in a similar way following the enumeration and scheme of the Figure D4



## Appendix bibliography

- [1] J. VandeVondele, M. Krack, F. Mohamed, M. Parrinello, T. Chassaing and J. Hutter. “Quickstep: Fast and accurate density functional calculations using a mixed Gaussian and plane waves approach”. *Comput. Phys. Commun.* 167, 103–128, **2005**. ISSN: 0010-4655. DOI: 10.1016/j.cpc.2004.12.014. (Cit. on p. 150).
- [2] J. Hutter, M. Iannuzzi, F. Schiffmann and J. VandeVondele. “cp2k: atomistic simulations of condensed matter systems”. *WIREs Comput Mol Sci* 4, 15–25, **2014**. ISSN: 1759-0884. DOI: 10.1002/wcms.1159. (Cit. on p. 150).
- [3] J. P. Perdew, K. Burke and M. Ernzerhof. “Generalized Gradient Approximation Made Simple”. *Phys. Rev. Lett.* 77, 3865–3868, **1996**. DOI: 10.1103/PhysRevLett.77.3865. (Cit. on p. 150).
- [4] S. Grimme, J. Antony, S. Ehrlich and H. Krieg. “A consistent and accurate *ab initio* parametrization of density functional dispersion correction (DFT-D) for the 94 elements H–Pu”. *J. Chem. Phys.* 132, 154104, **2010**. DOI: 10.1063/1.3382344. (Cit. on p. 150).
- [5] S. Goedecker, M. Teter and J. Hutter. “Separable dual-space Gaussian pseudopotentials”. *Phys. Rev. B* 54, 1703–1710, **1996**. DOI: 10.1103/PhysRevB.54.1703. (Cit. on p. 150).
- [6] J. D. Sherman. “Synthetic zeolites and other microporous oxide molecular sieves”. *Proc. Natl. Acad. Sci. U. S. A.* 96, 3471–3478, **1999**. (Cit. on p. 153).
- [7] C. S. Cundy and P. A. Cox. “The Hydrothermal Synthesis of Zeolites: History and Development from the Earliest Days to the Present Time”. *Chem. Rev.* 103, 663–702, **2003**. DOI: 10.1021/cr020060i. (Cit. on p. 153).
- [8] P. Lu, L. A. Villaescusa and M. A. Cambor. “Driving the Crystallization of Zeolites”. *Chem. Rec.* 10.1002/tcr.201700092. ISSN: 1528-0691. DOI: 10.1002/tcr.201700092. (Cit. on p. 153).
- [9] M. E. Davis and R. F. Lobo. “Zeolite and Molecular Sieve Synthesis”. *Chem. Mater.* 4, 756–768, **1992**. (Cit. on p. 153).
- [10] P. Caullet, J. L. Paillaud, A. Simon-Masseron, M. Soulard and J. Patarin. “The fluoride route: A strategy to crystalline porous materials”. *C. R. Chim.* 8, 245–266, **2005**. (Cit. on p. 153).
- [11] M. A. Cambor and S. B. Hong. In: “Porous Materials”. D. W. Bruce, D. O’Hare and R. I. Walton, eds. 265–325. Chichester: Wiley, 2011. (Cit. on p. 153).
- [12] T. Conradsson, M. S. Dadachov and X. D. Zou. “Synthesis and structure of  $(\text{Me}_3\text{N})_6[\text{Ge}_{32}\text{O}_{64}](\text{H}_2\text{O})_{4.5}$ , a thermally stable novel zeotype with 3D interconnected 12-ring channels”. *Micropor. Mesopor. Mat.* 41, 183–191, **2000**. (Cit. on p. 153).
- [13] A. Corma, M. T. Navarro, F. Rey, J. Rius and S. Valencia. “Pure polymorph C of zeolite beta synthesized by using framework isomorphous substitution as a structure-directing mechanism”. *Angew. Chem., Int. Ed.* 40, 2277–2280, **2001**. (Cit. on p. 153).
- [14] L. A. Villaescusa and M. A. Cambor. “The fluoride route to new zeolites”. *Recent Res. Dev. Chem.* 1, 93–141, **2003**. (Cit. on p. 153).
- [15] L. A. Villaescusa and M. A. Cambor. “Framework Reduction of GeO<sub>2</sub> Zeolites During Calcination”. *Chem. Mater.* 28, 7544–7550, **2016**. (Cit. on pp. 153, 158).
- [16] M. V. Shamzhy, P. Eliašová, D. Vitvarová, M. V. Opanasenko, D. S. Firth and R. E. Morris. “Post-Synthesis Stabilization of Germanosilicate Zeolites ITH, IWW, and UTL by Substitution of Ge for Al”. *Chem.–Eur. J.* 22, 17377–17386, **2016**. ISSN: 1521-3765. DOI: 10.1002/chem.201603434. (Cit. on p. 153).
- [17] C. Baerlocher and L. B. McCusker. *Database of Zeolite Structures*. 2015. URL: <http://www.iza-structure.org/databases/> (cit. on p. 153).
- [18] W. J. Roth, P. Nachtigall, R. E. Morris, P. S. Wheatley, V. R. Seymour, S. E. Ashbrook, P. Chlubná, L. Grajciar, M. Položij, A. Zukal, O. Shvets and J. Čejka. “A family of zeolites with controlled pore size prepared using a top-down method”. *Nat. Chem.* 5, 628–633, **2013**. ISSN: 1755-4330. (Cit. on p. 153).

- [19] P. Eliášová, M. Opanasenko, P. S. Wheatley, M. Shamzhy, M. Mazur, P. Nachtigall, W. J. Roth, R. E. Morris and J. Čejka. "The ADOR mechanism for the synthesis of new zeolites". *Chem. Soc. Rev.* 44, 7177–7206, **2015**. (Cit. on p. 153).
- [20] P. S. Wheatley, P. Chlubná-Eliášová, H. Greer, W. Zhou, V. R. Seymour, D. M. Dawson, S. E. Ashbrook, A. B. Pinar, L. B. McCusker, M. Opanasenko, J. Čejka and R. E. Morris. "Zeolites with Continuously Tuneable Porosity". *Angew. Chem. Int. Edit.* 53, 13210–13214, **2014**. ISSN: 1521-3773. DOI: 10.1002/anie.201407676. (Cit. on p. 153).
- [21] P. Chlubná-Eliášová, Y. Tian, A. B. Pinar, M. Kubøu, J. Čejka and R. E. Morris. "The Assembly-Disassembly-Organization-Reassembly Mechanism for 3D-2D-3D Transformation of Germanosilicate IWW Zeolite". *Angew. Chem. Int. Edit.* 53, 7048–7052, **2014**. ISSN: 1521-3773. DOI: 10.1002/anie.201400600. (Cit. on p. 153).
- [22] M. Mazur, P. S. Wheatley, M. Navarro, W. J. Roth, M. Položij, A. Mayoral, P. Eliášová, P. Nachtigall, J. Čejka and R. E. Morris. "Synthesis of unfeasible zeolites". *Nat. Chem.* 8, 58–62, **2016**. (Cit. on p. 153).
- [23] F. Gao, M. Jaber, K. Bozhilov, A. Vicente, C. Fernandez and V. Valtchev. "Framework Stabilization of Ge-Rich Zeolites via Post-synthesis Alumination". *J. Am. Chem. Soc.* 131, 16580–16586, **2009**. DOI: 10.1021/ja904458y. (Cit. on p. 153).
- [24] L. Burel, N. Kasian and A. Tuel. "Quasi All-Silica Zeolite Obtained by Isomorphous De-germanation of an As-Made Germanium-Containing Precursor". *Angew. Chem. Int. Edit.* 53, 1360–1363, **2014**. ISSN: 1521-3773. DOI: 10.1002/anie.201306744. (Cit. on p. 153).
- [25] H. Xu, J.-g. Jiang, B. Yang, L. Zhang, M. He and P. Wu. "Post-Synthesis Treatment gives Highly Stable Siliceous Zeolites through the Isomorphous Substitution of Silicon for Germanium in Germanosilicates". *Angew. Chem. Int. Edit.* 53, 1355–1359, **2014**. ISSN: 1521-3773. DOI: 10.1002/anie.201306527. (Cit. on p. 153).
- [26] L. Tang, L. Shi, C. Bonneau, J. Sun, H. Yue, A. Ojuva, B.-L. Lee, M. Kritikos, R. G. Bell, Z. Bacsik, J. Mink and X. Zou. "A zeolite family with chiral and achiral structures built from the same building layer". *Nat. Mater.* 7, 381–385, **2008**. DOI: 10.1038/nmat2169. (Cit. on pp. 153, 155).
- [27] A. Rojas and M. A. Cambor. "A Pure Silica Chiral Polymorph with Helical Pores". *Angew. Chem. Int. Ed.* 51, 3854–3856, **2012**. DOI: 10.1002/anie.201108753. (Cit. on p. 153).
- [28] J. E. Schmidt, M. W. Deem and M. E. Davis. "Synthesis of a Specified, Silica Molecular Sieve by Using Computationally Predicted Organic Structure-Directing Agents". *Angew. Chem. Int. Ed.* 53, 8372–8374, **2014**. DOI: 10.1002/anie.201404076. (Cit. on pp. 153, 155).
- [29] S. K. Brand, J. E. Schmidt, M. W. Deem, F. Daeyaert, Y. Ma, O. Terasaki, M. Orazov and M. E. Davis. "Enantiomerically enriched, polycrystalline molecular sieves". *P. Natl. Acad. Sci. USA* 114, 5101–5106, **2017**. DOI: 10.1073/pnas.1704638114. (Cit. on pp. 154, 155).
- [30] P. Lu, L. Gomez-Hortiguera, L. Xu and M. A. Cambor. "Synthesis of STW zeolites using imidazolium-based dications of varying length". *J. Mater. Chem. A* 6, 1485–1495, **2018**. DOI: 10.1039/C7TA10002G. (Cit. on pp. 154, 155).
- [31] R. Bueno-Pérez, S. R. G. Balestra, M. A. Cambor, J. G. Min, S. B. Hong, P. J. Merklings and S. Calero. "Influence of Flexibility on the Separation of Chiral Isomers in the STW-Type Zeolite". *Chem.–Eur. J.* **2018**. DOI: 10.1002/chem.201705627. (Cit. on p. 154).
- [32] A. Rojas, O. Arteaga, B. Kahr and M. A. Cambor. "Synthesis, Structure, and Optical Activity of HPM-1, a Pure Silica Chiral Zeolite". *J. Am. Chem. Soc.* 135, 11975–11984, **2013**. DOI: 10.1021/ja405088c. (Cit. on pp. 154, 158, 160, 163, 165).
- [33] T. J. B. Holland. "Unit Cell Refinement from Powder Diffraction Data: The Use of Regression Diagnostics". *Mineral. Mag.* 61, 65–77, **1997**. DOI: 10.1180/minmag.1997.061.404.07. (Cit. on p. 154).

- [34] A. C. Larson and R. B. V. Dreele. *General Structure Analysis System (GSAS)*. Los Alamos National Laboratory Report LAUR 86-748, 2004. (Cit. on pp. 155, 163, 165).
- [35] B. H. Toby. “EXPGUI, a graphical user interface for GSAS”. *J. Appl. Crystallogr.* 34, 210–213, **2001**. (Cit. on p. 155).
- [36] A. Rojas, L. Gómez-Hortigüela and M. A. Cambor. “Zeolite Structure Direction by Simple Bis (methylimidazolium) Cations: The Effect of the Spacer Length on Structure Direction and of the Imidazolium Ring Orientation on the 19F NMR Resonances”. *J. Am. Chem. Soc.* 134, 3845–3856, **2012**. DOI: 10.1021/ja210703y. (Cit. on p. 155).
- [37] N. Zhang, L. Shi, T. Yu, T. Li, W. Hua and C. Lin. “Synthesis and characterization of pure STW-zeotype germanosilicate, Cu- and Co-substituted STW-zeotype materials”. *J. Solid State Chem.* 225, 271–277, **2015**. DOI: 10.1016/j.jssc.2014.12.031. (Cit. on p. 155).
- [38] J. Dwyer and K. Karim. “The incorporation of heteroatoms into faujastic framework by secondary synthesis using aqueous fluoride complexes”. *J. Chem. Soc., Chem. Commun.* 905, **1991**. DOI: 10.1039/c39910000905. (Cit. on p. 156).
- [39] M. A. Cambor, A. Corma, A. Martinez and J. Pérez-Pariente. “Synthesis of a titaniumsilicoaluminate isomorphous to zeolite beta and its application as a catalyst for the selective oxidation of large organic molecules”. *J. Chem. Soc., Chem. Commun.* 0, 589–590, **1992**. DOI: 10.1039/c39920000589. (Cit. on p. 156).
- [40] . Sulikowski. *Heterog. Chem. Rev.* 203–268, **1996**. (Cit. on p. 156).
- [41] M. A. Cambor, S. B. Hong and M. E. Davis. “Unexpected contraction of a zeolite framework upon isomorphous substitution of Si by Al”. *Chem. Commun.* 425, **1996**. DOI: 10.1039/cc9960000425. (Cit. on p. 156).
- [42] H. Kosslick, V. A. Tuan, R. Fricke, C. Peuker, W. Pilz and W. Storek. “Synthesis and characterization of Ge-ZSM-5 zeolites”. *J. Phys. Chem.* 97, 5678–5684, **1993**. DOI: 10.1021/j100123a036. (Cit. on p. 157).
- [43] J. E. Schmidt, S. I. Zones, D. Xie and M. E. Davis. “The synthesis of aluminophosphate and germanosilicate LTA using a triquaternary structure directing agent”. *Microporous Mesoporous Mater.* 200, 132–139, **2014**. (Cit. on p. 159).
- [44] P. Caullet, J. Guth, J. Hazm, J. Lamblin and H. Gies. “Synthesis, Characterization, and Crystal Structure of the New Clathrasil Phase Octadecasil”. *Eur. J. Sol. State Inor.* 22, 345–361, **1991**. (Cit. on p. 160).
- [45] L. A. Villaescusa, P. A. Barrett and M. A. Cambor. “ITQ-7: A New Pure Silica Polymorph with a Three-Dimensional System of Large Pore Channels”. *Angew. Chem. Int. Ed.* 38, 1997–2000, **1999**. ISSN: 1521-3773. DOI: 10.1002/(SICI)1521-3773(19990712)38:13/14<1997::AID-ANIE1997>3.0.CO;2-U. (Cit. on p. 160).
- [46] M. A. Cambor, P. A. Barrett, M.-J. Díaz-Cabañas, L. A. Villaescusa, M. Puche, T. Boix, E. Pérez and H. Koller. “High silica zeolites with three-dimensional systems of large pore channels”. *Microporous Mesoporous Mater.* 48, 11–22, **2001**. DOI: 10.1016/s1387-1811(01)00325-0. (Cit. on p. 160).
- [47] P. A. Barrett, T. Boix, M. Puche, D. H. Olson, E. Jordan, H. Koller and M. A. Cambor. “ITQ-12: a new microporous silica polymorph potentially useful for light hydrocarbon separations”. *Chem. Commun.* 2114, **2003**. DOI: 10.1039/b306440a. (Cit. on p. 160).
- [48] L. A. Villaescusa, P. Lightfoot and R. E. Morris. “Synthesis and structure of fluoride-containing GeO<sub>2</sub> analogues of zeolite double four-ring building units”. *Chem. Commun.* 2220–2221, **2002**. DOI: 10.1039/b207374a. (Cit. on p. 160).
- [49] G. Sastre, J. A. Vidal-Moya, T. Blasco, J. Rius, J. L. Jordá, M. T. Navarro, F. Rey and A. Corma. “Preferential Location of Ge Atoms in Polymorph C of Beta Zeolite (ITQ-17) and Their Structure-Directing Effect: A Computational, XRD, and NMR Spectroscopic Study”. *Angew. Chem. Int. Ed.* 41, 4722–4726, **2002**. DOI: 10.1002/anie.200290028. (Cit. on p. 160).

- [50] T. Blasco, A. Corma, M. J. Díaz-Cabañas, F. Rey, J. A. Vidal-Moya and C. M. Zicovich-Wilson. "Preferential Location of Ge in the Double Four-Membered Ring Units of ITQ-7 Zeolite". *J. Phys. Chem. B* 106, 2634–2642, **2002**. DOI: 10 . 1021 / jp013302b. (Cit. on p. 160).
- [51] K. Wang, J. Yu, C. Li and R. Xu. *Inorg. Chem.* 42, 4597–4602, **2003**. (Cit. on p. 160).
- [52] Y. Wang, J. Song and H. Gies. "The substitution of germanium for silicon in AST-type zeolite". *Solid State Sci.* 5, 1421–1433, **2003**. DOI: 10 . 1016 / j . solidstatesciences . 2003 . 09 . 003. (Cit. on pp. 160–162).
- [53] L. A. Villaescusa and M. A. Cambor. "Time Evolution of an Aluminogermanate Zeolite Synthesis: Segregation of Two Closely Similar Phases with the Same Structure Type". *Chem. Mater.* 28, 3090–3098, **2016**. DOI: 10 . 1021 / a c s . chemmater . 6b00507. (Cit. on p. 160).
- [54] G. Sastre, A. Cantin, M. J. Diaz-Cabañas and A. Corma. "Searching Organic Structure Directing Agents for the Synthesis of Specific Zeolitic Structures: An Experimentally Tested Computational Study". *Chem. Mater.* 17, 545–552, **2005**. DOI: 10 . 1021 / cm049912g. (Cit. on p. 160).
- [55] A. Pulido, G. Sastre and A. Corma. "Computational Study of  $^{19}\text{F}$  NMR Spectra of Double Four Ring-Containing Si/Ge-Zeolites". *ChemPhysChem* 7, 1092–1099, **2006**. DOI: 10 . 1002 / cphc . 200500634. (Cit. on pp. 161, 163).
- [56] D.-Y. Peng and D. B. Robinson. "A New Two-Constant Equation of State". *Ind. Eng. Chem. Fundamen.* 15, 59–64, **1976**. DOI: 10.1021/i160057a011. (Cit. on p. 174).
- [57] D. S. Jovanović. "Physical adsorption of gases". *Kolloid-Zeitschrift & Zeitschrift für Polymere* 235, 1214–1225, **1969**. DOI: 10 . 1007 / bf01542531. (Cit. on p. 174).
- [58] R. Sips. "Combined form of Langmuir and Freundlich equations". *J. Chem. Phys.* 16, 490–495, **1948**. (Cit. on p. 174).
- [59] I. Langmuir. "The constitution and fundamental properties of solids and liquids". *J. Am. Chem. Soc.* 38, 2221–2295, **1916**. DOI: 10 . 1021 / ja02268a002. (Cit. on p. 174).
- [60] M. Eddaoudi, H. Li and O. M. Yaghi. "Highly Porous and Stable Metal-Organic Frameworks: Structure Design and Sorption Properties". *J. Am. Chem. Soc.* 122, 1391–1397, **2000**. DOI: 10 . 1021 / ja9933386. (Cit. on p. 174).
- [61] W.-G. Shim, K.-J. Hwang, J.-T. Chung, Y.-S. Baek, S.-J. Yoo, S.-C. Kim, H. Moon and J.-W. Lee. "Adsorption and thermodesorption characteristics of benzene in nanoporous metal organic framework MOF-5". *Adv. Powder Technol.* 23, 615–619, **2012**. (Cit. on p. 174).



# List of publications

The following publications are directly related with this Thesis:

## Peer reviewed journals

- S. R. G. Balestra, J. J. Gutierrez-Sevillano, P. J. Merklng, D. Dubbeldam and S. Calero. “Simulation Study of Structural Changes in Zeolite RHO”.. *J. Phys. Chem. C* 117, 11592–11599, **2013**. DOI: 10.1021/jp4026283.
- S. R. G. Balestra, S. Hamad, A. R. Ruiz-Salvador, V. Domínguez-García, P. J. Merklng, D. Dubbeldam and S. Calero. “Understanding Nanopore Window Distortions in the Reversible Molecular Valve Zeolite RHO”.. *Chem. Mater.* 27, 5657–5667, **2015**. DOI: 10.1021/acs.chemmater.5b02103. arXiv: 1605.06338.
- S. R. G. Balestra, R. Bueno-Perez, S. Hamad, D. Dubbeldam, A. R. Ruiz-Salvador and S. Calero. “Controlling Thermal Expansion: A Metal–Organic Frameworks Route”. *Chem. Mater.* 28, 8296–8304, **2016**. DOI: 10.1021/acs.chemmater.6b03457. arXiv: 1610.08122.
- S. Hamad, S. R. G. Balestra, R. Bueno-Perez, S. Calero and A. R. Ruiz-Salvador. “Atomic charges for modeling metal–organic frameworks: Why and how”. *J. Solid State Chem.* 223, 144–151, **2015**. DOI: 10.1016/j.jssc.2014.08.004. arXiv: 1802.08771.
- R. Bueno-Pérez, S. R. G. Balestra, M. A. Cambor, J. G. Min, S. B. Hong, P. J. Merklng and S. Calero. “Influence of Flexibility on the Separation of Chiral Isomers in the STW-Type Zeolite”. *Chem.–Eur. J.*, **2018**. DOI: 10.1002/chem.201705627.
- J. Sánchez-Laínez, A. Veiga, B. Zornoza, S. R. G. Balestra, S. Hamad, A. R. Ruiz-Salvador, S. Calero, C. Téllez and J. Coronas. “Tuning the separation properties of zeolitic imidazolate framework core–shell structures via post-synthetic modification”. *J. Mater. Chem.A* 5, 25601–25608, **2017**. DOI: 10.1039/c7ta08778k.
- A. Sławek, J. M. Vicent-Luna, B. Marszałek, S. R. G. Balestra, W. Makowski and S. Calero. “Adsorption of n-Alkanes in MFI and MEL: Quasi-Equilibrated Thermodesorption Combined with Molecular Simulations”. *J. Phys. Chem. C* 120, 25338–25350, **2016**. DOI: 10.1021/acs.jpcc.6b06957.

- P. Gómez-Álvarez, J. Perez-Carbajo, S. R. G. Balestra and S. Calero. “Impact of the Nature of Exchangeable Cations on LTA-Type Zeolite Hydration”. *J. Phys. Chem. C* 120, 23254–23261, **2016**. DOI: 10.1021/acs.jpcc.6b06916.
- J. J. Gutiérrez-Sevillano, S. Calero, S. Hamad, R. Grau-Crespo, F. Rey, S. Valencia, M. Palomino, S. R. G. Balestra and A. R. Ruiz-Salvador. “Critical Role of Dynamic Flexibility in Ge-Containing Zeolites: Impact on Diffusion”. *Chem. Eur. J.* 22, 10036–10043, **2016**. DOI: 10.1002/chem.201600983.
- A. Torres-Knoop, S. R. G. Balestra, R. Krishna, S. Calero and D. Dubbeldam. “Entropic Separations of Mixtures of Aromatics by Selective Face-to-Face Molecular Stacking in One-Dimensional Channels of Metal-Organic Frameworks and Zeolites”. *ChemPhysChem* 16, 532–535, **2014**. DOI: 10.1002/cphc.201402819.

### Non-peer reviewed journals

- S. Rodriguez-Gomez. “El metodo Monte Carlo”. *MoleQla* 5, 133–135, **2012**. ISSN: 2173-0903.
- S. Rodriguez-Gomez. “Diagrama de fases de un sistema de esferas duras”. *MoleQla* 6, 161–162, **2012**. ISSN: 2173-0903.

### Software

- S. R. G. Balestra, R. Bueno-Perez and S. Calero. *Genetic Algorithm IAST*. 2016. DOI: 10.5281/zenodo.165844. We use Ideal Adsorbed Solution Theory (IAST) to predict the loading of the gas mixture on the bundle, based only on the knowledge of the pure adsorption isotherms of the individual components.

### Unpublished work

- R. T. Rigo, S. R. G. Balestra, S. Hamad, A. R. Ruiz-Salvador, S. Calero and M. A. Cambor. “The Si-Ge substitutional series in the chiral STW Zeolite Structure Type”. submitted Chem. Mater., Manuscript ID: cm-2018-00786e. 2018.
- J. G. Min, A. Luna-Triguero, Y. Byun, S. R. G. Balestra, J. M. Vicent-Luna, S. Calero, S. B. Hong and M. Cambor. “Stepped Propane Adsorption in Pure-Silica ITW Zeolite”. submitted Langmuir, Manuscript ID: la-2018-00628f. 2018.



